NASA TECHNICAL MEMORANDUM

NASA TM X-53568

October 15, 1966

NASA TM X-53568

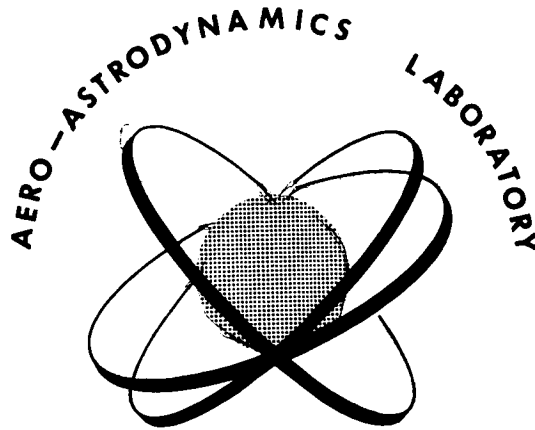# AERO-ASTRODYNAMICS
RESEARCH REVIEW NO. 5

AERO-ASTRODYNAMICS LABORATORY
RESEARCH AND DEVELOPMENT OPERATIONS
GEORGE C. MARSHALL SPACE FLIGHT CENTER
HUNTSVILLE, ALABAMA

NASA-GEORGE C. MARSHALL SPACE FLIGHT CENTER

TECHNICAL MEMORANDUM X-53568

RESEARCH REVIEW NUMBER FIVE
January 1, 1966-June 30, 1966
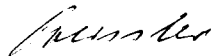
William D. Murphree - Editor

RESEARCH AND DEVELOPMENT OPERATIONS
AERO-ASTRODYNAMICS LABORATORY

October 15, 1966

PREFACE

The topics discussed in this fifth Aero-Astrodynamics
Research Review cover a variety of subjects. Included
are Aerodynamics, Orbit Flight Mechanics, Atmos-
pheric Physics, Control Studies, Aerothermodynamics,
Electromagnetic Theory, Control System Analysis,
Instrumentation, Selenography and Structural Dynamics.
It should be noted that no single review treats all sub-
ject areas being investigated by the Laboratory. Further,
these reviews are not progress reports; rather it is
attempted here to publish works of a research nature
which have reached a milestone worthy of note. Other
subjects will be discussed in forthcoming reviews.

It is hoped that these reviews will be interesting and
helpful to other organizations engaged in space flight
research and related efforts. Criticisms of this re-
view and discussions concerning individual papers
with respective authors are invited.

/geissler/

E. D. Geissler
Director, Aero-Astrodynamics Laboratory

CONTENTS...   Page

I. AERODYNAMICS

DISCONTINUOUS FLOWS AND FREE STREAMLINE SOLUTIONS FOR AXISYMMETRIC BODIES AT ZERO AND SMALL ANGLES OF ATTACK

By

Heinz G. Struck

SUMMARY

Except for a few numerical results, nothing has been published comparable in magnitude to the two-dimensional case concerning free streamline solutions of the axisymmetric problem. Since the method of using conformal transformations is not available in axisymmetric and three-dimensional flows, it is necessary to adapt approximate methods for the free streamline analysis.

In this study an integral equation procedure has been applied to calculate the free streamline flow behind axisymmetric bodies at zero and small angles of attack. The method uses a modified condition for irrotational flow and iterates until the proper streamline location is found. Some of the results obtained by this procedure will be given and discussed in this report.

I. INTRODUCTION

The flow field about a body of revolution is usually determined by placing singularities along the axis of symmetry. Rankine [1] was thus able to calculate families of bodies by distributing point sources of variable strengths on the axis. Later, this method was improved by Taylor [2] and Fuhrmann [3]. Many years later, Weinstein [4] applied surface singularities to determine the flow fields about obstacles such as rings, disks, and cylinders. Further contributions to the indirect problem, in which the source strength is given and the corresponding body shape is sought, were made by Van Tuyl [5] and Sadowsky and Sternberg [6].

The direct problem, where the contour of the body is given and the corresponding strengths of the sources are to be determined, was first solved by von Karman [7] with an axial distribution of singularities for the zero and finite-angle-of-attack case. Lotz [8] probably published the first method utilizing surface singularities; however, before that, Trefftz [9] had used annular sources to calculate

the contraction coefficient of the vena contracta. Later, Riegels [10] extended the method of Lotz [8] and applied it to bodies of revolution that deviate slightly from rotational symmetry. All the above mentioned methods dealt with Dirichlet flows that do not permit the calculation of any drag.

The Helmholtz flow concept meant an improvement since it enabled the aerodynamicist to calculate a drag coefficient. Over the years a tremendous amount of literature on the two-dimensional Helmholtz-flow has accumulated. The first approximate solution of the axisymmetric problem was published by Bauer [11]. He applied an axial distribution of sources to determine the drag of a sphere. However, this method is not well suited, since the flow field is everywhere continuous except on the axis. Therefore, the proper discontinuities cannot be duplicated at the separation point of the flow.

Consequently, Armstrong and Dunham [12] applied a surface distribution and devised an iterative scheme to determine the proper location of the free streamline. However, results calculated with this method were never published. The first numerical results for a disk placed normally to the stream were given by Garabedian [13].

In this report, the method of Riegels [10] is extended to the Helmholtz-flow concept. The surface of the forebody and the free streamline are replaced by surface singularities. The location of the free streamline must be assumed for the first iteration. The final proper location must be obtained by an iteration that satisfies certain specified boundary conditions. The problem contains at least one parameter for a forebody with fixed separation, probléme du sillage, the base pressure c_{pB} right behind the separation point, which is assumed to be constant along the remainder of the streamline. However, if the flow separates from a smooth body, for example, a sphere or ellipsoid, the problem will have one additional parameter, the separation point s_B, (probléme de la proue). In the case of cavitational flow, the base pressure is approximately equal to the vapor pressure of the liquid, and the pressure is

. constant throughout the cavity. For the case of wake flow, the base pressure must be obtained from experimental data, and the assumption that the pressure is constant along the wake is questionable. Boundary layer theory can be applied to determine the separation point.

A new linearized model is developed for the lifting body. The assumption of the Helmholtz flow is also valid for this model. The pressure within the separated cavity remains constant, and additional pressures due to the normal flow are equalized across the circumference of the cavity, thus causing the local lift along the cavity to vanish. The cavity is therefore shifted to an asymmetrical location to satisy the no-lift condition.

II. THE DIFFERENT CAVITY OR WAKE MODELS

Three free streamline models are indicated in Figure 1 in comparison with the original Helmholtz-Kirchhoff classical model. The three models B, C, and D are all characterized by the fact that the free streamline velocity $V_T(s)$ is greater than the approach velocity U_∞.
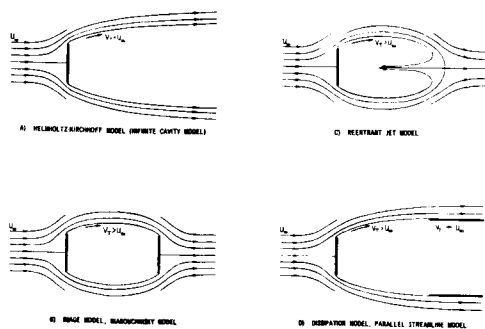

FIGURE 1. FREE STREAMLINE MODELS FOR SEPARATED FLOW BEHIND A NORMAL FLAT PLATE OR DISK

In the Helmholtz-Kirchhoff model A, the infinite cavity model, the base pressure c_{pB} is zero, and consequently the calculated drag is less than the drag observed in experiments. To correct this deficiency, higher velocities must be permitted on the free streamline. Then, however, the streamlines curve back to the axis of symmetry, and certain cavity closure devices must be introduced. Thus, in model B, the image or Riabouchinsky model, the

free streamline reattaches to an artificial image plate or disk introduced at the end of the cavity. Only the drag of the first body is determined. The ultimate wake thickness is zero. In model C, the reentrant jet model, the wake or cavity ends in a stagnation point from which a reentrant jet projects forward toward the body base and vanishes there. This is an unreal feature, though it has some similarity to the often forward-thrown spray observed in cavities at low pressure. As in the Riabouchinsky model, there is a stagnation point at the end of the cavity, and the ultimate wake thickness is slightly negative because of the fluid removed in the reentrant jet. Model D is sometimes called the dissipation model or parallel streamline model. It probably describes the wake flow better than the cavity flow. Here, the downstream wake thickness is not zero. The pressure is initially constant along the streamline springing from the disk edges, until they reach their maximum wake diameter. From here on, the direction of the velocity vector remains constant; its magnitude, however, decreases until $V_T(s)$ is equal to U_∞, the velocity of the undisturbed flow field.

III. THE AXISYMMETRIC CAVITY

Following Helmholtz's suggestion, the free streamline discontunity surface is taken as an idealization of the separation surface which divides the main flow from the wake which follows separation. In idealizing, the separation surface, like a vortex sheet in wake flows, grows in thickness through viscous action as the flow proceeds. The thickness of the sheet is taken vanishingly small, and the flow on one side is assumed to have no effect on the other except via the pressure. For cavitating flows with ratios of cavity density to fluid density vanishingly small, the flow in the cavity is assumed as quiescent, and it is therefore a constant pressure region.

The blunt-based obstacles, including the free streamline emanating at s_B and extending downstream, are considered as one body (Fig. 2). The boundary conditions along the contours Γ_1, Γ_2 are of mixed kind. Upstream of the separation point, s_B, the contour Γ_1 is given and rigid. Downstream of the separation point, s_B, the potential $\Phi(s)$ --$\partial\Phi(s)$ = $V_T(s)\partial s$--is specified along the free streamline, Γ_2, since the tangential velocity component, $V_T(s)$, or the pressure coefficient, $c_{pW}(s) = 1 - V_T^2(s)$, is

given. For the first approximation a tentative free streamline, Γ_2^*, is chosen on some reasonable basis. However, the potential, Φ^* (s), will in
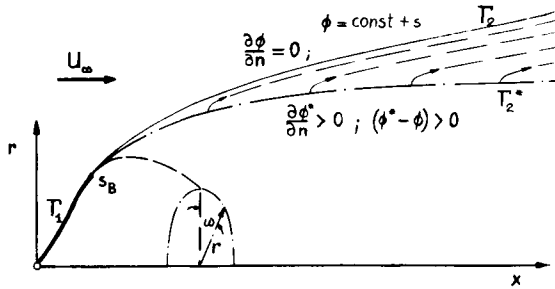

FIGURE 2. THE FREE STREAMLINE FOR AXISYMMETRIC FLOW

general not correspond to the specified Φ(s) along the proper, yet unknown contour, Γ_2. Therefore, a normal velocity component, $\partial\Phi^*/\partial n$, which is proportional to the potential-difference, $(\Phi^* - \Phi)$, on the assumed free streamline, Γ_2^*, will be allowed to form, with the undisturbed outer flow U_∞, a new

streamline, Γ_2^{**}. A procedure which converges automatically on the proper streamline, Γ_2, can be obtained by a modification of the condition for irrotational flow which reads in streamline coordinates.

$$\frac{\partial^2\Phi}{\partial s\partial n} = \kappa \frac{\partial\Phi}{\partial s} ,$$

where κ is the curvature of the streamline, s the arc length along the contour, and n the direction normal to s pointing in the positive outward direction. For the solution of the problem, we assume that (1) the influence of the boundary layer on the drag of the body is negligible, (2) the influence of gravity is not important, and (3) the cavity remains axisymmetric and the outer flow remains stationary. The problem is thus completely determined.

IV. THE CAVITY OF THE LIFTING BODY

The cavity or wake of a body placed at a small angle of attack to the undisturbed flow will, under the influence of the outer field, shift to an asymmetric position. The rigid forebody is subjected to a lift force which is proportional to the angle of attack, $\overline{\alpha}$ and the downwash angle of the cavity will be proportional to the lift of the body. This is similar to the vortex sheet emanating from the trailing edge of a wing. The circumferential velocity component,

$w(s, \overline{\alpha})$, will be carried past the separation point, s_B, on to the free stream tube, Γ_2, and additional pressures on the cavity or wake contour will deform and stretch it normal to the angle-of-attack plane, thus satisfying the pressure continuity condition again. A necessary conclusion, assuming that the free stream tube cannot sustain any pressure gradient normal to its axis, is therefore the vanishing of the local normal force. In the plane of the separation point, however, the wake is rotational and for small angles of attack, $\overline{\alpha}$, will only slightly deviate from rotational symmetry for some distance downstream of the separation point, s_B. In proceeding to calculate the flow field about a body at small angles of attack, we develop the potential of an axisymmetric body where part of the axis is bent and follows the function, z(x) (Fig. 3). The bending function z(x) is connected
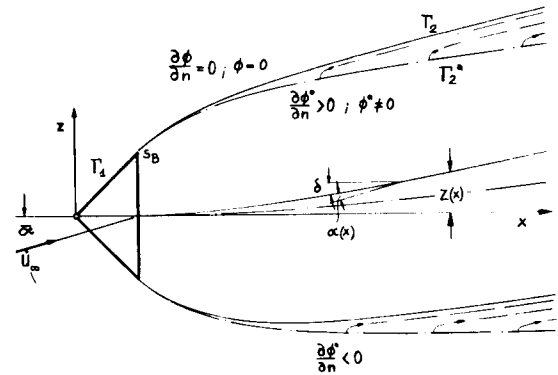
FIGURE 3. THE FREE STREAMTUBE FOR THE LIFTING BODY

with the local angle of attack α(x) along the wake line by

$$\frac{dz}{dx} = \overline{\alpha} \left(1 - \frac{\alpha(x)}{\overline{\alpha}}\right).$$

The approximate potential of this body can be developed into a series with $\overline{\alpha}$, and we obtain the perturbation potential:

$$\varphi(s, \alpha) \approx -\frac{\overline{\alpha}}{4\pi} \left\{ \iint\limits_{(s)} \mu(\sigma)\cos\omega' \rho \left(\frac{1}{R} - \frac{2\overline{\alpha}(r\cos\omega - \rho\cos\omega')}{R^3}\right) \left[\int_{x_B}^{x}\frac{dz(x)}{dx}dx - \int_{x_B}^{\xi}\frac{dz(\xi)}{d\xi}d\xi\right] + O(\alpha^2)\right] d\omega'd\sigma\right\} ,$$

where R is the distance between the points on the contour P(x, r, ω) and P(ξ, ρ, ω').

The strength of the source distribution, $\mu(s)$, is a function of the local angle of attack, $\alpha(x)$, along the wake centerline, since it was obtained by satisfying the boundary condition along the bent wake contour. We observe that the second term under the double integral is of the order of $\bar{\alpha}^2$. For small angles of attack, we can neglect it, and the remaining term is again the potential of a straight axisymmetric body although with a variable angle of attack distribution along the wake. Furthermore, velocity components originating from the second term of the above equation are connected with $\cos^2\omega$, where ω is the meridian angle of the body and will thus give no contribution to the lift of the body. Keeping this in mind, we can formulate the problem now under simplified assumptions.

1. The contour of the stream tube remains, for small angles of attack, rotational symmetric; its diameter will be adopted from the axisymmetric flow.

2. The wake sections are displaced parallel so that the center falls on a curve, $z(x)$, the bending function of the centerline of the wake.

3. The local normal force shall vanish along the wake. Satisfaction of the local pressure continuity condition around the circumference of the wake is neglected.

4. Only linear influences of $\bar{\alpha}$ are considered.

5. Only bodies of revolution are considered whose separation points are lying in one normal plane to the body axis and do not change with angle of attack, thus excluding round bodies such as spheres, ellipsoids, etc., which permit an inner separation (separation occurs between stagnation and end point of the fixed contour).

With assumption 3, the determination of the proper location of the streamline Γ_2 is attempted. We can obtain an automatic convergence procedure by using again the condition for irrotational flow, now modified, since the curvature, κ, changes around the circumference.

$$\frac{\partial}{\partial s}\left[\frac{\partial}{\partial n}(\Phi_0 + \Phi_1)\right] = \left(\kappa + \frac{d\alpha}{dx}\cos\omega\right)\frac{\partial}{\partial s}(\Phi_0 + \Phi_1),$$

where Φ_0 is the total potential of the axisymmetric flow and Φ_1 the potential of the body in normal flow. Superposition of Φ_0 and Φ_1 produces the flow field about an inclined body of revolution.

For the first approximation, a reasonable angle-of-attack distribution, $\alpha(x)$, along the wake is assumed. The remaining local normal force is converted into the potential function, and again a normal velocity component, $\partial\Phi_1/\partial n$, is allowed on Γ_2^*. With the potential difference, $(\Phi_1^* - \Phi_1)$, a new free streamline, Γ_2^{**}, and consequently an angle-of-attack distribution, $\alpha^{**}(x)$, is calculated. This procedure is continued until the local normal force $c_n(s)$ vanishes.

V. CALCULATED CASES AND COMPARISON WITH EXPERIMENTS

Garabedian [13] determined the flow field around a disk using the Riabouchinsky model for two base pressures. For the disk with $c_{pB} = 0$ (the infinite streamline case), he obtained the drag coefficient, $c_D(0) = 0.827$. The corresponding drag coefficient calculated with the present method for the same base pressure yielded $c_D(0) = 0.825$. (From now on the number in the parentheses designates the base pressure at which the drag coefficient was determined.) For the calculation, the boundary condition was satisfied at discrete points along the arc-length of the contour, 16 points were distributed on the forebody, and 64 points on the free stream line up to a downstream distance of 30 radii. The points were more closely placed at the separation point. In Figure 4 the difference in the location of the free streamlines of plane and rotational symmetric flow for the same base pressure is presented. It shows one main feature of the rotational symmetric flow field. The wake is narrower than that of the plane flow field. The second drag coefficient, obtained by Garabedian with a different method, was for a base pressure of $c_{pB} = -0.2235$. The modified drag coefficient, $c_D'(-0.2235) = c_D/(1 - c_{pB})$, had the bounds $0.85 < c_D' < 0.88$. His best estimate was $c_D' = 0.865$. A recalculation of this case produced $c_D' = 0.8295$, a rather marked difference, though the maximum cavity diameter in both cases agreed much better, $D_C/2R = 2.3$, as compared with 2.28 obtained by the present method.

In Figure 5 a comparison of the drag coefficient obtained from water tunnels, [14, 15], and the present numerical method is given. Cones of different vertex angles were placed into a water tunnel and their bases
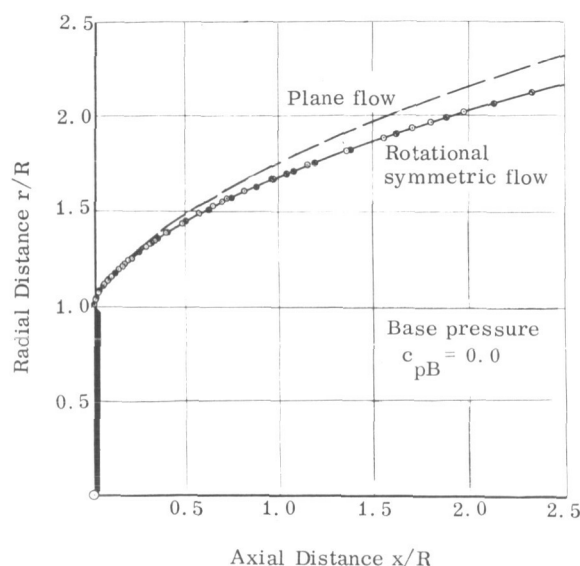
FIGURE 4. THE FREE STREAMLINE FOR
VANISHING BASE PRESSURE IN PLANE AND
ROTATIONAL SYMMETRIC FLOW

of cones are given in Table I. The numbers designated with an asterisk are obtained with the Riabouchinsky model; the rest were obtained by the dissipation model. It might be noted that all models, despite their differences, converge to the infinite streamline model for a base pressure of $c_{pB} = 0$.

A comparison of the two drag coefficients for $c_{pB} = -0.41$ and the disk, $\beta = 90°$, gives an indication of the difference between the Riabouchinsky and the dissipation model. However, for smaller c_{pB}, the difference in drag will definitely become greater.

TABLE I. DRAG COEFFICIENTS OF CONES

$c_{pB} =$	0.0	−0.05	−0.10	−0.20	−0.2235	−0.30	−0.41	−0.60
$\beta = 15$	.1460		.2014					
45	.5042		.5694	.6360				
63.4	.6679							
90	.8238	.8664	.9092	.9955		1.0822	1.1777	1.3455
					1.0144*		1.1767*	

The cavity behind a disk was photographed in Kiceniuk [15] and is reproduced in Figure 6. The measured base pressure for this case, $c_{pB} = -0.188$, was remarkably constant throughout the cavity up to a distance of six disk-diameters downstream. The free streamline for the same c_{pB} was drawn on the photograph, and a very good result was obtained. The free streamline corresponds to the dissipation model, and therefore the streamlines run parallel from the maximum cavity diameter on downstream.

FIGURE 5. THE DRAG COEFFICIENT OF THE
STAGNATION CUP AND DIFFERENT CONES AS
A FUNCTION OF THE BASE PRESSURE
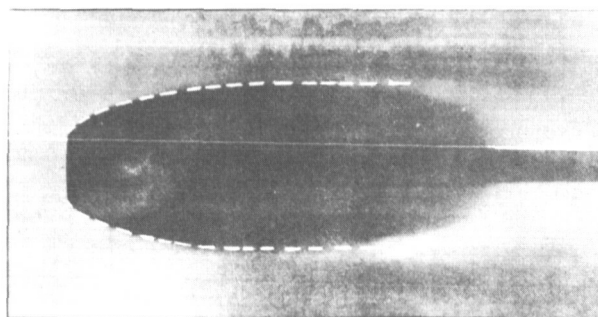
FIGURE 6. THE CAVITY BEHIND A DISK.
BASE PRESSURE COEFFICIENT $c_{pB} = -0.188$

were ventilated to obtain different base pressures. The theoretical results reproduce perfectly the experimental data. Some numerical results for drag

The flow field and the wake behind a disk with a base pressure of $c_{pB} = -0.41$ were surveyed in a

6

wind tunnel [16]. The pressure and velocity profiles in radial direction were measured, and the corresponding mean streamline $\psi = 0$ was calculated. The theoretical free streamlines obtained with two different models were compared with the experimental one in Figure 7. The measured drag was given as $c_D = 1.13$, whereas the theoretical yielded $c_D = 1.18$. The free streamline of the Riabouchinsky model was not continued beyond $x/R > 3$, since the measured pressures along the wake differed greatly from the assumption of constant pressure for the theoretical model.
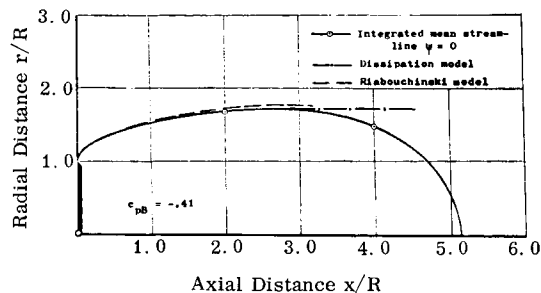
FIGURE 7. COMPARISON OF THEORETICAL FREE STREAMLINES WITH MEAN STREAMLINE OBTAINED FROM EXPERIMENTS. BASE PRESSURE COEFFICIENT $c_{pB} = -0.41$

For the case where the free streamline separates from a curved obstacle, the problem contains a second parameter, the separation point, which is not fixed as in the case of separation from a body with a sharp corner.

Figure 8 shows the indeterminacy of the separation point on a sphere for a base pressure coefficient of $c_{pB} = 0$. Three separation points are chosen. The corresponding pressure distributions on sphere surface and free streamline are plotted in Figure 8a. The radial derivative with respect to the arc length is plotted in Figure 8b for the three cases and Figure 8c shows the corresponding curvature κ of the free streamlines. The curve with the index 2 indicated the case for smooth separation. Here, the derivative of the pressure coefficient with respect to the arc length, dc_p/ds, is a continuous function on the wetted sphere and free streamline. This is the condition for smooth separation. At this point, the radial derivative and the curvature are smooth functions of the arc length. The curve with the index 1 shows the case where the flow separates upstream of the point of smooth separation. The pressure
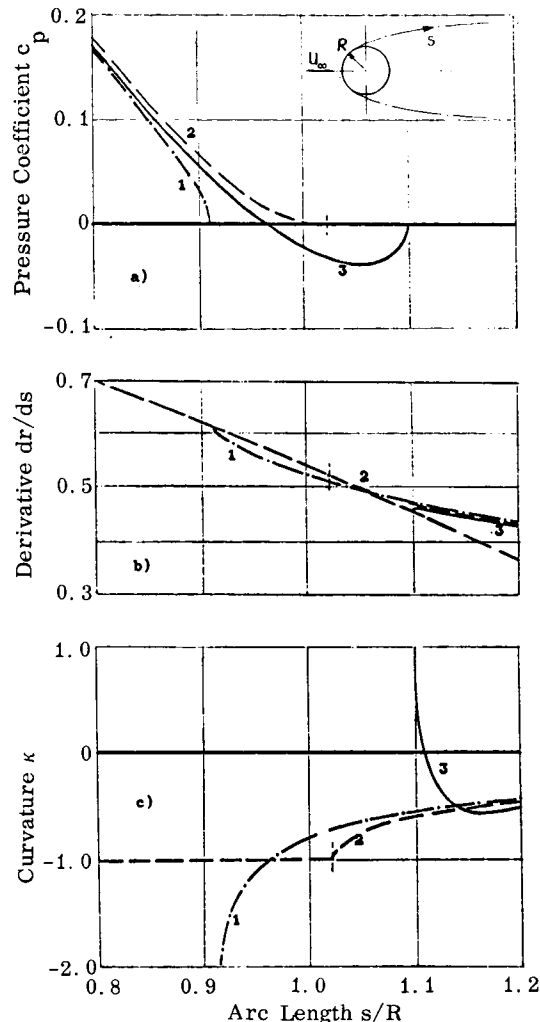
FIGURE 8. THE POSSIBILITIES OF SEPARATION FROM A SMOOTH SURFACE. BASE PRESSURE COEFFICIENT $c_{pB} = 0$

coefficient, $c_p(s)$, on the sphere vanishes with an infinite negative tangent at the separation point, and the curvature, κ, is convex and greater than the curvature of the sphere. The free streamline consequently penetrates the solid body, and this case of an abrupt separation is therefore physically unrealistic. One other abrupt separation is shown by the curve with the index 3 downstream of the point of smooth separation. The pressure vanishes at the separation point with a positive infinite tangent. The minimum pressure occurs on the sphere, and the pressure in the cavity is higher. The curvature of the free streamline at the separation point is concave

for a short distance, then has an inflection point and becomes convex further downstream and decreases monotonically. For cavitational flow, one can argue that the pressure must be a minimum in the cavity, for otherwise, even small reduction in the pressure coefficient, c_p, would induce cavitation elsewhere. This implies that the free streamline must be convex toward the cavity. By Bernoulli's Theorem, this is equivalent to the condition that the velocity is a maximum on the free streamline. Assuming convexity, for the free streamline not to penetrate the obstacle, the free streamline must have finite curvature. In fact the local curvature of the obstacle cannot be exceeded. These Brillouin separation conditions point out that the smooth separation is the only physical possibility for cavitation to occur.

The Brillouin separation conditions were tested in a water tunnel [17] on a sphere. The results are plotted in Figure 9. The drag coefficients on spheres obtained by the use of axial singularities

smooth separation occurring at an angle of about $\Phi_S \approx 56°$ to $57°$ measured from the stagnation point.

The corresponding drag coefficient obtained by the present method yields $c_D(0) = 0.31$. It seems, however, that cavitation does not occur at the point of smooth separation, probably because of surface tension. The cavitation occurs, rather, at greater angles, $\Phi_S \approx 80°$, depending mildly on base pressure coefficient. Using these separation angles, the corresponding drag coefficients were calculated. By varying the separation angle by a few degrees and plotting the corresponding drag result, it was found that the drag coefficients as shown in Figure 9a were close to the minimum drag coefficient of the sphere for fixed base pressure coefficient.

In Figure 10 an attempt was made to predict the laminar separation point of the sphere. The boundary layer method used can be found in Schlichting [18]. The boundary layer equation is solved by a series approximation of the "separated" velocity distribution;
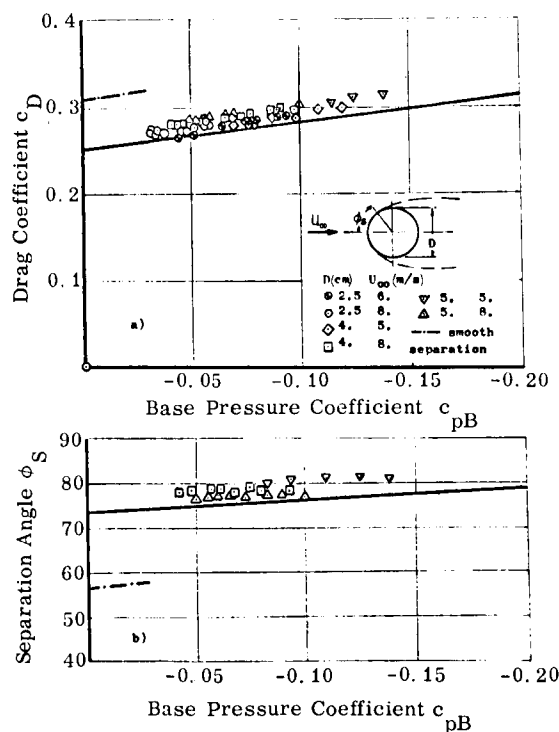

FIGURE 9. DRAG COEFFICIENT AND SEPARATION ANGLE FOR A CAVITATING SPHERE. (SMOOTH AND ABRUPT SEPARATION)

(flow past a half body) were given as $c_D(0) = 0.30$ in Bauer [11]. This result can be compared to the
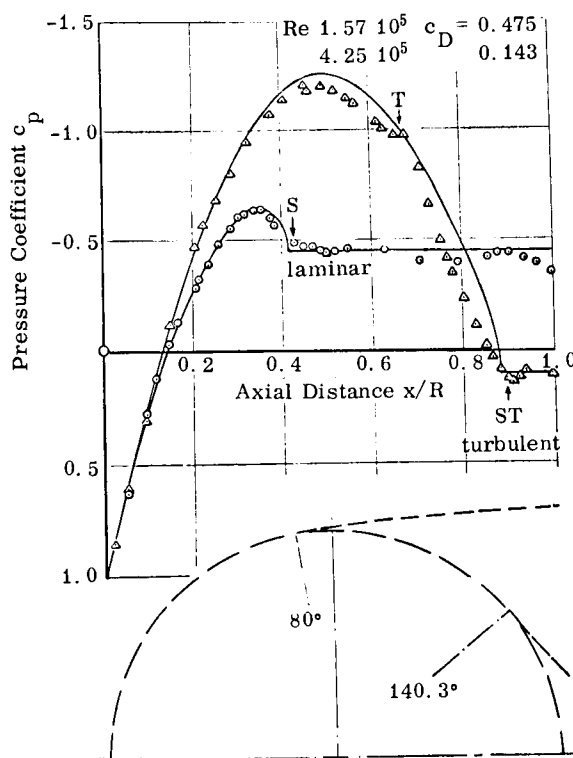

FIGURE 10. THE PRESSURE DISTRIBUTION ABOUT A SPHERE FOR LAMINAR AND TURBULENT SEPARATION

the solution was obtained by an iterative procedure. For a fixed base pressure coefficient of c_{pB} = -0.45, an arbitrary separation point around $\Phi_S \approx 80°$ was chosen. The resulting velocity distribution on the sphere was developed into a polynomial containing terms of up to (s^7) where s is again the arc length. The boundary layer equations were then solved, and a new separation point was obtained.

The wind tunnel experiment yielded a separation point of $\Phi_S \approx 81°$. The iteration procedure predicted a separation point of $\Phi_S \approx 77^4+$. One of the difficulties was to reproduce the velocity distribution in the neighborhood of the separation point. A more modern procedure might have given a much closer result. Figure 10 shows the theoretical pressure distribution for a laminar separation at Φ_S = 80°. The turbulent theoretical pressure distribution is also plotted in Figure 10. Turbulent separation was measured at Φ_S = 143°. Because of the laminar separation bubble (T) on the lee side of the sphere, the theory does not quite reproduce the actual pressure distribution over that portion of the surface.

The lift of cones was measured in the water tunnel [15]. Figure 11 shows the lift gradient for zero angle of attack and a base pressure of c_{pB}=0.0 and -0.1. The base pressure, a function of the angle of attack, was held constant for these investigations. One notices that, with decreasing base pressure coefficient, the lift gradient also decreases. For very small cone half angles, the lift slope approaches the "slender body" result of $dc_L/d\bar{\alpha}$ = 2. With increasing cone half angle, however, the lift gradient decreases and becomes negative until at β = 90° only the drag component contributes to the lift.

The lift, moment, and drag coefficient of cones with half angles of β = 15°, 45°, and 90° and a constant base pressure coefficient of c_{pB} = -0.1 are plotted as a function of the angle of attack in Figure 12. The disk is here considered as a cone of 90° half-angle. For technical reasons the angle of attack was chosen to be negative. The drag coefficient, $c_D(\bar{\alpha})$, as a function of the angle of attack is fairly well reproduced by the linearized theory except for the cone of β = 15° where the theory does not quite predict the increase in drag with angle of attack. It is possible that some higher terms in $\bar{\alpha}$ which are neglected here play a certain role. The lift coefficient is satisfactorily reproduced as is the moment coefficient over the angle-of-attack range where separation
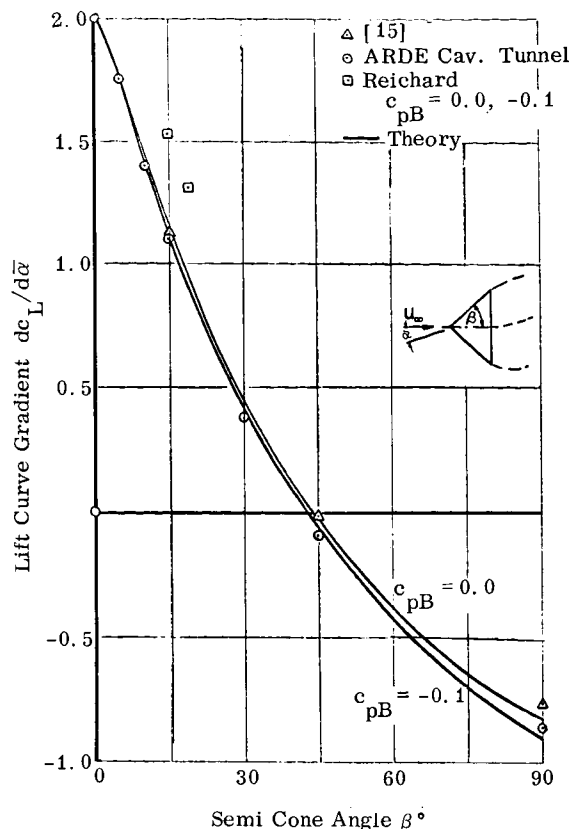
FIGURE 11. LIFT CURVE GRADIENT FOR CONES OF DIFFERENT VERTEX ANGLES AND CONSTANT BASE PRESSURE COEFFICIENT

of the flow from the lee side of the body is not expected, $\bar{\alpha} \leq \beta$. The reference point for the momentum coefficient was in all cases the center of cone bases and the stagnation point of the disk.

A comparison of the downwash angle behind cones of 15°, 45°, and 90° half-angles is given in Figure 13. With decreasing cone half-angle β, which corresponds to increasing lift of the forebody, the ratio of the local wake angle of attack, $\alpha(x)$, to the angle of attack of the forebody, $\bar{\alpha}$, increases. For a disk, therefore, the wake leaves the base essentially in the same direction as the free stream, whereas for cones the downwash angle increases behind the base and approaches asymptotically a certain limiting value at infinity, according to the normal force of the forebody.

To obtain an idea of how well the approximate theory describes the wake of a body at angle of attack, the free streamlines were drawn into the shadow-graphs of the flow configurations of Figures 14 and 15.

9
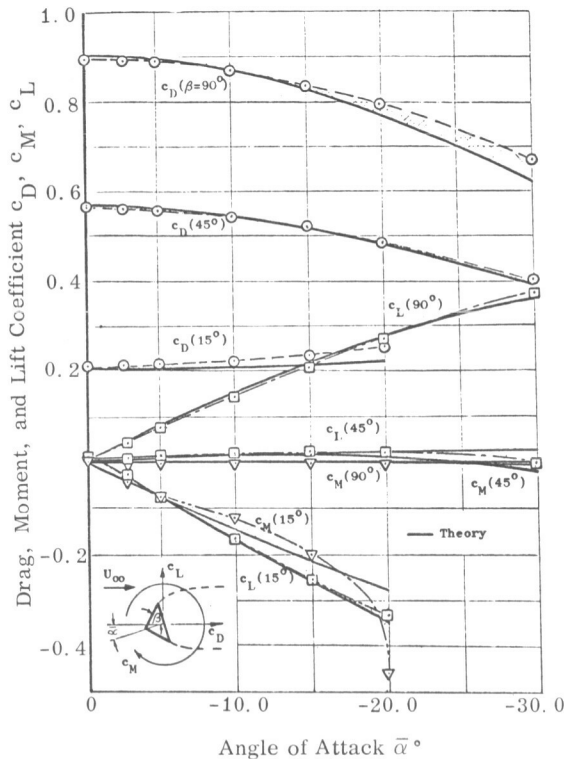
FIGURE 12. DRAG, MOMENT, AND LIFT
COEFFICIENT FOR THREE DIFFERENT CONES
AS A FUNCTION OF ANGLE OF ATTACK
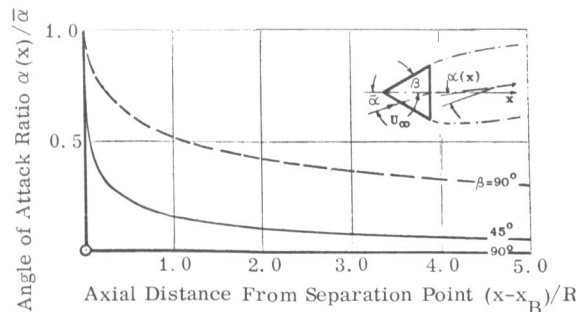
FIGURE 13. THE NONDIMENSIONAL
DOWNWASH ANGLE BEHIND CONES AT
ANGLE OF ATTACK

Figure 14 shows a cone of 50° half-angle at an angle
of attack of $\bar{\alpha} = 10°$. The base pressure coefficient
was measured at $c_{pB} - 0.4$. The lower edge of the
wake is fairly well represented close to the body
where the shear layer of the wake is relatively small.
Figure 15 shows the wake of a 15° cone at $\bar{\alpha} = 10°$
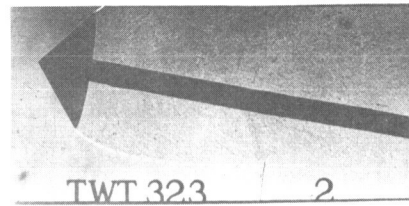
FIGURE 14. FLOW ABOUT A 50° CONE AT
10° ANGLE OF ATTACK. BASE PRESSURE
COEFFICIENT $c_{pB} = -0.4$
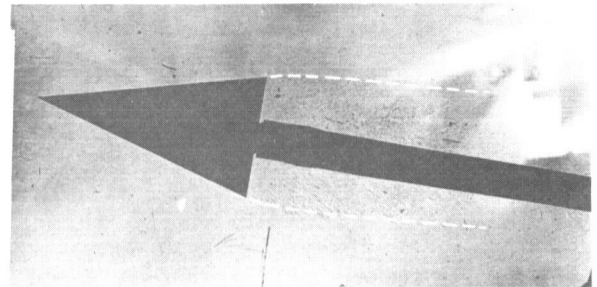
FIGURE 15. FLOW ABOUT A 15° CONE
AT 10° ANGLE OF ATTACK. BASE PRESSURE
COEFFICIENT $c_{pB} = -0.32$

with a base pressure of approximately $c_{pB} = -0.32$.
Wake boundary and free streamline show again a
fair coincidence, at least up to two diameters behind
the base of the cone. The free streamlines for both
cones were obtained with the dissipation model.

VI. FURTHER APPLICATIONS

In the area of steady discontinous flows, other
applications of the theory are possible. In some
engineering problems, the added or virtual masses
of bodies at separated flow conditions (for instance,
meteorological balloons and parachute canopies)
must be known to determine their dynamical be-
havior. The theory yields these quantities readily.
Furthermore, rotational symmetric bodies can be
constructed whose surfaces have a certain prescribed
pressure distribution. However, the given distri-
bution must obey certain rules in order not to pro-
duce negative body radii. Into the same category

falls the problem of designing the optimum shape of the cowl of a rotational symmetric jet intake. Another class of problems is the flow out of an orifice, jet penetration, and cavity and jet flows under the influence of gravity fields. The theory is directly applicable to some of the mentioned problems, whereas for certain others, slight modifications in the boundary conditions must be made.

VII. CONCLUSIONS

The flow about bodies of revolution with blunt bases separates and forms a free streamline which divides the flow field into an outer flow region and the wake region with zero velocities. In case of cavitational flow this free streamline is clearly visible in flow pictures. For wake flows the free streamline concept is merely an idealization of the free shear layer.

An integral equation method using singularities on the surface of the body and the free streamline was applied to obtain solutions for the mixed boundary-value problem. A condition for rotational free flow was utilized in the iteration procedure to calculate the position of the free streamline for axially symmetric and normal flow. The problem contained two parameters for the case of separation from a smooth body: the base pressure c_{pB} and the separation point s_B on the surface of the rigid body. With the help of boundary layer theory the second parameter can be eliminated, as was proven with an example (laminar separation from a sphere). The base pressure c_{pB} for wake flow must be obtained from experiment. For cavitational flow c_{pB} is equal to the vapor pressure of the liquid.

A number of examples were given, and theoretical and experimental results were compared. Excellent to good agreement of drag, lift, moment, and induced drag coefficients was achieved even at moderate angles of attack. The excellent agreement between theory and experiment proves further that the free streamline concept can be applied to wake flows as long as one is concerned with the forces of the rigid body only.

REFERENCES

1. Rankine, W. J. M.: Phil. Trans., 1871.

2. Taylor, D. W.: Transactions of the Inst. of Naval Archit., vol. 35, 1894.

3. Fuhrmann, G.: Jahrb. der Motorluftschiff-Studienges., 1911-1912.

4. Weinstein, A.: Quart. Appl. Math., vol. 5, no. 4, 1948.

5. Van Tuyl, A.: Quart. Appl. Math., vol. 7, no. 4, 1950.

6. Sadowsky, M. A. and Sternberg, E.: Quart. of Appl. Math., vol. 8, no. 2, 1950.

7. Karman, Th. v.: NACA TM 574, 1930, oder Abhandl. aus dem Inst. der TH Aachen Heft 6 3-17, 1937.

8. Lotz, I.: NACA TM 675, oder Ing. Arch., vol. 2, 1931, p. 507.

9. Trefftz, E. Z.: Math. Phys., vol. 64, 1916, pp. 34-61.

10. Riegels, F.: Mitteil. Max-Plank-Inst. f. Strömungsf, no. 5, 1952.

11. Bauer, W.: Ann. der Physik, vol. 80, 1926, pp. 232-244.

12. Armstrong, A. and Dunham, J.: Armament Res. Est. Rep., no. 12/53, 1953.

13. Garabedian, P. R.: Pacif. J. Math., vol. 6, 1956, and Bull. Amer Math. Soc., vol. 62, 1956, pp. 611-684, pp. 219-243.

14. Reichart, H.: Min. Aircraft Prod. Rep. and Transl., no. 766, 1946.

15. Kiceniuk, T.: Cal. Inst. of Techn. Hydrodyn. Lab. Rep., no. E-12.17, 1954.

REFERENCES (Concluded)

16. Carmody, T.: J. Basic Engin., Dec. 1964, pp. 869-882.

17. Hsu, E. Y. and Perry, B.: Cal Inst. Of Techn. Hydrodyn. Lab.

18. Schlichting, H.: Grenzschicht Theorie, G. Braun Verlag, Karlsruhe, 1951.

BIBLIOGRAPHY

1. Birkhoff, G. and Zarantonello, E. H.: Jets, Wakes and Cavities. Academic Press Inc., 1957.

2. Gilbarg, D., Jets and Cavities. Handbuch der Physik, vol. IX, Springer Berlin, 1960, pp. 311-445.

3. Roshko, A.: NACA TN 3168, 1954.

4. Eppler, R. J.: Rat. Mech. and Analysis. Vol. 3, 1954, pp. 591-644.

II. AEROTHERMODYNAMICS

ACOUSTIC AND HEAT TRANSFER ASPECTS OF LAUNCH VEHICLE TURBULENCE

By

F. Krause and W. K. Dahm

I. INTRODUCTION

The development of large launch vehicles presents the aerodynamic engineer with unusual problems, since the main emphasis is on structural integrity rather than on minimum drag. Cost savings caused by drag reduction are sometimes more than offset by the additional cost of carrying the weight of an aerodynamically smooth enclosure into orbit. As a result, rockets exhibit sharp corners, frustrums, protuberances, external packages, and pipe lines, which produce all sorts of flow separations and generate intense local turbulence and oscillating shocks. Thus, vehicle shapes are horrible contraptions from the point of view of the aerodynamicist, who is accustomed to designing airplanes smooth and sleek, with the drag-producing flow separations and shock waves kept as weak as possible.

The arts of aerodynamics, fluid mechanics, and chemical engineering are needed to reduce the undesirable unsteady forces and heating loads, which are produced by flow separation, reattachment, and oscillating shocks in the aerodynamic environments of launch vehicles. The problems associated with turbulence, acoustics, and heat transfer go beyond previous, more fundamental studies which treated only clean and simple geometries, uniform approach flows without shocks, and forebody boundary layer development derived from flat plate investigations. Furthermore, flow separations associated with surfaces of airfoils differ from the local flow separations on launch vehicles to such an extent that the existing information cannot be used directly. Therefore, launch vehicle turbulence and the associated acoustical and heating loads offer exciting and challenging advanced research problems, the solutions of which are urgently needed because of their practical implications to the space program.

In the following review, we will try to classify the regions of intense turbulences that have been identified from schlieren and shadowgraph pictures. The wall pressure fluctuations below these regions lead to aerodynamic forcing functions which excite vibrations of the vehicle skin. The pressure fluctuations below the different flow fields are therefore discussed with respect to broad-band and narrow-band

excitation of single modes. The final section deals with heat conduction in recirculation areas at the vehicle base and the associated turbulent heat transfer.

II. LOCAL FLOW SEPARATION

Regions of intense turbulence are characterized by large fluctuations of velocity, pressure, and other thermodynamic properties. These are to be expected in areas of separated flows. We have therefore used schlieren and shadowgraph pictures to locate the main regions of flow separations. Subsequent spot checks of wall pressure fluctuations are discussed in later sections to describe the turbulence in these separation areas.

Most flow separations are produced by shock waves in front of forward-facing protuberances and interstage areas. Two good examples are shown by Figure 1. Another type of separation is provided by
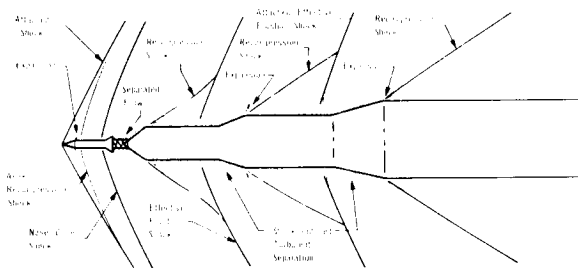
FIGURE 1. FLOW FIELD ABOUT TYPICAL SATURN SERIES VEHICLE

the wakes which are shed from the escape tower and rearward-facing protuberances. All shock wave and separation patterns vary with Mach number in a complicated, but systematic fashion These variations are summarized in Figures 2 and 3. The pattern differs for initially attached and initially separated flows, and for transonic and supersonic flows.

In transonic and initially attached flows, a forked shock wave which moves slowly downstream as the Mach number increases is produced. Its position is
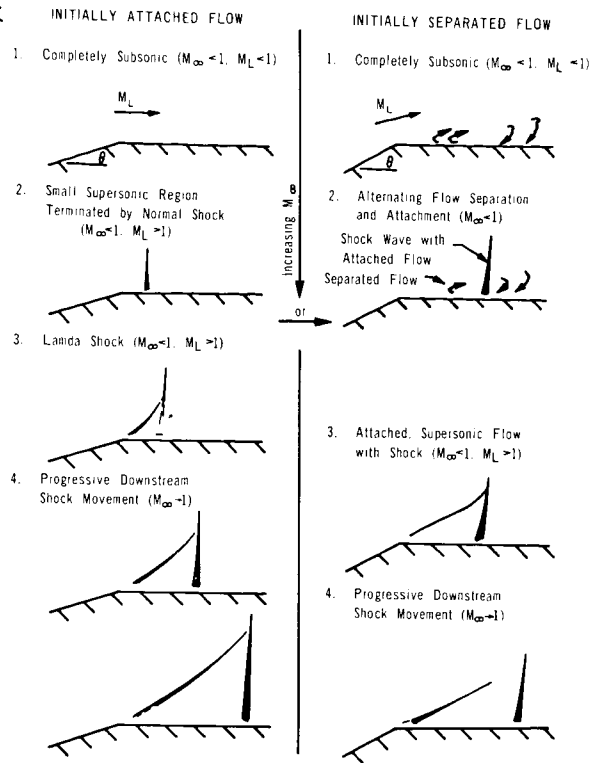
FIGURE 2. DEVELOPMENT OF SHOCK WAVES BEHIND EXPANSION CORNERS IN TRANSONIC FLOW

FIGURE 3. SHOCK WAVES IN COMPRESSION CORNERS

determined by the area rule, that is, by the streamwise distribution of the vehicle cross sections. The shocks are relatively stable; only their roots may oscillate. In initially separated flows, a similar shock configuration is finally developed. However, at intermediate Mach numbers, sometimes a violent oscillation is observed between a separated high subsonic flow without shocks and an attached supersonic flow which is terminated by a shock. In practical applications, the disappearance and reappearance of the shock is not of great practical importance, since the instability is confined to a narrow range of transonic flight velocity which is passed quickly by the accelerating vehicle.

Increase of the Mach number to the supersonic range leads to flows in which the shocks are always anchored at compression corners. These corners might be actual forward-facing steps or could be produced by the flow impingement downstream of rearward-facing protuberances. The flow is either attached or separated, depending on the maximum pressure rise that the turbulent boundary layer can

overcome without separation. Extensive experiments on separation for two-dimensional and axisymmetrical steps have been conducted by Kuehn. He found a strong Reynolds number dependence of the separation pressure ratio and separation length. The latter is plotted in Figure 4. The most striking feature is that the separation length increases with Reynolds number. Consider, for example, a typical wind tunnel model of the Saturn V. The model has to be scaled down very much to fit into small tunnels, and the forebody boundary layer thickness δ is small, such that the associated Reynolds number $Re\delta$ is less than 3×10^4. At $M = 2.92$, this model does not show any separation. However, a larger model and especially the flight vehicle will experience sizable separation lengths for Reynolds numbers in excess of 10^5. Model tests of flow separation and the associated turbulence generation are thus faced with this dilemma: that the model might indicate small or no separation, whereas the vehicle is exposed to large separation bubbles.

This dilemma has already occurred in the prediction of the temperature time history at the Saturn

15
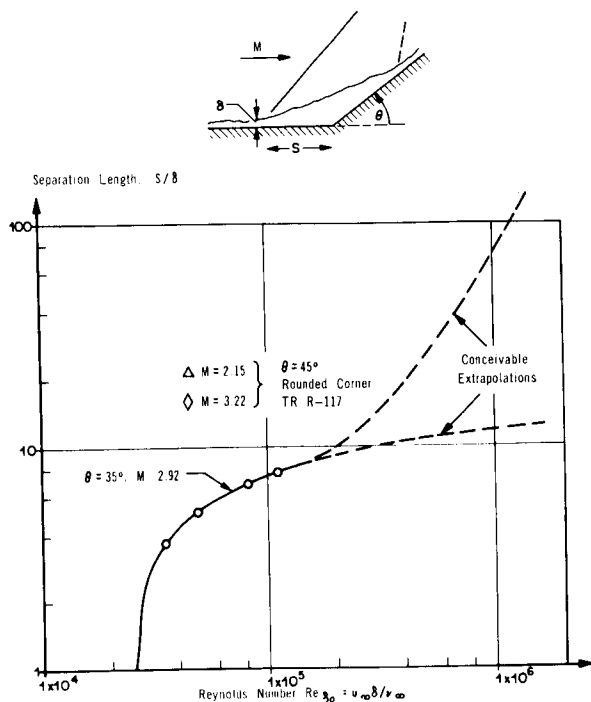
FIGURE 4. EFFECT OF REYNOLDS NUMBER
ON SEPARATION LENGTH
(From Kuehn, NASA TR R-117)

FIGURE 5. TEMPERATURE-TIME HISTORY FOR
SA-7, S-IV FORWARD INTERSTAGE

IV forward interstage. The predicted and measured
temperatures are shown in Figure 5. Their dif-
ference indicates that the aerodynamic heating may
have been decreased by the separation and recircula-
tion process.

III. TURBULENCE IN LOCALLY-SEPARATED
FLOWS

We measured wall pressure fluctuations to in-
vestigate the suspected high-intensity turbulence in
the locally separated flows. A typical flight test is
indicated in Figure 6. Three dynamic pressure
transducers were located near the S-IV/S-I inter-
stage of a Saturn I vehicle. The superimposed wind
tunnel shadowgraph shows that these transducers
should be exposed to a detached flow, which was
caused to separate by upstream shocks and protu-
berances (ullage rocket). Also, a local I-beam
protuberance is close to the transducer D159-20 and
might have caused additional local shock wave oscil-
lations.

FIGURE 6. FLOW FIELD REPRODUCED FROM
WIND TUNNEL SHADOWGRAPH

The results of the flight test are summarized in
Figures 7 and 8. Figure 7 gives the root-mean-square
pressure fluctuation as a function of flight time. All
fluctuations were averaged over 2 sec. At the local
supersonic Mach number of 1.6, the fluctuation level

$\Delta p_{RMS} = \sqrt{(\bar{p} - p)^2} \sim db$

----- Transducer D 159-20
——— Transducer L 65-20
----- Transducer L 64-20

170

Shock Induced
$\Delta p > 10\% q$

Power Plant
Noise

150

Free Shear Layer

Attached Boundary Layer
$\Delta p_{RMS} \leq .5\% q$

130

110

0   20   40   60   80   100
              Time (sec)

0   .5   1.0   1.5   2.0   2.5
              Local Mach Number

FIGURE 7.   ROOT MEAN SQUARE PRESSURE
FLUCTUATIONS DURING SA-4 FLIGHT

Frequency (sec⁻¹)

□ □   D 159-20
○ ○   L 64-20 $f = 0.2 \dfrac{\text{Local Velocity}}{\text{Protub ht: 0.508 m}}$
--△-△-- L 65-20

400

300

Shock Induced Noise

200

Free Shear Noise

100

0
30   40   50   60   70   80   90
              Time (sec)

.5   1.0   1.5   2.0   2.5
              Local Mach Number

FIGURE 8.   FREQUENCIES FOR THE PEAKS
OF THE POWER SPECTRA

of transducer D159-20 reached 17 percent of the
local dynamic pressure, which is 14 dB higher than
at launch. Because of the supersonic flow, an up-
stream propagation of jet noise is not possible and
the high levels must be induced by a local noise
generation process.

In attached supersonic shear layers, the wall
pressure fluctuations are usually below 0.5 percent,
and in the near field of free shear layers, the root-
mean-square levels usually stay below 10 percent.
Therefore, the area between the 10 percent and 0.5
percent dynamic pressure curves has been shaded
and called "free shear layer noise." RMS values
below the shaded area are called "attached boundary
layer noise," and those above 10 percent dynamic

pressure are called "shock induced noise." Ap-
parently, two of the transducers are exposed to free
shear layer noise. The high fluctuations in the vi-
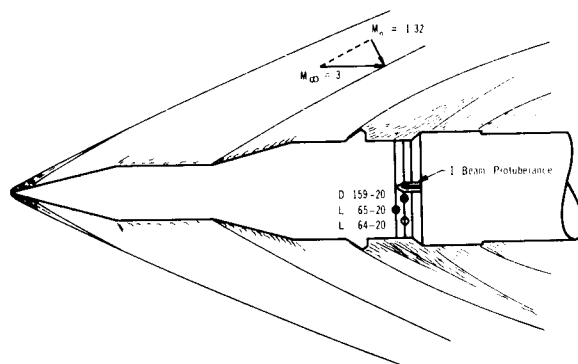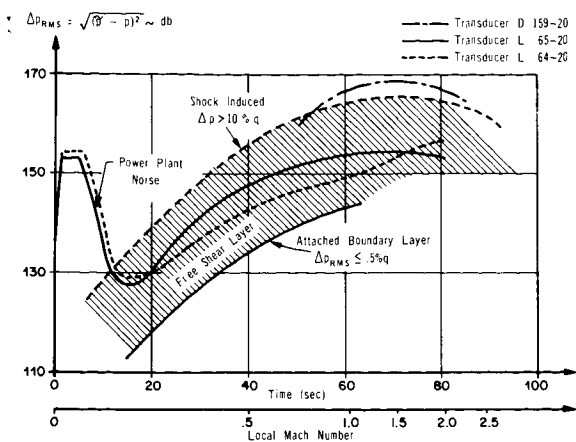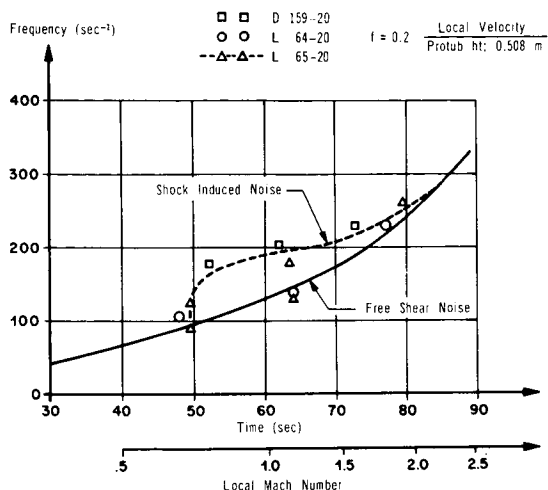cinity of the I-beam protuberance probably indicate
oscillations of the I-beam bow shock.

The above speculation on free shear layer and
shock induced noise are confirmed to some extent
by a frequency decomposition of the three transducer
outputs. The power spectrum indicated several peaks,
one of which was centered around a Strouhal number
of 0.2 as shown in Figure 8. Such peaks are as-
sociated with vortex shedding behind two-dimensional
cylinders and might thus be taken as further evidence
of a flow separation. The peaks, which belong to the
high "shock induced" RMS levels, are centered at
slightly higher frequencies. This frequency increase
might be associated with increased convection speed
in the outer supersonic portions of the separated
shear layer. We speculate that the roots of the local
protuberance shocks reach down into the outer portions
and oscillate, since they are driven by the free shear
layer turbulence, which is transmitted through the
shock roots.

The regions of supersonic separation and re-
attachment have been studied in more detail using
axisymmetric step models. Typical results are
shown in Figure 9. The mean values of the wall pres-
sure show the usual plateau in front of the step, which
indicates the extent of the "dead air" region beneath
the separated flow. The root mean square pressures
likewise show a plateau which is approximately at
2 percent of the dynamic pressure. This is well
within the range between 0.5 and 10 percent, which
was mentioned previously for free shear layer noise.
The interesting observation is now that there are
sometimes distinct peaks of the pressure fluctuations
associated with separation and reattachment. The
peak at the separation zone has been discussed by
Kistler and is generally associated with shock wave
oscillations. The peak at the reattachment zone is
even higher, and results have not been found in the
literature.

Some information about pressure fluctuations
below reattaching turbulent shear layers may be
taken from the oscilloscope trace shown in Figure
10. These tracers were taken at the base of a Saturn
I model. In this case, the free shear layers are
provided by the inboard and outboard engine jets.
Under high-altitude conditions, the plumes of dif-
ferent engines impinge upon each other, and the pres-
sure rise in the associated plume impingement shocks
leads to the reattachment of the low momentum
portion of the free shear layer. According to Figure
10, both pressure fluctuations and heat transfer
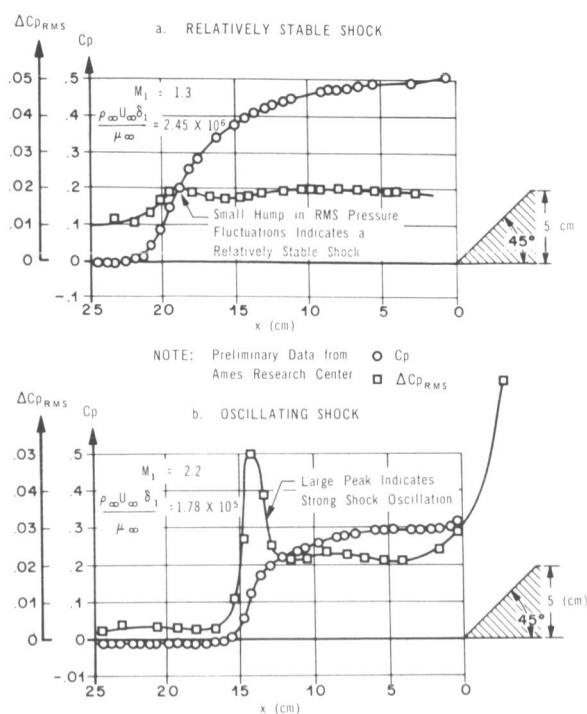
FIGURE 9. STATIC AND FLUCTUATING
PRESSURES IN AN AXISYMMETRIC COMPRESSION
CORNER IN SUPERSONIC FLOW
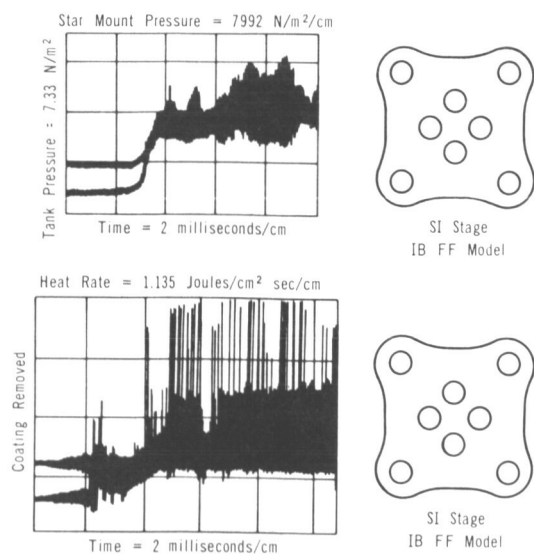
FIGURE 10. TURBULENT FLUCTUATIONS OF
BASE PRESSURE AND HEAT TRANSFER RATES

fluctuations are bigger than the mean values. Also,
the traces look like narrow-band components. A
zero count reveals a center frequency of approximately 5000 Hz.

Recirculation and reattachment in base areas
have been investigated in more detail by the two-dimensional model shown in Figure 11. A blunt
trailing edge separates the flow of a Mach 3 wind
tunnel thereby creating two "clustered jets." The jet
expansion, the free shear layer, and the plume impingement shocks are clearly illustrated. The blunt
trailing edge may therefore be considered as a simple
two-dimensional model of clustered rocket exhausts.
Obviously, the base flow behind reentry capsules and
bodies is simulated to an even greater extent. More
general cases of turbulent reattachment are provided
by compression corners, backward-facing steps,
protuberances, etc. They differ mostly in the direction of the reattaching flow.
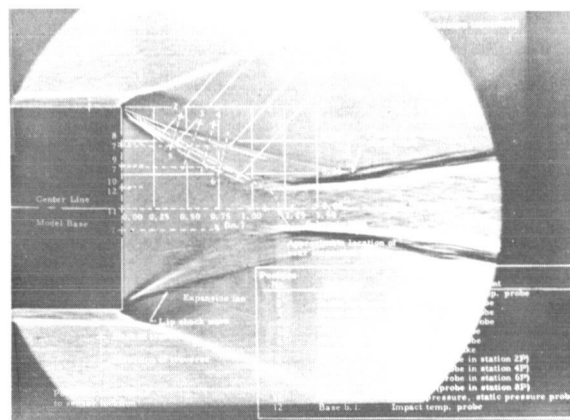
FIGURE 11. LOCATIONS OF PROBING
MEASUREMENTS

The turbulence in the recirculation zone behind
the blunt trailing edge has been measured with hot
wires protruding from the base plate. Figure 12
shows turbulent levels in excess of 60 percent of the
mean velocity. Other probings revealed that the
reattaching flows give rise to a "base boundary layer."
The RMS velocity profiles across this boundary layer
are shown in Figure 13. The absolute values show
the usual "hump" attributed to turbulence amplification by vortex stretching and image vortices. The
indicated turbulence levels reach values up to
200 percent at the wall, whereas turbulence levels in
attached turbulence seldom surpass 60 percent. However, the root mean square values in the recirculation
zone reach only 65 ft/sec (19.812 m/sec). This is
considerably smaller than the velocity fluctuations
in the adjacent free shear layers, which are estimated

Mean Velocity $\overline{U}(x, 0, 0)$ and RMS Velocity Fluc $U_{RMS}(x, 0, 0)(m/sec)$
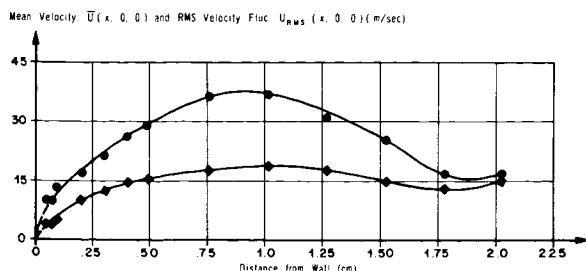
FIGURE 12. VELOCITY VARIATION ALONG
CENTER LINE

Distance from Wall, x (cm)

Miniature Hot-Wire Probe (0.00025" Dia. Wire, $\Delta T = 400° C$)

Probing Positions

Turbulence Intensity $\dfrac{u'(x, y)}{\overline{U}(x, y)}$ (%)

Distance from Wall, x (cm)

○ △ □ } Uncorrected
● ▲ ■ } Corrected
1 2 3 } Positions

RMS Velocity Fluctuation $u'(x, y)(m/sec)$
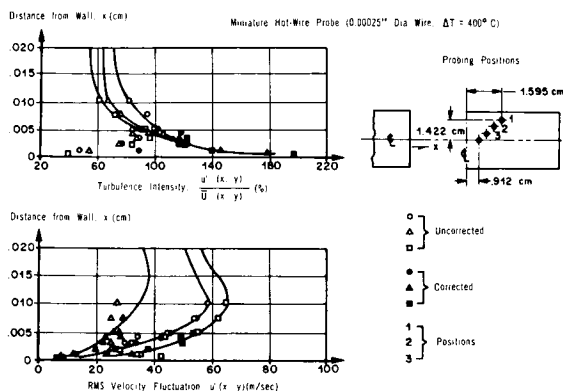
FIGURE 13. RMS VELOCITY PROFILES IN
TWO DIMENSIONAL BASE FLOW WITH AND
WITHOUT WALL EFFECT

at 20 percent of the free stream velocity, or 420 ft/sec (128.016 m/sec).

IV. ACOUSTICAL LOADS

Wall pressure fluctuations below reattaching flows and oscillating shocks provide aerodynamic forcing functions, which could lead to dangerous skin vibrations. In fact, these skin vibrations did probably cause the failure of the first Centaur flights.

For the purpose of this paper, it seems sufficient to demonstrate the relation between aerodynamic excitation and structural response for the simplest of all cases, the rectangular flat with simply supported edges. The results will be valid for all structural components, the free vibration of which can be described by orthogonal modes.

Individual panels of the vehicle skin are defined approximately by stiffening ribs and heavy internal masses. Each of these panels has a number of resonance frequencies or modes which describe the possible standing flexural waves. The fundamental mode is shown in Figure 12. It is given by the first wave, which is continuously reflected to and fro between opposite edges of the plate, that is, the wave where the distance between the modal points is equal to the distance between edges. Higher order modes follow by counting the number of modal lines in x and y direction.

Typical Saturn V panels have edge lengths between 2 and 5 ft (0.6096 and 1.524 m) and fundamental resonance frequencies between 10 and 200 Hz. The excitation of the corresponding modes may be calculated by comparing each standing wave with a linear harmonic oscillator, which is driven by a generalized force. This force follows from a Fourier decomposition of the wall pressures. The exciting force is, in fact, that Fourier component or pressure, the space and time periods of which correspond to those of the standing flexural waves. Dangerous skin vibrations are thus possible whenever the pressure power spectrum shows large values at frequencies which coincide with the panel resonances. The corresponding excitation is particularly dangerous if the associated pressure fluctuations have a phase relation in space. Such phase relations are always present if the turbulence is amplified by aerodynamic feedback loops such as sound radiation or turbulent convection.

The available meager information about wall pressure fluctuations below reattaching flows and oscillating shocks has been scanned for dangerous acoustical loads by the following procedure:

1. The measured power spectra were scanned for large peaks, the center frequencies of which fall into the range of panel resonance frequencies.

2. The measured power spectra were scanned for narrow bandwidths which might indicate selective turbulence amplification by aerodynamic feedback loops.

The survey was restricted to supersonic flight Mach numbers since the location of shock waves and reattachment waves is then almost independent of further increase in Mach number, such that the

turbulence excitation stays on the same panel until the dynamic pressure has dropped because of the high altitudes reached. For the spacecraft and the inter-stage areas, the excitation will last approximately 30 sec. At the base, a cushion of exhaust products is always present and an acoustic excitation will persist also at the upper stages until the engines are stopped.

Typical power spectra of wall pressure fluctuations below shocks oscillating at higher supersonic Mach numbers are not yet available. A spectrum below a transonic and oscillating shock is shown in Figure 14. It had two peaks. Scaling of the center frequencies to the vehicle scale shows that the shock wave oscillations would not be rapid enough to cause an excitation of skin panels. Also, the peaks do not indicate self-induced oscillations, since they disappeared when the sting support was changed or when the test was run in a different tunnel.

Oscillating shock roots in the outer edge of an upstream separated free shear layer occur at much higher frequencies. The data of Figure 8 show center frequencies between 100 and 200 Hz, which coincide with panel resonance frequencies. The occurrence of self-induced pressure fluctuations is unlikely, but cannot be ruled out entirely.

Power spectra below reattaching turbulent flows have been measured with hot wires behind our two-dimensional model. A third octave band frequency decomposition is shown in Figure 14a, and reveals five distinct peaks. The higher frequency peaks do not occur in normal turbulent stagnation point flows or free shear layers. We speculate that they may be associated with sound radiation phenomena.
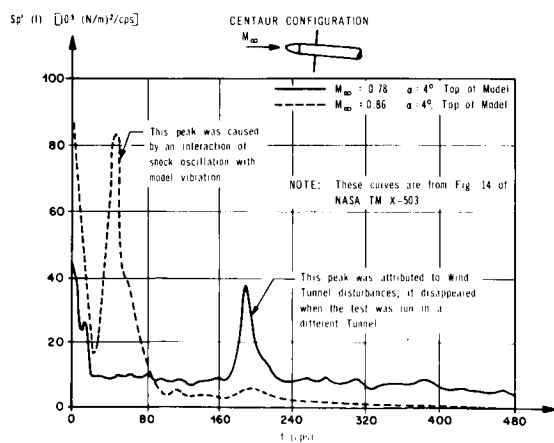
FIGURE 14. POWER SPECTRAL DENSITY OF WALL PRESSURE FLUCTUATIONS BELOW NORMAL SHOCKS IN TRANSONIC FLOW
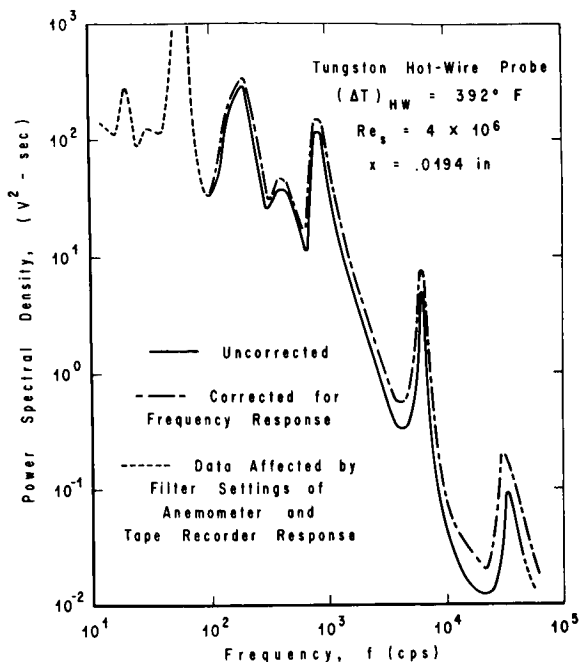
FIGURE 14a. PRELIMINARY POWER SPECTRUM OF HOT-WIRE SIGNAL IN TURBULENT BASE FLOW

An aerodynamic feedback loop may be provided by the sound radiation emanating from the "subsonic hole" between the plume impingement shocks. The sound waves might be reflected at the base and support reverberations between the base and the subsonic hole. This situation is similar to an open pipe and the associated second harmonic of this open pipe agrees roughly with the observed center frequency at 6 kHz. The same peak or resonance frequency was found throughout the recirculation zone; this also substantiates the speculation of standing waves and feedback loops.

The higher center frequency probably originates in the adjacent free shear layers. The highest center frequency of 30 kHz would lead to a free shear layer Strouhal number of roughly 0.25. Ffowcs-Williams' description of Mach wave sound emission indicates a mechanism by which such high-frequency fluctuations could be propagated across the dead air region toward the base.

If speculation about the above two sound radiation phenomena is borne out by future experiments, then we have to expect dangerous acoustical loads wherever a portion of a supersonic free shear layer reattaches. In particular, the base recirculation process might lead to a noise problem on the upper stages which cannot be investigated on static firings,

20

'since the plumes do not expand and impinge at sea
level pressures. A conservative estimate of the
upper stage noise might be found considering a fluc-
tuation between vacuum and two times the mean
static pressure. This leads to 153 dB for the S-II
and 180 dB for the S-1 stage.

V. HEAT TRANSFER LOADS

Heat transfer to the vehicle skin occurs wherever
hot flows are convected across the surface. The
heating loads caused by the high flow enthalpies at
reentry are well known from astronaut reports. Also
dangerous, but less well known, is the "base heating"
during the launch phase, which is generated by the
hot jet fluid that is recirculated towards the base.

Base heating during first stage flight is affected
by secondary burning of entrained combustibles. The
fuel for this burning comes from gas turbine exhausts
from the jets of the rocket engines, and potentially
from hydrogen vented from fuel tanks. In some
ballistic missiles of the past, the associated base
heating destroyed the missiles.

The entrainment, combustion, and quenching
processes in the base area cannot be predicted
analytically. As a consequence, gas temperatures
for the Saturn V design had to be approximated by
those from the Saturn I flight results. We will not
know before the first flight whether this assumption
was correct. Air scoops are used on both Saturn I
and Saturn V to flush the base. Since they had to be
designed on guesses, their effectiveness could not be
determined. Additional heating problems arise from
vented hydrogen which dissipates slowly and may end
up burning at the base.

We have tried to predict gas temperatures from
a 5.47 percent model at full-scale pressure levels
simulating the turbine exhausts calorically with hy-
drogen. The gas temperatures from wind tunnel and
S-I flight tests are shown in Figure 15. At low al-
titudes, the model gas temperatures follow the full
scale values, but drop off rapidly at altitudes beyond
10 km because of quenching of the secondary com-
bustion.

Heat and mass transfer as well as the secondary
combustion in the recirculation zone are probably
greatly affected by the extremely high turbulence
levels in the recirculation area. This is shown in-
directly by the large Reynolds number effects on
film coefficient and recovery temperature, which
has been measured on model tests. Typical results
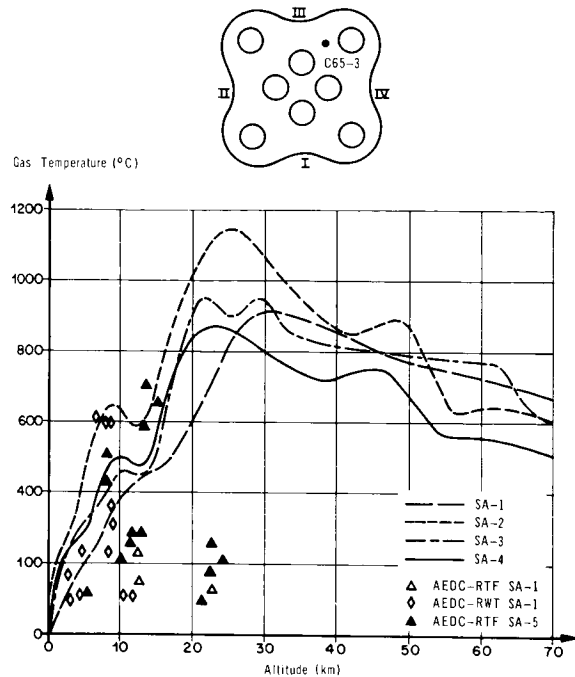
FIGURE 15. GAS TEMPERATURES FROM
SATURN I BLOCK II FLIGHT DATA COMPARED
WITH MODEL DATA

from hot-flow, short-duration tests are shown in
Figure 16. We have started simple two-dimensional
base heating tests to assess the turbulence effects on
base heating rates. All tests have used our blunt
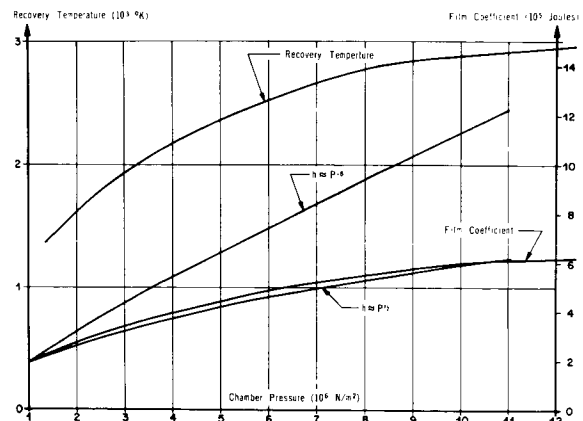
FIGURE 16. SOME EFFECTS OF REYNOLDS
NUMBER ON FILM COEFFICIENT AND RECOVERY
TEMPERATURE FOR S-IV FOUR ENGINE
CONFIGURATION

trailing edge in a Mach 3 tunnel. Secondary combustion is therefore not included.

Hot wire and total temperature traverses, together with base plate pressure and heat transfer measurements, allow several conclusions about turbulence effects on base heating rates.

The first conclusion concerns changes of the shapes of the mean velocity and mean temperature profiles. This was established by comparing experimental results with the laminar stagnation point solutions of the Navier Stokes equations which were adjusted to the full turbulent shear stress by taking the stagnation point velocity gradient from the measured base pressure distribution. In spite of this adjustment, the nondimensional mean velocity profiles differ considerably, as shown in Figure 17. The shapes of the correspondent mean temperature profiles are shown in Figure 18. The experimental profile is steepened at the wall. The corresponding heat transfer rates are plotted as a function of base cooling in Figure 19. Apparently, turbulence effects have increased base heating approximately 100 percent above the levels which are predicted from turbulence adjusted stagnation point solutions.

FIGURE 18. BOUNDARY LAYER PROFILES OF STAGNATION TEMPERATURE FOR DIFFERENT COOLING RATES
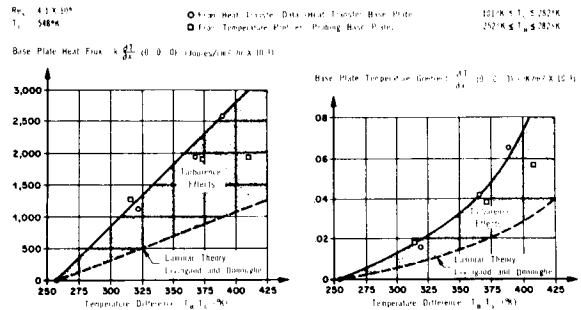
FIGURE 19. THE EFFECT OF TURBULENCE LEVEL ON BASE HEAT TRANSFER

The second conclusion describes the heat flow resistance (inverse heat transfer coefficient). The highly turbulent recirculation process only serves to establish a well mixed region of constant total temperature in the recirculation area between the dividing streamline and the boundary layer. The total heat transfer can therefore be related to a conduction through the free shear layers and the base boundary layer, which act like two heat flow resistances in series. The base boundary layer now contributes 86 percent of the total heat flow resistance and therefore dominates base heating.

The associated free shear layer Stanton numbers St_{SL} (Fig. 20) are almost double the values predicted by H. H. Korst's theory. This suggests that the high turbulence makes the free shear layer spread twice as fast as the equivalent shear layers of semi-infinite jets or flows over backward-facing steps.

FIGURE 17. MEAN VELOCITY PROFILES
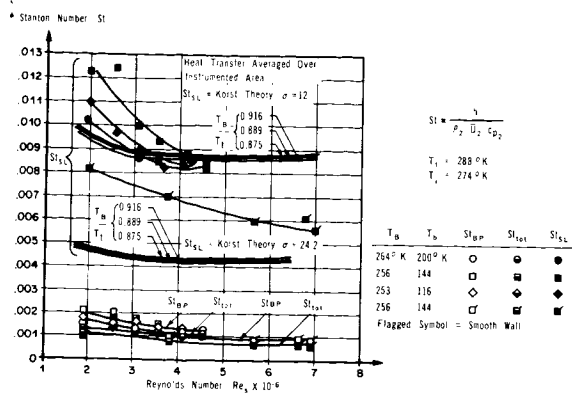
FIGURE 20. VARIATION OF TOTAL, SHEAR
LAYER, AND BASE PLATE HEAT TRANSFER
COEFFICIENTS WITH REYNOLDS NUMBER

OPTICAL METHODS FOR REMOTE SENSING OF LOCAL THERMODYNAMIC PROPERTIES AND TURBULENCE

By

F. R. Krause, A. J. Montgomery*, W. O. Davies* and M. J. Fisher*

ABSTRACT

Four different optical methods for the remote sensing of local thermodynamic properties and turbulence in model flows or in the atmosphere are described and compared. The Abel integral and zone approximation methods are most appropriate for the measurement of mean values, while the cross-beam correlation technique primarily measures fluctuating quantities. Viewing techniques are restricted to applications in which a flow contains particulate matter or a tracer is introduced.

DEFINITION OF SYMBOLS

Symbol	Definition
ΔA	area of light source seen by detecting system
$\Delta A'$	area of source image accepted by detector
B	noise bandwidth
C_1, C_2	first and second radiation constants
f	turbulence frequency
$R(x+\xi, y, z, \tau)$	area integral over space-time correlation function, or "two-beam product mean value"
I	intensity at x or at detector system with external light source
$I_0(\lambda)$	intensity at x = 0
$I_g(\lambda)$	intensity received by detector in absence of external light source
$I_b(\lambda, T_x)$	intensity of radiation of wavelength λ that would be received by the detector from a blackbody, at temperature T_x and position x

Symbol	Definition
K	spectral extinction coefficient
k	fluctuating component of extinction coefficient
L_x L_y L_z	integral scale of turbulence in x, y and z directions, respectively
r	radial coordinate used where axial symmetry is assumed
t	time
T	static temperature or integration time
$\tau(\lambda)$	spectral transmission at wavelength λ
τ	variable time delay
x, y, z	Cartesian coordinates – in crossed-beam technique, the beams are assumed to be directed along the y and z axes
W	spectral radiance (watts/unit area/ steradian/ unit wavelength interval

I. INTRODUCTION

By using optical sensing methods, information concerning local thermodynamic and turbulent flow properties may be obtained at a point remote from that at which the sensing system is located. Thus, in astronomy, temperatures, pressure, and abundance of elements in stars may be obtained, and similar spectroscopic techniques are used in the laboratory to determine temperatures in arcs and to study plasmas. Measurements in the earth's atmosphere to remotely sense the local generation, generation, distribution, and motion of atmospheric and ionospheric contaminants and constituents could have a potential impact on national programs in defense, health and welfare, weather forecasting and in space science. In rocket testing, by measurement of both mean values and fluctuations of local temperatures

and densities, a true spatial distribution of heat transfer and acoustical loads may be found. Regions of particular interest are the vehicle base, interstage and venting areas, around protrusions and in combustion chambers. Such results would allow less conservative weight, stress and cooling requirements to be adopted.

Although, for measurements in the atmosphere or in rocket exhausts, the local region in which the thermodynamic or turbulence properties are required is accessible per se, as distinct from stellar measurements, remote sensing methods may still possess many advantages. For example, in the atmosphere, at altitudes above aircraft ceilings but below satellite orbits, sounding rockets may be used to obtain local information, but these do not yield enough information to establish statistically meaningful results. In rocket design studies, presently used ground testing procedures employ solid probes of which the hot wire anemometer is a typical example. However, it is only in cold subsonic flow that the probe disturbance is kept within acceptable limits so that meaningful measurements of the true flow properties may be obtained. In supersonic and/or hot flows, normally of prime interest in launch vehicle technology, insertion of probes is not generally permissible or possible. The existence of supersonic velocity components usually means that the presence of any probe creates shock waves which change drastically the very properties of the flow that we wish to measure. Furthermore, in the case of hot flows such as a launch vehicle exhaust, the results obtained with a cooled probe are difficult to interpret or the probe itself may be destroyed.

Optical remote sensing methods are therefore very attractive. Most standard measurement techniques using photometer, interferometer, schlieren or shadowgraph systems, however, suffer from the disadvantage that the recorded optical signal depends on an integral along the entire light path. This, in general, yields no information about the thermodynamic or turbulent flow properties at any particular point in the path. Several methods exist by which point measurements may be obtained, and it is the purpose of this paper to discuss and compare such methods with a view to their application to remote sensing of local thermodynamic and flow properties in the atmosphere, in rocket exhausts and in fluid flows generally.

II. REMOTE SENSING OF LOCAL THERMODYNAMIC PROPERTIES

In the simplest situation, we have a remote blackbody which may or may not be resolved by the optical sensing system. If the object is resolved, then the optical properties of the detecting system determine the portion, ΔA, of the object that is contributing to the signal, the solid angle in which radiation is collected, Ω, and the spectral bandwidth of the radiation, $\Delta\lambda$. In such a case the spectral radiance of the distant body can be obtained from the spectral radiance of its image. Neglecting the losses in the detecting system, the spectral radiance of the distant source is directly proportional to the radiative power, I, which is radiated by the area, $\Delta A'$, of the source image, into the wavelength interval, $\Delta\lambda$, and the solid angle, Ω'.

$$W = \frac{I}{\Delta\lambda\Delta A\,\Omega} = \frac{I}{\Delta\lambda\Delta A'\Omega'} \tag{1}$$

In case of a blackbody, the spectral radiance is a known unique function of wavelength and temperature; this "blackbody function" is given by

$$\frac{I_b}{\Delta\lambda\Delta A\,\Omega} = W_b = \frac{C_1}{\lambda^5}\left(e^{\frac{C_2}{\lambda T}} - 1\right)^{-1} \,, \tag{2}$$

where $C_1 = 1.191 \times 10^{-6}$ W m^2

$C_2 = 1.439 \times 10^{-2}$ m °K.

Thus, the temperature of the distant blackbody can be determined from a single intensity measurement at a known wavelength.

If the object is not resolved, then the distribution of intensity in the image is determined by diffraction and optical aberrations of the system. Two or more measurements are required for a temperature determination, since the ratio of the measured signal at two different wavelengths permits the temperature to be determined from the shape of the blackbody curve.

This paper reviews remote sensing methods which could give the local thermodynamic properties of partially transparent media, as distinct from the determination of the thermodynamic properties of distant sources. To understand these methods, some fundamentals of radiative transfer are discussed. For more detailed treatment, the reader is referred to classical texts on the subject [1, 2].

The spectral analysis of distant sources breaks down if emission and absorption of radiation occur along the line of sight of the detecting system. The associated change of spectral radiance between source and detector may be treated in the following manner. Consider the column of radiating and absorbing gas defined by the field of view of the detector as shown below, and imagine all matter and radiation removed between cross section x and detector.

W | $I(x,t,\lambda)$ $I(x+\Delta x,t,\lambda)$ | | Detecting System

Source | x → | Matter and radiation removed |

x | x + Δx
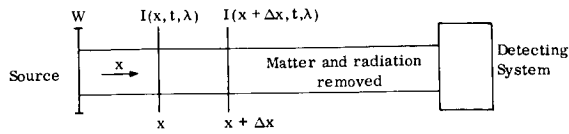
Because of the absence of any further absorption or emission, the detecting system would measure the radiative power $I(x,t,\lambda)$ at plane x. If the measurement is now repeated at the new position $x + \Delta x$, the detector would measure $I(x + \Delta x, t, \lambda)$. Then the difference in radiative power ΔI for the volume element shown is

$$\Delta I = I(x + \Delta x, t, \lambda) - I(x, t, \lambda); \tag{3}$$

that is,

$$\Delta I = \frac{\partial I}{\partial x} \Delta x. \tag{4}$$

This change of power is caused by light emission, absorption and scattering in the volume element, where

$$\Delta I = \Delta I_e + \Delta I_a + \Delta I_s \tag{5}$$

ΔI_e = radiation emitted in volume element Δx reaching detector

ΔI_a = radiation absorbed in volume element Δx that would otherwise have reached detector

ΔI_s = radiation scattered in volume element Δx that would otherwise have reached detector.

The radiation loss caused by scattering and absorption is proportional to the product of the radiation incident I, and the length, Δx, of the volume element; that is,

$$\Delta I_a + \Delta I_s = -K(x,t,\lambda) I \Delta x, \tag{6}$$

where the constant of proportionality $K(x,t,\lambda)$ is known as the extinction coefficient. In addition, the emitted, ΔI_e, and absorbed radiation, ΔI_a, in volume element Δx are related by Kirchoff's law:

$$I(x,\lambda,t) = -\frac{\Delta I_e}{\Delta I_e} I_b [\lambda, T(x,t)], \tag{7}$$

if the absorbed power is converted into heat. By substitution from equations (6) and (7) into (5), we obtain

$$\Delta I = -\frac{\Delta I_a}{I(x,\lambda,t)} I_b (\lambda, T) - K(x,t,\lambda) I(x,\lambda,t) \Delta x. \tag{8}$$

Since the detected radiation power, I, is proportional to the spectral radiance, W, the above equations could equally well be written with W in place of I.

A simplification occurs in equation (8) if absorption and scattering predominate and emission can be neglected or vice versa. In these cases,

either $\left| KI\Delta x \right| \gg \left| \frac{\Delta I_a}{I} I_b \right|$, when extinction

is dominant, or $\left| \frac{\Delta I_a}{I} I_b \right| \gg \left| KI\Delta x \right|$, when

emission is dominant. In the former case, equation (8) becomes

$$\frac{1}{I} \frac{\partial I}{\partial x} = -K(x,\lambda). \tag{9}$$

Thus, the detected radiated power at position x is given by the radiation, I_0, received from the distant source at x = 0 and the integrated extinction coefficient of the medium in between.

$$I = I_0 e^{-\int_0^x K \, dx} \tag{10}$$

If, on the other hand, emission is dominant, and if we assume further that scattering can be neglected relative to absorption, then from equations (6) and (8)

$$\Delta I = -\frac{\Delta I_a}{I} I_b = \frac{KI\Delta x}{I} I_b ,$$

leading to

$$I = \int_0^x I_b K \, dx. \tag{11}$$

The integration is over the distance between the distant source (x = 0) and the detector, or between the source and position x, where the detector is assumed to be situated a distance from the source greater than x, and there is no absorption or emission

óf radiation contributing to the detector signal from gas between x and the detector.

A third case to be considered is that for which scattering can be neglected, but emission and absorption are of the same order of magnitude. K is then determined entirely by absorption, and, from equations (6) and (8), we obtain the partial differential equation:

$$\frac{1}{I(\lambda,x)} \frac{\partial I(\lambda,x)}{\partial x} = K(\lambda,x) \left(1 - \frac{I_b(\lambda,T_x)}{I(\lambda,x)}\right), \quad (12)$$

the solution of which is

$$I(\lambda,x) = \exp\left(\int_0^x K(\lambda,x)\,dx\right) \int_0^x I_b(\lambda,T_x)$$

$$\exp\left(-\int_0^x K(\lambda,x')\,dx'\right) K(\lambda,x)\,dx. \quad (13)$$

In summary we find that the received signal, I, is always some integral over the generalized extinction coefficient, K. The form of this integral can be found only if at least one simplifying assumption is made. If none of the simplifying assumptions made are permissible, then the generalized extinction coefficient, K, is not sufficient to relate the detected signal to the optical properties of the medium.

Statistical thermodynamics shows that the generalized extinction coefficient is a unique function of the partial pressures of each species, p_i, the temperature, T, and the hydrostatic pressure, P.

$$K = K(p_i, T, P, \lambda)$$

Knowledge of it could therefore be used to analyze local thermodynamic properties of the transmitting medium. In any atmospheric phenomenon or model flow, the thermodynamic properties are functions of space and time:

$$p_i = p_i(\vec{x},t)$$

$$T = T(\vec{x},t)$$

$$P = P(\vec{x},t).$$

The extinction coefficient is, therefore, similarly dependent:

$$K = K(\vec{x},t,\lambda).$$

The problems associated with the remote sensing of local thermodynamic properties is thus two-fold. First, the optical integration has to be eliminated to obtain local values of K. This problem is reviewed in this paper. Second, the local values of K have to be related to the spatial and temporal distribution of dynamic and thermodynamic properties. This problem will be treated in other papers to be published.

To retrieve the local information from the integrated spectral intensity, I, a transformation with respect to the independent variables, space ($\vec{x} = x$, y, z), time, t, and wavelength, λ, is utilized. The Abel integral transformation technique applies to the space variables, the zonal approximation method uses the variation of λ, and the cross-beam correlation technique makes use of the temporal fluctuations of the measured radiation, I. All three methods use similar optical hardware and design concepts since they are dependent on a measured spectral intensity, $I(x,y,z,\lambda,t)$. They differ only in the test arrangement, which is needed to cover the range of the independent variable used. Furthermore, they are all limited by one of the above simplifying assumptions, since the relationship between local K values and the integrated signal has to be explicitly known.

The fourth approach to the problem differs from methods discussed above in that integration along the path between the source and detector is avoided by projecting the image of light source into the flow and viewing this image, by means of the scattered radiation, with a detecting system with a narrow field of view. To obtain information, it is necessary to assume that scattering losses between the source and its image, and between the source image and the detector, are small compared with the incident and scattered beam intensities, respectively.

These four different methods of remote sensing, the Abel integral transformation method, the zonal approximation method, and cross-beam correlation method, and viewing techniques, are considered in detail in this paper.

III. ABEL INTEGRAL TRANSFORMATION METHOD

The general type of optical measurement used in the Abel integral transform method [3,4,5] is illustrated in Figure 1. The source emits a radiation beam of constant intensity, $I_0(\lambda)$, at wavelength, λ. This radiation passes through the region of interest,
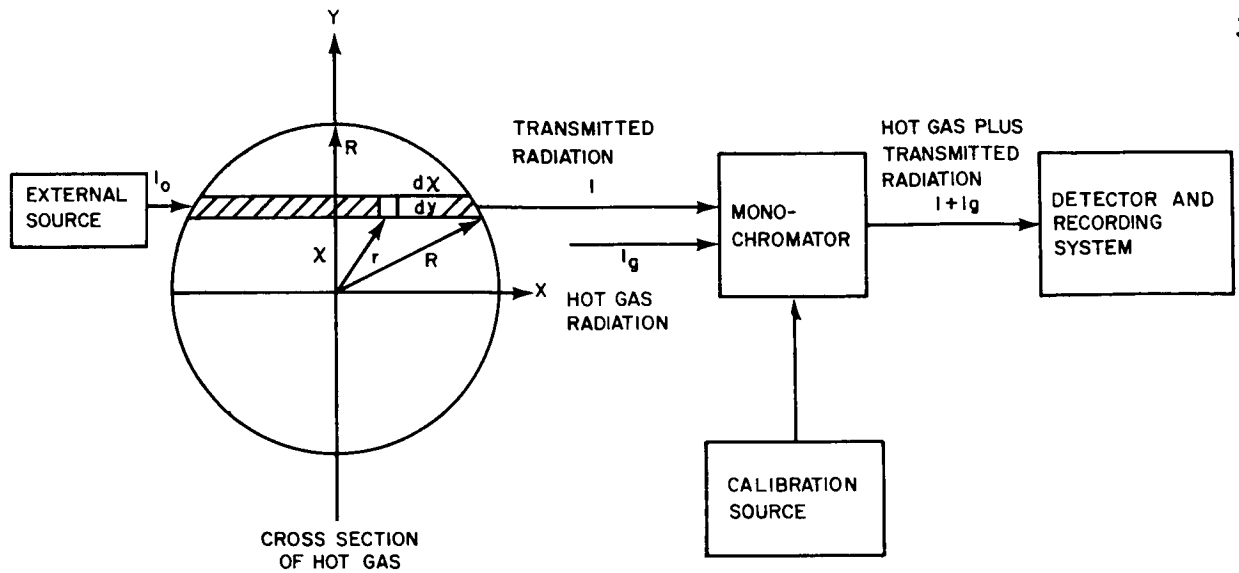
FIGURE 1. ILLUSTRATION OF INFRARED METHODS FOR GAS TEMPERATURE MEASUREMENTS

being attenuated by the hot gas, and is received by the detection system. The emitted radiation $I_g(\lambda)$ can be measured separately with the source absent.

If the temperature of the hot gas is uniform, the temperature can be calculated from two measurements. The first is an absorption measurement. That is, the spectral transmission, $\tau(\lambda)$, at wavelength, λ, is determined by the ratio of the source intensity, I_0, and the detected intensity, I.

$$\tau = \frac{I(\lambda)}{I_0(\lambda)} . \tag{14}$$

In the second experiment the emitted intensity, $I_g(\lambda)$, is measured by repeating the experiment without an external source. As long as scattering can be neglected, this emitted power is related to the emission, $I_b(\lambda)$, of a blackbody by Kirchhoff's law:

$$I_b(\lambda) = \frac{I_g(\lambda)}{1-\tau} . \tag{15}$$

However, we have already mentioned that a single value of a blackbody intensity, I_b, is enough to determine the temperature from Planck's law, equation (2). Substituting equation (7a) into equation (2) and solving for temperature gives

$$T = \left\{ \frac{\lambda}{C_2} \cdot \ln \left[1 + \frac{(1-\tau) C_1}{\lambda^5 \cdot I_g(\lambda)} \Delta\lambda \, \Delta A \, \Omega \right] \right\}^{-1} . \tag{16}$$

In the practical case, the temperature will vary through the hot gas region, and the radiation intensity detected by an optical system is an integration of the intensities over the depth of this nonisothermal source. The associated equations of radiative transfer were discussed in the last chapter. If we assume that we deal with axisymmetric jets, the optical integration may be expressed in terms of the local radius $r = (x^2 + y^2)^{1/2}$ as follows:

$$\tau(y) = \frac{I(\lambda)}{I_0(\lambda)} = \exp\left(- \int K(x,y) \cdot dx \right)$$

$$= \exp\left(- 2 \int_{r=y}^{R} K(r) \frac{r}{(r^2 - y^2)^{1/2}} \, dr \right) \tag{10}$$

and

$$I_g(y) = \int I_b K(x,y) \, dx$$

$$= 2 \int_{r=y}^{R} I_b K(r) \frac{r}{(r^2 - y^2)^{1/2}} \, dr. \tag{11}$$

The retrieval of local information at radius r is now possible by measuring the transmission, $\tau(y)$, and the emission, $I_g(y)$, along perpendicular traverses in the y direction. These results are then used as an input to an Abel integral transformation program, which converts the chordal or "y" distribution into the desired radial or "r" distribution.

28

If the transmission is greater than 80 percent, or the absorption coefficient varies smoothly over the slit width, the results of the absorption and emission measurements can be transformed as follows:

$$\left\langle K(r)\right\rangle_{\Delta\lambda} = \frac{1}{\pi r}\cdot\frac{\partial}{\partial r}\left(\int_r^R \left\langle\ln\tau(y)\right\rangle_{\Delta\lambda}\cdot\frac{y}{(y^2-r^2)^{\frac{1}{2}}}\cdot dy\right)$$
(17)

and

$$\left\langle I_b(r)\cdot K(r)\right\rangle_{\Delta\lambda} = -\frac{1}{\pi}\int_r^R\left\langle I_g(y)\right\rangle_{\Delta\lambda}\cdot\frac{y}{(y^2-r^2)y^2{}^{\frac{1}{2}}}\cdot dy$$
(18)

where the brackets indicate an average over the monochromator band pass, $\Delta\lambda$. The temperature profile, $T(r)$, follows from equation (16). Furthermore, if the transmission is independent of the hydrostatic pressure, the expression for the absorption coefficient can be used to provide the radial distribution of infrared active molecules that contribute to the absorption and emission.

In summary, we find that local thermodynamic properties such as temperature can be retrieved, if both emission and absorption measurements are repeated, driving the monochromator slit across an entire section of the flow. Practical limitations are imposed by symmetry assumptions. The most common one of axial symmetry has been illustrated in this section. Theoretical restrictions are inherent in the radiative transfer equation used. Referring to the previous chapter, we may summarize this restriction as follows:

    1. Scattering is negligible relative to absorption.

    2. All energy absorbed is converted into heat.

    3. The external source is so powerful that absorption dominates emission while the source is being used.

    4. In the absence of the external source, power gains by emission dominate power losses by absorption.

IV. ZONAL APPROXIMATION METHOD

In the zonal approximation method [6] the path through the hot flow between the source and detector

is divided into n zones (Fig. 2). Each of these zones is assumed to be at a particular temperature and to have a given number density of absorbing molecules. By making both absorption and emission measurements for n different wavelengths, 2n equations are obtained. It is thus possible to solve for the unknown temperatures and number densities.
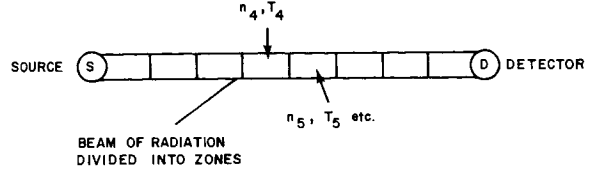
FIGURE 2. ZONAL APPROXIMATION METHOD

For a hot gas in local thermodynamic equilibrium, the spectral intensity of a one-dimensional beam of monochromatic radiation depends on the decrease in intensity due to self absorption and the increase due to the hot gas in the region dx, and is given by the expression derived in section II.

$$I(\lambda,x) = e^{\int_0^x K(\lambda,x)\,dx}\int I_b(\lambda,T_x)e^{-\int_0^x K(\lambda,x')\,dx'}K(\lambda,x)\,dx,$$
(19)

where $I(\lambda,x)$ is the intensity at wavelength λ and position x, $I_b(\lambda,T_x)$ is the blackbody function at wavelength λ and temperature T_x at position x, and $K(\lambda,x)$ is the absorption coefficient at wavelength λ and position x. Scattering has been neglected.

This equation cannot be evaluated in a completely general case because the dependence of the absorption coefficient on position is unknown. However, if the hot gas, i, as outlined above, is divided into n isothermal, isobaric zones, the absorption coefficient is independent of position within each zone, and the intensity at wavelength λ that reaches the detector can be written

$$\left\langle I(\lambda)\right\rangle_{\Delta\lambda} = \sum_{i=1}^n\left\langle I_b(\lambda,T_i)\right\rangle_{\Delta\lambda}\left[\left\langle\tau_{i-1}(\lambda)\right\rangle_{\Delta\lambda}-\left\langle\tau_i(\lambda)\right\rangle_{\Delta\lambda}\right],$$
(20)

where $I_b(\lambda,T_i)$ and $\tau_i(\lambda)$, respectively, the blackbody function and the transmission of the sample for zones 0 through i at wavelength λ averaged over the monochromator band pass. The transmission at wavelength λ can be measured with the aid of an external radiation source, and is given by

$$\tau_n(\lambda) = \prod_{i=1}^{n} \tau_i(\lambda). \tag{21}$$

For an isothermal temperature profile, i.e., $n=1$, only one wavelength need be considered, and equation (20) reduces to

$$\left\langle I(\lambda) \right\rangle_{\Delta\lambda} = \left\langle 1 - \tau(\lambda) \right\rangle_{\Delta\lambda} \left\langle I_b(\lambda, T) \right\rangle_{\Delta\lambda}, \tag{22}$$

which is a form of Kirchoff's law. In this simple case, transmission is given by Lambert's law:

$$\left\langle \tau(\lambda) \right\rangle_{\Delta\lambda} = \left\langle I/I_0 \right\rangle_{\Delta\lambda}. \tag{23}$$

Thus, for the isothermal temperature, the zonal approximation reduces to the infrared brightness method of temperature measurement [7].

For application to a nonisothermal temperature profile, the spectral emission is measured at $\underline{n}$ different wavelengths, each of which consists of $\underline{n}$ different sets of values for $\tau_i(\lambda)$. This yields $\underline{n}$ independent simultaneous equations for calculating the $\underline{n}$ temperatures; the temperatures are implicit in the Planck blackbody functions, which must be inverted to provide the temperature profile. It should be recognized that the values of transmission used in this expression are also somewhat temperature dependent, and, furthermore, only one of these (τ_n) can be measured directly. Thus, the use of this method also requires some independent prior knowledge of the transmission characteristics of molecular species that give rise to the emission and absorption. Where such exists, one might use empirical data to express the transmission as a function of temperature, path length and total pressure [8, 9, 10], but a deeper insight and a more general facility for handling such problems is offered by the band model theories that are based on fundamental molecular properties [11, 12, 13, 14].

If this information exists, the system of equations given above [14, 15] can be solved to yield the thermal structure of the hot gas. An iterative procedure for accomplishing this has been suggested by Krakow [15] in a successful application of this method to the determination of temperatures in CO_2 flames. As compared to the Abel integral inversion technique described above, the use of the zonal approximation method is of recent origin; there has therefore been relatively little effort expended in devising useful analytical procedures for evaluating the temperatures from the empirically determined set of equations. It seems likely that the inherent advantages of this method, (i.e., the application is not essentially more difficult for gases that are not symmetrical or optically thin) will provide the impetus for further development of iterative methods such as that used by Krakow. In addition to a knowledge of the dependence of transmission on temperature, transmission and emission measurements made at $\underline{n}$ different wavelengths are required. In general, it is desirable that each wavelength correspond to an isolated vibration-rotation band, or, at least, that a single band be predominant in the selected monochromator slit width. This implies that there should be at least $\underline{n}$ distinguishable spectral regions of significant strength that contribute to the emission.

If the temperature gradients are steep, the regions would have to be small, and the number of wavelengths would be correspondingly large. Although, in principle, this division into a series of isothermal zones can always be made, the accurate measurements of so many bands will be difficult in practice.

V. THE CROSSED-BEAM METHOD

The crossed-beam method uses a mathematical transformation in time to retrieve local information. The main idea is to eliminate integration by a cross correlation of fluctuations [16]. The measurement procedure is explained in Figure 3. Two colliminated beams intersect at a space-fixed point. These lines define a plane which we shall call "turbulence wave front" and a normal in the intersection point (x, y, z)
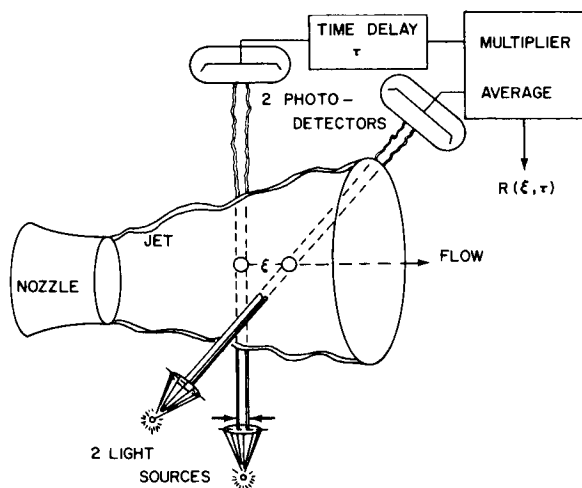

FIGURE 3. CROSS-BEAM CORRELATION METHOD

30

which is called the wave normal. We then measure the radiative power $I(t,\lambda)$ along both fields of view, split off the time average signal, $\bar{I}$, cross correlate the fluctuations, $i(t)$, and calculate the quantity, R, as described in Figure 3. Let us assume that the two detecting telescopes have been aligned to the y and z axis of a Cartesian, space-fixed coordinate system. Each line of sight is denoted by a y or z subscript, and each point on the line of sight by the distances η or ζ relative to the intersection point. The quantity R is then equal to

$$R(\vec{x},\lambda) = \frac{\overline{i_z(t,\lambda_1)\, i_y(t,\lambda_2)}}{\bar{I}_y \cdot \bar{I}_z} . \qquad (24)$$

The fluctuation of the optical original i is related to the fluctuation of the extinction (or emission) co-efficient along each beam by the equations of radiative transfer. In case of dominant emission, equation (10) may be applied. This leads to

$$I = \bar{I} + i = I_0 \exp\left(-\int_{-\infty}^{+\infty} (\bar{K} + k)\,dx\right) . \qquad (25)$$

Linearzing the underlined integrated fluctuation of extinction coefficients,

$$\exp\left(-\int k\,dx\right) = 1 - \int k\,dx, \qquad (26)$$

the fluctuation of the optical signal becomes

$$i_x(t) = -\bar{I}_x \int_{-\infty}^{+\infty} k(\vec{x},t,\lambda)\,dx. \qquad (27)$$

The interpretation of the measured quantity, R, follows by relating it to the local fluctuations of the extinction coefficient. Substituting expressions for i_y and i_z into equation (24) and assuming statistical, homogeneity along one of the beams [17] leads to an optical integration over the turbulence wave front.

$$\left\langle R(\vec{x},\lambda_1,\lambda_2)\right\rangle_{\Delta\lambda} =$$

$$\int\int_{source}^{detector} \overline{k(x,y,z,t,\lambda_1)\, k(x,y+\eta,z+\zeta,t,\lambda_2)}\;d\eta d\zeta. \qquad (28)$$

Two important conclusions can be derived from equation (4):

1. For a pair of statistically independent light sources, the source fluctuations and characteristics do not have to be known. The method would work for any source, such as ground beacons, the sun or thermal radiation from extended background like the sky.

2. The random nature of turbulent fluctuations assures that integrand drops to zero over distances which are comparable to a typical eddy size. This explains, qualitatively, why the cross correlation partially eliminates the usual optical integration along a line of sight.

According to equation (28), the crossed-beam correlation works whenever the wanted signal is common to both lines of sight. The way in which the wanted signal is then pulled out of the integrated signal may be described best by splitting each of the integrated signals in two parts. The first describes the contribution of the "correlated volume" where the integrand of equation (4) does not vanish. The second part describes the rest of the integrated signal. Multiplying the fluctuations of the two integrated signals then leads to four products. Three of these change between positive and negative values in a random fashion. If we now average these products over time, their mean value will go to zero, whereas the deviation from the mean will increase with the square root of time.

The fourth product describes the contribution of the correlated volume, which is common to both lines of sight. The associated product is always positive and its summation over time should increase linearly with time. Therefore, it will be the dominant one, if one goes on adding long enough. Even small contributions at the beam intersection can be pulled out provided that (1) the integrated signals show detectable fluctuations and (2) the combination of light source fluctuations, shot noise and instrument noise is not orders of magnitude larger than the root mean square value of the integrated signal.

The optical integration is restricted to the wave front. Along the wave normal, no integration takes place, and local information inside a correlated volume may be obtained by repeating the crossed-beam experiment for several beam separations along the normal as shown in Figure 3. The space separation, ξ, describes the minimum beam distance, which defines the wave normal. Also a time separation is introduced electronically by a time delay unit. With these alterations on the experiment, the measured quantity, R, becomes

$$\left\langle R(\vec{x},\lambda_1,\lambda_2,\xi,\tau)\right\rangle_{\Delta\lambda} =$$

$$\int\int_{-\infty}^{+\infty} \left\langle k(x,y,z,t,\lambda_1)\, k(x+\xi,y+\eta,z+\zeta,t+\tau,\lambda_2)\right\rangle d\eta dS. \tag{29}$$

Some general analytical arguments [18] led us to believe that the measured correlation, R, closely approximates the correlation between the local fluctuations of k, which imaginary point-probes would have measured in the two points of minimum beam separation. These points are dotted in Figure 3. However, the statistical description of random fields is based on "two-point product mean values." The crossed-beam method thus gives an approximation of any turbulence parameter, which is commonly derived from two-point product mean values. Some of these parameters are

    a. space-time correlation coefficient:

$$r(\xi,\tau) = \frac{R(x+\xi,y,z,\tau)}{R(x,y,z)} \tag{30}$$

    b. the "size" of the correlation volume or "integral length scale" of turbulence along the beam normal:

$$L_x = \int_0^\infty r(\xi,0)\, d\xi \tag{31}$$

    c. mean square values of the fluctuating quantity:

$$\overline{k^2(x)} = \frac{R(\xi=0,\tau=0)\,\vec{x}}{\bar{I}_y \bar{I}_z L_y L_z} \quad , \tag{32}$$

where L_y and L_z are integral length scales. Species concentration or temperature fluctuations are derivable from this quantity.

    d. turbulence spectrum:

$$S(\omega) = \int_{-\infty}^\infty r(0,\tau)\, e^{i\omega\tau}\, d\tau \tag{33}$$

    e. convection speed, obtained from the time delay, $\tau_m(\xi)$, at which a particular $r(\xi,\tau)$ curve touches the envelope common to all such curves as illustrated in Figure 4

$$U_c = \frac{\xi}{\tau_m(\xi)} \tag{34}$$

    f. moving axis autocorrelation $r^*(\xi,\tau_m)$, the envelope defined in (e). A temporal turbulent frequency spectrum which would be felt by an observer traveling with the average eddy is given by

$$S^*(\omega) = \int_{-\infty}^\infty r^*(\xi,\tau_m)\, e^{i\omega\tau}\, d\tau. \tag{35}$$

    g. eddy lifetime τ_e corresponding to the time delay for which

$$r^*(\xi,\tau_m=\tau_e) = \frac{1}{e} . \tag{36}$$

These measurable turbulence properties are approximations to the two-point product mean values, because the correlation between the two detected signals will include contributions from turbulent fluctuations that would not be felt by a point probe on the normal to the turbulence wave front. However, experiments in a subsonic jet have shown [18] that
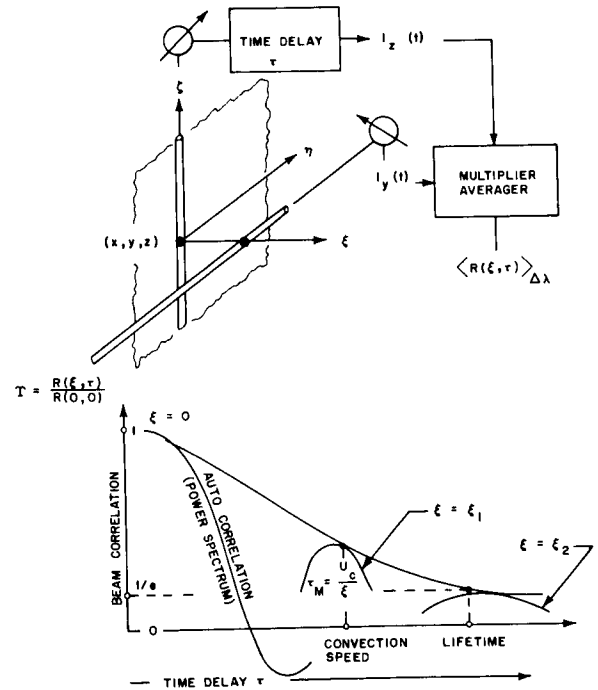

FIGURE 4. LOCAL POWER SPECTRA CONVECTION SPEEDS AND EDDY LIFETIMES FROM CROSSED-BEAM CORRELATION MEASUREMENTS

weighing of contributions close to the wave normal is sufficiently strong to yield good spatial resolution.

To measure thermodynamic properties, the fluctuations in extinction coefficient or, in the case of hot flows such as rocket exhausts, fluctuations in emission coefficient have to be related to variations in species concentrations and temperatures. By proper choice of optical wavelength and spectral bandpass, it should prove possible to measure fluctuations in these quantities and, hence, to apply the technique to the study of multicomponent or two-phase flow phenomena.

The crossed-beam concept has the following potential advantages:

1. The spatial and temporal variation of turbulence parameters is given, while other methods average over the optical paths.

2. The continuous and simultaneous monitoring of separate locations allows us to obtain accurate statistical estimates, while other direct or remote sensors are restricted to a few single-path or single-point experiments.

3. The evaluation of moving axis autocorrelations permits the study of the full life cycle of targets of opportunity such as shocks, flames, weather fronts and pollutants.

4. A single sweep of frozen atmospheric patterns may establish the complete altitude profiles of turbulent intensity, turbulence length scales and wave member components.

The crossed-beam method will work only if the following requirements are met:

1. Particulate or gaseous tracers must produce local changes in radiative power which are not lost during transmission to the detector.

2. Light source fluctuations, shot noise and instrument noise must be reduced to mean square levels which are not several orders of magnitude greater than the integrated signal. This is a far less restrictive requirement than the normal, which is that the erroneous noise should be at least one, and preferably two or three, orders of magnitude less than the genuine signal.

3. The lines of sight must intersect at or scan over a selected position for a sufficiently long integration period to pull the correlated signals out of the light source fluctuations, flow fluctuation, shot

noise and instrument noise. The necessary integration time is intimately related to the magnitudes of the various noise contributions to the detected signals. Although, in principle, any degree of noise can be eliminated with suitable integration periods, the finite record lengths and the dynamic interchannel displacement set practical limitations to pulling the local signal out of the integrated signal and the combined light source noise, shot noise and instrument noise.

On occasions the problems of meeting the above requirements will be formidable and may prohibit some of the desired applications. However, since we can pick the detected radiation from any region of the electromagnetic spectrum and since atmospheric applications allow large beam diameters and arbitrary orientations of the two lines of sight, we believe that there are many experiments where the above problems may be overcome, and useful, hitherto unavailable, data obtained.

The interpretation of the beam correlation (two-beam product mean value) is subject to the following theoretical restrictions.

1. The number of statistically independent regions and gas dynamic phenomena is small enough to avoid cancellation of local fluctuations which would occur when integrating over too many statistically independent parts.

2. Either emission or extinction dominates the local change of radiative power inside the correlation volume.

3. The integrated fluctuation of the generalized extinction coefficient is sufficiently small to permit linearization. However, large changes in the mean value of the transmitted radiative power are permissible. Also, large local fluctuations are tolerable, if one integrates over several statistically independent regions.

4. The fluctuations of radiative power are locally isotropic and homogeneous over the plane of the two beams. This assumption is sufficient but does not appear necessary. Crossed-beam experiments in anisotropic and inhomogeneous jet shear layers [18] have already yielded a good approximation of two-point product mean values.

VI. VIEWING TECHNIQUES

In viewing techniques a lens or mirror collects scattered light from a small volume element in the

flow defined by the field of view of the detector and the dimensions of the incident light beam. A schematic diagram of an optical system suitable for this type of measurement is shown in Figure 5. The small

```
              LIGHT
              SOURCE
                ⊙
COLLECTING LENS

APERTURE

PROJECTION LENS

SCATTERING
PARTICLES

DETECTOR          VIEWED
                  VOLUME

VIEWING
LENS
```
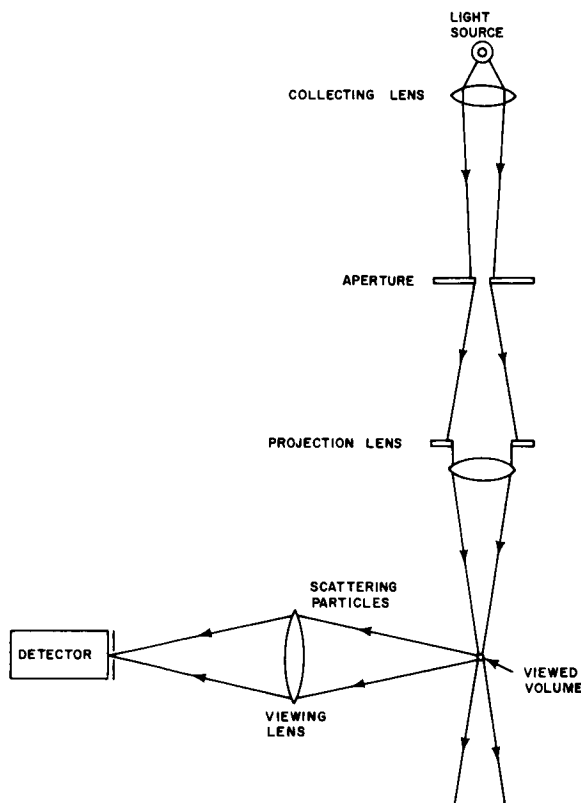
FIGURE 5. VIEWING TECHNIQUES SCHEMATIC DIAGRAM (Sound detector system at right angles to planned paper)

volume element in which the scattered light received by the detector originates may be considered as a source of light, and its spectral radiance calculated in terms of watts/unit area/unit solid angle/unit wavelength interval. This assumes that multiple scattering can be neglected. In theory, by measuring the spectral radiance, it is possible to obtain species concentrations and temperatures for the volume element being measured.

The intensity and spectral composition of the light received by the detector will obviously depend on the nature of the scattering particles. Scattering by both free and bound electrons can occur but, in addition, contaminants such as oil, fog, smoke and

other solid or liquid particles can act as strong scattering centers. It has been shown that scattering by bound electrons (Rayleigh scattering) is extremely sensitive to the slightest contamination in the flow [19]. For example, the Rayleigh scattering cross section for most common gases is approximately 10^{-28} cm^2, whereas the scattering cross section of free electrons (Thomson scattering) is about 6×10^{-25} cm^2. This is more than three orders of magnitude higher so that the number density of free electrons should be four to five orders of magnitude smaller than the number density of bound electrons if Rayleigh scattering were to be used. The scattering cross section of solid and/or liquid particles (Mie scattering) is so much larger ($10^{-16} < \sigma < 10^{-8}$cm^2) than either of these, however, that the slightest particle contamination would mask both Rayleigh and Thomson scattering. Even under carefully controlled laboratory conditions, background scattering from solid and liquid particles often makes electron scattering unobservable.

Viewing techniques thus appear destined to be related only to large particle scattering since the detector viewing any flow of practical interest will see scattered light which has its dominant contribution from such "contaminants" as water droplets, dust, fuel droplets, carbon particles, etc. Viewing techniques could, therefore, be used to study contaminations, or a known distribution of scattering particles could be introduced. This leads to the combination of viewing and tracer techniques.

Both mean values and fluctuations of oil-fog concentrations have been measured on ducted jets [20] by projecting the image of an incoherent source into the flow. The spectral radiance of the scattered light was high enough to obtain a good comparison between the optically measured two-point oil-density correlations and hot-wire recorded two-point velocity correlations. During these fluctuation measurements, it was found that reliable results depend on a very careful adjustment of the fog concentrations. A very narrow margin existed between the lowest fog concentration that would prevent the signal fluctuations from being buried in the shot noise, and the highest fog concentrations that still lead to meaningful correlation functions. A further problem is caused by temporal fluctuations of the scattered light which are not the result of changes of scatterer concentration in the viewed region. Although the light source itself might be quite stable, the spectral radiance of its image will fluctuate because of the fluctuating losses in the flow which occur between the source and its image. A theoretical analysis showed [21] that these "light source fluctuations" will plague any correlation analysis using viewing techniques.

The problem of mean value measurements prevents a further difficulty. This is associated with the uniform distribution of the tracer which will determine whether or not the tracer density is, in any way, a measure of the flow density. Further, in hot flows it is likely to be difficult to find a suitable tracer that does not burn or evaporate [22]. It therefore appears questionable that a particle-tracing technique would be applicable where high temperatures and large density gradients exist. It is also questionable whether or not tracer particles will follow fluctuations of turbulent motion at high or supersonic velocities. Thus, viewing techniques using tracers will probably be limited in range of application.

VII. SUMMARY

The use of Abel integral inversion techniques is perhaps the most well known of the methods described for retaining local mean values of species concentration and temperatures out of integrated signals. The Abel integral and zonal approximation methods are similar in that they require a combination of transmission and emission measurements. In the Abel integral inversion method, it is sufficient to isolate one or a small number of absorption bands, and view these bands over various chords of the cross section of the exhaust. The application of this method is considerably simplified when the gas possesses circular symmetry and is optically thin. With the zonal approximation method, it is not necessary to scan over a series of geometrical paths, and the method is not inherently more complicated if the gas is neither circularly symmetrical nor optically thin. However, the optical properties must be measured at a number of wavelengths equal to the number of zones considered; in a practical application, the suitability of this method could well be limited by the number of individual bands that it is possible to isolate.

In choosing between these two methods, one must consider the relative disadvantages in either observing over a number of geometrical paths or at a number of wavelengths. The use of either technique requires some prior knowledge of the variation of the optical and total gas pressure. One feature, implicit in the evaluation of these optical properties, that is generally not explicitly stated is that these methods may also provide the radial distribution of pressure in the exhaust region.

Neither method is particularly suited to making fluctuation measurements. In the Abel integral method, it would be necessary to make measurements over a large number of paths simultaneously, whereas with the zonal approximation technique, simultaneous measurements at a number of different wavelengths would be needed. Errors in the instantaneous values or in the calculation of temperatures could lead to very large errors in the values for rms fluctuations.

The crossed-beam correlation technique is best suited to measurement of turbulence properties and fluctuations in thermodynamic properties. Mean value information cannot be directly obtained; however, it may be possible to do this indirectly and this problem is being studied. By proper choice of the wavelength of radiation, detected rms fluctuations in both species concentrations and temperature may be measured with good spatial resolution. In addition, information as to eddy scales, and lifetimes, convection velocities, cross-power spectra and three-dimensional wave number spectra may be obtained. The applicability of the crossed-beam correlation technique in terms of spatial and spectral resolution will be determined by maximum source intensities and by the spectroscopy of the system to be investigated.

In comparison with the Abel integral transformation and zonal approximation methods, the crossed-beam technique does not need elaborate mathematical transformations, but uses existing standard analog or digital computer programs developed for vibration analysis and dynamic calibrations. In addition, no prior information on flow symmetry or temperatures is needed. The rms value of correlated fluctuations may be calculated when the uncorrelated fluctuations are up to approximately ten times larger using integration times of the order of one second.

Viewing techniques to measure thermodynamic properties would be difficult to apply in a practical case because of the relative scattering cross sections. Since, for most common gases, the Rayleigh scattering cross section is of the order of 10^{-28} cm^2 compared to 10^{-16} to 10^{-8} cm^2 for scattering by solid or liquid particles, the slightest contamination in the flow will mask the Rayleigh scattering. The use of a tracer will allow kinematic flow properties to be measured, but for hot flows a tracer that does not burn or evaporate may be hard to find. Fluctuations in the intensity of light scattered out of the viewed

volume element caused by variations in intensity of the incident radiation are a problem which can be overcome only by the use of very intense light sources and very accurate control of tracer particle concentration.

In conclusion, the techniques discussed in this paper are, to a large extent, complementary. Mean temperatures and densities may be obtained with the Abel integral and zonal approximation methods. Viewing techniques are restricted to measurement of kinematic flow properties using light scattered by particulate matter in the flow or tracers that are introduced. The cross-correlation technique is best suited to fluctuation measurements and determination of kinematic flow properties.

REFERENCES

1. Chandrasekhar, S.: Radiative Transfer. Oxford University Press, 1950.

2. Kourganoff, V.: Basic Methods in Transfer Problems. Oxford University Press, 1950.

3. Freeman, M. P. and Katz, S.: J. Opt. Soc. Am., vol. 53, 1963, p. 1172.

4. Pearce, W. J.: Optical Spectrometric Measurements of High Temperatures, P. J. Dickerman, ed., Univ. of Chicago Press, 1961, p. 125.

5. Elder, P.; Jerrich, T.; and Birkeland, J. W.: Appl. Opt., vol. 4, 1965, p. 589.

6. Tourin, R. H. and Krakow, B.: Appl. Opt., vol. 4, 1965, p. 237.

7. Silverman, S.: J. Opt. Soc. Am., vol. 39, 1949, p. 275.

8. Howard, J. N.; Burch, D. E.; and Willians, D.: J. Opt. Soc. Am., vol. 46, 1956, pp. 186, 237, 242, 334, 452.

9. Burch, D. E.; Gryvnak, D.; Singleton, E. B.; France, W. L.; and Williams, D.: AFCRL Rept., AFCRL-62-698, 1962.

10. Burch, D. E. and Williams, D.: Appl. Opt., vol. 1, 1962, p. 473.

REFERENCES (Concluded)

11. Edwards, D. K.: J. Opt. Soc. Am., vol. 50, 1960, p. 617.

12. Plass, G. N.: J. Opt. Soc. Am., vol. 48, 1958, p. 690.

13. Plass, G. N.: J. Opt. Soc. Am., vol. 49, 1959, p. 821.

14. Plass, G. N.: J. Opt. Soc. Am., vol. 50, 1960, p. 868.

15. Krakow, B.: AIAA J., vol. 3, 1965, p. 1359.

16. Fisher, M. J.: IIT Research Institute, Project Suggestion #64-107NX.

17. Krause, F. R. and Fisher, M. J.: Optical Integration over Correlation Areas in Turbulent Flows, Proceedings 5th International Congress on Acoustics, Liege, 1965.

18. Fisher, M J. and Krause, F. R.: The Crossed-Beam Correlation Technique. J. Fluid Mech., to be published.

19. Watson, H. J. and Mitchell, R. R.: Experimental Study of Scattering of Coherent Beams on Gases. Brown Engineering Company TN R-135, 1965.

20. Becker, A.: Concentration Fluctuations on Ducted Jet Mixing. Thesis, MIT, Dept. of Chem. Engineering, Aug. 1961.

21. Fisher, M. J.: Optical Measurements with High Temporal and Spatial Resolution. Contract NAS 8-11258, IIT Research Institute Progress Report N6092-5, Nov. 1964.

22. Profnikov, A. G.: The Optical Diffusion Method of Measuring Turbulence in Air Flows and Flames. Combustion in Turbulent Flows, L. N. Khitsin, ed., Israel Program for Scientific Translation, Jerusalem 1963.

III. ATMOSPHERIC PHYSICS

ATMOSPHERIC APPLICATIONS OF THE CROSS-BEAM TECHNIQUE

By

William O. Davies* and Robert W. Deuel*

ABSTRACT

The investigation of atmospheric phenomena using a cross-beam technique is considered for two particular cases, quiet nightglow radiation fluctuations and emission or absorption changes due to atmospheric ozone. For each case, experiments would begin with a single-beam observation to determine integrated path signal characteristics. Subsequent cross-beam observations would resolve fluctuating phenomena to the isolated volume of the correlated paths. Calculations indicate an expected high-frequency contribution to the fluctuation spectrum due to the generation-decay processes of the species involved in the observed radiative transition. Variations caused by the transport of cells representative of wind and turbulence characteristics across and within the field of view are expected to produce lower frequency spectral features. Details of source strength, extinction effects, and correlated volume resolution must be considered for each case.

I. INTRODUCTION

This paper outlines some specific problems that might be considered in determining the feasibility of the cross-beam method for investigating atmospheric phenomena. The optical cross-beam method [1,2] can be described briefly as follows: Two spectrophotometer systems, including the light source, dispersing instrument, and radiation detector, are used to investigate gas flows or planetary atmospheres. The light paths of these two systems are arranged to cross in the region being investigated, and the radiation received at each detector is monitored in such a manner that the correlation of the fluctuations in the two beams can be determined. These signal fluctuations may result from variations of density, temperature, pressure or velocity mass motion, and variations in excitation and de-excitation processes. The basic requirements for using the cross-beam method in atmospheric measurements are that (1) a sufficiently strong radiation source exist, (2) fluctuations of atmospheric phenomena are evident in the signal detected from this source, and (3) the fluctuating signal can be interpreted in terms of the phenomena being studied.

In atmospheric tests the primary consideration should be given to the observation of atmospheric constituents that are nonuniformly described in the atmosphere. This approach offers the greatest possibility of obtaining measurable fluctuations in a localized region of an atmosphere, while utilizing spectral regions in which the transmission of radiation through the earth's atmosphere is sufficiently high. Of the large number of phenomena that exist the two specific examples considered here are observations of airglow and ozone. These phenomena were chosen because it has been demonstrated experimentally that the application of the cross-beam method to the study of airglow will yield results in agreement with other methods and because the motion and distribution of ozone is of importance in a number of atmospheric phenomena.

The origin of airglow and atmospheric ozone is discussed briefly, the source and the nature of expected fluctuations are considered, quantitative estimates of the detected signal are given, and some specific experimental arrangements are discussed.

II. AURORA AND AIRGLOW

A. GENERAL DESCRIPTION OF THE PHENOMENA

Aurora and airglow are the terms used to describe nonthermal optical emission generated in the atmosphere at altitudes from 70 to 350 km [3,4]. Although the complete excitation processes are not known, the sources of this energy are believed to be the interaction of air molecules and atoms with energetic particles and solar radiation. The particles that cause aurora are protons and electrons traveling along the geomagnetic field lines, while those producing airflow are primarily electrons in the ionosphere. Solar radiation produces delayed excitation

through chemical reactions and electron-ion recombination that occurs during the night following daytime photo-dissociation or excitation. The mass motion of air, which dissipates energy through viscous interaction, might also be a source of excitation energy if there exists some mechanism to convert the translational energy to atomic and molecular potential energy, but mass motion is a more likely source of intensity variations than excitation.

Airglow is often divided into day glow, night glow, and twilight glow, depending on the time of day it is observed. Day glow is difficult to observe because of the background of scattered solar radiation, and in this discussion the interest is in night glow. Night glow is a faint multi-colored glow of almost uniform brightness that appears in the sky in temperate latitudes; at high latitudes airglow is a relatively weak background for the more intense aurora. The borderline between airglow and weak aurora is nebulous and is defined differently by various authors.

The spectrum of night airglow is made up primarily of atomic lines and molecular bands, with some evidence of continuum sources. The major emitting species appear to be atomic oxygen, singly ionized nitrogen molecules, sodium atoms, and hydroxyl radicals. Some of the interesting features that have been identified include the green and red lines of atomic oxygen at 5577 and 6300 Å, respectively, the sodium D lines 5893 Å, molecular bands of O_2 and N_2^+ at 3914 and 4278 Å, and the Meinel bands of OH. The continuum or group of unresolved lines observed in the green is believed to arise from photochemical reactions of nitrogen oxides. These different emission sources are generally associated with different altitudes.

It is not possible to present a thorough discussion of airglow processes in this short summary. The brief description given here will provide a basis for considering the nature of airglow intensity fluctuations, but it should not be assumed that the mechanisms given for airglow excitation are complete, or even that these mechanisms are entirely understood. The primary interest in this study is the red and green lines of atomic oxygen and the 3914- and 4278-Å bands of N_2^+. The red airglow at 6300 Å is emitted primarily from the F region of the ionosphere (200 to 300 km). A number of processes are believed to contribute to this emission, including

$$O_2^+ + e \rightarrow O(1S) + O(1D)$$

$$NO^+ + e \rightarrow N + O(1D)$$

$$O(1D) \rightarrow O(3P) + h\nu \ (6300 \ \text{Å}).$$
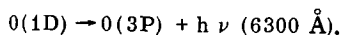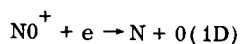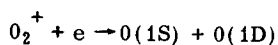
Various photochemical reactions may provide other sources of excitation, but because of the long radiative lifetime of the $O(1D)$ state, most of the radiation will be suppressed by collisions in the altitude region where chemical reactions are significant.

The green airglow at 5577 Å is emitted primarily from the lower E region at about 100 to 120 km altitude, which is also the height of maximum atomic oxygen concentration [5]. It is believed to result primarily from a three-body recombination of oxygen atoms to form O_2 molecules and $O(1S)$ atoms, after which the excited oxygen atoms undergo a radiative transition to the $O(1D)$ state. This mechanism is summarized by the reactions

$$O + O + O \rightarrow O_2 + O(1S)$$

$$O(1S) \rightarrow O(1D) + h\nu \ (5577 \ \text{Å})$$
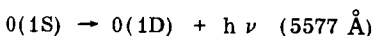
in which the third body (O) is excited by energy liberated in the recombination.

Emission from the N_2^+ First Negative band system provides a measure of total nitrogen ionization in the lower ionosphere. It has been suggested that the N_2^+ emission is a result of bombardment of the upper atmosphere by extraterrestrial particles that may have escaped from the trapped radiation belts; however, ionization of N_2 by cosmic rays may also play a role in the N_2^+ emission. The emission is primarily from below the 100-km altitude region, and variations in intensity during periods of hours are apparently covariant with the 5577 Å oxygen emission which is from the same altitude region. The (0,0) and (0,1) bands at 3914 and 4278 Å, respectively, are the strongest ones observed; however, it is probable that more sensitive instruments could also detect weaker transitions of this band system. This emission is a convenient measure of the ionization rates in the lower ionosphere because the transitions are allowed and therefore radiate the excitation energy very rapidly after the ionization process.

B. FLUCTUATIONS IN AIRGLOW INTENSITY

The basic requirement for using the cross-correlation technique to investigate atmospheric phenomena is that fluctuations exist in the emission (or absorption) being observed, and that fluctuations be quantitatively related to the phenomena of interest. Two possible sources of high-frequency fluctuations in the night glow emission intensity are (1) mass motion of emitting species, i.e., winds and turbulence, and

(2) the statistical processes involved in the generation and decay of excited energy level populations, which are referred to in random process theory as birth-death phenomena. The fluctuation periods for radiative transitions between atomic and molecular energy levels are the same order of magnitude as the radiative lifetime of the energy level on which the transition originates. This is a result of the statistical nature of atomic and molecular processes, for which the occurrence of a transition can only be stated as a probability that, in a given time, the atomic or molecular species will undergo a spontaneous or induced change from one energy level to another; the term "lifetime" denotes the average time a species will remain in a given state before making such a transition. In general, the periods of interest for allowed and forbidden transitions would cover the range from 10^{-8} to 10^{2} sec, with most cases of interest between 10^{-7} and 10^{-1} sec [6].

Thus, when considering atomic and molecular phenomena, one is always dealing with statistical processes, for which the mean fluctuation period can be determined as a fundamental property of the species of interest. If, for example, the time-dependent intensities are recorded for the atomic oxygen transition at 5577 Å, at an altitude where collisional quenching is negligible, the information concerning the generation and decay of $0(1S)$ atoms would be contained in the fluctuations with periods of the order of 0.75 sec [7]. Similar information concerning the $0(1D)$ and N_2^+ ($B\Sigma_u^+$) energy levels would be contained in fluctuations with periods of about 10^2 and 10^{-7} sec [8], respectively.

The wind and turbulence properties of the atmosphere are less well understood, and, to characterize the turbulence properties even approximately, it is necessary to consider specific altitude regimes. It is fairly well established that oxygen atom emission at 5577 Å is primarily from an altitude of about 100 km [9,10]. This airglow occurs in patches with horizontal dimensions on the order of 1000 km, which are observed to drift at speeds on the order of 100 m/sec. The mesosphere and lower thermosphere (60 to 105 km) are characterized by strong wind shears and turbulence, and there is a tendency for the wind direction to reverse every 3 to 4 km, producing an effective wavelength of 6 to 8 km [11]. Within these turbulent cells, rocket trails have been observed to disrupt into eddies of sizes 100 m and up, with the most probable size being about 1 km. The horizontal drift of the globules corresponds to the vertical wavelength of 7 km. Figure 1 (from Kellogg [12]) shows this structure in a general circulation diagram of the atmosphere up to about 100 km.
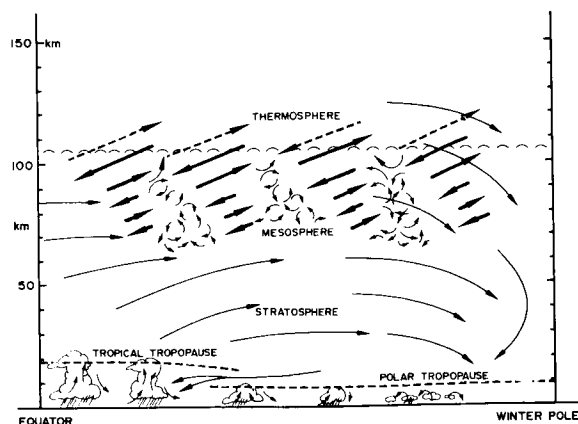
FIGURE 1. SCHEMATIC REPRESENTATION OF THE MIXING PROCESS IN THE ATMOSPHERE

If one viewed a fixed position in the night sky, any variation due to the "patch" motion as a whole would occur in times of the order of 10^4 sec, so that there should be no difficulty in distinguishing these slow variations from the generation and decay processes. For the most probable turbulent cell size with a dimension the order of 1 km, the typical fluctuation period is the order of 10 sec; with cell sizes of 100 m to 10 km, the fluctuation periods would range from 1 to 100 sec.

For the airglow at 5577 Å, it appears possible to separate the fluctuations resulting from turbulence from those associated with the radiative lifetime by (1) considering different periods of the fluctuations and (2) varying the photometer field of view. Although the fluctuation frequencies for turbulence and lifetime would overlap somewhat, the mean periods for these processes of 10 sec and 1 sec, respectively, are sufficiently different so that some differentiation appears possible.

C. OBSERVATIONS OF AIRGLOW FLUCTUATIONS

Several airglow experiments have been conducted in which some physical property was deduced by cross-correlating intensity fluctuations recorded by two photometers. The experimental arrangement for a cross-beam covariance airglow experiment is shown in Figure 2 [13]. Two photometers, designed to record emission intensities of selected airglow emission lines, are placed about 100 km apart, and their fields of view are crossed at a given altitude. The time-dependent intensities are recorded on magnetic tape, and the data are analyzed to determine the statistical correlation of the two signals and to

AIRGLOW FLUCTUATION MEASUREMENT—I

6300
5577   LINE AND CONTINUUM
4278   ZENITH OBERSVATIONS

PHOTOMETER → 400 CHANNEL PULSE COUNTER 1.0-0.001 SEC/CH → PUNCHED PAPER TAPE STORAGE → IITRI COMPUTER → AUTOCOVARIANCE & SPECTRAL INTENSITY OUTPUT

IITRI-KOP SITE
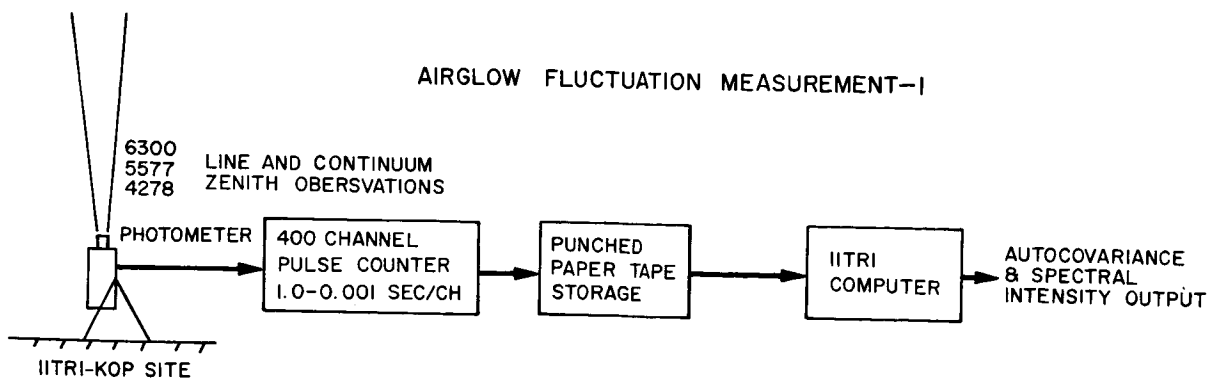
FIGURE 2a. AIRGLOW FLUCTUATION MEASUREMENT

IONOSPHERE

DATA SYSTEM 1 → IITRI OR NASA COMP ← DATA SYSTEM 2

IITRI-KOP SITE   AUTOCOVARIANCE & CROSS CONVARIANCE & SPECTRA OF BOTH   FIELD SITE
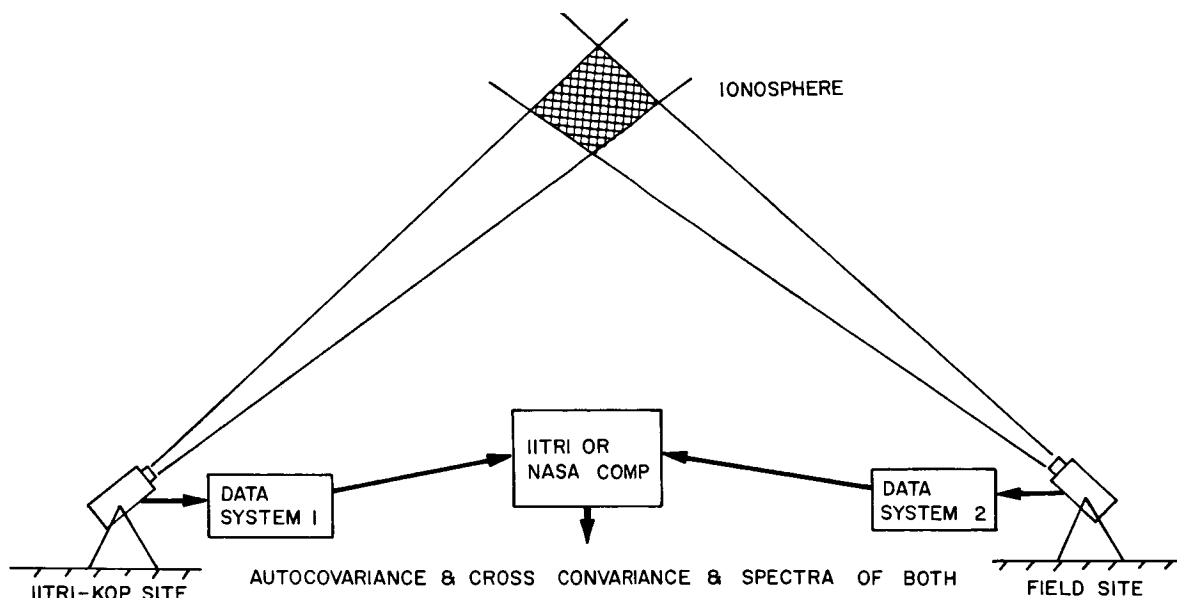
FIGURE 2b. AIRGLOW CROSS BEAM CORRELATION

relate these quantities to atmospheric phenomena at the intersection.

Paulson and Shepherd [14] used a cross-correlation of auroral intensities from atomic oxygen at 5577 Å and the N_2^+ at 3914 Å, to obtain the lifetime of the $0(1S)$ energy level. This was a cross-correlation experiment but not a cross-beam experiment, as the two photometers viewed the same integrated path in the atmosphere. The photometer field of view defined a diameter of about 1.5 km at an altitude of 100 km. However, the integration over the entire path probably averages out the fluctuations caused by turbulence, permitting a measurement of the energy level lifetime. Assuming the excitation

rates of the $0(1S)$ and N_2^+ ($B\Sigma_u^+)_{v=0}$ energy levels are proportional, the fluctuating intensities are related by the expression

$$dI_1/dt + \tau^{-1} I_1 = KI_2$$

where $I_{1,2}$ are the intensities at 5577 and 3914 Å, respectively, τ is the lifetime of the $0(1S)$ state, and K is the ratio of the excitation rates of the two energy levels involved. One of the intentions of these authors was to use the measured de-activation rates to infer the airglow altitude, but these efforts yielded inconsistent results. Altitude measurements could be made more easily and reliably by separating the two photometers by a distance on the order of the altitude.

A cross-beam, cross-correlation airglow experiment has been performed by Wolff [15] to determine the airglow altitude. Two photometers, both viewing the atomic oxygen emission at 5577 Å, were placed 246 km apart; they scanned the atmosphere in such a manner that the intersection of their fields of view moved in a horizontal line at a constant speed. Observations were made over a range of altitude, and it was suggested that the altitude of maximum correlation (97 km) is the height at which the maximum intensity of the 5577 Å oxygen line originates. The field of view was 1 by 8 degrees, which defines an area of about 1.5 by 12 km at 100 km. Based on the discussion above, this measurement would include fluctuations generated by both turbulence and birth-death processes. This experiment suffered from a paucity of data, as only 4 out of 30 attempts yielded useful information, the remainder being destroyed by inclement weather or recording difficulties. Nevertheless, when the correlation data for these 4 sets of measurements are combined, the 5577 Å airglow altitude obtained from these observations (97 ± 2 km) is in excellent agreement with results obtained from rocket flights and triangulation by time variation [9,10].

A similar airglow experiment is being conducted at the IIT Research Institute, using a modification of photometers [16] that have been used frequently to measure slower variations of airglow intensity [e.g., 12]. These are three color photometers that include wavelengths of 6300, 5577, and 4278 Å; the instrument automatically switches colors and subtracts the continuum background from the desired line or band intensity. In this study, the nightly and dawn variations of airglow intensity and their correlation with daytime ionospheric absorption are being investigated, and the altitude of airglow emission will be measured. The statistical fluctuation spectrum for a single photometer has been determined at a wavelength of 6350 Å, and a time series autocovariance program was used to compute the harmonic components of the airglow variations. The results show maximum fluctuations at a frequency corresponding to the $0(1D)$ lifetime. The addition of a second photometer will permit observations on a volume of the same order as the turbulent size.

OZONE

A. GENERAL DESCRIPTION OF THE PHENOMENA

Ozone is formed in the upper layers of the atmosphere by the action of solar ultraviolet radiation on oxygen molecules [5]. Photodissociation of oxygen molecules produces atomic oxygen, after which a three-body collision between O_2, O, and any third body (M) results in the production of ozone. The major ozone concentration lies within a band at an altitude of 10 to 30 km, with the peak near 20 km. The ozone decay process is photodissociation at higher altitudes (stratosphere) and chemical recombination in the lower (tropospheric) region. A typical ozone profile, which can be calculated within the accuracy of the measurements by making use of known reaction rates, radiation intensities, and particle number densities, is shown in Figure 3.
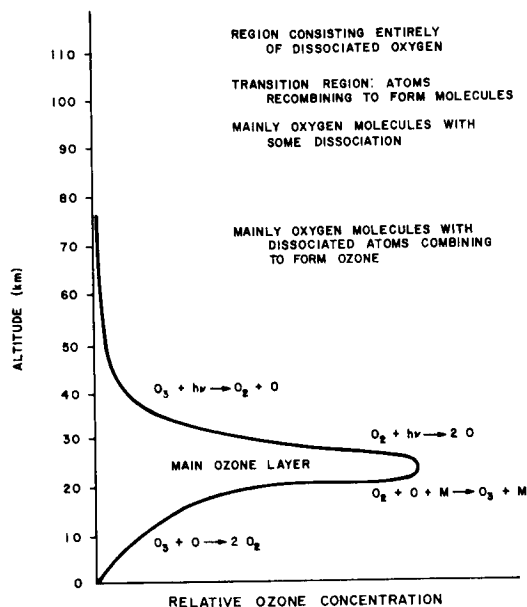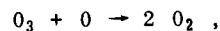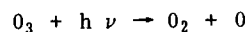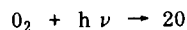

FIGURE 3. GENERAL FORM OF OZONE DISTRIBUTION

In a dry atmosphere the ozone concentration depends on the reactions:

$$O_2 + h\nu \rightarrow 2O$$

$$O_2 + O + M \rightarrow O_3 + M$$

$$O_3 + h\nu \rightarrow O_2 + O$$

$$O_3 + O \rightarrow 2O_2 ,$$

and the steady-state ozone concentration is given by

$$(O_3) = \frac{(k_2/k_4)\ (O_2)\ (M)}{1 + k_3(O_3)/k_1(O_2)} ,$$

Where the k_i are the reaction rates or absorption coefficients for the relevant processes, and the parentheses indicate species concentrations. In some recent work on ozone formation mechanisms, it has been suggested that the ozone concentration is very sensitive to water vapor concentration [17]. Thus, these reactions and the expression for the equilibrium concentration must be considered approximate. The method of analyzing fluctuations would remain the same, but the photochemistry of ozone in a moist atmosphere should be considered in much greater detail before attempting to apply the cross-beam method.

A study of the ozone concentration and motion in the atmosphere could be one of the most rewarding applications of the cross-beam method. Monitoring atmospheric ozone atmosphere could serve two purposes. First, the distribution and motion of ozone are of interest because of their meteorological significance, and second, ozone could be used as a tracer to monitor wind motion, air pollution, temperature, or reaction rates in the atmosphere. A significant contribution could be made to the understanding of vertical transport processes in the region of the tropopause with a method that is capable of monitoring ozone motion as well as concentration.

B. FLUCTUATIONS OF ATMOSPHERIC OZONE

The ozone concentration in a given region of the atmosphere may undergo fluctuations of widely differing frequencies because of variations in the excitation source, recombination rates, mass motion, and other effects. The fact that different concentrations and distributions with altitude are observed on different balloon and rocket flights attests to the long term variations [18,19], but little is known concerning the ozone variations on a shorter time scale. However, the high-frequency fluctuations observed on airglow phenomena are subject to the same type of generation and decay processes, and one would expect similar effects for ozone. An estimate of the fluctuation periods associated with the generation-decay processes can be based on the kinetics of ozone formation in the atmosphere and the radiative properties of ozone. This can be accomplished by comparing the rates of the reactions involved in the ozone production mechanisms to determine the rate-determining step. In a first approximation one can assume that the end products of the other reactions are in a steady state, so that the mean frequency of fluctuations due to birth-death processes is approximately equal to that of the rate-determining step.

At an altitude of 20 km, the O_2 dissociation occurs through an allowed optical transition at the rate of approximately 10^8 sec^{-1}, while the three-body recombination process generates ozone at the rate of 10^5 sec^{-1}. This implies that in the presence of solar radiation the three-body recombination process is the rate-limiting step in the ozone generation process, and the fluctuation period associated with this process is the order of 10^{-5} sec. The disappearance of O_3 is determined primarily by absorption of solar radiation in the upper atmosphere and chemical recombination in the lower atmosphere. If the chemical recombination rate of 20 km is approximately 10^3 sec^{-1} and the photodissociation occurs at the rate of 10^6 sec^{-1}, a typical value for the period associated with these fluctuations is 10^{-3} sec.

Based on this estimate, the rate-controlling step is the chemical recombination ($O_3 + O \rightarrow 2 O_2$), and there should exist periods for ozone fluctuations resulting from generation-decay processes of the order 10^{-3} seconds. It is emphasized that this value is a very rough estimate based on average values for atmospheric processes, which should be considered in much more detail during the design of an experiment. Any attempt at a cross-beam experiment should be preceded by an experimental investigation of fluctuations observable with a single photometer.

The atmosphere in the ozone layer is generally characterized by thermal stability. It is expected that the periods associated with turbulent processes would be long compared to those of birth-death processes. Some of the more interesting measurements would be of the upper and lower portions of the ozone layer, where ozone concentration is very low; for sufficiently high and low altitudes the turbulence increases, and it would be necessary to consider the effect of turbulence on the intensity fluctuations. At the higher altitudes the fluctuations associated with turbulence will approach the values described above (i.e., mean periods of 10 sec).

C. OBSERVATIONS OF OZONE FLUCTUATIONS

The optical detection of fluctuations in the ozone layer could be accomplished with a spectrophotometer system that measures ozone absorption of an external light source or from observations of ozone emission intensity. In either case it is necessary to use a wavelength region in which the ozone can be spectroscopically distinguished from other atmospheric constituents. The ozone absorption

bands that might be used include the Hartley and Huggins band systems in the ultraviolet and the fundamental vibration band in the infrared at 9.6 μ. In order to offer some quantitative estimates of the feasibility of observing ozone fluctuations, the atmospheric absorption of the entire 9.6-μ ozone band is considered. In a more detailed treatment of this problem, one should also consider the use of the ultraviolet absorption bands and the variation of intensity with wavelength in the 9.6-μ fundamental band.

The absorption of the 9.6-μ ozone band has been investigated by a number of authors [20,21], and several attempts have been made to extrapolate laboratory results to atmospheric conditions. The fractional transmission through the entire ozone layer for wavelength from 9.0 to 10.3 μ is about 0.63 [22]. The extinction caused by molecular scattering can be neglected compared to absorption, because Rayleigh scattering for the entire atmosphere at 10 μ has an extinction coefficient of 10^{-6}.

The solar radiation incident on the earth at a wavelength of 10 μ is of the order of 2×10^{-5} W/cm^2 - μ. If 60 percent of this radiation is transmitted through the ozone, the signal of about 10^{-6} W/cm^2 on the detector is well within the detection capability of present technology. In a cross-correlation experiment, it is necessary to monitor the fluctuating intensity, and it is therefore of interst to estimate the signals that would result from a typical fluctuation. If there is a 1-percent variation of ozone in the wings of the ozone distribution, e.g., at an altitude of 10 km, the change in the signal received at a detector on the ground is 8×10^{-8} W/cm^2. Presently available solid-state infrared detectors would offer a signal-to-noise ratio of about 200 for a fluctuating signal of this magnitude. Thus, it is possible to detect 1-percent fluctuations of ozone in regions of low ozone concentrations, and smaller fluctuations in regions of larger ozone concentrations.

The possibility of fluctuation measurements of ozone emission from the atmosphere has been demonstrated in a number of investigations. The emission intensity of the infrared band at 9.6 μ was reported to be about 70 erg sec^{-1} cm^{-2} ster^{-1} wave no.$^{-1}$ with more than half originating above the tropopause [23,24]. Although the amount of ozone at the higher levels is much greater than that below the tropopause, the higher temperature near the surface is responsible for the large contribution by tropospheric ozone to the total radiation. A preliminary investigation to an ozone cross-beam experiment would necessarily include a more detailed study of the emission contributions from various levels in the atmosphere,

extinction by intervening layers, and emission/absorption effects of other constituents [25,26]. Some possible experimental configurations are shown in Figure 4. A study of ozone fluctuations in the atmosphere could be conducted with a single ground-based photometer viewing solar radiation at a wavelength near 10 μ to provide measurements of temporal and spatial variations in ozone concentration over a region that corresponds to the photometer field of view. Even the single-beam experiment would provide a knowledge of the ozone fluctuations in a small part of the atmosphere, because of the nonuniform distribution of ozone.

For a cross-beam experiment, one could consider the use of one detector at a ground station and one on a satellite; the former could be used to monitor variations of the amount of solar radiation absorbed by ozone, while the latter would monitor the variations of ozone absorption of the earth's thermal radiation at 10 μ.

One could also consider the two ground-based radiation sources with both detectors in orbit; three possible radiation sources for this configuration are reflected sunlight, thermal emission from the earth, and an artificial light source. Solar radiation diffusely reflected from the surface of the earth at 10 μ is about 1.5×10^{-5} W/cm^2-μ, while thermal radiation from the earth at this wavelength is 3×10^{-3} W/cm^2-μ. Thus, at this wavelength, thermal emission from the earth far surpasses the reflected solar radiation and could therefore be used as a radiation source for a cross-beam experiment; this situation would be reversed if ultraviolet radiation were used for the experiment.

CONCLUSION

It appears that, as far as airglow and aurora are concerned, there always exist measurable fluctuations that cover a wide range of frequencies [14]. Therefore, the problem is not one of finding a fluctuating phenomenon, but of focusing one's attention on fluctuations with periods that can be related to some specific atmospheric phenomenon. The results described above suggest that fluctuations exist even in so-called quiet airglow and aurora, and the fluctuation spectrum includes a broad range of frequencies which are presumably related to different physical phenomena. Of particular importance is the conclusion that one can deduce mean values such as lifetime of molecular energy levels or atmospheric altitudes corresponding to given phenomena from a frequency decomposition of the fluctuating signal. The method
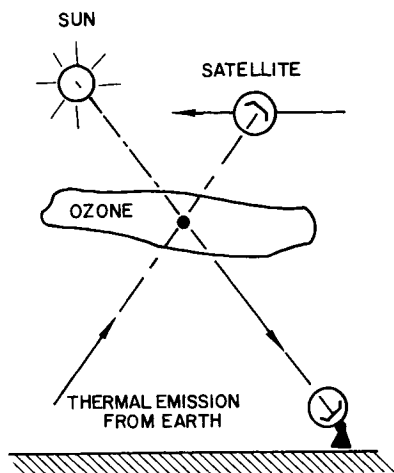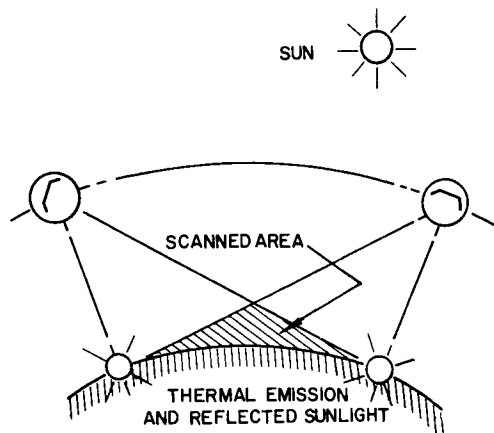
FIGURE 4a. GROUND AND ORBITAL DETECTORS

FIGURE 4b. SATELLITE-BASED DETECTORS

FIGURE 4. CROSSED BEAM TEST ARRANGE-
MENTS FOR OZONE ABSORPTION STUDIES

appears to offer promise of diagnosing atmospheric phenomena, with a spatial resolution hitherto unavailable, in studies of both turbulence and mean values of atmospheric properties.

The results of this brief investigation also suggest that the possibility of monitoring atmospheric

ozone with the cross-beam technique is quite promising. Solar tracking stations would be relatively easy to construct and operate with readily available equipment; time-delay correlation of the results and integrated energy-frequency spectra could provide information on the statistics of generation and decay processes, as well as temporal and spatial resolution of fluctuations in ozone density. In a more elaborate experiment, two detectors could be placed on a satellite and maneuverable sub-satellite to provide real-time spatial correlation. Black-body emission by the earth is dominant over reflected solar radiation at the $10\text{-}\mu$ wavelength, and could be used as the intensity source for real-time correlation by satellite detection. This technique would be of particular advantage in experiments designed to correlate ozone concentration with production and decay mechanisms, define atmospheric reaction processes, correlate ozone density fluctuations and transport with air motion, and examine the relation of vertical mixing in the region of the tropopause. Although the details of such applications have not been evaluated, it is conceivable that ozone detection may be used in diagnosing or detecting meteorologically significant processes and in studying turbulence associated with tropospheric-stratospheric mixing.

REFERENCES

1. Fisher, M. J. and Krause, F. R.: Local Measurements in Turbulent Flows Through Cross-Correlation of Turbulent Fluctuations. NASA TM X-53295, Apr. 1965.

2. Krause, F. R. and Fisher, M. J.: Remote Sensing with Optical Cross-Correlation Methods. Presented at the Interdisciplinary Symposium on AAP, Huntsville, Alabama, Jan. 1966.

3. Chamberlain, J. W.: Physics of the Aurora and Airglow. Academic Press, 1961.

4. Ratcliffe, J. A., ed.: Physics of the Upper Atmosphere. Chapt. 5, "The Airglow," by Bates, D. R., Academic Press, 1960.

5. Kuiper, G., ed.: The Earth as a Planet. "Physics of the Upper Atmosphere," by Bates, D. R., U. of Chicago Press, 1954.

6. Herzberg, G.: Spectra of Diatomic Molecules. Van Nostrand and Co., 1945.

7. Garstang, R. H.: Nat. R. Astr. Soc. Vol. 111, 115, 1951.

REFERENCES (Cont'd)

8. Bennett, R. G. and Dalby, F. W.: J. Chem. Phys. Vol. 31, 434, 1959.

9. Toosey, R.: Ann. Geophys. Vol. 14, 186, 1958.

10. Packer, D. M.: Ann, Geophys. Vol. 17, 65 1961.

11. Kellogg, W. W.: Pollution of the Upper Atmosphere by Rockets. Rand Corp. Rept. RM 3961-PR, June 1964.

12. Sears, R. D.: Trans. Amer. Geophys. Union, Vol. 71, 77, 1966.

13. Sears, R. D.: IIT Research Institute Rept 1195-2, 1962.

14. Paulson, K. V., and Shepherd, G. G.: J. Atm. Terr. Phys. Vol. 27, 831, 1965.

15. Wolff, M.: Trans. Amer. Geophys. Union, Vol. 47, 75, 1966.

16. Filosofo, I.; Greenspan, J. A.; and Groom, C. M.: Appl. Optics; Vol. 4, 215, 1965

17. Hunt, B. G.: Photochemistry of Ozone in a Moist Atmosphere. J. Geophys. Res. Vol. 71, 1385, 1966.

REFERENCES (Concluded)

18. Van Allen, J. A., and Hopfield, J. J.: Preliminary Report on Atmospheric Ozone Measurements from Rockets. Mem. Soc. Roy. Sci. Liege, Vol. 12, 1952, pp. 179-183.

19. Pittock, A. B.: Determination of the Vertical Distribution of Ozone by Twilight Balloon Photometry. J. Geophys. Res. vol. 68, no. 18, Sept. 15, 1963, pp. 5143-5155.

20. Walshaw, C. C.: Quart. J. Roy. Meteorol. Soc. vol. 83, 315, 1955.

21. Kaplan, L. D.; Migeotte, M. V.; and Neven, L.: J. Chem. Phys. Vol. 24, 1183, 1956.

22. Kondratyev, K. Ya., and Niylish, Kh. Yu.: NASA TT F-207, 1964.

23. Goody, R. M., and Roach, W. T.: Quart. J. Roy. Meteorol. Soc. Vol. 82, 217, 1956.

24. Epstein, E. S.; Osterberg, C.; and Adel, A.: J. Meteorol. Vol. 13, 319, 1956.

25. Goody, R. M., and Roach, W. T.: Quart. J. Roy. Meteorol. Soc. Vol. 84, 108, 1958.

26. Walshaw, C. D.: Quart. J. Roy. Meteorol. Soc., vol. 86, 519, 1960.

FEASIBILITY AND POTENTIAL OF ATMOSPHERIC CROSSED-BEAM EXPERIMENTS

By

F. R. Krause, J. C. LaFrance*, S. V. Paranjape**, and J. B. Stephens

I. INTRODUCTION

The crossed-beam method, a new test arrangement for the remote sensing of atmospheric phenomena, employs the triangulation of two collimated light beams for local studies of a preselected region. This region is centered around the line of minimum separation between the almost intersecting beams. The radiative power received at each detector is monitored in such a way that the fluctuations of the radiative power can be determined. The fluctuations of the two beams are then multiplied and averaged. The resulting "two beam product mean value" allows one to compare the fluctuations of radiative power which are produced simultaneously in two separate locations [1]. These two locations are defined by the two points of minimum beam separation. The fluctuations of radiative power in these points, at the region of interest, indirectly carry the information about any atmospheric phenomenon that modifies the local emission or extinction of the light beams.

In most remote sensing methods, the attenuation or emission of electromagnetic radiation is measured along the entire path from the source to the detector. To interpret the results of such an observation, some assumption is generally required that implied prior knowledge of the system being measured. This knowledge is usually in the form of a model of the phenomenon being observed; for example, in atmospheric studies one might use the adiabatic or isothermal model atmosphere. Assumptions for dynamic studies are made concerning the symmetry, expansion properties, and temperature. The important point is that with single path observations it is not generally possible to obtain spatially resolved measurements of the thermodynamic or flow properties without invoking such models.

In crossed-beam experiments, theoretical models need not be invoked. The spatial and temporal variation of turbulence and, hopefully, thermodynamic properties would be measured by the crossed-beam method on sometimes inaccessible regions, where other methods are restricted to a mean value over the entire optical path or to a direct measurement in a single point. The potential applications of crossed-beam experiments, therefore, include almost every conceivable experiment in which the basic measurement requires monitoring the concentration of atmospheric species and contaminants. This could include observations of low level and clear-air turbulence, motion and distribution of air pollution from industrial wastes and rocket tests, weather fronts, and ozone motion and distribution (which bears some relation to global weather patterns). It might also be possible to study the nature and motion of targets of opportunity such as storms, hurricanes, meteors, cometary dust, and noctilucent clouds.

The crossed-beam method could thus prove to be a powerful tool to study a wide range of problems that involve health and navigational hazards, weather forecasting, and radio communications on a global scale. The validity of the crossed-beam concept has already been established by the results of existing measurements. These results show that correlations from hot-wire and crossed-beam observations in subsonic jets yield identical results for convection speeds [1], and that crossed-beam observations of the airglow altitude are in agreement with rocket observations [2]. Thus, the crossed-beam

correlation method is theoretically sound, and it has been shown experimentally to provide results in agreement with more accepted methods.

The feasibility and potential of crossed-beam experiments in the lower atmosphere are illustrated in this paper by considering the operation which would be necessary to measure a horizontal wind profile up to altitudes of 30 km. Scattering reflection of sunlight, thermal radiation from the atmosphere of the earth, and nonthermal emission in the atmosphere provide extended natural sources of radiative power that need not be tracked. Measured modulations of laser light indicate that atmospheric fluctuations do produce detectable fluctuations, even under a clear sky, which are not obscured by receiver noise. The use of these natural sources then provides for extremely flexible test arrangements, which could sweep the entire altitude profile of horizontal winds with a single flyby using orbital detectors or with a repeated scan utilizing ground detectors. Several fundamental experiments which would indicate the resolution of such wind profiles in space and time are designed.

II. OBJECTIVES OF METEOROLOGICAL APPLICATIONS

At present the horizontal winds and the thermodynamic parameters of the atmosphere are monitored by instruments on meteorological towers, balloons, aircraft, and rockets. These monitoring systems have the following inherent limitations associated with their operation: (1) single path experiments, (2) restricted altitude ranges, (3) limited control over horizontal traverse, (4) interference with the phenomenon of interest, and (5) relatively large scale averaging. Because of these limitations, some meteorological problems partially defy the use of existing instrumentation. Some of these problems are listed in Table I. Meteorologists have already turned to remote sensing devices to overcome part of the above instrumentation problems. It is hoped that remote sensing devices accomplish the following three objectives [3]: (1) establish global observation of the entire earth's atmosphere on a regular basis, (2) provide observations for direct use in mathematical prediction models, and (3) follow the full life cycle of weather systems such as hurricanes. In meeting these objectives, one could overcome the two main problems which at present plague numerical weather prediction. These problems are (1) insufficient grid points and (2) the unknown effect of small-scale disturbances on the nonlinear behavior of large-scale motions.

At present, a grid of observation stations is available only in North America, Europe, and the northern part of Asia. Except for Australia and very few observation stations in Africa, South America, and Antarctica, the Southern Hemisphere is void of data. Attempts are presently being made to measure winds with long-lived constant pressure balloons, tracked either from the ground or by satellite. The spatial positions of these balloons depend on the circulation pattern and not on the desires of the meteorologist. Any improvement in providing meteorological information at discrete levels in the atmosphere (≈50 to 100 mb pressure level) at discrete time intervals (≈4 times a day) and with discrete spacing (≈322 km) would be greatly welcomed and would be considered a big leap forward in improving forecasting conditions. The remainder of this report shall indicate how crossed-beam test arrangements may be used in remote sensing missions to supply the missing information at the desired location.

The second problem was to estimate the effect of small-scale disturbances, such as convective cloud patterns, small vortices, turbulence, etc., on the nonlinear behavior of larger-scale motions. Attempts are presently made to estimate such small-scale systems from a stationary satellite which takes cloud pictures over the Pacific Ocean. However, commensurate information on winds, temperature, etc., is still lacking. This means that, in addition to the large-scale information mentioned previously, small-scale measurements should be available for certain time intervals and certain critical regions, which may be specified on short notice by weather prediction centers. Here again, a crossed-beam monitoring system might be the answer. In the following pages, we will indicate that scanning crossed-beam systems give turbulence length scales and wave number components in addition to wind information. These results are necessary to study the transfer of kinetic energy between atmospheric motions, which are characterized in terms of macroscales, mesoscales, and microscales. Single point probings such as balloon-borne beam instruments cannot provide this information.

III. REMOTE SENSING OF METEOROLOGICAL PHENOMENA EMPLOYING NATURAL LIGHT SOURCES

A fundamental requirement for crossed-beam experiments is the existence of measurable fluctuations of radiative power caused by the phenomenon under investigation. To fulfill this requirement, the source of radiation must (1) be an extended source of

Parameter	Current Limitations	Desired Coverage	Extent	Time Period Requirements	Resolution
Wind velocity including jet stream wind shears	inadequate resolution, sparse network	vertical structure minimum of two components, three desired	world	6 hrs	± 1 km 0. 5 m/s ± 5 (m/vertical)
Fronts	sparse network in certain areas (over oceans)	position and structure	world	6 hrs	± 0. 25 km
Water vapor	inadequate resolution, sparse network	vertical structure	world	6 hrs	± 0. 25 km
Air pollution	inadequate resolution, sparse network	concentration movement	U. S. (mainly)	6 hrs	50 m
Ozone Distribution	insufficient statistical information	distribution and movement	world	6 to 12 hrs	10 m 0. 5 m/s
Hurricane structure	inadequate resolution	movement, internal structure	temperate and tropical ocean areas	continuous (target opportunity)	50 m

radiation as opposed to a point source, and (2) be of sufficient intensity so that induced fluctuations of radiative power may be detected by spectrophotometry. Thus, it will be necessary to evaluate the following three parameters to determine the feasibility of atmospheric crossed-beam experiments: (1) the tracer to be employed to monitor the turbulence fluctuations, (2) the radiative power of the source, and (3) available detector technology within the atmospheric windows.

A. TRACERS

A tracer is defined here as any nonuniformly distributed constituent of the atmosphere that attenuates or emits radiation. This implies that temporal density fluctuations of the tracer, due to atmospheric turbulence, will modulate the radiation. Aerosols, water vapor, and ozone are tracers suitable for crossed-beam experiments, which could be used to cover different altitude regions.

B. MEAN RADIANCE OF EXTENDED NATURAL SOURCES

Consider a photometer coupled to an astronomical telescope. The detectable radiative power is contributed by all radiative phenomena inside the collimated field of view of the telescope as has been illustrated in Figure 1. In atmospheric applications,
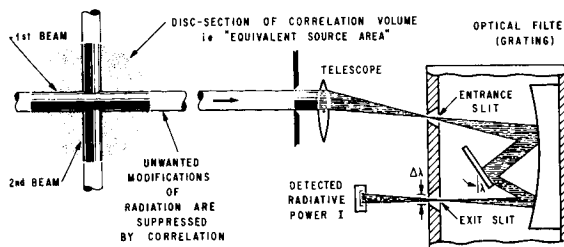
FIGURE 1. CROSS-BEAM SPECTROSCOPY

the detector is placed on either the ground or orbit-ing spacecraft as shown in Figure 2. Because of light absorption in the atmosphere, remote sensing of meteorological phenomena inside the atmosphere requires work in regions of the electromagnetic spectrum, where the atmosphere is at least partially transparent. These "optical windows" may be found from typical transmission spectra like the one shown in Figure 3. The lower portion of this figure shows the spectral region where suitable windows exist.

FIGURE 3. AVAILABLE ATMOSPHERIC WINDOWS FOR THE CROSSED-BEAM APPLICATION

3. Solar radiation reflected and scattered by the earth's surface

4. Thermal radiation from the earth and the atmosphere

} orbital detector

All these sources constitute an extended background of radiation. We will discuss the characteristics of these sources that are potentially useful as part of a weather monitoring system.

C. GROUND-BASED DETECTORS

Ground-based detectors (Fig. 2) can use scattered sunlight and infrared emission from the atmosphere as radiation sources to monitor atmos-pheric phenomena.

1. Scattered sunlight. - The solar radiant energy passing through the atmosphere experiences complex transformations. On the part from the outer bound-ary of the atmosphere to the earth's surface, there are observable both direct solar radiation in the form of a parallel beam of rays emanating from the sun and scattered radiation incident from all points of the sky. The total flux of scattered radiation reaching an object depends on the sun angle, the cloud cover, the albedo of the ground, and the concentration of tracers in the atmosphere.

The flux of the scattered radiation is weakly dependent upon earth latitude and more strongly dependent upon sun elevation angle, as shown in Figure 4.

Influenced by the various parameters expressed above, scattered solar radiation fluxes have been

FIGURE 2. CROSSED-BEAM TEST ARRANGE-MENT FOR HORIZONTAL WINDS

Remote sensing within the "optical windows" re-quires the existence of either man-made or natural radiation sources. For monitoring vast and sparsely instrumented areas, man-made sources or direct sunlight are disadvantageous since they lead to diffi-cult technical tracking problems. Point sources (man-made or natural) must also be discarded be-cause they suffer scintillation. Natural, extended background sources which require no tracking and suffer no scintillation are ideal sources for use in the crossed-beam technique.

The following sources are conceivable:

1. Scattered solar radiation

2. Emission from the atmosphere

} ground detector

APPROXIMATE LATITUDE	LOCATION	SCATTERED SOLAR RADIATION FLUX (10^3 WATTS/CM^2)			
		SUN ELEVATION ANGLE			
		10°	20°	30°	40°
60°	HELSINKI	3.5	4.9	6.3	7.0
50°	VIENNA	3.5	6.3	8.4	9.8
40°	NICE	--	7.0	8.4	9.1

BOLOMETER COLLECTS RADIATION FORM 2π STERADIANS

FIGURE 4. DEPENDENCE OF SCATTERED
SOLAR RADIATION ON LATITUDE AND
SUN ELEVATION ANGLES

measured ranging from 0.35 to 2.80 x 10^{-2} W/cm^2
[4]. Kondrat' yev [4] cites individual cases where
the value of the flux of the scattered radiation ex-
ceeds 7 x 10^{-2} W/cm^2. A conservative figure for the
flux from a cloudless sky with a solar altitude of
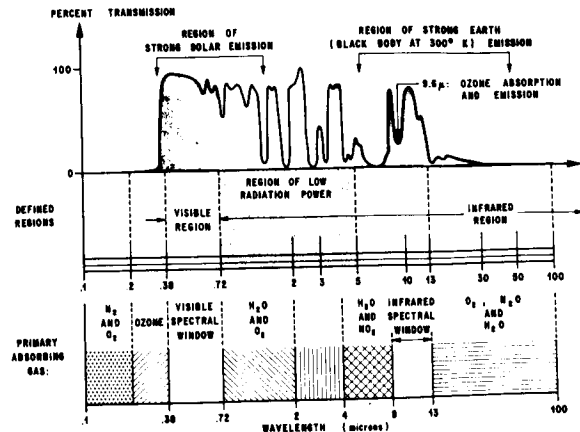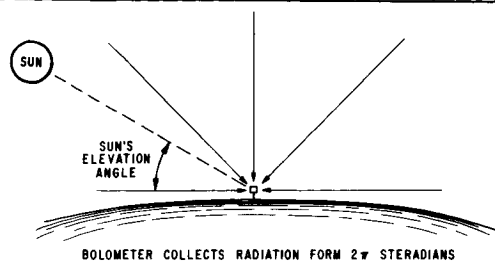45 degrees would be about 1.4 x 10^{-2} W/cm^2.

In crossed-beam experiments, we are not
interested in the total flux which is received from
the entire sky (hemisphere = 2π sr) but only in the
sky radiance which is available to the small angle of
view $\Delta\alpha$ of a telescope [$4\pi \sin^2 \left(\dfrac{\Delta\alpha}{4}\right)$ sr]. Assuming,
that Lambert's law gives a reasonable approximation
of the angular distribution of scattered sunlight, the
radiance of a vertically pointing telescope becomes

$$1.4 \cdot 10^{-2}/\pi = 4.5 \cdot 10^{-3} \text{ W/cm}^2 - \text{sr}.$$

Of prime importance in our study of the scattered
radiation is the radiance available in an emission
bandwidth, $\Delta\lambda$. The spectral radiance of scattered
radiation is shown in Figure 5 [5] for a cloudless sky
with the sun at a zenith angle of 45 degrees for an
observer located on the earth's surface and at an al-
titude of 30 km. This establishes a useful bandwidth
of emission for scattered solar radiation of 0.38 to
0.72μ with a maximum intensity between 0.4 and
0.5μ. The remaining radiation is found in the infra-
red region. It is not due to scattering of solar radi-
ation, but to thermal emission in the atmosphere.

The flux of scattered sunlight is, in first approx-
imation, roughly proportional to the density of the
scattering molecules above the detector. At 30 km,
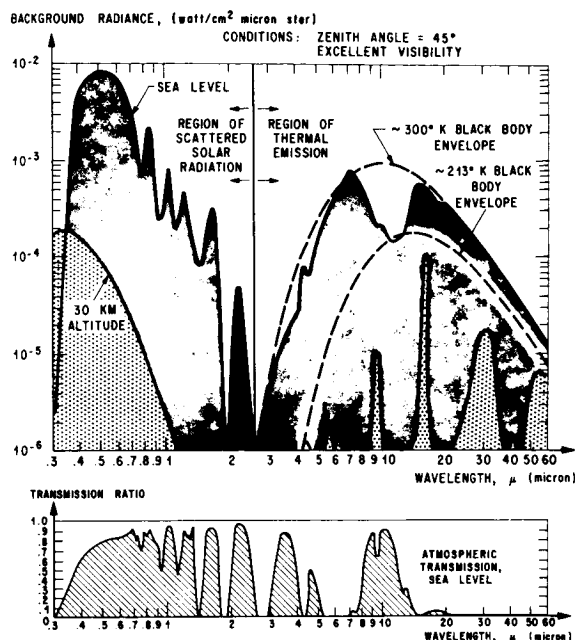
FIGURE 5. ATMOSPHERIC BACKGROUND
RADIANCE AS A FUNCTION OF
ALTITUDE [4]

the atmospheric density is 10^{-2} that of sea level.
Hence, we may expect the local source strength of
scattered solar radiation at these altitudes to be of
the order of 10^2 times smaller than at sea level.
This is found to be so, as shown on Figure 5 [5].

2. Ozone emission. - Besides scattered sunlight,
the ground detector could also use the thermal emis-
sion in the atmosphere. Typical experimental re-
sults were already shown in Figure 5 for wavelengths
in excess of 2.8μ. For crossed-beam experiments,
we need an atmospheric window to "see" through the
troposphere. However, some absorption must be
left; otherwise, there would be no thermal emission.
For the purposes of this study, we selected the at-
mospheric window between 8 and 12μ. Inside this
window, the thermal emission is primarily provided
by the 9.6 thermal emission band of ozone. This
band is clearly indicated by the "dip" in the atmos-
pheric transmission (Fig. 5). For ground detectors
this band is important because (1) it is in a spectral
region where it is the only active tracer (there exists
no water vapor or strong CO_2 bands to interfere) and
(2) the ozone emission, up to an altitude of 30 km,
is constant, showing that ozone produces an extended
background source which is located above the tropo-
sphere during the day and at night. The following

51

table [6] shows the spectral radiance of ozone emission in the 9.6μ band as a function of zenith angle, with the background continuum subtracted.

The atmosphere comprises three layers and the contribution from each is given.

The first line of Table II provides a conservative estimate of the radiance, which is provided to ground

reflection at the earth's surface produces an extended background of radiation, the radiance of which is equal to the radiance of the clear sky. A conservative estimate of the radiance available to orbital detectors from the sunlit portions of the earth's surface would be $4.0 \cdot 10^{-3}$ W/cm^2 -sr.

The actual radiance which is available to orbiting detectors is changed from the above ground value be-

TABLE II. 9.6μ OZONE EMISSION INTENSITY (W/cm^2 -sr-μ)

Zenith Angle	Ground to Tropopause (0 - 10 km)	Trop. to 30 mb (10 - 24 km)	Above 30 mb (above 24 km)
0	1.3×10^{-5}	2.75×10^{-5}	3.8×10^{-5}
60°	2.75	4.0	4.2
75° 31'	5.25	5.25	3.50
80° 24'	7.25	6.00	3.00
82° 40'	8.75	6.00	2.75

detectors by the 9.6μ ozone emission band. Assuming that this band is roughly $\Delta \lambda = 1 \mu$ wide (Fig. 5), the infrared radiance becomes

$$\Delta \lambda (1.3 + 2.75 + 3.8) \cdot 10^{-7} = 7.8 \cdot 10^{-5} \text{ W/cm}^2 \text{-sr}.$$

D. ORBITAL DETECTORS

Orbital detectors can also use scattered sunlight and ozone emission. Additional extended radiation sources are provided by the reflected sunlight and by the earth's thermal emission. The following discussions are restricted to the same atmospheric windows that have been chosen for the discussion of ground detectors, since the utilization of these windows would allow the direct simulation of in-flight experiments.

1. Scattered and Reflected Sunlight. - The reflection of the sunlight from typical topographical characteristics on the earth surface, such as the oceans, airfields, or streets, creates the sensation of brightness. This sensation has been used to measure the radiance of this object or the sky by a photometric comparison with calibrated lamps. One could use these comparisons to estimate scattered sunlight since the human eye reacts to the light in the visible atmospheric window between 0.38 and 0.72μ. The brightness of the clear sky and most objects on the surface is now of the same order of magnitude. For this paper, it is sufficient to assume that diffused

cause of scattering and reflection in the atmosphere. Typical changes due to atmospheric scattering and terrain reflectance are summarized in Table III. In view of these data the radiance which is available in the visible region to orbiting detectors was assumed to be

$$4.2 \cdot 10^{-3} \text{ W/cm}^2 \text{-sr}$$

Several satellites have measured the infrared radiation emitted by the earth's surface and atmosphere (Fig. 6). This radiation shows a marked
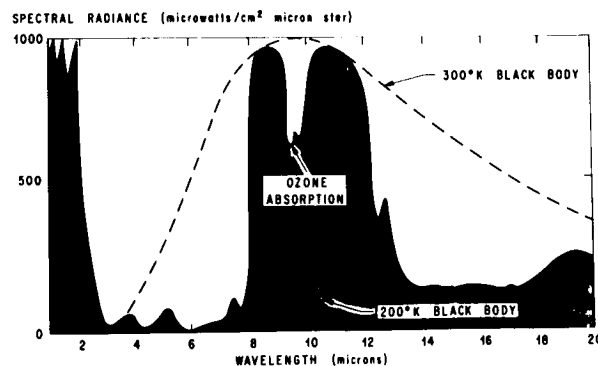
FIGURE 6. SPECTRAL RADIANCE OF THE SUNLIT SIDE OF EARTH AS OBSERVED FROM A SATELLITE

TABLE III. SPECTRAL RADIANCE OF SUN'S RAYS AT NORMAL INCIDENCE

a) Underline Outside Atmosphere

Wavelength (μ)	Intensity watts/cm^2/μ
0.4	1.74×10^{-1}
0.5	1.96
0.6	1.8
0.7	1.5

b) At Sea Level-Zenith Angle 60°

Wavelength (μ)	Intensity watts/cm^2/μ
0.4	0.47×10^{-1}
0.5	1.2
0.6	1.17
0.7	1.11

c) Typical Values of Terrain Reflectance (0.4-0.7μ)

Terrain	Reflectance
Snow	0.8
Water	0.05
Forests	0.03
Open grassland	0.06
Dark brown soil	0.11

dependence on the temperature of the earth's surface and atmosphere, the nature of the surface, the presence of clouds, and the distribution of absorptive molecules in the atmosphere.

Most substances on the surface of the earth have nearly unit emissivity in the spectral range over which an appreciable amount of radiation is emitted at terrestrial temperatures. In the relatively transparent infrared regions of the atmosphere and on clear days, this radiation is nearly free to escape unaltered to space. The main variations observed are from equator to pole as the earth's surface temperature changes. The radiance of the sun side of the earth observed outside the earth's atmosphere by a satellite is shown in Figure 6. In the transparent regions, the radiance corresponds to a black body at the surface temperature of the earth, while in the strongly absorbing regions, it corresponds to the black-body radiance at stratospheric temperatures. Between 8 and 12μ, a satellite-borne detector will therefore see the same radiance both on the night and on the day

side of the earth. Since the 8 to 12μ band of emission is near the peak of the 300°K black-body radiation, the thermal emission, which is picked up by an orbiting telescope, can be calculated from the black-body curve. The associated radiance is

$$4 \cdot 10^{-3} \text{ W/cm}^2 \text{ -sr}$$

E. METEOROLOGICAL POWER MODULATIONS

In the crossed-beam methods, one has to detect fluctuations of radiative power which are common to the two lines of sight. These fluctuations are produced by the generation, convection, and decay of emitting, scattering, and absorbing particles, which follow the atmospheric motions. The following discussion is restricted to scattering, which produces local fluctuations of radiative power by a modulation of the mean power of the extended background source. The same modulation would also occur when tracking man-made sources or the sun. The only direct measurements of extinction modulations currently

known to us have been made in conjunction with optical communication studies.

Meteorological modulations of a He-Ne laser have been measured over optical paths up to 6.8 km long (mountain range). The laser output of 0.8 mW was collected by a 24-inch reflecting telescope. By using the full aperture of the telescope, it was hoped that no "spill-over" of the laser light occurred and that the attenuation measured by the detector was caused entirely by atmospheric attenuation and not to the bending of the light beam away from the sensor. Figure 7 gives the power spectrum and spectral distribution of the intensity fluctuations. Their integration indicates that the ratio of the root-mean-square value to the mean (d.c.) level of the fluctuating signals is the order of 1 percent. Over shorter ranges and along paths close to the ground, the fluctuations were of the order of 0.1 percent to 10 percent. This 0.1 percent fluctuation is taken as representative of the intensity fluctuations occurring over large atmospheric distances.
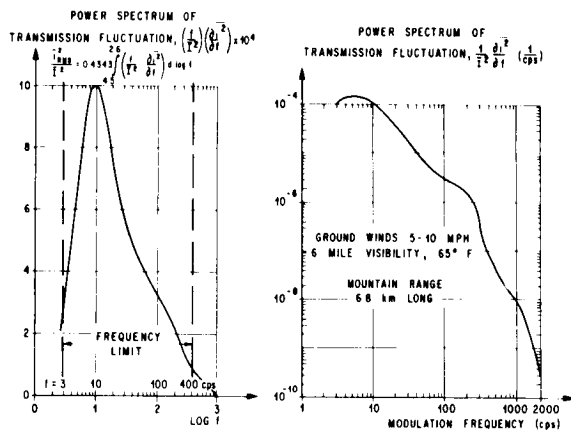

FIGURE 7. ATMOSPHERIC MODULATION OF LASER BEAM

In view of the laser experiments, one may expect that radiative power fluctuations of 0.1 percent ($i_{RMS}/\bar{I} = 0.001$) are produced by meteorological phenomena close to the ground (= 500 m altitude). The frequency of these fluctuations should be roughly proportional to the speed with which atmospheric inhomogeneity is pulled broadside through the collimated beam. The range of energy bearing frequencies for the laser experiments extends from approximately 2 to 300 Hz for a wind speed of 2 to 4 m/sec (Fig. 7). The limits for other speeds should scale proportionally to the relative motion between atmospheric inhomogeneity and the beam. If we take on orbital scanning speed of 8000 m/sec and a field of

view equivalent to 50 meters, then frequencies up to 160 cycles per second are to be expected. In the computations of detector noise a figure of 1000 cps was taken as the upper frequency limit for the orbital case.

Other evidence of fluctuation levels to be expected in atmospheric crossed-beam experiments is available from measured temperature fluctuations. Since in the atmosphere velocities vary much less than the speed of sound, density variations arise from temperature variations. Typically variations of the order of a few tenths to over one degree centigrade are observed, which therefore correspond to density variations of up to one percent. The number density of aerosol particles might be expected to show similar fluctuations. The integrated tracer concentration fluctuation is thus assumed to be larger than 10^{-3} times that of the ground level concentration.

The modulations of radiated power, which are produced at higher altitudes, are very difficult to estimate. In the case of scattered sunlight, variations in aerosol concentrations are likely to be the main source of fluctuations at low altitudes (Fig. 8). At higher altitudes fluctuations in air density are more important.

This difficulty is not present in the case of ozone emission because of the distribution of ozone in the atmosphere. The altitude of maximum ozone concentration varies from about 10 to 30 kilometers depending on latitude, time of year, etc. Thus, ozone is likely to be useful in tracing atmospheric motions at higher altitudes. For the purpose of calculations in this paper, fluctuations in the integrated optical signals will be assumed to be similar to those of the laser experiment, that is, of the order of one percent. The associated RMS value of the radiance modulation through meteorological phenomena is listed in Table IV.

F. DETECTOR NOISE

The above meteorological modulations of the incident radiative power can be measured if the associated RMS value, i_{RMS}, is larger than the detector noise i_d. The crossed-beam method appears feasible whenever $i_{RMS}/i_d \geq 1$. Smaller signal-to-noise ratios are possible in a correlation technique, and values as small as 0.1 still get successful convection speed measurements in the wind tunnel. However, the atmosphere may have more statistically independent layers and less stationary signals, such that
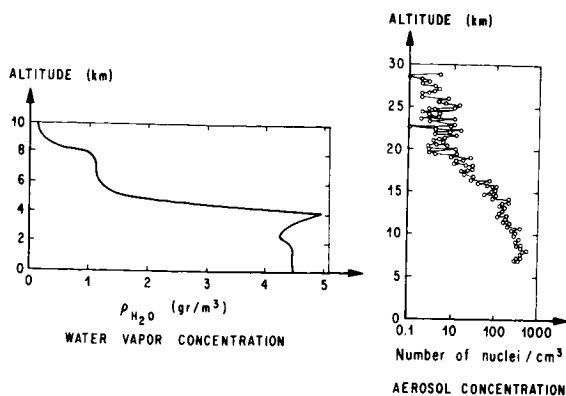
54

ALTITUDE (km)

ALTITUDE (km)

ρ_{H_2O} (gr/m³)

WATER VAPOR CONCENTRATION

Number of nuclei / cm³

AEROSOL CONCENTRATION

FIGURE 8. ATMOSPHERIC TRACER CONCENTRATION

$i_{RMS}/i_d = 1$ is demanded to include a certain safety factor.

Detector noise has been calculated for detectors operating in the visible ($\lambda = 0.55\,\mu$) and the infrared ($\lambda = 9.6\,\mu$) atmospheric windows (the main steps of this calculation are summarized in Table V). The area of the assumed telescope mirrors has the same order of magnitude as commercially available telescopes (10^2 cm²), orbiting telescopes, and search lights or astronomical telescopes (10^4 cm²). The solid angle $4\pi \sin^2 \frac{\Delta\alpha}{4}$ follows from the pointing and tracking accuracies, $\Delta\alpha$; $\Delta\beta$, which are listed

in Table VII. These values, together with the estimates of mean radiance, listed in Table IV, provide the information required to calculate the mean radiative power I (W) collected by the telescopes from the four previously discussed extended sources of radiation. From these values, one obtains the photon flux by dividing by

TABLE V. DETECTOR OPERATION AND NOISE

Power \ Operation	Visible Light ($\lambda = 0.55\mu$) Ground	Visible Light ($\lambda = 0.55\mu$) Orbit	Infrared ($\lambda = 9.6\mu$) Ground	Infrared ($\lambda = 9.6\mu$) Orbit
Mirror cross-section (cm²)	10^2	10^4	10^4	10^4
Field of view minutes of arc ($\Delta\sigma$) $4\pi\sin^2(\frac{\Delta\sigma}{4})$ sr	15' $1.5 \cdot 10^{-5}$	0.34' $7.8 \cdot 10^{-9}$	15' $1.3 \cdot 10^{-5}$	0.34' $7.8 \cdot 10^{-9}$
Mean radiance (W/cm²-sr)	$4.5 \cdot 10^{-3}$	$4.2 \cdot 10^{-3}$	$7.8 \cdot 10^{-5}$	$4 \cdot 10^{-3}$
Minimum of mean radiative power I (W)	$5.8 \cdot 10^{-4}$	$3.3 \cdot 10^{-7}$	10^{-5}	$3.1 \cdot 10^{-7}$
Photon current $\frac{I}{h\nu}$ (photons/sec)	$16 \cdot 10^{12}$	$8.9 \cdot 10^{11}$	$4.8 \cdot 10^{14}$	$1.5 \cdot 10^{13}$
Modulation bandwidth B (Hz)	300	1000	300	1000
Detector	Output	Output	Input	Input
Mean signal $\overline{I}_d$	$2.6 \cdot 10^{-7}$ A	$1.4 \cdot 10^{-8}$ A	10^{-5} W	$3.1 \cdot 10^{-7}$ W
Detector noise i_d	Output $5 \cdot 10^{-12}$	Output $2.1 \cdot 10^{-12}$	Noise equivalent power $1.7 \cdot 10^{-10}$ W	Noise equivalent power $3.2 \cdot 10^{-10}$ W
Atmospheric Modulation i_{RMS}	Output $2.6 \cdot 10^{-10}$ A	Output $1.4 \cdot 10^{-11}$ A	Input 10^{-8} W	Input $3.1 \cdot 10^{-10}$ W
Signal/noise i_{RMS}/i_d	52	6	59	1

TABLE IV. ESTIMATION OF RADIANCE AVAILABLE TO GROUND AND ORBITAL DETECTORS

Detector Location	Ground	Ground	Orbit	Orbit
Extended source	scattered sunlight	ozone emission	reflected and scattered sunlight	thermal emission of earth
Monochromator bandpass $\Delta\lambda$	0.38μ to 0.72μ	9μ to 10μ	0.38μ to 0.72μ	8μ to 12μ
Estimated mean radiance $\overline{I}$	$4.5 \cdot 10^{-3}$ W/cm² sr	$7.8 \cdot 10^{-5}$ W/cm² sr	$4.2 \cdot 10^{-3}$ W/cm² sr	$4 \cdot 10^{-3}$ W/cm² sr
Estimated modulation in spectral radiance i_{RMS}	$4.5 \cdot 10^{-6}$ W/cm² sr	$7.8 \cdot 10^{-8}$ W/cm² sr	$4.2 \cdot 10^{-6}$ W/cm² sr	$4 \cdot 10^{-6}$ W/cm² sr
Modulation bandwidth	300 Hz	300 Hz	1000 Hz	1000 Hz

$hv = 3.7 \cdot 10^{-19}$ W-sec for $\lambda = 0.55 \mu$ or by

$hv = 2.1 \cdot 19^{-20}$ W-sec for $\lambda = 9.6 \mu$.

Photocathodes operating with visible light may use tri-alkali cathode coatings, which have a high quantum efficiency of

$$QE = 0.1 \left(\frac{electrons}{photon}\right)$$

$$= 1.6 \cdot 10^{-20} \left(\frac{ampere\text{-}sec}{photon}\right) \quad .$$

The photocathodes therefore give an output current of

$$\bar{I}_d \, (A) = QE \, \bar{I} \, (W)/hv \, (W\text{-}sec),$$

The main noise of these detectors is provided by shot noise:

$$i_d^2 = 2e \, \bar{I}_d \cdot B \, ,$$

where B(Hz) is the modulation bandwidth (Tab. IV) and $e = 1.6 \cdot 10^{-19}$ A-sec, the charge of one electron. Comparing the associated shot noise levels with the expected meteorological modulations $i_{RMS} = 10^{-4} \, \bar{I}_d$, one finds that the signal-to-noise ratio i_{RMS}/i_d exceeds one for both ground and orbiting detectors.

The noise analysis for infrared detectors is somewhat easier, since the noise of these detectors is listed in terms of the equivalent radiative input power i_d, which would produce the same RMS value of the detector output in an imaginary experiment, conducted with a "perfect" noise-free detector. For commercially available, cooled, infrared detectors operating between 8 and 15 μ, the noise equivalent power has been estimated [7,8,9] as

$$i_d \, (W) = 1 \cdot 10^{-11} \sqrt{B(Hz)} \, .$$

Comparing the expected meteorologic modulations of the infrared background sources $I_{RMS}(W) = 10^{-3} \, \bar{I} \, (W)$ with the noise equivalent power i_d of the infrared detectors gives a signal-to-noise ratio of i for orbiting telescopes. Based on this fact, infrared crossed-beam sweeps from orbit appear feasible.

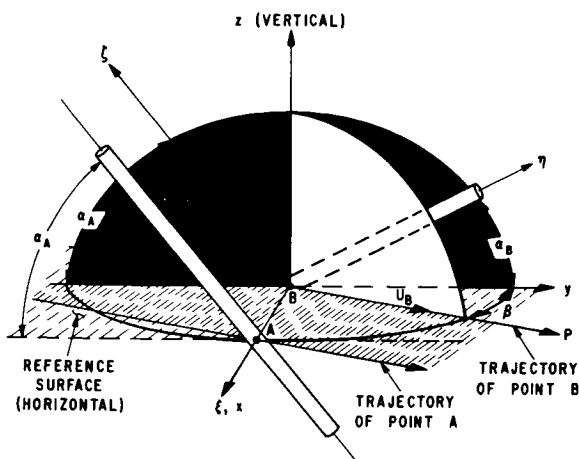The signal-to-noise ratio of infrared ground detectors is 52.

IV. THEORY OF CROSSED BEAM SCANNING

In the global coverage of vast and sparsely instrumented areas, environmental monitoring systems would have to gather information quickly enough, such that the results can be used for the prediction of weather and the prediction of navigational and communicational hazards. This consideration leads to the extension of the crossed-beam concept from space-fixed beams to scanning or sweeping beams. The theory of crossed-beam scanning has therefore been developed to indicate how the two-beam product mean values from moving beams are to be interpreted in terms of convection speeds, turbulence length scales, and space correlations (wave number components). The following theoretical treatment is kept general and could be applied to orbital as well as ground detectors.

A. DEFINITION OF SCANNING BEAMS

We define the scanning or sweeping motion of crossed beams by the motion of the points of minimum beam separation A and B. The straight line, which goes through these two points, had been introduced as the beam normal. In case of crossed-beam scanning, this normal moves broadside and sweeps out a certain surface. We have chosen to classify crossed-beam systems in terms of the motion of the beam normal and through the orientation of the beams relative to the surface of the sweeping normal. This gives a unified treatment which can be applied to both orbital and ground detectors. The following discussions are restricted to a crossed-beam system where both the speed of the normal and the orientation of the beams relative to the surface of the normal are time invariant. Such crossed-beam systems are shown in Figure 9 and may be compared to the translation of a rigid mechanical structure. The beam arrangement is thus uniquely classified in terms of the following invariant parameters:

1. The scanning speed U_B describing the speed of the point B of minimum beam separation inside the surface of the sweeping normal.

2. The inclination β of the path of B relative to the beam front, that is, relative to a plane, which is parallel to both beams. The path of point B will be called the "intersection path."

3. The inclinations α_A and α_B of the two beams relative to the surface of the sweeping normal.

z (VERTICAL)

ζ

η

α_A α_A

α_B

U_B

y

β

P

REFERENCE
SURFACE
(HORIZONTAL)

TRAJECTORY
OF POINT B

ξ, x

TRAJECTORY
OF POINT A

x, y, z, ATMOSPHERE FIXED COORDINATES
ξ, η, ζ, BEAM FIXED COORDINATES

THE NORMAL ξ SWEEPS OUT THE HORIZONTAL x, y PLANE

FIGURE 9. TRANSLATION OF A RIGID CROSSED-
BEAM ARRANGEMENT

The motion of the individual beam is now de-
scribed in two different space-fixed coordinate sys-
tems, which are also shown in Figure 9. The first
system is needed to describe the position of a beam
point relative to the earth's surface. The z-axis
points vertically upward and the x-axis follows the
line of minimum beam separation. The y-axis fol-
lows from the condition that the x, y, z-system should
be an orthogonal system. The coordinates ξ, η, ζ of
the second system are defined in terms of the posi-
tion which the sweeping beams occupied at the instant
t = 0; that is, at the start of the experiment. The
ξ-axis follows the beam normal, the η-axis the lead-
ing beam, and the ζ-axis the trailing beam. This
system is not necessarily orthogonal, since the
angle

$$\alpha_{AB} = \pi - \alpha_A - \alpha_B \qquad (1)$$

between the beams is not necessarily a right angle.
The relation between the two coordinate systems
follows from geometrical considerations and may be
given in covariant form as follows:

$$\vec{x}(\xi) = x_0 + \xi$$

$$\vec{y}(\xi) = y_0 + \eta \cos \alpha_B - \zeta \cos \alpha_A \qquad (2)$$

$$\vec{z}(\xi) = z_0 + \eta \sin \alpha_B + \zeta \sin \alpha_A$$

Here $\vec{x_0}$ denotes the origin of the ξ, η, ζ-system, that
is, the position of the moving point B at time zero.
The trajectory of point B follows the "intersection
path." Each point on this path shall be denoted by
the path length P relative to the point $\vec{x_0}$.

$$\vec{x}_B(P) = \begin{pmatrix} x_0 \\ y_0 \\ z_0 \end{pmatrix} + P \begin{pmatrix} \sin \beta \\ \cos \beta \\ 0 \end{pmatrix} \qquad (3)$$

The scanning speed U_B describes a velocity vector
which follows the intersection path. This vector may
thus be denoted by

$$\vec{U}_s = \begin{pmatrix} U_s \\ V_s \\ W_s \end{pmatrix} = U_B \begin{pmatrix} \sin \beta \\ \cos \beta \\ 0 \end{pmatrix} . \qquad (4)$$

Similar trajectories can be written for any other point
of the trailing beam "1." At time zero this beam
coincides with the ξ-axis and may thus be found at
position x(0, 0, ζ). The trajectory of this point is
then given by

$$\vec{x}_1(\zeta, t) = \vec{x}(0, 0, \zeta) + \vec{x}_B[P(t)]$$

$$\begin{pmatrix} x_1(\zeta,t) \\ y_1(\zeta,t) \\ z_1(\zeta,t) \end{pmatrix} = \begin{pmatrix} x_0 + U_B t \sin \beta \\ y_0 - \zeta \cos \alpha_A + U_B t \cos \beta \\ z_0 + \zeta \sin \alpha_A \end{pmatrix} . \qquad (5)$$

The fluctuations $i_1(t)$, which are recorded for the
trailing beam, follow from the optical integration
along this beam.*

$$i_1(t) = \langle I_1 \rangle \int_{-\infty}^{\infty} k[\vec{x}_1(\zeta,t); t] \, d\zeta \qquad (6)$$

Similarly, an arbitrary point on the leading beam "2"
is denoted by the beam length η and moves along the
trajectory.

$$\vec{x}_2(\xi, \eta, t) = \vec{x}(\xi, \eta, 0) + \vec{x}_B[P(t)]$$

$$= \begin{pmatrix} x_2(\xi, \eta, t) \\ y_2(\xi, \eta, t) \\ x_2(\xi, \eta, t) \end{pmatrix}$$

---

* Light source fluctuations are neglected since they
are mostly uncorrelated; i.e., a further noise con-
tribution, which is suppressed by correlation
techniques.

$$= \begin{pmatrix} x_0 + \xi + U_B t \sin\beta \\ y_0 + \eta \cos\alpha_B - \zeta\cos\alpha_A + U_B t \cos\beta \\ z_0 + \eta \sin\alpha_B + \zeta \sin\alpha_A \end{pmatrix}. \quad (7)$$

The optical integration along the leading beam can thus be expressed by

$$i_2(t) = <I_2> \int_{-\infty}^{\infty} k[\vec{x_2}(\xi,\eta,t); t] \, d\eta . \quad (8)$$

The two-beam product mean value of a sweeping crossed-beam system follows from the time average of the instantaneous product

$$R(\xi, \tau = 0) = <i_1(t) \, i_2(t)>_\xi$$

$$= \int_{-\infty}^{\infty} \int <k[\vec{x_1}(\zeta,t); t] \, k[\vec{x_2}(\xi,\eta,t); t]> d\zeta \, d\eta \quad (9)$$

$$= \iint_{-\infty}^{\infty} R_k (\vec{\xi}, 0) \, d\eta \, d\zeta .$$

One finds that the two-beam product mean value is an area integral over a great number of observer pairs each of which travels parallel to the intersection path.

B. LENGTH AVERAGES OF FROZEN PATTERNS

The individual observer averages over the fluctuations which he encountered along his trajectory. The fluctuations are produced by scanning inhomogeneous spatial distributions of radiative power and by true temporal variations as communicated by a space-fixed observer. We have thus a mixed space and time average. This averaging process is analogous to the way the human eye evaluates a TV picture. Each frame of the television is displayed on the screen by a rapidly moving electron beam. To the viewer the modulations of the electron beam are displayed so rapidly that the resulting image appears as a "frozen pattern," that is, like a flashlight image. Although the information which is displayed by the scanning beam was recorded as a time function, its interpretation assumes a space history. Only by comparing several frames is it possible to detect generation, convection, and decay of new patterns.

We now assume that an observer pair scans so rapidly that the associated two-point product mean value R_k closely approximates a length average R_k^P along the observer trajectory. This approximation is

$$R_k(\vec{\xi}) = <k[\vec{x_1}(\zeta,t); t(P)] \, k[\vec{x_2}(\xi,\eta,t(P); t]>$$

$$\approx \lim_{U_B T \to \infty} \frac{1}{U_B T} \int_{P=0}^{P=U_B T} k[\vec{x_1}(\xi,P); t=0] \, k[\vec{x_2}(\xi,\eta,P); t=0] \, dP = \vec{R_k^P}(\vec{\xi}) .$$

$$(10)$$

This approximation is valid whenever the spatial distribution or "pattern" of k is frozen $[k(\vec{x}, t) = k(\vec{x}, 0)]$ over the time period T of the scan. It is also valid if a frozen pattern is convected at a constant speed U_C, since this would alter only the effective scanning speed of the moving observer pair. The last equation is therefore valid for all convected frozen patterns; that is, for all possible directions of the convection speed. Furthermore, it can be shown that the pattern does not have to be entirely frozen. The approximation of length averages is still good as long as the temporal variations, which are experienced by a third observer who travels with the convection speed, can be treated as small perturbations and are statistically stationary.

Replacing the time average of scanning observers with a length average over the observer's trajectory leads to the following expression for the two-beam product mean value of a rapidly scanning system:

$$< i_1(t) \, i_2(t-) >_\xi = <I_1><I_2> \iint_{-\infty}^{\infty} \vec{R_k^P}(\vec{\xi}) \, d\eta \, d\zeta$$

$$= <I_1><I_2> \iint_{-\infty}^{\infty} \overline{k[\vec{x_1}(\zeta,P), \, t=0] \, k[\vec{x_2}(\xi,\eta,P), \, t=0]}^{\,P} \, d\eta \, d\zeta .$$

$$(11)$$

In the above averaging procedure, it was always assumed that no time lag was introduced in the data reduction. However, in space-fixed crossed-beam arrangement the systematic variation of time lags was required to separate convection and generation and decay processes and to measure the convection speed. Similar interpretations of temporal correlations hold for moving beams and shall now be discussed.

The fluctuations of radiative power, which produce the signal $i_2(t)$ along the leading beam, have been on another position $\vec{x_2}$, imag at the time $t - \tau$.

In case of a convected frozen pattern, this earlier position is parallel to the leading beam and may be found by tracing back the scanning motion $\vec{U}_B$ and the

convective motion $\vec{U}_C \equiv (U_C, V_C, W_C)$. The signal of the delayed beam $i_2(t - \tau)$ is thus identical with the signal from an imaginary undelayed beam, each point of which could be found by the translation.

$$\vec{x}_{2,\,imag}(\xi,\eta,P,\tau) = \vec{x}_2[\xi,\eta,t(P)] - (\vec{U}_S + \vec{U}_C)\,\tau. \quad (12)$$

It follows that the above optical integration of two-beam product mean values, equation (1), can be extended to the analysis of a delayed beam, if one replaces $\vec{x}_2$ with $\vec{x}_{2,\,imag}$.

$$\langle i_1(t)\, i_2(t + \tau) \rangle_\xi$$

$$= \langle I_1 \rangle \langle I_2 \rangle \int\!\!\int_{-\infty}^{\infty} \frac{P}{k[\vec{x}_1(\xi,P),\,0]\,k\,[\vec{x}_{2,\,imag}(\,\xi,\eta,P,\tau),\,0]} \,d\eta\,d\xi \quad (13)$$

The interpretation of this two-beam product mean value follows in analogy to the discussion of space-fixed beams by considering the two-point product mean value between the two points A_i and B_i, which are defined through the minimum separation $\xi(\tau)$ between the trailing beam and the imaginary beam. The position of these two points is indicated on Figure 10 by projections of the imaginary beam into the side view and top view of the plane of the sweeping normal. The figure shows that the two pairs of points A_i, B_i and A, B differ by a translation and a change of separation distance. The translation occurs inside the beam front and may be characterized by its z and y components.

$$\Delta z(-\tau) = z_{B_i} - z_B = \frac{(V_S + V_C)\,\tau}{\cot \alpha_A + \cot \alpha_B} \quad (14)$$

$$\Delta y(-\tau) = y_{B_i} - y_B = \frac{(V_S + V_C)\,\cot \alpha_B}{\cot \alpha_A + \cot \alpha_B}\,\tau. \quad (15)$$

The change in separation distance is given by

$$\Delta \xi(-\tau) = \xi_{A_i} - \xi_A = -\,\frac{U_S + U_C}{V_S + V_C}\,\Delta y$$

$$= \frac{\cot \alpha_B}{\cot \alpha_A + \cot \alpha_B}\,(U_S + U_C)\,(-\tau). \quad (16)$$

SIDE VIEW

TOP VIEW
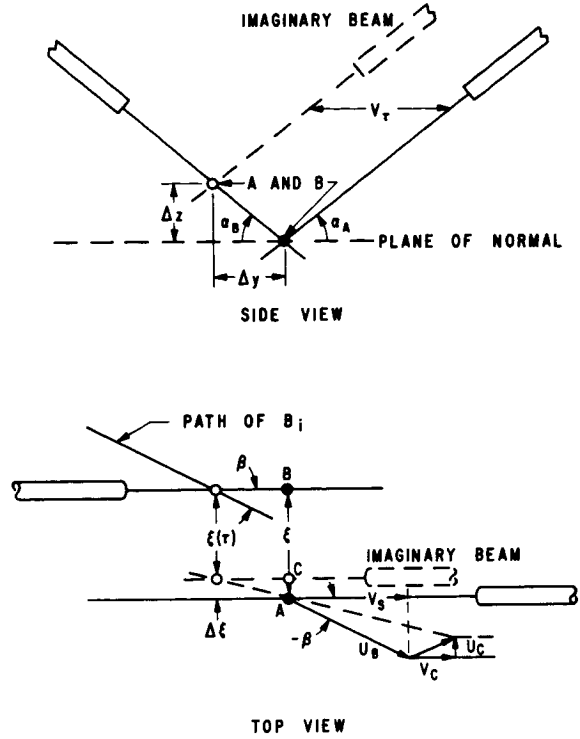
FIGURE 10. POINTS OF MINIMUM SEPARATION A_i AND B_i BETWEEN IMAGINARY AND UNDELAYED BEAMS

As long as the frozen pattern of k is statistically homogeneous over the beam front, a translation by $-\Delta z$, $-\Delta y$ would not affect the two point product mean value. However, this translation brings the pair $A_i B_i$ back to the original normal (i. e., $\eta_0 = \zeta = 0$). In fact, the translated point B_i coincides with B. The translated point point A_i, which is denoted in Figure 10 by C, defines the new beam separation

$$\xi^*(-\tau) = \xi + \Delta \xi(-\tau) = \xi + C_{AB}(U_B \sin \beta + U_C)(-\tau), \quad (17)$$

where the constant C_{AB} abbreviates the cotangent factor

$$C_{AB} = \frac{\cot \alpha_B}{\cot \alpha_A + \cot \alpha_B}. \quad (18)$$

The only effect of a time delay is thus to change the actual beam separation to the effective beam

separation $\xi^*(\tau)$. The approximation of two-point product mean values may therefore be extended from space-fixed to moving beams in the following way

$$\left| \frac{U_B \sin \beta}{U_C} \right| = \left| \frac{U_S}{U_C} \right| \geq 5, \qquad (22)$$

$$\frac{<i_1(t)\, i_2(t+\tau)>_\xi}{<i_1(t)\, i_2(t)>_\xi} \simeq \frac{\overline{R}_k^P\,[\xi^*(\tau);\eta=0;\zeta=0]}{\overline{R}_k^P\,(\xi,\eta=0;\zeta=0)}$$

$$= \frac{\overline{k(x_0 + P\sin\beta, y_0 + P\cos\beta; z_0, 0)\, k[x_0 + P\sin\beta + \xi(\tau); y_0 + P\cos\beta, z_0, 0]}^P}{\overline{k(x_0 + P\sin\beta, y_0 + P\cos\beta; z_0, 0)\, k(x_0 + P\sin\beta + \xi; y_0 + P\cos\beta, z_0, 0)}^P}. \qquad (19)$$

The physical meaning of this approximation is that the temporal correlation function between the moving points A and B is produced by pulling a space correlation curve $\overline{R}_k^P\,(\xi^*)$ broadside through the moving beam front with the relative speed $U_C + U_B \sin\beta$. Although the actual beam separation ξ is time invariant during the sweep, the introduction of time lag produces an effective space lag ξ^*, which is variable.

C. INTERPRETATION OF TWO-BEAM PRODUCT MEAN VALUES

The above approximation of space correlation curves, equation (19), allows several important applications. The first application is the measurement of convection speeds. It follows from the fact that space correlation curves have a maximum at zero space lag. Therefore, the time lag $T_M(\xi)$, which is indicated by the maximum of the temporal beam correlation curve $<i_1(t)\, i_2(t+\tau)>_\xi$, should correspond to $\xi^* = 0$.

$$\xi^*(\tau_M) = 0 = \xi + C_{AB}(U_C + U_B \sin\beta)\,\tau_M. \qquad (20)$$

This is an equation which may be solved for the convection speed:

$$U_C = \frac{\xi}{C_{AB}\,\tau_M(\xi)} - U_B \sin\beta. \qquad (21)$$

The associated estimates of convection speeds are graphically illustrated in Figure 11. In equation (21), the second term, $U_B \sin\beta$, corrects for the beam motion. If this term is large compared to the convection speed,

then the measurement of U_C becomes difficult since it involves the subtraction of two large quantities of about equal magnitude. This leads to the following range for the inclination between beam front and the intersection path.

$$\sin \beta \leq 5 \left| \frac{U_C}{U_B} \right| \qquad (23)$$

Since the scanning speed U_B must be much larger than the convection speed U_C to justify the assumption of a frozen pattern, the last inequality implies that β will always be a small angle. In other words, the beam front moves almost parallel to itself.

—— ACTUAL CORRELATION

---- EXPECTED FOR FROZEN PATTERNS
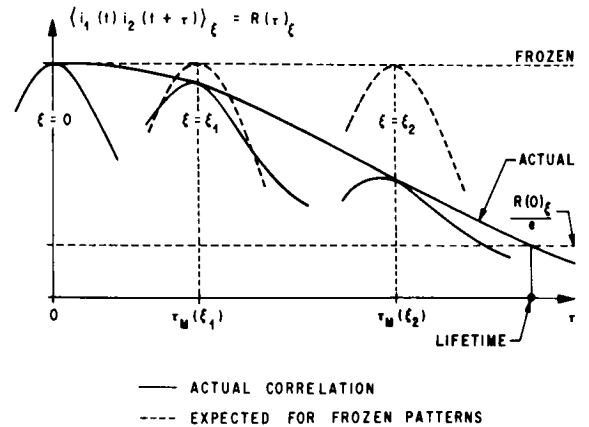
CONVECTION SPEED FOLLOWS FROM POSITION OF MAXIMUM :

$$U_C = \frac{\xi}{C_{AB}\,\tau_M(\xi)} - U_B \sin\beta$$

FIGURE 11. ESTIMATION OF CONVECTION SPEEDS

The second application is the estimate of the integral length scale L_x. Since the two-beam product mean value is proportional to the space correlations curve $\overline{R}_k^P(\xi*)$, the normalized space correlation curve can be approximated by normalizing the two-beam product mean values with their maximum

$$\phi\left(\xi* = \frac{\tau - \tau_M(\xi)}{U_C}\right) = \frac{\overline{R}_k^P(\xi*, 0, 0)}{\overline{R}_k^P(0, 0, 0)}$$

$$\simeq \frac{<i_1(t)\, i_2(t + \tau)>_\xi}{<i_1(t)\, i_2[t + \tau_M(\xi)]>_\xi} \quad , \quad (24)$$

and by plotting this coefficient as a function of the effective space lag $\xi*$. Once the convection speed U_C is known, this lag may be calculated without using the scanning speed, U_B. Substituting equation (20) into equation (17) shows

$$\xi* = \frac{\tau - \tau_M(\xi)}{U_C} \quad . \quad (25)$$

The integral length scale, L_x, in the direction of the beam normal follows from integration

$$L_x = \tfrac{1}{2} \int_{-\infty}^{\infty} \phi(\xi*)\, d\xi* \quad . \quad (26)$$

The third application is the estimate of three-dimensional wave number components. The components result if one wants to describe the space history of a frozen pattern of extinction coefficients $k(\vec{x}, t = 0)$ through a superposition of harmonic waves. Each of these waves is characterized by the number of cycles per unit length ψ_1, ψ_2, ψ_3 which may be oriented in either the ξ, η, or ζ direction. The individual wave number component, S_k, denotes the mean square amplitude of such an individual wave and follows from a three-dimensional Fourier transform of the two point product mean value.

$$S_k(x) = \frac{1}{8\pi^3} \iiint_{-\infty}^{\infty} \overline{R}_k^P[\xi*(\tau); \eta, \zeta]\, e^{-i\vec{\xi}\cdot\vec{\psi}}\, d\zeta\, d\eta\, d\xi$$

$$(27)$$

For wave fronts which are parallel to the plane of the beams, we get $\psi_2 = \psi_3 = 0$, and the inner two integrals describe nothing but an integration over the beam front which is automatically performed.

$$\iint \overline{R}_k^P(\xi*)\, e^{-i\vec{\xi*}\cdot\vec{\psi}}\, d\eta\, d\zeta$$

$$= e^{-i\xi* \psi_1} \iint_{-\infty}^{\infty} \overline{R}_k^P(\xi*)\, d\eta\, d\zeta$$

$$= \frac{<i_1(t)\, i_2(t + \tau)>_\xi}{<I_1><I_2>} e^{-i\xi* \psi_1} \quad (28)$$

Substituting into the previous equation gives the three-dimensional wave number component by a one-dimensional integration

$$S_k(\psi, 0, 0) = \frac{1}{8\pi^3} \int_{-\infty}^{\infty} \frac{<i_1(t)\, i_2[t + \tau(\xi)]>_\xi\, e^{-i\psi_1 \xi*}}{<I_1><I_2>}\, d\xi* \quad . \quad (29)$$

All properties of the integrand are experimentally accessible to a moving crossed-beam system.

The fourth application is an estimate of the normalized power spectrum. Consider several crossed-beam systems with different beam separations $\xi = \xi_0, \xi_1, \xi_2 \ldots$ which scan the same integration path simultaneously. According to equation (24), the associated temporal correlation curves $R_0(\tau)_\xi = <i_1(t)\, i_2(t + \tau)>_\xi$ should all collapse into a single curve if they are translated along the time-lag axis until the maximum coincides with the ordinate. In other words, each of the individual space-time correlations $R_S(\tau)_\xi$ could be generated by translating the autocorrelation $R_S(\tau)_\xi = 0$ by the amount $\tau_M(\xi)$. This is indicated in Figure 12 by the dashed curves and follows from the assumptions of a frozen pattern. Therefore, by replotting the normalized two-beam product mean value of a single run $\xi = \xi_i$ as a function of the "retarded time lag,"

$$\tau* = \tau - \tau_M(\xi_i) \quad (30)$$

should give a curve $\phi(\tau*)$ which closely resembles the normalized autocorrelation function. The Fourier transformation of this curve should then give an estimate of the normalized power spectrum

$$S_k(f) = \frac{1}{2\pi} \int_{-\infty}^{\infty} \phi(\tau*)\, e^{-i\, 2\pi f \tau*}\, d\tau* \quad (31)$$

The consideration of several simultaneously estimated time correlations curves $R_S(\tau)_\xi$ also implies a lower limit on the scanning speed. The assumption of a frozen pattern is obviously wrong if the individual curves $R_S(\tau)_\xi$ depart considerably from the

$$h(\tau_M) = \tau_0 + U_B \tau_M \, t \, g \, \alpha \, C_{AB}. \qquad (32)$$

$\phi(\tau^*)$ or $\phi(\xi^*)$

$$\frac{\langle i_1(t) \, i_2(t+\tau) \rangle_\xi}{\langle i_1(t) \, i_2(t+\tau_M) \rangle_\xi} = \phi$$

$\xi = \xi_1$

$\xi = 0$

$\xi^* = \tau - \tau_M / U_c$ EFFECTIVE SPACE LAG

$\tau^* = \tau - \tau_M$ RETARDED TIME LAG

LENGTH SCALE

$$L_x = 1/2 \int_{-\infty}^{+\infty} \phi(\xi^*) \, d\xi^*$$

WAVE NUMBER COMPONENT

$$E[x, i, 0, 0] = \frac{1}{8\pi^3} \int_{-\infty}^{+\infty} \phi(\xi^*) \, e^{-i x_1 \xi^*} \, d\xi^*$$

POWER SPECTRUM

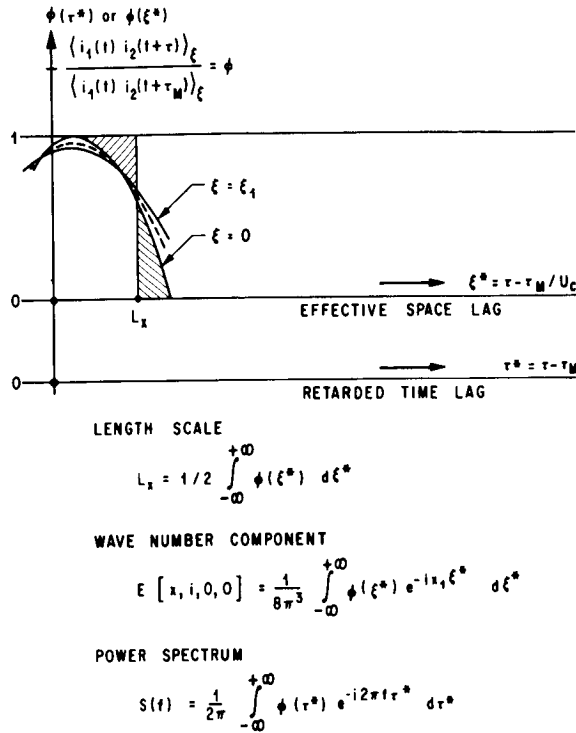$$S(f) = \frac{1}{2\pi} \int_{-\infty}^{+\infty} \phi(\tau^*) \, e^{-i 2\pi f \tau^*} \, d\tau^*$$

FIGURE 12. ESTIMATION OF LENGTH SCALE
AND SPECTRUM

translated autocorrelation $R_S(\tau)_{\xi=0}$. This case is illustrated in Figure 12 for $\xi = \xi_3$. The concept of a frozen pattern therefore seems justified only as long as the range of time lags used is small compared to the eddy lifetime. In the atmosphere, eddy lifetimes are usually in excess of 5 min, except for layers very close to the ground. On the other hand, our wind tunnel tests suggest that one would probably have to scan over 50 statistically independent regions to retrieve the local information. An average integral length scale of L_y = 300 meters gives a region of $L = 50 L_y$ = 15 km length. To scan this region in a tenth of the average lifetime, one needs a scanning speed in excess of 15km/30sec = 0.5 km/sec.

D. MEASUREMENT OF ALTITUDE PROFILES

It remains to consider the altitude variation that is introduced when setting a time lag. The convection speed is determined from a single time lag τ_M and its value belongs to the altitude that is indicated by τ_M.

If one wants to measure an altitude profile of convection speeds in a single sweep, one needs several independent detectors which view the altitude range simultaneously. Each of these detectors should indicate a correlation maximum at a different τ_M. One easy solution is suggested by equation (20). All it takes is setting the photodetectors at different inclinations β against the flight path. Since all of these inclinations are small, as discussed previously, this can be accomplished using only one telescope. One simply collects the radiative power from several off-axis pin-holes in the focal plane of the collecting mirror, as shown in Figure 13.
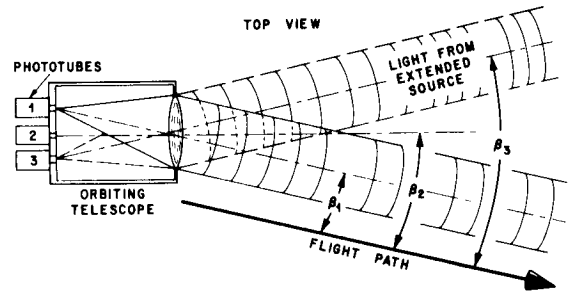

FIGURE 13. PHOTO DETECTOR ASSEMBLY FOR
SWEEPING ALTITUDE PROFILES

Multiple recorders are mandatory when measuring the space correlation $R_S(\tau^*)$. The calculation of integral length scales, equation (26), and wave number components, equation (29), requires a knowledge of the spatial beam correlation $R_S(\xi^*)$ over the entire range of recorded space lags,

$$\xi^*_{max} \leq \xi^* \leq \xi^*_{min}, \qquad (33)$$

where $\phi(\xi^*)$ is not zero. The associated range of time lags is fixed by the convection speed and cannot be shortened by special test arrangements.

$$\frac{\tau_{max} - \tau_{min}}{\xi^*_{max} - \xi^*_{min}} = \frac{1}{U_C}$$

Typical time lag intervals may be derived setting $\xi_{max} - \xi_{min} < 3L_x \leq 1000M$ and $U_C \leq 100M/sec$. They are of the order of 10 sec, which is much too long when considering the altitudes that are covered

meanwhile by scanning speeds in excess of 0.5 km/sec (orbital speed 8 km/sec). Instead, one has to break up the required time lag interval into subintervals of length $\Delta\tau$, which are derived from the permissible altitude error Δh.

$$\Delta\tau = \frac{\Delta h}{U_B + \text{tg } \alpha_A \, C_{AB}} \quad .$$

Each of these subintervals is then used on one of the independent photodetectors, and the associated β angles must be arranged in such a way that the associated lag "points" $\xi^*{}_\ell$ are spread throughout the desired range of retarded space lags. This procedure also reduces the requirement of homogeneity inside the wave front. Homogeneous behavior is demanded only on the now small translations $\Delta z(\Delta\tau)$ and $\Delta y(\Delta\tau)$.

V. PRELIMINARY DESIGN OF ATMOSPHERIC CROSSED-BEAM EXPERIMENTS

Having developed the interpretation of scanning beams, one now has to indicate how the underlying motion of a rigid beam structure can be activated in practice. The measurement of convection speeds, turbulence length scales, and wave number components requires a beam normal which moves broadside through the atmosphere at a scanning speed in excess of 0.5 km/sec. Furthermore, the telescope which defines this normal was restricted to a translation. A rotation of the beam structure around the normal, however, will not change the optical integration over the beam front. Therefore, the telescope motion may be characterized by the conditions α_{AB}, and β must be invariant. Such motion can be achieved with both orbiting and ground detectors. The associated test arrangements are illustrated in Figure 14. Using such arrangements has the great advantage that orbital experiments can be simulated and checked out in ground experiments.

A. TEST ARRANGEMENTS

For orbiting telescopes the beam separation distance ξ can be kept constant if the two detectors orbit at the same speed, that is, at the same height. The path of the normal is then horizontal and the surface of reference coincides with surfaces of constant altitude. For ground detectors a very similar sweep can be arranged by separating the two telescopes by a base line b and by rotating both beams at the same rate ($\dot{\alpha}_A = \dot{\alpha}_B = \dot{\alpha} = \text{const.}$) In this case, the normal is also horizontal and sweeps along a circular arc

such that the surface of reference almost coincides with a horizontal plane. The main difference between orbiting and ground detectors is not in the individual sweep but in the way in which the length averages of the two-beam product mean value are established. Orbiting detectors allow averaging over a single horizontal path of infinite length. Ground detectors sweep over the horizontal portion of a circular arc, the limits length of which is determined primarily by the telescope base line b. However, infinite statistical information can still be collected if one sweeps repeatedly and includes these repeated runs in the averaging procedure. Both averaging procedures give identical results, if the pattern of turbulence is spatially homogeneous over the interval of the orbital sweep or if it can be made homogeneous by subtracting large scale, inhomogeneous "means."

B. PRELIMINARY SPECIFICATIONS

We have tried to specify the crossed-beam test arrangements, which are shown in Figure 14,
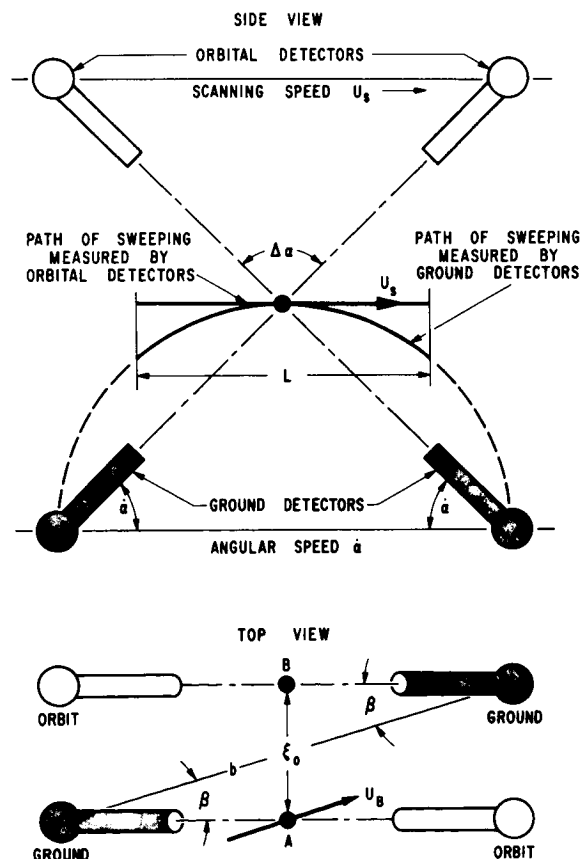

FIGURE 14. TELESCOPE MOTIONS FOR CROSSED BEAM SCANNING

in terms of the independent variables which describe the telescope operation and/or adjustment. These variables are as follows:

λ optical wavelength set by monochromator

b baseline or distance between telescopes

α_{AB} beam intersection angle

U_B scanning speed that is the speed of the moving normal

ξ_0 beam separation along beam normal defined by points of minimum beam separation

τ electronically introduced time lag between beams

β inclination between the plane of the beams and the path, which is followed by the point of minimum separation

N number of desired altitude positions, defining number of photodetectors in local plane of telescope

L interval of intersection path used in averaging procedures.

The desired test arrangement can now be specified in terms of the lower limit (minimum), upper limit (maximum), and tolerance (Δ) which is required for each of the independent variables. These limits and tolerances depend on the desired applications. The considerations of the previous sections allow us to establish rough estimates, the expressions of which are listed in Table VI.

The minimum spacing of space lags $\Delta\xi_0$ has been determined in our wind tunnel tests which seem to indicate that $\Delta\xi_0 = \frac{1}{5} L_x$ gives satisfactory space correlation curves. The tolerance on time lag $\Delta\tau$ is identical with the sampling period of the A/D converter. It has been approximated by the time the beams would need to scan over a space lag interval.

$$\Delta\tau = \Delta\xi_0 / U_B \approx \frac{L_x}{5U_B}$$

Some specifications for the collector optics (telescope) follow from the tolerance column. The angle of view or pointing accuracy is given by the smallest value of $\Delta\alpha$ or $\Delta\beta$. The rotation rates required for stabilization of the telescope platform follow from the condition that the beam oscillation

should be kept so small that it takes more than the sampling period $\Delta\tau$ to produce an angular error of size $\frac{1}{10} \Delta\beta$ or $\frac{1}{10} \Delta\alpha$

$$\Delta\alpha_\nu \leq \frac{1}{10} \frac{\Delta\alpha_{AB}}{\Delta\tau} \approx \cos^2\alpha_{AB} \frac{\Delta h}{b} \frac{U_B}{L_x}$$

$$\Delta\beta \leq \frac{1}{10} \frac{\Delta\beta}{\Delta\tau} \approx \frac{2}{10} \frac{U_B}{b} \quad.$$

Typical pointing and tracking accuracies have been calculated for orbital and ground-based detection (see Table VII).

The above considerations are sufficient to outline telescope arrangements needed to scan a certain altitude from either the ground or orbit. However, the characteristics of the crossed-beam system in terms of the length L of the scanned portion, the number of photodetectors N, and the spatial and temporal resolutions of convection speeds, length scales, and wave number components cannot be determined without conducting several experiments

C. EXPERIMENTAL PROGRAM

We plan to conduct several experiments, in which the true range and resolution of scanning crossed-beam systems is established by comparing the optically measured convection speeds with horizontal wind measurements from meteorological towers and radiosondes. These experiments represent a step-by-step approach from simple space-fixed beams to rapidly scanning beams.

D. FIRST GENERATION EXPERIMENTS

The two sensors of the crossed-beam arrangement are placed on a short baseline, their intersection point set at a moderate height (about 25 m) above ground so that the results of the experiments can be compared to tower-mounted anemometers. The intersection points are fixed in height, but the beam separation distance is varied from 0 to 20 m in a number of discrete steps. At each step the following results are obtained:

1. the rms intensity of the registered fluctuations,

2. the detector-signal-to-noise ratio,

3. the horizontal wind speed, turbulent lengths, and wavelength spectrum of the phenomena occurring in the region of beam crossing,

TABLE VI. ESTIMATES OF INDEPENDENT VARIABLES

Independent Variable	Minimum of Lower Limit	Maximum or Upper Limit	Tolerance Given by	Comment
Optical wavelength λ	0.38μ	0.72μ	entire window for particulate tracers	visible window
	8μ	12μ	for gaseous tracers	infrared window
Telescope separation b	$2\cot\alpha_{A;B}\,h_{min}$	$2\cot\alpha_{A;B}\,h_{max}$	position error $\Delta l = \Delta x$	h is the distance between the beam intersection path and the base line.
Beam intersection angle α_{AB}	$15°$	$75°$	altitude error $\Delta\alpha_{A;B} = 2\cos^2\alpha_{A;B}\dfrac{\Delta h}{b}$	depends on pointing accuracy
Beam separation ξ_0	$-2 L_x$	$2 L_x$	$\Delta\xi_0 \leq L_x/5$ (beam diameter)	L_x is the length scale. The beam diameter factor $\frac{1}{5}$ is obtained from wind tunnel experiments
Time lag $\lvert\tau\rvert$	0	$\xi_{max} - \xi_{min}/U_C$ $\approx 2 L_x/U_C$	$\Delta\tau = L_x/5U_B$	L_x and U_B depend on applications.
Inclination of intersection path with beam plane $\lvert\beta\rvert$	$2\left\lvert\dfrac{U_C}{U_B}\right\rvert$	$10\left\lvert\dfrac{U_C}{U_B}\right\rvert$	$\Delta\beta = 2\Delta\xi_0/b$ $= \dfrac{2}{5} L_x$	equation for $C_{AB} = \frac{1}{2}$ sets angle of view or horizontal pointing accuracy
Number of photodetectors	5	depends on hardware and receiver	----	at least five points on a curve to find a maximum
Length of intersection path	not known- length scale of homogeneous trend $>L_x$	not known- depends on correlation maximum and receiver noise	$\Delta L = L_x$	one sweep from orbit or pieces of repeated sweeps from ground.
Scanning speed	0.5 km/sec	8 km/sec (orbital speed)	$\dfrac{1}{5} U_B$	tolerance depends on application

TABLE VII. POINTING ACCURACIES AND STABILIZATION OF TELESCOPE PLATFORM

POINTING:

$$\Delta\beta \le \frac{2}{5}\frac{L_x}{b} \; ; \; \Delta\alpha \le 2\cos^2\alpha_{A;B}\frac{\Delta h}{b}$$

STABILIZATION:

$$\Delta\dot\beta \le \frac{2U_B}{10b} \; ; \; \Delta\dot\alpha \le \cos^2\alpha_{A;B}\frac{\Delta h\; U_B}{b\; L_x}$$

Detector Position	Baseline (kms)	Turbulence Length Scale L_x (m)	Altitude Tolerance Δh (m)	Accuracy
Ground (U_B = 500 m/sec)	10	100	40	$\Delta\alpha = \Delta\beta = 4\times10^{-3} = 15$ arc min
				$\Delta\dot\alpha = \Delta\dot\beta = 10^{-2}$ sec^{-1} = 34 arc min/sec
500 km Orbit (U_B = 8000 m/sec)	1000	250	100	$\Delta\alpha = \Delta\beta = 10^{-4} = 0.34$ arc min
				$\Delta\dot\alpha = \Delta\dot\beta = 1.6\times10^{-4} = $ sec^{-1} = 0.5 arc min/sec

Comment:

$$\alpha_A = \alpha_B = \frac{1}{2}\alpha_{AB} = 45°$$

4. the spatial and temporal resolution of the system, and

5. the effect, if any, of the beam diameter on the resolution of the system.

The first series of tests should serve to establish the soundness of the apparatus design. Once satisfactory results are obtained with this short range arrangement, the base line of the detectors will be increased to approximately 20 km to produce intersection heights of up to 10 km. The beam intersection point will be adjusted to discrete altitudes above tower heights to assess (1) rms levels and frequency range of fluctuations, which originate at higher altitudes, (2) the influence of the variation of the beam intersection angle on the measured correlation values, and (3) the scale of statistically inhomogeneous fluctuations.

These experiments will sense phenomena over longer ranges and under conditions of reduced light intensity and tracer concentration (see Section II)

and will therefore be a more severe test of the feasibility of the technique as applied to atmospheric phenomena. The beam separation distance, ξ, should be varied to approximately 600 m (approximately twice the mean eddy sizes at an altitude of 10 km) and data will be obtained on the five parameters listed at the beginning of Section V-D.

The considerations of Section II anticipate no signal detection problems up to a height of about 15 km. If the measurements are to be extended to an altitude of 30 km, a point might be reached where either the tracers or the light intensity or both fall below the minimum value necessary for producing a detectable signal. Since the aerosol concentration at a given height varies with weather conditions, only actual field experiments will define the height limitations of the system.

E. SECOND GENERATION EXPERIMENTS

Once the feasibility of applying the crossed-beam technique to the measurement of atmospheric

66

.turbulence phenomena has been established by the series of tests using fixed beams, an attempt will be made to obtain continuous coverage of turbulence phenomena by scanning the beams over the region of interest.

The two beams will be scanned in elevation so that their intersection point will describe horizontal traces in the region of interest. The scanning should require less than 1.5 min so that the turbulence phenomena can be considered as frozen during the period of one scan.

The main point of interest in this series of tests will be to determine the effect of the scanning speed of the beams on the measured quantities. As the scanning speed of the beams is increased, the detectors have a lesser amount of time to register individual fluctuations. This will cause an increase in received noise which we expect to be somewhat proportional to the (scanning speed)$^{-\frac{1}{2}}$.

The first and second generation experiments are planned for the immediate future. They should establish the feasibility and potential of the crossed-beam technique as applied to the measurement of atmospheric turbulence phenomena in the general vicinity of the sensors.

F. THIRD GENERATION EXPERIMENTS

The global potential of the crossed-beam technique can be realized only with the use of satellite-borne detectors. As shown in Sections II and III the feasibility of satellite-made measurements of the turbulence phenomena of the lower atmosphere can be demonstrated by performing the ground-based experiments discussed previously. Once these experiments have established the feasibility and potential of the technique, the next logical step will be to use satellite-borne detectors to make global scans of the earth's atmosphere.

VI. CONCLUSIONS

We have established that the crossed-beam technique is desirable because it would provide (1) global observation of the earth's atmosphere and its turbulence properties, (2) data for direct use in mathematical models of the atmosphere, and (3) continuous observations of weather patterns.

That it is also feasible was shown in Section III of this paper. We have seen that natural sources of radiation such as scattered solar radiation, ozone emission, and infrared radiation of the sky and earth's surface existed at sufficient level to be useful in the crossed-beam technique.

The natural traces without which the turbulence induced fluctuations are invisible exist in sufficient concentration up to a height of at least 15 km to produce detectable signals at the sensors. From 15 to 30 km the tracer concentration is reduced, but it may be sufficient to allow the crossed-beam technique to be used in the monitoring of turbulence phenomena.

The theory of crossed-beam scanning was generated based on the following three assumptions: that the region of interest was scanned rapidly enough to assume a frozen turbulence pattern over this region; that the region across the wavefront was statistically homogeneous over a typical turbulent scale or altitude error; and that the region around the beam normal could be weighted like that of a space-fixed beam such that a two-product mean value approximation was valid. Under these assumptions, it was demonstrated that we could determine convection speeds, length scales, wave number components, and the power spectrum using crossed-beam scanning.

REFERENCES

1. Krause, F. R. and Fisher, M. J.: Remote Sensing of Local Flow Instabilities and Turbulence. (Paper presented at the ASME Fluid Meters 50th Anniversary Conference Sept. 26-28, 1966).

2. Wolf, M.: Transactions. J. Geophys. Res., vol. 47, 75, 1966.

3. The director of the National Environment Satellite Center, ESSA.

4. Kondrat'yev, K. Y.: Actinometry. NASA TT F-9712.

5. Project Mesa: Present and Future Air Force Needs for Environmental Measurements. Geophysics Corp. of America, Jan. 1962.

6. Goody, R. M. and Roach, W. T.: Determination of the Vertical Distribution of Ozone from Emission Spectra. Quart. J. Roy. Meteorol. Soc., vol. 82, 1956, pp. 217-221.

7. Smith, R. A.; Jones, F. E.; and Chasmar, R. P.: The Detection and Measurement of Infrared Radiation. Oxford Press, 1957.

8. Morton, G. A.: Infrared Detectors. RCA Review, Mar. 1965.

9. Montgomery, A. J.; Davies, O. W.; et. al.: IIT Research Institute, Progress Reports under Contract No. NAS8-20107, IITRI Project A6139.

IV. CONTROL SYSTEM ANALYSIS

RLC SYNTHESIS OF TRANSFER FUNCTIONS

By

James W. Fontenot* and Don H. Townsend

SUMMARY

This paper presents a method and a digital computer program for Resistance-Inductance-Capacitance (RLC) synthesis of minimum-phase transfer functions. The method realizes the network in ladder form with a resistance termination. Every inductor has an associated series resistance. All realizations are within a constant multiplier, provided that no poles occur on the $j\omega$-axis, including infinity. Complex curve-fitting techniques are used for determining if there is a lower-order transfer function, $H(s)$, which satisfies the requirements used to arrive at the transfer function to be synthesized. The synthesis problem can always be reduced to synthesizing driving-point functions of the complexity no greater than the ratio of fourth-order polynomials in s. Sensitivity studies are possible by a computer program from which the frequency response of the network can be determined. Numerical examples are given, and frequency response curves are compared with ideal curves to illustrate that the desired transfer response is obtained.

I. INTRODUCTION

A number of synthesis techniques have been developed for the realization of minimum-phase transfer functions into RLC networks. However, for many of these techniques, digital computer programming is prohibitive because of limited storage space, excessive iterations, and the number of decisions involved. Efficient designs for the general RLC cases are harder to achieve than RC design because the added dimension greatly increases the degree of indeterminateness and may obscure preferable choices. An obvious disadvantage of applying a general synthesis procedure to a particular problem is that the network obtained usually contains more circuit elements than are actually needed.

This report presents the results of theoretical and computer studies of the synthesis procedure using a special application of Pantell's method [1, 2, 3]. The matrix factorization scheme is inherently capable of producing a realizable network, although one may not always obtain the best design because of the various combinations of transfer function factors.

II. T-MATRIX FOR A TWO-PORT NETWORK

The transmission or T-matrix is a circuit matrix which is useful for expressing the relation between a two-port network and its subnetworks. The subsequent derivation will verify that the T-matrix for the overall network is the matrix product of each subnetwork.

Reference directions for voltage and current will be taken as shown in Figure 1.

FIGURE 1. GENERAL FORM OF TWO-PORT NETWORKS

A network containing only passive bilateral elements has the following linear relations:

$$E_1 = Z_{11} I_1 - Z_{12} I_2$$

and

$$E_2 = Z_{21} I_1 - Z_{22} I_2 . \qquad (1)$$

The Z_{11} and Z_{22} terms represent driving-point impedances of terminals 1-1' and 2-2', respectively, with the opposite set of terminals open-circuited. Impedances Z_{12} and Z_{21} are mutually shared by the input and output circuits and are the transfer impedances of the network. A network consisting of only

---

*Northrop Space Laboratories, Huntsville, Alabama

passive bilateral elements such as resistors, inductors, and capacitors allows Z_{12} to equal Z_{21}.

Solving equations (1) for E_1 and I_1 in terms of E_2 and I_2, and expressing the results in matrix form yields

$$\begin{bmatrix} E_1 \\ \\ I_1 \end{bmatrix} = \begin{bmatrix} \dfrac{Z_{11}}{Z_{12}} & \dfrac{Z_{11}Z_{22} - Z_{12}{}^2}{Z_{12}} \\ \\ \dfrac{1}{Z_{12}} & \dfrac{Z_{22}}{Z_{21}} \end{bmatrix} \begin{bmatrix} E_2 \\ \\ I_2 \end{bmatrix}$$

$$= T \begin{bmatrix} E_2 \\ \\ I_2 \end{bmatrix} \qquad (2)$$

where T is the square matrix

$$T = \begin{bmatrix} A & B \\ C & D \end{bmatrix} . \qquad (3)$$

The square matrix, T, is usually called the transmission matrix of the network.

The determinant of equation (4) equals unity because of the reciprocity property of physically realizable RLC networks.

$$\begin{vmatrix} A & B \\ C & D \end{vmatrix} = AD - BC = 1 \qquad (4)$$

Note that A and D are dimensionless, B is dimensionally an impedance, and C is an admittance. The term A, for our application, is of interest because it represents the inverse voltage ratio of a network. Two four-terminal networks (Fig. 2) of transmission matrix T_1, T_2 are connected in cascade. The relations between the input and output parameters are given by equation (5),

$$\begin{bmatrix} E_1 \\ \\ I_1 \end{bmatrix} = T_1 T_2 \begin{bmatrix} E_2 \\ \\ I_2 \end{bmatrix} = T \begin{bmatrix} E_2 \\ \\ I_2 \end{bmatrix}, \qquad (5)$$
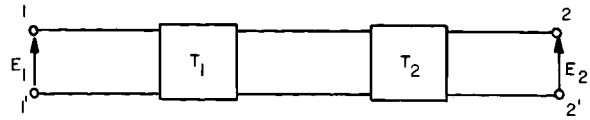

FIGURE 2. TWO SUBNETWORKS IN CASCADE

where T is the transmission matrix of the overall network.

It is possible to cascade several two-port networks, and the overall transmission matrix of the network is the matrix product of the individual T-matrices taken in the order of connection. The T-matrices of a series and shunt network are listed in Table I.

TABLE I. TRANSMISSION MATRICES FOR A SERIES AND SHUNT NETWORK

NETWORK	TRANSMISSION MATRIX $T = \begin{bmatrix} A & B \\ C & D \end{bmatrix}$
SERIES IMPEDANCE	$\begin{bmatrix} 1 & Z \\ 0 & 1 \end{bmatrix}$
SHUNT IMPEDANCE	$\begin{bmatrix} 1 & 0 \\ Y & 1 \end{bmatrix}$

III. T-MATRIX EXPANSION

Specification of only one T-matrix function is not sufficient to completely define a particular network. Fortunately, specification of one of the four transmission functions does not rule out matrix factorization as a realization technique. The following expansion of the transmission matrix will establish the relation between the transfer function and the cascaded connection of series and shunt arm networks as depicted in Table I.

The square matrix, T, is factored into three component matrices by a series of linear transformations [4].

$$\begin{bmatrix} A & B \\ C & D \end{bmatrix} = \begin{bmatrix} 1 & 0 \\ C/A & 1 \end{bmatrix} \begin{bmatrix} A & 0 \\ 0 & 1/A \end{bmatrix} \begin{bmatrix} 1 & B/A \\ 0 & 1 \end{bmatrix} \quad (6)$$

The factorization of equation (6) takes advantage of the determinant of the square matrix being equal to unity (equation (4)).

Given a voltage transfer ratio E_2/E_1, for a specific network, the transmission function A is known from equation (2). The following derivation is for n subnetworks, representing the product of n factors, where n is an even integer. The A's in the expression listed below are transmission functions for each subnetwork.

$$A = A_1 A_2 A_3 \ldots A_n \quad (7)$$

Substituting equation (7) into the center diagonal matrix yields the following expansion:

$$\begin{bmatrix} A & B \\ C & D \end{bmatrix} = \begin{bmatrix} 1 & 0 \\ C/A & 1 \end{bmatrix} \begin{bmatrix} A_1 & 0 \\ 0 & 1/A_1 \end{bmatrix} \begin{bmatrix} A_2 & 0 \\ 0 & 1/A_2 \end{bmatrix}$$
$$\ldots \begin{bmatrix} A_n & 0 \\ 0 & 1/A_n \end{bmatrix} \begin{bmatrix} 1 & B/A \\ 0 & 1 \end{bmatrix} . \quad (8)$$

Multiplying every odd and even subscripted diagonal yields

$$\begin{bmatrix} A & B \\ C & D \end{bmatrix} = \begin{bmatrix} 1 & 0 \\ C/A & 1 \end{bmatrix} \begin{bmatrix} A_1 A_2 & 0 \\ 0 & \frac{1}{A_1 A_2} \end{bmatrix}$$
$$\ldots \begin{bmatrix} A_{n-1} A_n & 0 \\ 0 & \frac{1}{A_{n-1} A_n} \end{bmatrix} \begin{bmatrix} 1 & B/A \\ 0 & 1 \end{bmatrix} . \quad (9)$$

The following identity matrix (10) is substituted into equation (9).

$$\begin{bmatrix} A_{g-1} A_g & 0 \\ 0 & \frac{1}{A_{g-1} A_g} \end{bmatrix} = \begin{bmatrix} 1 & 0 \\ -\frac{1}{A_{g-1}} & 1 \end{bmatrix} \begin{bmatrix} 1 & A_{g-1} - \frac{1}{A_g} \\ 0 & 1 \end{bmatrix}$$

$$\begin{bmatrix} 1 & 0 \\ A_g & 1 \end{bmatrix} \begin{bmatrix} 1 & \frac{1}{A_{g-1} A_g^2} - \frac{1}{A_g} \\ 0 & 1 \end{bmatrix} \quad (10)$$

$$g = 2, 4, 6, 8, \ldots n.$$

Observe that the multiplication of a diagonal h-matrix by a triangular r-matrix forms equation (11).

$$\begin{bmatrix} 1 & r \\ 0 & 1 \end{bmatrix} \begin{bmatrix} h & 0 \\ 0 & 1/h \end{bmatrix} = \begin{bmatrix} h & 0 \\ 0 & 1/h \end{bmatrix} \begin{bmatrix} 1 & \frac{r}{h^2} \\ 0 & 1 \end{bmatrix} \quad (11)$$

where

$$r = \frac{1}{A_{g-1} A_g^2} - \frac{1}{A_g}$$

and

$$h = A_{g+1} A_{g+2} .$$

Successive application of equation (10) into the diagonal matrices of equation (9), then applying equation (11) plus multiplying together similar adjacent matrices, leads to the following expanded form.

$$\begin{bmatrix} A & B \\ C & D \end{bmatrix} = \begin{bmatrix} 1 & 0 \\ \frac{C}{A} - \frac{1}{A_1} & 1 \end{bmatrix} \begin{bmatrix} 1 & A_1 - \frac{1}{A_2} \\ 0 & 1 \end{bmatrix} \begin{bmatrix} 1 & 0 \\ A_2 - \frac{1}{A_3} & 1 \end{bmatrix}$$
$$\ldots \begin{bmatrix} 1 & 0 \\ A_{n-2} - \frac{1}{A_{n-1}} & 1 \end{bmatrix} \begin{bmatrix} 1 & A_{n-1} - \frac{1}{A_n} \\ 0 & 1 \end{bmatrix} \begin{bmatrix} 1 & 0 \\ A_n & 1 \end{bmatrix}$$

$$\begin{bmatrix} 1 & \frac{B}{A} + U_{n-1} \\ 0 & 1 \end{bmatrix} , \quad (12)$$

where U_{n-1} is defined as

72

$$U_1 = 0$$

$$U_3 = (U_1 + r_2)/(A_3 A_4)^2$$

$$U_5 = (U_3 + r_4)/(A_5 A_6)^2$$

$$\cdot \qquad \cdot$$
$$\cdot \qquad \cdot$$
$$\cdot \qquad \cdot$$

$$U_{n-1} = (U_{n-3} + r_{n-2})/(A_{n-1} A_n)^2$$

$$r_2 = (\frac{1}{A_1 A_2} - 1)/A_2$$

$$r_4 = (\frac{1}{A_3 A_4} - 1)/A_4$$

$$r_6 = (\frac{1}{A_5 A_6} - 1)/A_6$$

$$\cdot \qquad \cdot$$
$$\cdot \qquad \cdot$$
$$\cdot \qquad \cdot$$

$$r_{n-2} = (\frac{1}{A_{n-3} A_{n-2}} - 1)/A_{n-2} \, .$$

Equation (12) represents a particular physically realizable RLC ladder network when all four transmission functions are defined. However, if only the voltage ratio E_2/E_1 is given, then A is the only transmission function known. Therefore, the first and last matrices on the right-hand side of equation (12) can be deleted, but the new functions B^*, C^*, and D^* will not necessarily be equal to B, C, and D of equation (12).

$$\begin{bmatrix} A & B^* \\ C^* & D^* \end{bmatrix} \begin{bmatrix} 1 & A_1 - \frac{1}{A_2} \\ 0 & 1 \end{bmatrix} \begin{bmatrix} 1 & 0 \\ A_2 - \frac{1}{A_3} & 1 \end{bmatrix}$$

$$\cdots \begin{bmatrix} 1 & 0 \\ A_{n-2} - \frac{1}{A_{n-1}} & 1 \end{bmatrix} \begin{bmatrix} 1 & A_{n-1} - \frac{1}{A_n} \\ 0 & 1 \end{bmatrix} \begin{bmatrix} 1 & 0 \\ A_n & 1 \end{bmatrix} . \quad (13)$$

By definition, the transmission function A can be expressed as

$$A = \frac{1}{K\,H(s)} = \frac{1}{\prod\limits_{i=1}^{n} K_i f_i} \, , \qquad (14)$$

where the multiplying constant,

$$K = \prod_{i=1}^{n} K_i \, , \qquad (15)$$

and $H(s)$ is the rational polynomial for the voltage ratio E_2/E_1. Substituting equation (14) into equation (13) gives

$$\begin{bmatrix} A & B^* \\ C^* & D^* \end{bmatrix} = \begin{bmatrix} 1 & \frac{1}{K_1 f_1} - K_2 f_2 \\ 0 & 1 \end{bmatrix} \begin{bmatrix} 1 & 0 \\ \frac{1}{K_2 f_2} - K_3 f_3 & 1 \end{bmatrix}$$

$$\cdots \begin{bmatrix} 1 & 0 \\ \frac{1}{K_{n-2} f_{n-2}} - K_{n-1} f_{n-1} & 1 \end{bmatrix} \begin{bmatrix} 1 & \frac{1}{K_{n-1} f_{n-1}} - K_n f_n \\ 0 & 1 \end{bmatrix}$$

$$\begin{bmatrix} 1 & 0 \\ \frac{1}{K_n f_n} & 1 \end{bmatrix} . \qquad (16)$$

The resulting expression represents the physically realizable ladder network which will yield the prescribed transfer function, H(s), within a constant multiplier, K. Theoretically, the synthesis of H(s) is assured regardless of its complexity, and the problem reduces to the synthesis of series and shunt driving-point functions [1,2].

Observe that each individual matrix represents a series or shunt network as listed in Table I. The matrix

$$\begin{bmatrix} 1 & \frac{1}{K_1 f_1} - K_2 f_2 \\ 0 & 1 \end{bmatrix}$$
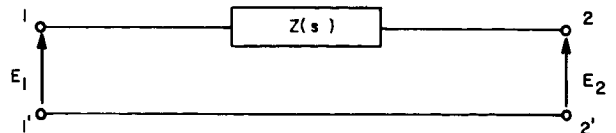
is the representation for Figure 3,

FIGURE 3. SERIES NETWORK

where

$$Z(s) = \frac{1}{K_1 f_1} - K_2 f_2 . \tag{17}$$

Similarly, the matrix

$$\begin{bmatrix} 1 & 0 \\ \frac{1}{K_2 f_2} - K_3 f_3 & 1 \end{bmatrix}$$
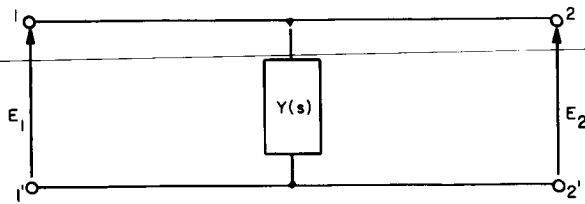
is the representation for Figure 4,

FIGURE 4. SHUNT NETWORK

where

$$Y(s) = \frac{1}{K_2 f_2} - K_3 f_3 . \tag{18}$$

IV. FACTORIZATION OF A TRANSFER FUNCTION

Certain restrictions on the factorization of a transfer function will be discussed. These restrictions are primarily derived from the positive-real concept.

A reduction in circuit elements is accomplished when synthesizing transfer functions, if restrictions are imposed on the degree of the numerator and denominator. The numerator will be at least one degree lower than the denominator for this application. This restriction satisfies many of the filter requirements encountered; however, cases with equal-order denominator and numerator can sometimes meet the requirement by employing complex curve-fitting techniques [5,6].

A minimum-phase transfer function can be defined as

$$H(s) = \prod_{i=1}^{n} f_i(s) \tag{19}$$

where $f_i(s)$ is positive-real. The factorization of $H(s)$ for many cases will require the multiplication

of excess factors in the numerator and denominator, as follows:

$$H(s) = \frac{s^2 + c_1 s + d_1}{(s^2 + c_2 s + d_2)(s + c_3)} \tag{20}$$

$$= \frac{s + \alpha}{s^2 + c_2 s + d_2} \cdot \frac{s^2 + c_1 s + d_1}{s + \alpha} \cdot \frac{1}{s + c_3} .$$

A second-order polynomial taken from $H(s)$ can always be made positive-real by selecting an appropriate positive constant, α. The even function of any f_i must meet the following requirements for all ω:

$$Ev [f_i (j\omega)] \geq 0 . \tag{21}$$

A sufficient condition for positive-reality can be determined for equation (22) when $c_2 > \alpha$ for all ω.

$$Ev \left[\frac{s + \alpha}{s^2 + c_2 s + d_2} \right] = \frac{(\alpha - c_2) s^2 + d_2}{(s^2 + c_2 s + d_2)(s^2 - c_2 s + d_2)} \tag{22}$$

Similarly, the reciprocal function of equation (22) can be shown to be positive-real [7].

The elements of a series or shunt network are made realizable if equation (23) is positive-real.

$$\frac{1}{K_i f_i} - K_{i+1} f_{i+1} \tag{23}$$

Equation (23) can always be made positive-real by choosing K_{i+1} sufficiently small, if

$$Ev \left[\frac{1}{K_i f_i} - K_{i+1} f_{i+1} \right] \geq 0 \text{ for every value of } \omega ,$$

$$f_i(j\omega) = 0 \text{ for every value of } \omega \text{ where } f_{i+1}(j\omega) = \infty.$$

If the first condition is not satisfied, the even function of equation (23) is negative at some frequency, ω; thus, the positive-real concept fails. Since $H(0) \neq \infty \neq H(\infty)$, the second condition indicates that every $f_i(s)$ that has a pole at $s = 0$ or $s = \infty$ must be preceded and followed by functions that have zeros at $s = 0$ or $s = \infty$. All complex zeros of $H(s)$ will have factors with poles at $s = \infty$ for a surplus factor $s + \alpha$. Cases where n factors have poles at $s = \infty$ must have at least $n + 1$ factors with zeros at $s = \infty$. Therefore, it is always possible to choose $f_1(s)$ and $f_n(s)$ to preclude a pole at $s = \infty$ which satisfies the preceding rule. Therefore,

$f_1(s)$ and $f_n(s)$ can be made nonminimum conductive, and a resistance termination at both ends of a network is always possible [8]. Nonminimum conductive means that zero conductance for an admittance function cannot be obtained at any frequency ω. Thus, a resistance can be removed in the synthesis process without causing the real part of the remaining admittance function to be negative at any frequency ω. Because of the preceding rule and because $H(\infty) = 0$, any surplus factors need be no more complicated than $(s+\alpha)/(s+\alpha)$. When a specific ratio of output to input resistance is desired, the output resistance can be divided into two series or parallel resistors with the desired resistor value at the termination.

Several points regarding Pantell's method of two-port synthesis are worthy of note.

1. The method is not unique. Many different possibilities for factoring $H(s)$ into positive-real functions exist. Once the factorization has been determined, different sequences of $f_i(s)$ yield different networks.

2. The synthesis problem is reduced to the realization of driving-point functions of order no greater than four regardless of the complexity of the transfer function. This is true when $H(s)$ is factored into nonminimum conductive factors of order no greater than two; sometimes third-order factors are applicable.

3. The factorization into quadratic terms is not necessary; any factorization into a nonminimum conductive (with the possible exception of $\omega = 0$ or $\omega = \infty$) positive-real function is adequate. For example, when transfer function $H(s)$ is a nonminimum conductive positive-real function, the matrix can be represented by

$$
\begin{bmatrix} 1 & \dfrac{1}{K_1 H(s)} - K_2 \\ 0 & 1 \end{bmatrix}
\begin{bmatrix} 1 & 0 \\ \dfrac{1}{K_2} & 1 \end{bmatrix} , \qquad (24)
$$

and the realization is shown below.
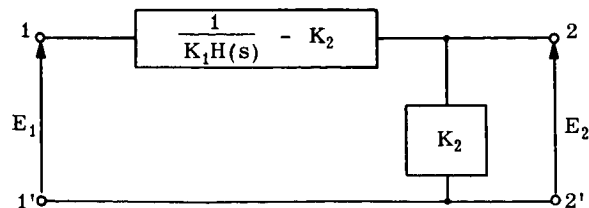
Factorization into functions of order greater than two may or may not require fewer elements, depending upon whether minimum functions appear during the realization process.

4. Changing the magnitude of the load resistor is permissible by shifting a portion of the resistance to the arm of the inverted-L section. This will change the multiplying constant K, where K_n is equal to the new R_L.

V. COMPLEX CURVE FITTING

The number of circuit elements in the synthesis of a minimum-phase transfer function depends upon (1) the method employed and (2) the degree of the rational polynomial being synthesized. Application of complex curve-fitting techniques in obtaining a simpler transfer function is presented.

A lower-order transfer function can sometimes satisfy the gain and phase requirements of another higher-order case, provided the gain and phase curves are within a predetermined stable bounded region. Given a designated function, complex curve-fitting techniques are available which facilitate the computation of a lower-order function by approximating the frequency response characteristics of the known case [5,6]. E. C. Levy devised a method capable of performing complex curve-fitting calculations by fitting regression curves to data obtained from the frequency response of a known function [9].

Given an analytic and stable bounded region as in example 1 (Fig. 5), a minimum-phase transfer function $H_0(s)$ was determined.
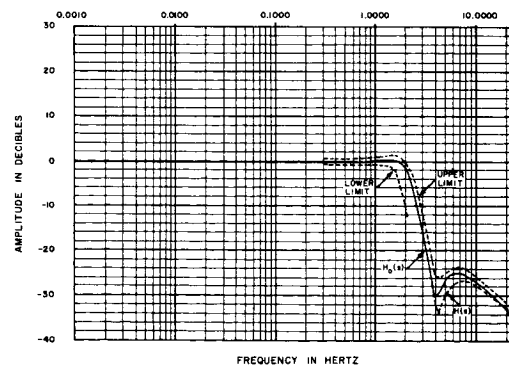

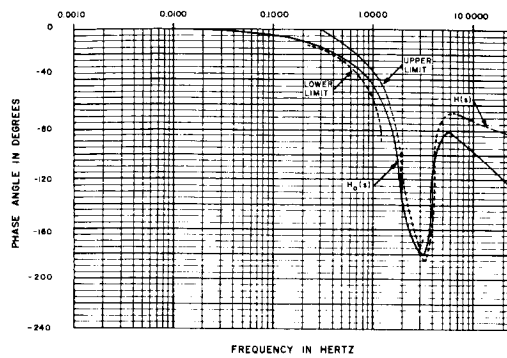FIGURE 5a. EXAMPLE 1, FILTER FREQUENCY RESPONSE FOR GAIN

FIGURE 5b. EXAMPLE 1, FILTER FREQUENCY RESPONSE FOR PHASE

$H_0(s) =$

$$\frac{0.0016s^2 + 0.008s + 1.0}{0.00000281s^4 + 0.000492s^3 + 0.0106s^2 + 0.128s + 1.0}$$

(25)

Zeros	Poles
-2.5 ± j24.874	-4.2279 ± j11.99
	-152.16
	-14.468

Another lower-order function, H(s), was computed by inputting data from $H_0(s)$ into the complex curve-fitting program. The fitted-phase and gain curves for H(s) are within the specified tolerance,

$$H(s) = \frac{0.0014022\ s^2 + 0.0052156\ s + 1.0}{0.00437\ s^3 + 0.00989999\ s^2 + 0.124\ s + 1.0}$$

(26)

Zeros	Poles
-1.8598 ± j26.64	-4.3019 ± j12.015
	-14.051

thus satisfying the filter requirements.

Complex curve-fitting should always be employed before synthesis of a transfer function since it is possible that a lower-order function may satisfy the gain-phase frequency specifications.

IV. SYNTHESIS BY COMPUTER

A. NETWORK SYNTHESIS PROGRAM

A digital computer program which performs Pantell's synthesis technique was developed. The network synthesis program contains a main program and three subroutines. Driving-point functions of order no greater than four can be synthesized. This limitation could be removed, but it is doubtful whether higher-order functions will yield fewer elements or even a network. Computation time for one network representing a third-over-fourth order transfer function is approximately 10 seconds including print-out time. It is possible to synthesize up to a fourteen-over-fifteen order function with this program; however, practical applications may be prohibitive for this size function.

The main program generates each driving-point function within a ladder network by successive sub-sitution of predetermined coefficients into an equation describing the individual branch network. Tabulation of the results is controlled by the program.

A continued fraction subroutine is employed after the main program has computed a rational polynomial. This program expands a positive-real function by a pattern of successive forward and backward division [8]. The magnitude of each element is checked to assure realization. That is, the program monitors the values of each resistor, inductor, and capacitor, and the ratio of an inductance to its associated resistance. If the expansion cannot be completed as a continued fraction, control is returned to the main program for computation of a new driving-point function. Control is again returned to the main program for computation of the subsequent driving-point function once the synthesis is complete.

Root-solver and predistortion subroutines are employed when the last element of a continued fraction expansion is an inductor without an associated resistance. The predistortion subroutine replaces the complex variable s in a driving-point function by a new variable $\lambda = s + \delta$, where δ is a constant which can be measured along the real axis of the s-plane [8]. The root-solver computes the roots of the numerator and denominator of the driving-point function. Delta must be less than or equal to the absolute value of the smallest root. The realization of a resistance with each reactive element is accomplished by performing the reverse transformation following the synthesis procedure.

The synthesis program will not synthesize every transfer function. Minimum functions and unrealizable elements will cause the synthesis method to fail.

B. T AND PI EXPANSION PROGRAM

The transfer function of a ladder network containing up to four inverted-L sections is determined.

$\dot{Z}(s)$'s and $Y(s)$'s of order less than five are acceptable. This program multiplies the driving-point factors composing the transmission function, A. A plotting routine plots the frequency response of the transfer function. This makes possible studies of sensitivity, which relate to component tolerances.

C. POSITIVE-REAL PROGRAM

The digital computer program determines whether or not the rational polynomial is positive-real. This program will perform an analytical test on rational polynomials of order less than 9/9. Input data consist of the numerator and denominator coefficients, title, and number of cases involved. Print-out of the results will include the title, numerator and denominator coefficients, and an indication of whether or not the rational polynomial is positive-real.

VII. NUMERICAL EXAMPLES

This section presents the result of synthesizing some particular transfer functions. The digital computer program described previously was used in determining the network parameters.

A. EXAMPLE 1.

The factorization of equation (26) is shown in equation (27):

$$H(s) = \frac{s^2 + 3.7196s + 713.1486}{(s + 14.051)(s^2 + 8.6038s + 162.8666)}$$

$$= \left[\frac{s + \alpha}{s^2 + 8.6038s + 162.866}\right] \quad (27)$$

$$\times \left[\frac{s^2 + 3.7196s + 713.1486}{s + \alpha}\right]\left[\frac{1}{s + 14.051}\right]\left[1\right].$$

The positive-real factors for equation (27) are

$$f_1(s) = \frac{s + \alpha}{s^2 + 8.6038s + 162.866}$$

$$f_2(s) = \frac{s^2 + 3.7196s + 713.1486}{s + \alpha}$$

$$f_3(s) = \frac{1}{s + 14.051}$$

$$f_4(s) = 1$$

For $K_1 = 1.0$, $K_2 = 0.205538$, $K_3 = 0.228056$, $K_4 = 55.45$, and $\alpha = 2.97384$, the realization is given in Figure 6.
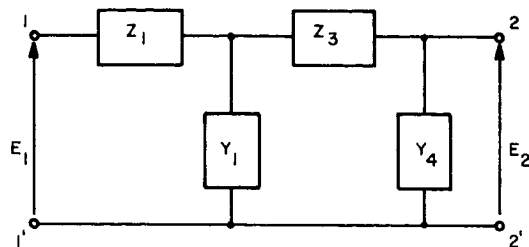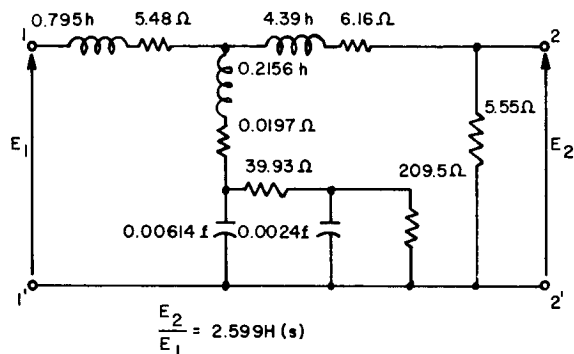

FIGURE 6a. GENERALIZED LADDER NETWORK

$$\frac{E_2}{E_1} = 2.599 H(s)$$

FIGURE 6b. CIRCUIT REALIZATION FOR H(s)

A similar frequency response to H(s) which is depicted in Figure 5 was obtained. The multiplying constant, K, was normalized to one.

B. EXAMPLE 2.

Factorization for the transfer function is shown below:

$$H(s) = \frac{s + 0.095057}{s^2 + 31.77316\,s + 1.20048}$$

$$= \left[\frac{s + \alpha}{s^2 + 31.77316\,s + 1.0}\right] \quad (28)$$

$$\times \left[\frac{s + 0.095057}{s + \alpha}\right]\left[1\right]\left[1\right].$$

A circuit was obtained with $K_1 = 1.0$, $K_2 = 11.366$, $K_3 = 0.0049$, $K_4 = 204.0$, and $\alpha = 0.005884$. A

better choice of circuit components is made available when magnitude scaling is employed. Magnitude scaling does not affect the multiplying constant. The elements shown in Figure 7 are manufacturable and approximate the ideal components.
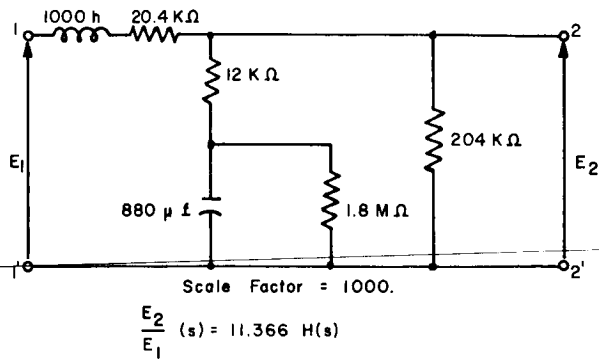

Scale Factor = 1000.

$$\frac{E_2}{E_1}(s) = 11.366 \ H(s)$$

FIGURE 7. CIRCUIT REALIZATION FOR H(s)

Frequency response plots for the circuit, labeled $H_c(s)$ and $H(s)$ are shown in Figure 8. The roots for $H(s)$ and $H_c(s)$ are as follows:

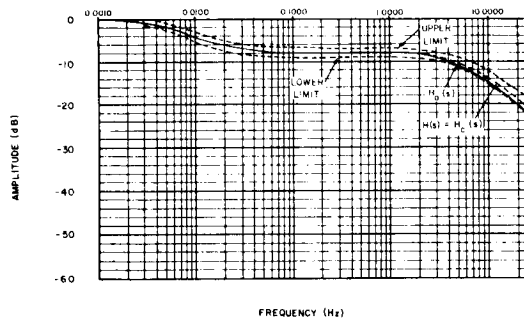| H(s)		$H_c(s)$	
Zeros	Poles	Zeros	Poles
-0.095057	-31.735	-0.095328	-31.70135
	- 0.037828		- 0.037872

FIGURE 8a. EXAMPLE 2, FILTER FREQUENCY RESPONSE FOR GAIN

Equation (28) could have been factored as shown in equations (29) and (30):

$$H(s) = \left[\frac{s + 0.095057}{s^2 + 31.77316 \ s + 1.20048}\right]\left[1\right] \quad (29)$$

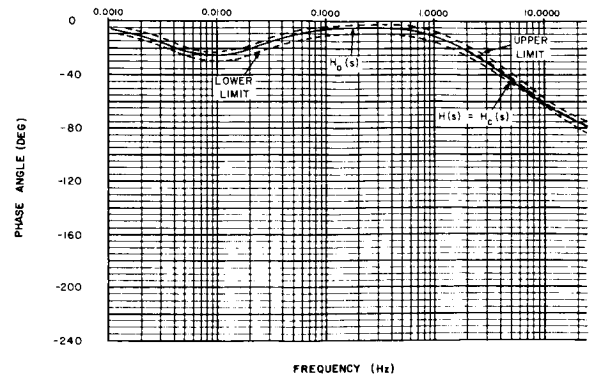$$H(s) = \left[\frac{s + \alpha}{s^2 + 31.77316 \ s + 1.20048}\right]\left[\frac{s + 0.095057}{s + \alpha}\right] \quad (30)$$

FIGURE 8b. EXAMPLE 2, FILTER FREQUENCY RESPONSE FOR PHASE
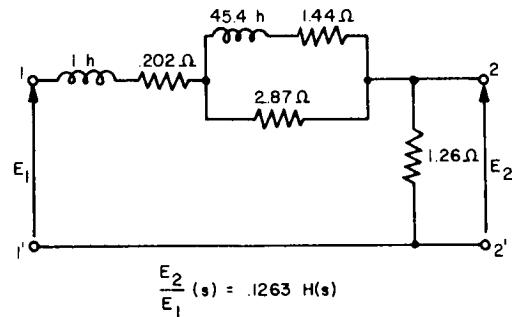
The networks obtained are shown in Figures 9 and 10.

$$\frac{E_2}{E_1}(s) = .1263 \ H(s)$$

FIGURE 9. REALIZATION FOR EQUATION (29)

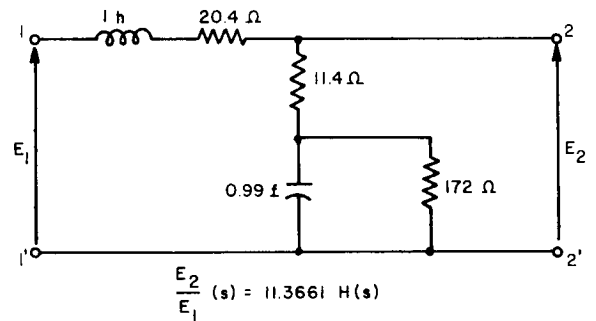$$\frac{E_2}{E_1}(s) = 11.3661 \ H(s)$$

FIGURE 10. REALIZATION FOR EQUATION (30)

The circuit of Figure 9 is less desirable than Figure 7 because of the ratio of inductance to associated resistance. Also, capacitors are preferable to inductors for low-frequency applications because the physical realization of those inductances become very impractical due to size, cost, and dissipation. The network of Figure 10 has no load resistor;

78

however, a shunt-connected resistor is permissible if its magnitude is large enough to permit the frequency response curve to be within the bounded region.

VIII. CONCLUSION

The synthesis method described is similar to Pantell's synthesis procedure in its application for synthesizing voltage transfer functions into RLC networks. It differs from Pantell's procedure in that additional simplification of circuit design is made possible through complex curve-fitting techniques which determine (if one exists) a lower-order transfer function. The new transfer function must be within a specified tolerance from a known gain-phase frequency characteristic. A particular advantage of this synthesis procedure is that excessive computer iterations and design decisions are minimized.

A digital computer program capable of synthesizing a fourteen-over-fifteen order transfer function into an RLC network was developed. Another program determines the frequency response of a ladder network, thus enabling sensitivity studies which relate to component tolerance.

The numerical examples demonstrated the feasibility of this synthesis approach. Substitution of standard off-the-shelf components for the ideal values is permissible if the network's response curve is within the specification limits.

Success in network synthesis is not assured for all transfer functions. Functions having irreducible (in the sense that further factorization is impossible with real coefficients) quadratic equations with small damping coefficients at low frequencies are especially difficult to synthesize. Additional complications arise as the degree of the transfer functions increases because of the interdependence of each driving-point function upon preceding functions.

REFERENCES

1. Pantell, R. H.: New Method of Driving-Point and Transfer-Function Synthesis. Technical Report No. 76, Electronics Research Laboratory, Stanford University, July 1954.

2. Pantell, R. H.: Minimum-Phase Transfer Function Synthesis. IRE Trans. on Circuit Theory, vol. CT-2, June 1955, pp. 133-137.

3. Fontenot, James W.: Transfer Function Synthesis and Digital Computer Application. NSL/Huntsville Tech. Memo. no. 186, June 1966.

4. Ho, E. C.: RLC Transfer Function Synthesis. IRE Trans. on Circuit Theory, vol. CT-3, Sept. 1956, pp. 188-190.

5. Fontenot, J. W. and Tung, S.: A Method to Define a Minimum-Phase Transfer Function Within the Bounded Region of Phase-Gain Specifications. NSL/Huntsville Tech. Memo. no. 55, Feb. 1965.

6. Wilcox, J.; Tung, S.; and White, K.: Network Synthesis and a Method to Define a Transfer Function from Prescribed Phase-Magnitude Characteristics. NSL/Huntsville Aero/Astro Tech. Memo no. 16, May 1964.

7. Weinberg, Louis: Network Analysis and Synthesis. McGraw-Hill Book Co., 1962.

8. Yengst, W. C.: Procedure of Modern Network Synthesis. The Macmillan Co., 1964.

9. Levy, E. C.: Complex Curve Fitting. IRE Trans. on Automatic Control, May 1959.

A SIMPLE FEEDBACK LAW FOR A COOPERATIVE RENDEZVOUS PROBLEM

By

Thomas E. Carter

SUMMARY

A cooperative rendezvous problem for two point masses sufficiently near each other that the accelerations caused by external forces are the same for both objects provides a simple example of a linear regulator problem in which the steady-state solution of the associated matrix-Riccati equation can easily be found. A simple linear feedback law with constant coefficients follows.

I. INTRODUCTION

The simultaneous maneuvering of two spacecraft to come together with the same velocity and acceleration is called a cooperative rendezvous. Cooperative rendezvous problems have recently been formulated [1, 2] in terms of the calculus of variations and the Pontryagin maximum principle. In this work a cooperative rendezvous problem is formulated as a linear regulator problem which belongs to a class of problems which were solved by Kalman [3] using a Hamilton-Jacobi approach. Using this approach, a very simple linear feedback law with constant coefficients is obtained for the thrust control of the two spacecraft. For a chase type rendezvous, in which one craft has no control acceleration, and for a soft landing problem, a similar feedback law can be found.

II. THE GENERAL PROBLEM

Two objects are moving in a three-dimensional Euclidean space subject to an external force and their own control forces, and they desire to cooperate in such a way that the positions, velocities, and accelerations of the two objects are eventually identical. The equations of motion of the two bodies are

$$\dot{r}_p = v_p \qquad \dot{r}_T = v_T \qquad (1)$$

$$\dot{v}_p = f + u_p \qquad \dot{v}_T = f + u_T , \qquad (2)$$

where r_p and r_T, v_p and v_T, and u_p and u_T are, in vector notation, the respective positions, velocities, and controlled accelerations of the two objects. It is assumed that the two bodies are sufficiently close together to be subject to the same acceleration vector which is caused by external forces. The dot denotes time differentiation. The relative motion is given by

$$\dot{r} = v \qquad (3)$$

$$\dot{v} = u_p - u_T , \qquad (4)$$

where $r = r_p - r_T$ and $v = v_p - v_T$.

The problem is to find simple stable feedback laws for u_p and u_T for which a soft rendezvous occurs. One way this can be accomplished is by formulating an optimization problem having a stable control law as its solution and using the machinery of optimal control theory to find this feedback law which can then be applied to the rendezvous problem. One such optimization problem is the linear regulator problem which has been solved by Kalman [3] via the Hamilton-Jacobi Caratheodory approach. This approach leads to the problem of solving a matrix-Riccati equation which, in general, must be solved numerically. The simplicity of equations (3) and (4) of the rendezvous problem, however, enables us to solve this equation algebraically in this case.

We shall consider the infinite time version of the linear regulator problem mentioned above in which the object is to find a control r-vector function, u, which minimizes the performance index.

$$J[u] = \int_{t_0}^{\infty} [x^T Q x + u^T R u] \, dt \qquad (5)$$

subject to the constraint equations

$$\dot{x} = Ax + Bu, \quad x(t_0) = x_0 , \qquad (6)$$

where x is an n-vector, A a real nxn matrix, B a real rxn matrix, and Q and R are positive definite

symmetric nxn and rxr matrices, respectively. The matrices Q and R are assumed positive definite and symmetric because these assumptions, along with the assumption of complete controllability, are sufficient to insure the existence of a unique stable solution of the regulator problem.

Considering the cooperative rendezvous problem as a special case of the linear regulator problem, we have the following relationships.

$$x = \begin{bmatrix} r \\ v \end{bmatrix}, \quad A = \begin{bmatrix} 0 & I \\ 0 & 0 \end{bmatrix}, \quad u = \begin{bmatrix} u_p \\ u_T \end{bmatrix} \quad B = \begin{bmatrix} 0 & 0 \\ I & -I \end{bmatrix}$$

$$Q = \begin{bmatrix} Q_r & 0 \\ 0 & Q_v \end{bmatrix} \quad R = \begin{bmatrix} R_p & 0 \\ 0 & R_T \end{bmatrix}, \quad (7)$$

where 0 is the 3x3 zero matrix, I is the 3x3 identity matrix, and Q_r, Q_v, R_p, R_T are positive definite symmetric "weighting" matrices for the vectors r, v, u_p, and u_T, respectively.

The solution of the linear regulator problem defined by equations (5) and (6) can be found by solving an associated Hamilton-Jacobi partial differential equation, which for this problem is

$$-V_t = x^T Q x + V_x^T A x - \tfrac{1}{4} V_x^T B R^{-1} B^T V_x, \quad (8)$$

where V_x denotes the gradient, with respect to x, of a scalar valued function of x and t, and V_t denotes the partial derivative of V with respect to time. Kalman [3, 4] has shown that the existence of a unique solution $V^0(x, t)$ of the Hamilton-Jacobi equation is necessary and sufficient for

$$V^0(x_0, t_0) = \min J[u]. \quad (9)$$

Furthermore, the optimum control for this problem is given by

$$u^0 = \tfrac{1}{2} R^{-1} B^T V_x^0. \quad (10)$$

From the symmetric positive definiteness of R and Q, it can be shown that the Hamilton-Jacobi equation for the linear regulator problem has a unique solution in quadratic form, if the plant is completely controllable, that quality being defined as the ability to

reach any desired state with a finite control in a finite time [5]. Under these assumptions the solution of equation (8) is

$$V^0(x, t) = x^T P x, \quad (11)$$

where P is the unique positive definite solution of the matrix-Riccati equation

$$-\dot{P} = P^T A + A^T P - P^T B R^{-1} B^T P + Q. \quad (12)$$

Two further considerations concerning equation (12) are (1) that P is a steady-state solution if the terminal time is infinite and (2) that $V^0 = V^0(x)$ is a Lyapunov function which assures asymptotic stability of equation (6). In other words, the comments following equation (10) may be summarized by saying that complete controllability is sufficient to insure that an infinite time cooperative rendezvous occurs.

III. A SPECIFIC FEEDBACK SOLUTION

For this problem, we pick $R_p = \rho_p I$ and $R_T = \rho_T I$, where ρ_p and ρ_T are positive numbers. Since P is positive definite and symmetric, it can be partitioned as follows:

$$P = \begin{bmatrix} P_I & P_s \\ P_s^T & P_{II} \end{bmatrix}, \quad (13)$$

where P_I and P_{II} are symmetric positive definite 3x3 matrices and P_s is a real 3x3 matrix. Substituting equation (11) into equation (10) and using the relations in equations (7) and (13), the optimal control in terms of the two rendezvous controllers becomes

$$u_p^0 = -\frac{1}{\rho_p} \left(P_s^T r + P_{II} v \right)$$

$$u_T^0 = \frac{1}{\rho_T} \left(P_s^T r + P_{II} v \right). \quad (14)$$

Thus, the optimal motion from equations (3) and (4) is governed by the second-order vector differential equation

$$\ddot{r} + \frac{1}{\rho} P_{II}\dot{r} + \frac{1}{\rho} P_s^T r = 0, \qquad (15)$$

where $\frac{1}{\rho} = \frac{1}{\rho_p} + \frac{1}{\rho_T}$. The matrices P_I and P_{II} are found from the steady-state part of equation (12) which is

$$\begin{bmatrix} Q_r & 0 \\ 0 & Q_v \end{bmatrix} + \begin{bmatrix} P_I & P_s^T \\ P_s & P_{II} \end{bmatrix} \begin{bmatrix} 0 & I \\ 0 & 0 \end{bmatrix}$$

$$+ \begin{bmatrix} 0 & 0 \\ 0 & 0 \end{bmatrix} \begin{bmatrix} P_I & P_s \\ P_s^T & P_{II} \end{bmatrix}$$

$$- \frac{1}{\rho} \begin{bmatrix} P_I & P_s^T \\ P_s & P_{II} \end{bmatrix} \begin{bmatrix} 0 & 0 \\ 0 & 0 \end{bmatrix} \begin{bmatrix} P_I & P_s \\ P_s^T & P_{II} \end{bmatrix} = \begin{bmatrix} 0 & 0 \\ 0 & 0 \end{bmatrix} . \qquad (16)$$

Performing the partition multiplication, we reduce the above sixth-order matricial equation to the following three third-order matricial equations:

$$Q_r - \frac{1}{\rho} P_s^T P_s^T = 0 \qquad (17a)$$

$$P_I - \frac{1}{\rho} P_s^T P_{II} = 0 \qquad (17b)$$

$$Q_v + 2P_s - \frac{1}{\rho} P_{II}P_{II} = 0. \qquad (17c)$$

Solutions of equations (17a) and (17c) are sufficient to determine the feedback law (14). If Q_r and Q_v are diagonal matrices, the solutions of equations (17) which insure positive definiteness of P_I and P_{II} are

$$P_s = \begin{bmatrix} \sqrt{\rho q_{r_1}} & 0 & 0 \\ 0 & \sqrt{\rho q_{r_2}} & 0 \\ 0 & 0 & \sqrt{\rho q_{r_3}} \end{bmatrix}$$

$$P_{II} = \begin{bmatrix} \sqrt{\rho\left(q_{v_1} + 2\sqrt{\rho q_{r_1}}\right)} & 0 & 0 \\ 0 & \sqrt{\rho\left(q_{v_2}+2\sqrt{\rho q_{v_2}}\right)} & 0 \\ 0 & 0 & \sqrt{\rho\left(q_{v_3}+2\sqrt{\rho q_{v_3}}\right)} \end{bmatrix} . \qquad (18)$$

(Note: For this particular problem, P_I is not required since equation (14) does not depend upon P_I.)

The q_{r_i} and q_{v_i} $(i=1,2,3)$ are the diagonal elements of Q_r and Q_v, respectively. Equations (14) and (15), written as scalar equations, are

$$u_{p_i}^0 = -\frac{1}{\rho_p}\left(\sqrt{\rho q_{r_i}}\, r_i + \sqrt{\rho(q_{v_i} + 2\sqrt{\rho q_{r_i}})}\, v_i\right)$$

$$u_{T_i}^0 = -\frac{1}{\rho_T}\left(\sqrt{\rho q_{r_i}}\, r_i + \sqrt{\rho(q_{v_i} + 2\sqrt{\rho q_{r_i}})}\, v_i\right)$$

$$\ddot{r}_i + \sqrt{\frac{q_{v_i}}{\rho} + 2\sqrt{\frac{q_{r_i}}{\rho}}}\,\dot{r}_i + \sqrt{\frac{q_{r_i}}{\rho}}\, r_i = 0$$

$$i = 1,2,3 . \qquad (19)$$

IV. CONCLUSIONS

The simple fixed coefficient linear feedback laws developed by optimal control theory enable the optimal relative motion to be described by an independent linear second-order differential equation in each of the three directions. The roots of the characteristic equation are

$$s_i = -\frac{1}{2}\left(\sqrt{\frac{q_{v_i}}{\rho} + 2\sqrt{\frac{q_{r_i}}{\rho}}} \pm \sqrt{\frac{q_{v_i}}{\rho} - 2\sqrt{\frac{q_{r_i}}{\rho}}}\right)$$

$$i = 1,2,3. \qquad (20)$$

A soft rendezvous (position, velocity, and acceleration of the two objects approach arbitrarily near each other as time increases) is assured by the asymptotic stability of the motion which comes from assigning positive values to q_{v_i}, q_{r_i}, and ρ. Unless the weighting factors are picked so that $q_{v_i} \geq 2\sqrt{\rho q_{r_i}}$, some of the roots will be complex, and the two bodies will rendezvous with an oscillating or spiraling motion. If the length of time required for the two objects to come within a specified distance apart is not prohibitive, low values of q_{v_i} and q_{r_i} are probably desirable. This can be seen from the cost function,

equation (5), by noting that a minimum effort criterion is approached as the q_{v_i} and q_{r_i} approach zero.

In this paper all forces were assumed to be acting through the centers of mass of the objects. The effects of torques can also be included in the Hamilton-Jacobi formulation, and a feedback law can be found by solving a matrix-Riccati equation similar to equation (12). The simplicity of the solution of the Riccati equation is lost, however, by introducing angular variables. With the increased complexity in solving the Riccati equation, it is probably best to analyze the system by a multivariable root square locus technique [6] before attempting to find a feedback law.

This paper illustrates a solution of a <u>cooperative</u> rendezvous problem; however, its formulation is sufficiently general to include a chase type rendezvous in which one craft is controlling its motion and the other is "coasting" (subject to external forces only). This special case can be obtained by taking the limit of equation (19) as ρ_T approaches infinity. With a slight modification of the original system the "coast" case can include a lunar soft landing problem. Removing the assumption that the acceleration f due to the external forces is the same on both objects, in the first equation of equations (2) we can set f = g, a constant gravitational acceleration acting on the landing craft, and f = 0 in the second equation of equations (2). By treating u_p -g as the control instead of u_p in first equation of equations (2) and using the Hamilton-Jacobi approach we obtain equations (19) with $u_{p_i}^0$ replaced by $u_{p_i}^0$ -g_i and $u_{T_i}^0$ = 0. Both the chase type rendezvous problem and the soft landing modification described in this paper should be compared with the results of Bryson [7], who solved a

similar rendezvous problem and a similar soft landing problem and obtained linear time-varying feedback laws. Bryson, however, assumed a fixed time, minimum effort criterion for the solution of his problems which explains the time-varying feedback laws for his problems.

REFERENCES

1. Kahne, Stephen J.: Optimal Cooperative State Rendezvous and Pontryagin's Maximum Principle. AFCRL-65-233, 1965.

2. Gieseking, D. L.: Control of Co-operative Systems: The Rendezvous Problem. Rept. R-218, Coord. Sci. Lab., Univ. of Ill., 1964.

3. Kalman, R. E.: Contributions to the Theory of Optimal Control. Bol. Sco. Mat. Mexicana, 1960, pp. 102-119.

4. Kalman, R. E.: The Theory of Optimal Control and the Calculus of Variations. Proc RAND-Univ. Calif. Symp. on Optimization Theory 1960, Chapt 16, Univ of Calif. Press, 1963.

5. Gilbert, E. G.: Controllability and Observability in Multivariable Control Systems. SIAM J. Control, 1963.

6. Rynaski, Edmund G.: The Multivariable Root Square Locus--An Optimal System Design Aid. AIAA Conference on Guidance and Control, Minneapolis, Minn., Aug. 1965.

7. Bryson, Arthur E.: Linear Feedback Solutions for Minimum Effort Interception, Rendezvous, and Soft Landing. AIAA J., Aug. 1965.

CALCULATION OF CONTROL GAINS WITH FILTERS FOR RIGID BODY MOTION OF A SPACE VEHICLE

By

William H. Beutjer

SUMMARY

The equations for calculating the control gains with filters for the rigid body motion of a space vehicle are derived. The control gains can be calculated for the drift-minimum condition and for conditions close to drift-minimum. A computer program, written to calculate the control gains for attitude control, accelerometer control, or angle-of-attack control, shows the effect of varying the location of the accelerometer, the damping, and the control frequency. The system considered for this analysis is the Saturn 504 vehicle. A comparative study of the control gains was made without filters and for a body-fixed accelerometer using two different filter configurations. The results are given in the form of plots of g_2 versus a_0, and g_2 versus a_1. Also included are plots which show how the control gains vary with frequency and time.

DEFINITION OF SYMBOLS

Symbol	Definition
a_0	gain factor of attitude channel
a_1	rate gain factor of attitude channel
A	real part of control root $= -\zeta\omega$
b_0	gain factor of angle-of-attack channel
B	imaginary part of control root $= \omega\sqrt{1-\zeta^2}$
$C_{z\alpha}$	normal lift coefficient
D_0	base diameter of vehicle
F_s	swivel thrust
F_T	total thrust
g_2	gain factor of accelerometer channel

Symbol	Definition
$\overline{g}$	longitudinal missile acceleration
I	vehicle moment of inertia
M_V	vehicle mass
q	dynamic pressure
s	complex control root (A + Bi)
T(s)	transfer functions
V	longitudinal velocity of missile
x_A	coordinate of accelerometer
x_{cg}	distance from gimbal plane to center of gravity
x_{cp}	distance from gimbal plane to center of pressure
y	lateral translation of rigid missile
α	angle of attack of rigid missile at center of gravity
β	engine deflection against missile center line
ϕ	rotation of rigid missile relative to space
ζ	damping ratio
ω	control frequency
ω_n	natural frequency
$\overline{x}_A$	$x_{cg} - x_A$
C_1	$\dfrac{x_{cg} - x_{cp}}{4I} \pi D_0^2 q\, C_{z\alpha}$

Symbol	Definition
C_2	$F_s\left(\dfrac{x_{cg}}{I}\right)$
K_1	$\bar{g}$
K_2	$\pi D_0^2 \, q \, C_{z\alpha}\left(\dfrac{1}{4M_V}\right)$
K_3	$\dfrac{F_s}{M_V}$

The dot appearing above symbols means differentiation with respect to time.

I. INTRODUCTION

The equations of motion of a space vehicle used in this report are taken from Research Review 1. The control equation is expressed as a coupling between the control system and the vehicle motions. The linear differential equations are then transformed into algebraic equations by using a differential operator, s, which is a symbol denoting the operation of differentiation with respect to the independent variable. These transformed equations, which lead to a characteristic equation, are then solved by matrix methods. Assuming a drift-minimum condition, the characteristic equation reduces to a relationship between the gains a_0, b_0, and g_2. The drift-minimum condition can be maintained by using accelerometer control for which $b_0 = 0$, or angle-of-attack control for which $g_2 = 0$.

These expressions for an ideal control system are straightforward; however, the inclusion of non-ideal control effects such as actuators and shaping networks lead to a much higher ordered characteristic equation. To calculate the control gains for these cases, the characteristic equation is solved by first substituting a known control root, which is a complex quantity, into the characteristic equation for the operator s values.

This leads to an equation with complex values a functions of the control gains. Setting the real and imaginary parts of the equation simultaneously to zero, we obtain two more equations for calculating the control gains. Using these two equations with the equation obtained from the drift-minimum condition, we can calculate the control gains for drift-minimum

control. When both the b_0 and g_2 terms are zero, the type of control is called "attitude" or "gyro" control. If b_0 is zero, it is called "accelerometer control"; if g_2 is zero, the expression "angle-of-attack control" is used. The b_0 and g_2 terms are not used simultaneously in the control system. Gains for cases other than drift minimum can be obtained by assuming a value for b_0 or g_2 and solving the two equations for the remaining control gains.

II. BASIC METHODS AND EQUATIONS

A. EQUATIONS OF MOTION

The standard rigid-body equations of motion used in this report are derived by Hoelker* and are shown below. (The terms are defined in the list of symbols.)

Angular motion

$$\ddot{\phi} + C_1 \alpha + C_2 \beta = 0 \tag{1}$$

Angular relationship

$$\alpha = \phi - \frac{\dot{y}}{V} \tag{2}$$

Lateral path motion

$$\ddot{y} = K_1 \phi + K_2 \alpha + K_3 \beta \tag{3}$$

B. CONTROL EQUATION

The control equation considers the engine deflection, β, in response to commands from a position-gyro, ϕ, the rate gyro, $\dot{\phi}$, and either the angle-of-attack, α, or the lateral acceleration, a_m, measured by an accelerometer. The β response is a linear combination of ϕ, $\dot{\phi}$, α and a_m and is of the form

$$\beta = a_0 \phi \, T_1(s) + a_1 \dot{\phi} \, T_2(s) +$$

$$g_2 a_m T_3(s) + b_0 \alpha T_4(s), \tag{4}$$

where

$$a_m = K_2 \alpha + K_3 \beta - \bar{x}_A \ddot{\phi}.$$

C. SOLUTION OF EQUATIONS

These equations will be solved by using the concept of a differential operator. By using the operator,

---

* Hoelker, R. F.: Theory of Artificial Stabilization of Missiles and Space Vehicle with Exposition of Four Control Principles. NASA TN D-555.

s, and its higher powers to represent the first and higher derivatives of the variables, the solution of these equations shows the characteristic equation to be of the form:

$$A_3 s^3 + A_2 s^2 + A_1 s + A_0 = 0,\qquad(5)$$

where

$$A_3 = 1 - g_2 (K_3 + C_2 \overline{x}_A) T_3(s)\qquad(6)$$

$$A_2 = a_1 C_2 T_2(s) + \frac{1}{V}(b_0 K_3 T_4(s) + K_2)$$

$$- g_2 \frac{\overline{x}_A}{V}(C_2 K_2 - C_1 K_3) T_3(s)\qquad(7)$$

$$A_1 = \left(\frac{a_1 T_2(s)}{V} + g_2 T_3(s)\right)(C_2 K_2 - C_1 K_3)$$

$$+ a_0 C_2 T_1(s) + b_0 C_2 T_4(s) + C_1\qquad(8)$$

$$A_0 = \left(\frac{a_0 T_1(s)}{V} - \frac{g_2 K_1 T_3(s)}{V}\right)(C_2 K_2 - C_1 K_3)$$

$$- \frac{K_1}{V}(b_0 C_2 T_4(s) + C_1).\qquad(9)$$

By setting filter transfer functions to one and assuming a drift-minimum condition which states that the constant term, A_0, of equation (5) is equal to zero, we obtain the following equation from equation (9):

$$a_0 \left[\frac{1}{K_1}\right] - b_0 \left[\frac{C_2}{D}\right] - g_2 - \frac{C_1}{D} = 0,\qquad(10)$$

where

$$D = C_2 K_2 - C_1 K_3.$$

We now nave an expression which relates a_0, b_0, and g_2. This condition requires the two gain values a_0 and g_2 (or a_0 and b_0) to satisfy only a linear relationship.

The transfer functions used in this report are of the following form:

$$T(s) = \frac{\sum\limits_{i=0}^{n} A_i s^i}{\sum\limits_{i=0}^{m} B_i s^i}.\qquad(11)$$

By using the assumed control root, s, we can reduce the transfer function to a complex number of the form X + Yi. Using this form for the transfer functions, the control filters can be represented by

$$T_1(s) = \text{Position Gyro Filter} = X_1 + Y_1 i\qquad(12)$$

$$T_2(s) = \text{Rate Gyro Filter} = X_2 + Y_2 i\qquad(13)$$

$$T_3(s) = \text{Accelerometer Filter} = X_3 + Y_3 i\qquad(14)$$

$$T_4(s) = \text{Angle-of-Attack Filter} = X_4 + Y_4 i.\qquad(15)$$

By substituting the known control root ($s = A+B_i$) and equations (12) through (15) into the characteristic equation and setting the real and imaginary parts equal to zero, we obtain the two following equations:

Real

$$a_0 [d_{11}X_1 - d_{12}Y_1] + a_1 [d_{21}X_2 - d_{22}Y_2] - g_2 [d_{31}X_3 - d_{32}Y_3]$$

$$+ b_0 [d_{41}X_4 - d_{42}Y_4] + [L + \frac{FK_2}{V} + AC_1 - \frac{K_1 C_1}{V}] = 0\qquad(16)$$

Imaginary

$$a_0 [d_{12}X_1 + d_{11}Y_1] + a_1 [d_{22}X_2 + d_{21}Y_2] - g_2 [d_{32}X_3 + d_{31}Y_3]$$

$$+ b_0 [d_{42}X_4 + d_{41}Y_4] + [M + \frac{GK_2}{V} + BC_1] = 0\qquad(17)$$

where

$$d_{11} = C_2 A + \frac{D}{V}, \quad d_{12} = BC_2$$

$$d_{21} = FC_2 + \frac{AD}{V}, \quad d_{22} = GC_2 + \frac{BD}{V}$$

$$d_{31} = EL - AD + \frac{D}{V}(F\overline{x}_A + K_1),\qquad(18)$$

$$d_{32} = EM - BD + \frac{GD\overline{x}_A}{V}$$

$$d_{41} = AC_2 + \frac{1}{V}(FK_3 - K_1 C_2),$$

$$d_{42} = BC_2 + \frac{GK_3}{V}.$$

$$\dot{E} = K_3 + C_2 \bar{x}_A, \quad F = \omega^2(2\zeta^2 - 1), \quad G = -2\zeta\omega^2\sqrt{1-\zeta^2}$$

$$L = \zeta\omega^3(3 - 4\zeta^2), \quad M = \omega^3(4\zeta^2 - 1)\sqrt{1 - \zeta^2}.$$

We now have the three equations, (10), (16), and (17), required to calculate gains with filters for either accelerometer or angle-of-attack control for the drift-minimum condition. To calculate the control gains off drift-minimum, we assume a value of g_2 or b_0 and then calculate a_0 and a_1 from equations (16) and (17).

For attitude control, equations (16) and (17) reduce to

$$a_0[d_{11}X_1 - d_{12}Y_1] + a_1[d_{21}X_2 - d_{22}Y_2]$$

$$+ \left[L + \frac{FK_2}{V} + AC_1 - \frac{K_1C_1}{V} \right] = 0 \qquad (19)$$

and

$$a_0[d_{12}X_1 + d_{11}Y_1] + a_1[d_{22}X_2 + d_{21}Y_2]$$

$$+ \left[M + \frac{GK_2}{V} + BC_1 \right] = 0. \qquad (20)$$

III. SYSTEM CONFIGURATION

The system considered for numerical results in this analysis is that of the SA-504 vehicle at t=75.117 and 83.633 sec. A comparative study of the control gains was made without filters and for a body-fixed accelerometer, using two different filter configurations called A-filters and B-filters. The control frequency was varied between 0.05 to 0.20 Hz, and the damping used was 0.3 and 0.7.

For the A-filter configuration, the accelerometer was located at $x_A = 41.4$ m and the coefficients of the numerator and denominator for the control filters (see equation (13)) are shown below.

Attitude Channel

$A_0 = 1.0$	$B_0 = 1.0$
$A_1 = 2.20 \times 10^{-1}$	$B_1 = 1.882 \times 10^{-1}$
	$B_2 = 3.963 \times 10^{-2}$
	$B_3 = 2.147 \times 10^{-3}$
	$B_4 = 1.279 \times 10^{-4}$
	$B_5 = 2.725 \times 10^{-7}$

Attitude Rate Channel

$A_0 = 1.0$	$B_0 = 1.0$
$A_1 = 9.049 \times 10^{-2}$	$B_1 = 3.368 \times 10^{-1}$
$A_2 = 6.355 \times 10^{-3}$	$B_2 = 5.880 \times 10^{-2}$
$A_3 = 1.664 \times 10^{-4}$	$B_3 = 7.301 \times 10^{-3}$
	$B_4 = 2.072 \times 10^{-4}$

Accelerometer Channel

$A_0 = 1.0$	$B_0 = 1.0$
$A_1 = 3.342 \times 10^{-1}$	$B_1 = 7.117 \times 10^{-1}$
$A_2 = 3.190 \times 10^{-2}$	$B_2 = 2.508 \times 10^{-1}$
$A_3 = 2.724 \times 10^{-3}$	$B_3 = 5.544 \times 10^{-2}$
$A_4 = 7.158 \times 10^{-5}$	$B_4 = 2.557 \times 10^{-3}$
	$B_5 = 3.089 \times 10^{-5}$

For the B-filters, the accelerometer was located at $x_A = 79.629$ m. The coefficients of the numerator and denominator for the control filters are shown below.

Attitude Channel

$A_0 = 1.0$	$B_0 = 1.0$

Attitude Rate Channel

$A_0 = 14.0$	$B_0 = 14.0$
	$B_1 = 7.5$
	$B_2 = 1.0$

Accelerometer Channel

$A_0 = 1.0$	$B_0 = 1.0$
	$B_1 = 20.0$

The figures indicate that plots of g_2 versus a_0 and a_1 are linear for the same frequency. A computer program, written to assist in the calculation of the control gains, consists of first reducing the control filters to the form $X_i + Y_i$. The filters are put in the program by entering the coefficients, A_i and B_i, of the transfer functions. Then, the control gains are calculated for as many time points as required. The appropriate data must be input for each time point desired. The program is capable of calculating the control gains for attitude control, accelerometer control, or angle-of-attack control.

IV. DISCUSSION OF RESULTS

First, we will consider what effect various parameters have on the control gains without filters at $t = 75.117$ sec. Figures 1 and 2, which are plots of g_2 versus a_0, show the effect of varying the location of the accelerometer, x_A, for $\zeta = 0.7$. As x_A increases, the slope of the constant frequency lines also
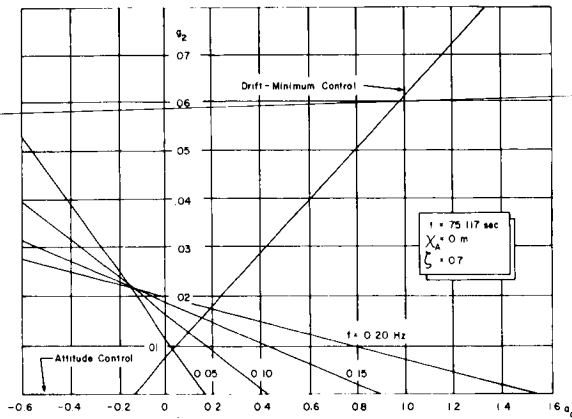

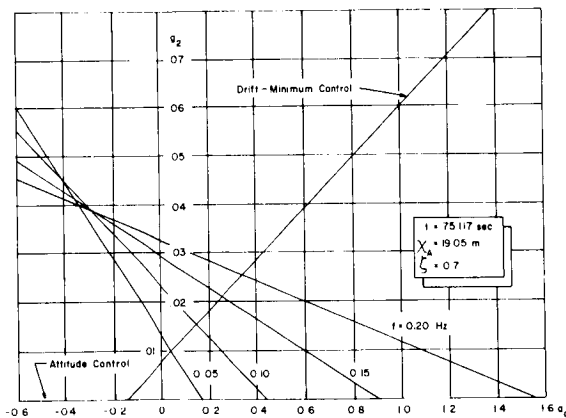FIGURE 1.   PLOT OF g_2 VERSUS a_0 WITHOUT
FILTERS

FIGURE 2.   PLOT OF g_2 VERSUS a_0 WITHOUT
FILTERS

increases.   The plot of g_2 versus a_0 for drift-minimum control is a straight line.   Therefore, as the location of the accelerometer, x_A, increases, the values of g_2 and a_0 also increase   for the drift-minimum condition.   Notice that when g_2 equals zero, the abscissa

of each figure indicates the value of a_0 for attitude control for the various frequencies under consideration.   Varying ζ from 0.7 to 0.3 has almost no effect on the value control gains (a_0 and g_2).

Figures 3 and 4 are plots of g_2 versus a_1 for $\zeta = 0.7$.   By increasing the value of x_A, we again see that the slope of the constant frequency lines increase. It is interesting to note that, for drift-minimum control, the plot of g_2 versus a_1 is no longer a linear relationship.
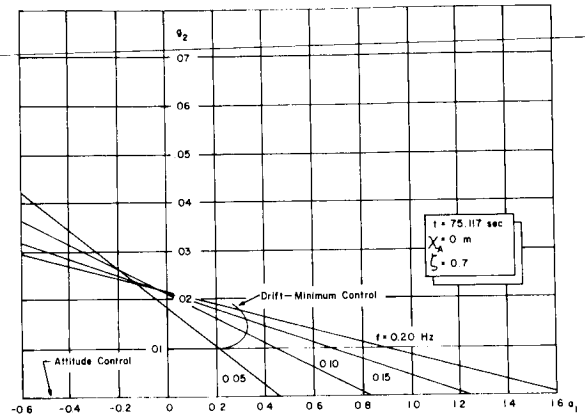

FIGURE 3.   PLOT OF g_2 VERSUS a_1 WITHOUT
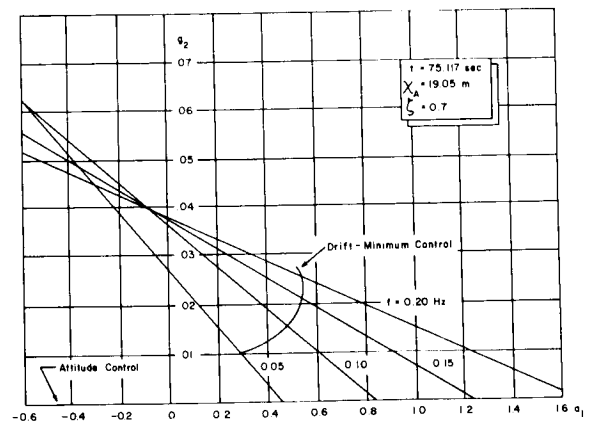FILTERS

FIGURE 4.   PLOT OF g_2 VERSUS a_1 WITHOUT
FILTERS

Figures 1 through 4, which show the case without filters, indicate that there is a region where the control gains are independent of the frequency.   To

explain this mathematically, we will examine the equations of motion. For the case without filters, using accelerometer control, we see that

$$T_1(s) = T_2(s) = T_3(s) = 1$$

$$T_4(s) = b_0 = 0.$$

Now by putting these values in equation (4) and then substituting α (equation (2)) and β (equation (4)) into equation (1), the system can be reduced to the following:

$$\ddot{\phi} + \left[\frac{a_1 C_2}{1 - g_2(K_3 + C_2 \overline{x}_A)} \right] \dot{\phi}$$

$$+ \left[\frac{C_1 + C_2 a_0 + g_2(C_2 K_2 - C_1 K_3)}{1 - g_2(K_3 + C_2 \overline{x}_A)} \right] \phi$$

$$= \frac{\dot{y}}{V} \left[\frac{C_1 + g_2(C_2 K_2 - C_1 K_3)}{1 - g_2(K_3 + C_2 \overline{x}_A)} \right] . \qquad (21)$$

Equation (21), which is usually considered as describing the rotational behavior of the missile about its center of gravity, is of the form

$$\ddot{\phi} + 2\zeta \omega_n \dot{\phi} + \omega_n^2 \phi = F(t). \qquad (22)$$

By comparing equations (21) and (22), we obtain the natural frequency by letting

$$\omega_n^2 = \frac{C_1 + C_2 a_0 + g_2(C_2 K_2 - C_1 K_3)}{1 - g_2(K_3 + C_2 \overline{x}_A)} . \qquad (23)$$

Then, by rearranging terms, we get

$$C_1 + C_2 a_0 + g_2(C_2 K_2 - C_1 K_3)$$

$$+ \omega_n^2 [g_2(K_3 + C_2 \overline{x}_A) - 1] = 0. \qquad (24)$$

If a_0 and g_2 are to be independent of the frequency, ω_n, it is apparent from equation (24) that the coefficient of the ω_n^2 term must be equal to zero. Therefore,

$$g_2(K_3 + C_2 \overline{x}_A) - 1 = 0, \qquad (25)$$

or

$$g_2 = \frac{1}{K_3 + C_2 \overline{x}_A} , \qquad (26)$$

and

$$a_0 = \frac{g_2}{C_2} (C_1 K_3 - C_2 K_2) - \frac{C_1}{C_2} . \qquad (27)$$

We see that equations (26) and (27) are independent of the damping, ζ. This is another way of observing that the damping has little effect on the value of the control gains (a_0 & g_2).

Using the input data for $t = 75.117$ sec and $x_A = 19.05$ m, we find that $g_2 = 0.0381$ and $a_0 = -0.241$, from equations (26) and (27), respectively. These values agree closely with the values shown in Figures 2 and 3. We must keep in mind that, even though equations (26) and (27) do predict the region where the control gains are independent of the frequency, they are only approximations.

Next, we will consider the effect on the control gains of using two different filter configurations. Figures 5 and 6 are plots of the control gains using the A-filter configuration for $\zeta = 0.7$ and $x_A = 41.4$ m. Figure 5, which shows g_2 versus a_0 at $t = 75.117$ sec, displays a good separation between the constant frequency lines. For this filter configuration, we notice that there is little change in the control frequency for small changes in a_0, and the good separation of the frequency lines makes the value of the control frequency easy to determine. The effect of
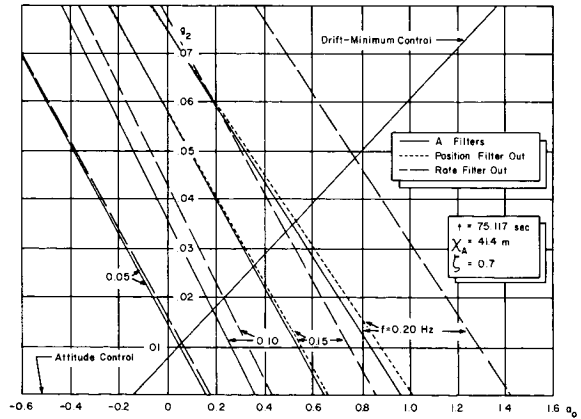

FIGURE 5.   PLOT OF g_2 VERSUS a_0 FOR A FILTERS

removing the different filters is also shown on this figure. With the position filter out, the change in the control gains is so small for the lower frequencies that it is not possible to plot. However, at a frequency of 0.15 and 0.20 Hz, we can begin to see that

the frequency lines move to the right a very small amount without the position filter. Removing the rate filter causes the constant frequency lines to move considerably to the right. Again the change is less for the lower frequencies than it is for the higher frequencies. The relationship between g_2 and a_1 is shown in Figure 6. Here, as in the case without filters, the drift-minimum line shown is only for the case with the complete A-filter configuration. As the filters are removed, the position of the drift-minimum line changes much in the same manner as Figure 5.
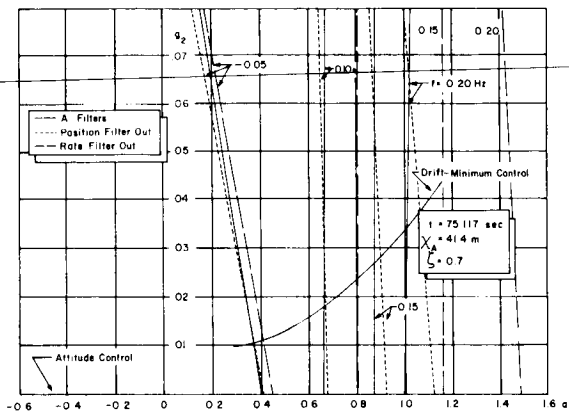
FIGURE 6. PLOT OF g_2 VERSUS a_1 FOR A FILTERS

Values of the control gains using the B-filter configuration are plotted on Figures 7 and 8 for $\zeta = 0.7$, $x_A = 79.629$ m. and t = 75.117 sec. Figure 7 is a plot of g_2 versus a_0 and shows that a_0 remains fairly constant for the same frequency. In other words, g_2 versus a_0 plots as nearly vertical lines. This trend is desirable as long as there is a good separation between the control frequencies. However, this separation is not apparent for this filter configuration especially at the higher frequencies. We also observe that for small changes in a_0 the control frequency change is significant, and for some values of a_0 versus g_2, it becomes difficult to determine the true value of the control frequency. This is because the control frequency of 0.20 Hz plots between 0.10 and 0.15 Hz. Removing the rate-gyro filter changes the control gains considerably just as in the case for the A-filters. Figure 8 shows the relationship of g_2 versus a_1 at t = 75.117 sec.

Figures 9, 10, and 11 are plots of the control gains versus frequency for drift minimum condition using accelerometer control at t = 75.117 sec. The
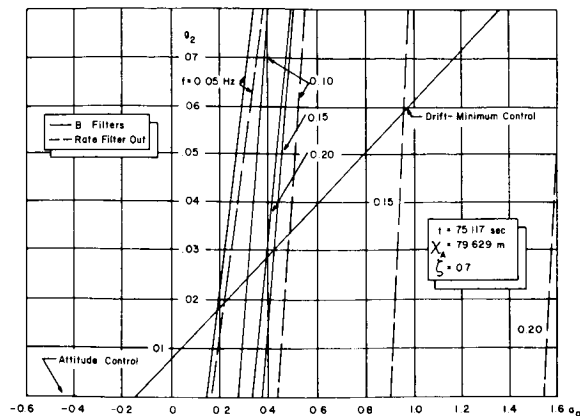

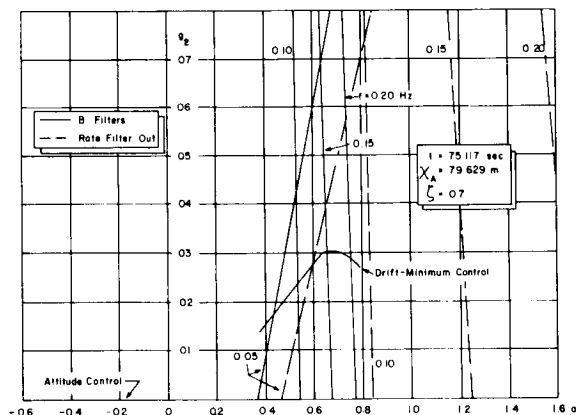FIGURE 7. PLOT OF g_2 VERSUS a_0 FOR B FILTERS

FIGURE 8. PLOT OF g_2 VERSUS a_1 FOR B FILTERS

damping used was $\zeta = 0.7$; the location of the accelerometer was based on stability considerations. These figures indicate how the control gains vary by adding the two different filter configurations.

Figures 12, 13, and 14 show how the control gains vary with time for drift-minimum condition using accelerometer control. The control damping was $\zeta = 0.7$ and the frequency used was 0.05 and 0.20 Hz. These figures show a comparison between the A-filters, B-filters, and the case without filters.

The program developed here can be used to investigate rigid body control gains for any vehicle configuration. Other parameters could be varied, and the effect of these changes on the control gains
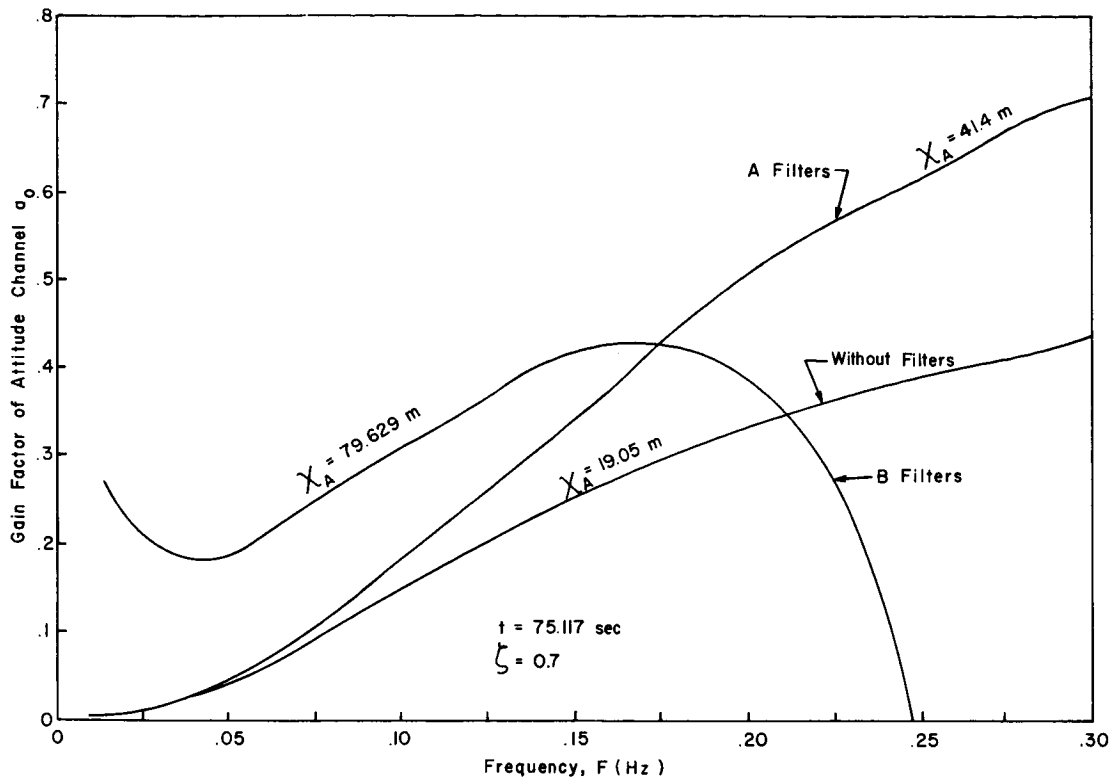
90

FIGURE 9.   PLOT OF a_0 VERSUS F FOR DRIFT MINIMUM USING ACCELEROMETER CONTROL
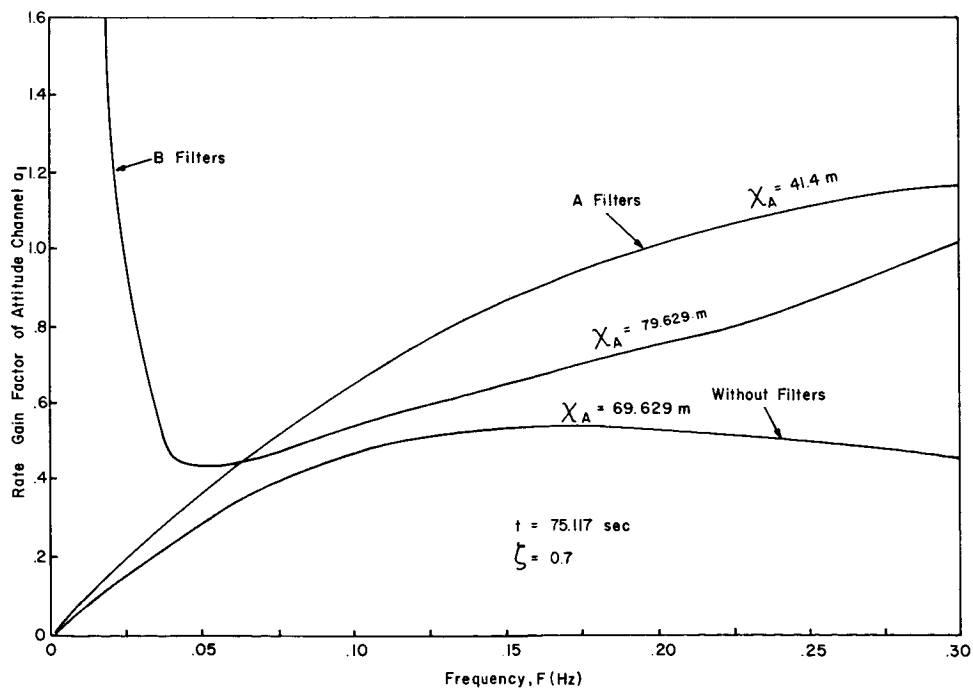

FIGURE 10.   PLOT OF a_1 VERSUS F FOR DRIFT MINIMUM USING ACCELEROMETER CONTROL
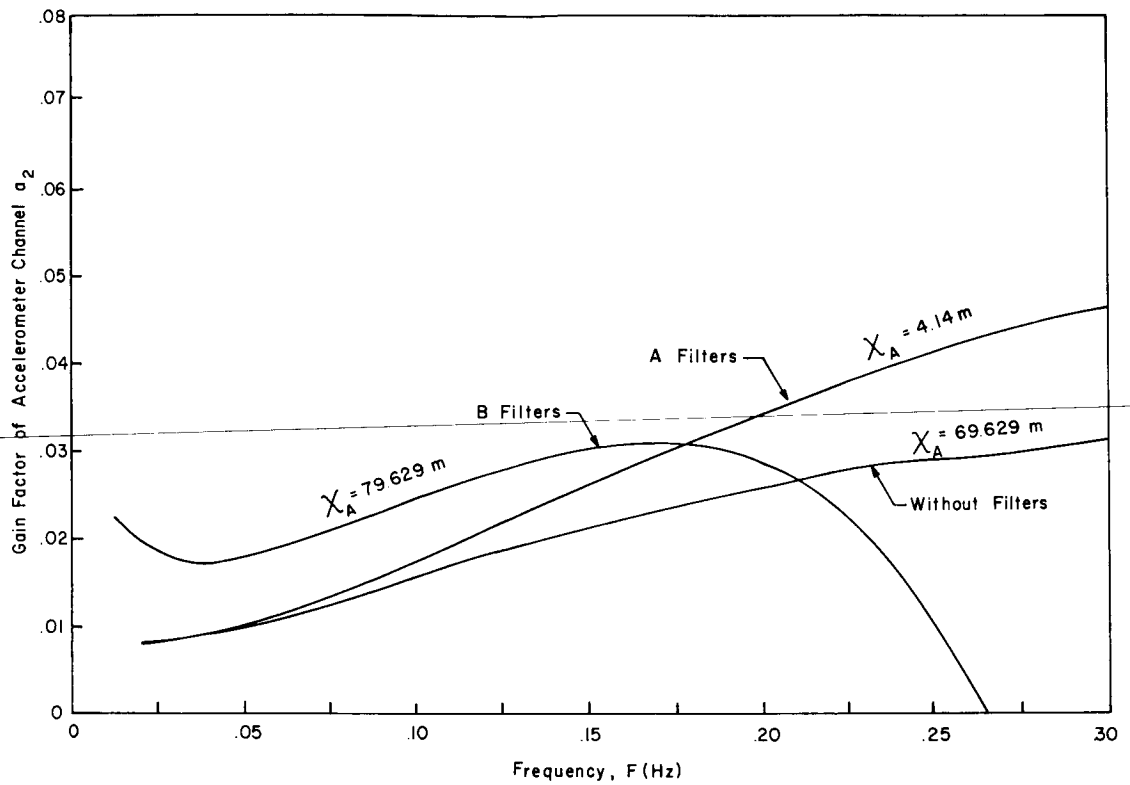
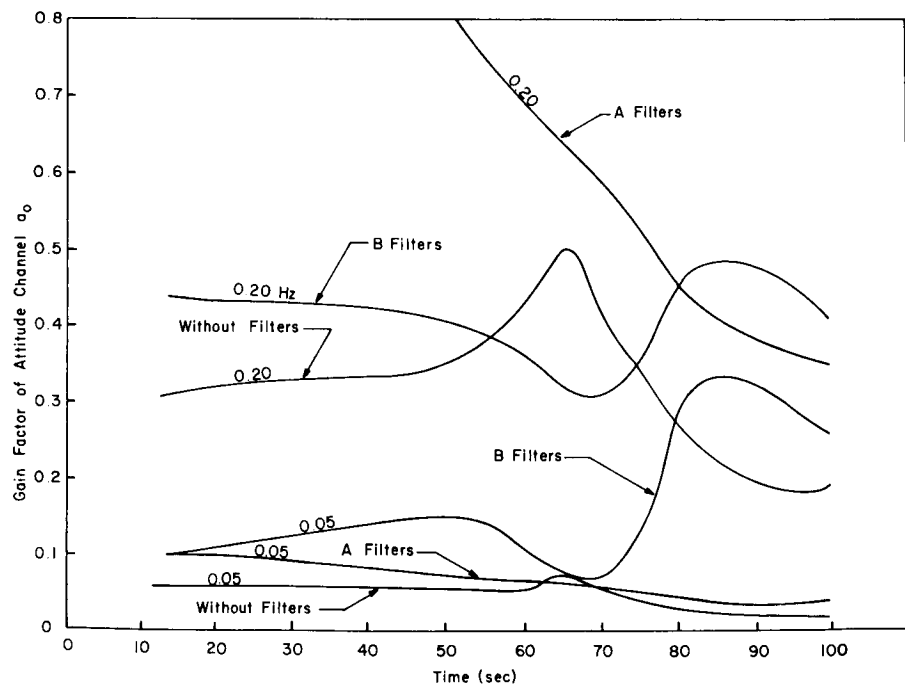FIGURE 11. PLOT OF g_2 VERSUS F FOR DRIFT MINIMUM USING ACCELEROMETER CONTROL

FIGURE 12. a_0 VERSUS TIME FOR DRIFT MINIMUM USING ACCELEROMETER CONTROL
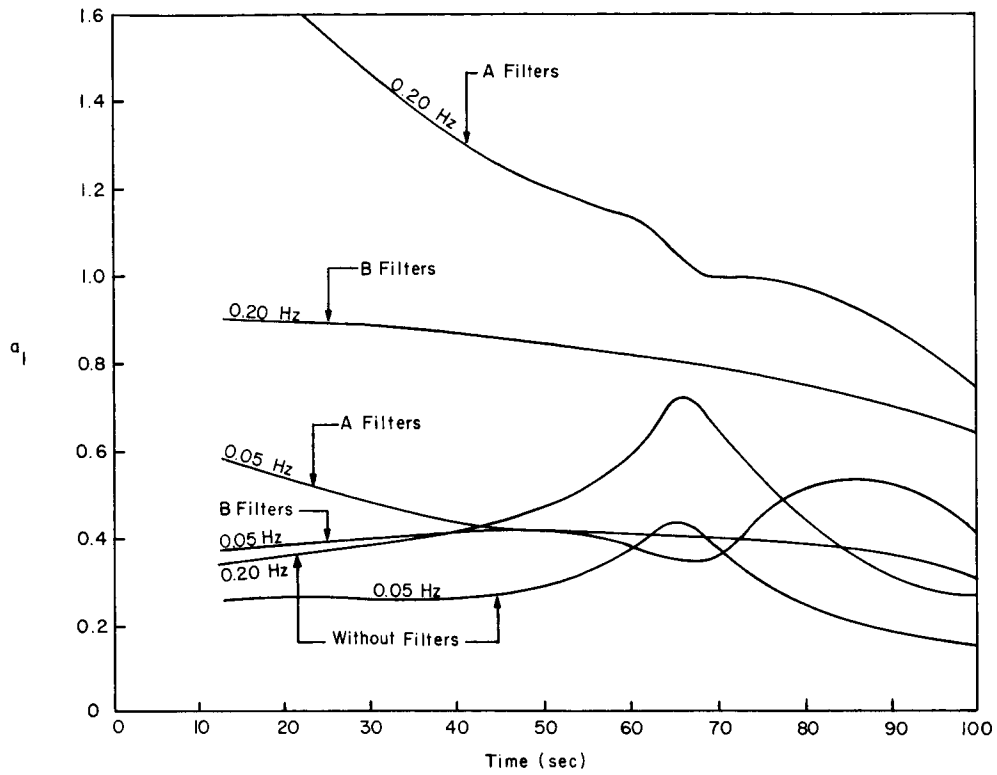
FIGURE 13. a_1 VERSUS TIME FOR DRIFT MINIMUM USING ACCELEROMETER CONTROL
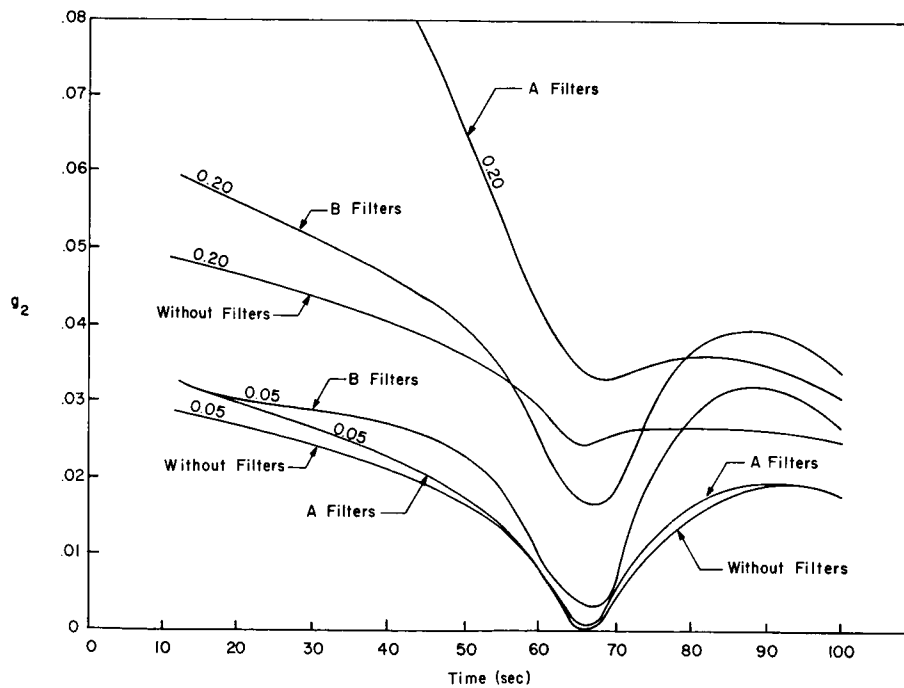
FIGURE 14. g_2 VERSUS TIME FOR DRIFT MINIMUM USING ACCELEROMETER CONTROL

could be studied. This study of the Saturn V vehicle is only an example of some of the knowledge that can be gained by studies of this type.

A study is now being made which includes the bending vibration and propellant sloshing. The results will be compared with this report to determine what effect bending vibration and sloshing have on the control gains.

V. ELECTROMAGNETIC THEORY

ON THE MOTION OF CONDUCTORS IN A MAGNETIC FIELD

By

W. H. Heybey

SUMMARY

In this paper the movements within a magnetic field of certain conducting configurations are studied on the basis of fundamental electromagnetic theorems. The field vector is not allowed to vary with time; if it varies in space, the motion of a loop is alone describable without extraordinary complications. Less involved relations are developed holding in a homogeneous field. It is shown that such a field has no effect on the translatory motion; the rotatory motion is retarded in general, although in special circumstances it may continue undisturbed. A principle of maximum retardation is introduced to define the systems of induced currents in two-dimensional bodies. It is applied to closed shells, with the sphere as simplest example, and to the circular disc. The motion of the latter is also studied when in addition the surface is subjected to the pressure of sunlight and is carrying an electric charge. The presence of the charge alone, if of constant density, would cause the mass center to wander on a spiral about a field line, while the disc performs a gyroscopic motion about shifting axes through the mass center.

I. INTRODUCTION

In keeping with the review character of this volume, it seems warranted to dispense with mathematical formulations whenever they can be spared without obscuring the argument of foregoing key relations. Derivations are largely omitted except those clarifying in what manner the results obtained are linked to basic electrodynamics. For a rapid exposition, use has been made of vector-analytic concepts and identities.

In general, vectors will be marked by underlining, aside from common unit vectors, as follows: i', j', k' on the axes (x, y, z) of a space-fixed rectangular Cartesian system; i, j, k on the (ξ, η, ζ)-axes of the principal moments of inertia. Dot and cross products are often indicated by parentheses and brackets, respectively. Thus,

$$ i \cdot \underline{B} \equiv (i\underline{B}) $$

is the component of the electromagnetic induction, $\underline{B}$, on the ξ-axis, and

$$ \underline{\omega} \times \underline{r} \equiv [\underline{\omega r}] $$

denotes the circumferential velocity a point has in a body that rotates with the angular velocity, $\underline{\omega}$, about an axis passing through the mass center, G. The position vector $\underline{r}$ connects G with the body point, P.

The total velocity of P includes the translational velocity, u, of the mass center and may be written as

$$ \underline{v} = \underline{u} + [\underline{\omega r}] . \qquad (1) $$

The force acting on a closed wire (loop) in the field $\underline{B}$ is mathematically represented as a line ("round") integral summing up the elemental forces on the directed length elements, d$\underline{s}$, of the wire. As such, it can also be described as a surface integral; Stokes' theorem states that, with any integrable vector field, $\underline{V}$, it holds that

$$ \oint \underline{V} \cdot d\underline{s} = \int \underline{n} \cdot \text{curl } \underline{V} \, dS . \qquad (2) $$

The shapes of the loop and the area it bounds are immaterial, so that, in particular, the normals (unit vectors $\underline{n}$) of the surface elements, dS can be assigned any directions one may find convenient.

A variant of the theorem, formulated for a scalar function, is also useful:

$$ \oint \varphi \, d\underline{s} = \int [\underline{n} \text{ grad } \varphi] \, dS . \qquad (3) $$

For simplicity it is assumed that all properties of matter are constant, such as mass density (ρ), specific conductance (σ) and the permeability (μ) of the surrounding nonconducting medium. The field strength, $\underline{H}$, then is proportional to the induction:

$$ \underline{B} = \mu \underline{H} $$

The electromagnetic system of units will be used throughout.

II. EFFECT OF A TIME-INVARIANT MAGNETIC FIELD ON THE MOTION OF A RIGID CONDUCTING WIRE

The basic force law is commonly derived for a fixed loop in which a current of constant strength, I, is flowing:

$$\underline{F}_i = -I \oint \underline{B} \times d\underline{s}. \tag{4}$$

The index i refers to the induction process which causes the force to act on the wire. The elemental vector, $d\underline{s}$, indicates the local direction of the current. Since expression (4) is a line integral, the wire's cross section must be viewed as quasi-infinitesimal. Indeed, the derivation from Biot and Savart's law makes it necessary that the distance from a wire element to a point outside it is a well defined quantity.

It should be recalled that, with constant conductance, a current of constant strength can exist only with constant cross section. If it changed from station to station along the wire, the symbol I would have to be shifted under the integral sign.

The wire will also experience the torque.

$$\underline{M}_i = -I \oint \underline{r} \times [\underline{B} \, d\underline{s}], \tag{5}$$

which, in a free loop, would bring on a rotatory motion about the mass center.*

In our case the current does not issue from a generator or battery, but comes into being through the motion of the loop which sets up a tension in it. The velocity in turn is worked on by the force and moment it creates. Thus, a kind of feedback system is in operation.

It is necessary to find the strength of that current.

If the magnetic field does not vary in time, and if the loop is not deformable, the induced tension is given by the expression

$$U = \oint [\underline{v} \, \underline{B}] \cdot d\underline{s}. \tag{6}$$

This round integral can be permanently zero when the loop moves parallel to the lines of a homogeneous

---

* This torque (rather than the force) is driving the electric motor.

field $\underline{B}$. In such a case there exists neither force nor torque on the wire. Otherwise, a current will spring up in the loop according to Ohm's law:

$$IR = U - L \, \frac{dI}{dt}, \tag{7}$$

where R and L are the resistance and self-inductance of the wire. The presence of a force and torque is now assured causing the velocity, $\underline{v}$, to change, so that both U and I are functions of time. However, the self-inductance is usually very small for a single wire loop. Except in switching-on processes, the last term in relation (7) can be safely neglected. The field has been already introduced as time-independent; if, in addition, we exclude any abrupt local changes as well as any sudden variations in the velocity, $\underline{v}$, such processes need not be considered, since I will be a slowly varying function of time. Expression (7) then becomes an integral law yielding immediately the current strength I(t), once U(t) has been computed for a given value of $\underline{v}$(t). Nevertheless, determining the motion is still very laborious, requiring a stepwise procedure. Three numerical quadratures must be performed at each step, and a system of six second-order differential equations must be handled to arrive at new values for $\underline{u}$ and $\underline{\omega}$, for position and attitude, and for U and T. In addition, single cases only can be treated that way, and general conclusions will be hard to come by. In dealing with shells and discs the difficulties grow all but insurmountable, as will be seen in later sections.

The burden is vastly alleviated even then if the vector $\underline{B}$ can be considered invariant in space, too. This will be taken for granted in all that follows.

III. EFFECT OF A HOMOGENEOUS FIELD ON THE WIRE MOTION

Significant results evolve here almost immediately. Since the translational velocity in the expression (1) is the same at all wire points, one finds that the first summand in the integral (6):

$$\oint [\underline{u} \, \underline{B}] \cdot d\underline{s} = [\underline{u} \, \underline{B}] \cdot \oint d\underline{s} = 0.$$

The round integral is zero according to identity (3), as $\varphi \equiv 1$ here. The velocity, $\underline{u}$, does not contribute to the induced tension U (the number of field lines passing through the loop's interior remains constant as far as the motion is translatory).

The force integral (4) also vanishes:

$$\underline{F}_i = -I \, B \times \oint d\underline{s} = 0,$$

and the translational velocity remains unchanged. In a homogeneous field, it suffices to consider the rotatory motion alone. It is then feasible and convenient to halt the translation completely, so that the origin of the space-fixed system can be made to coincide with that of the body-fixed system (at the mass center). This can be done even if the translation should be accelerated or decelerated by some other force, such as gravity.

The angular velocity, $\underline{\omega}(t)$, again is the same vector for all points of the wire. The vector identity

$$[\underline{\omega}\,\underline{r}] \times \underline{B} = (\underline{B}\,\underline{\omega})\,\underline{r} - \underline{\omega}\,(\underline{B}\,\underline{r})$$

then leads to

$$U = \oint \left\{ [\underline{\omega}\,\underline{r}] \times \underline{B} \right\} \cdot d\underline{s}$$

$$= (\underline{B}\,\underline{\omega}) \oint \underline{r} \cdot d\underline{s} - \underline{\omega} \cdot \oint (\underline{B}\,\underline{r})\, d\underline{s}.$$

Considering that the curl of a position vector is zero and that, with $\underline{B} = $ const.,

$$\text{grad}\,(\underline{B}\,\underline{r}) = \underline{B}\,,$$

we see, on applying Stokes' transformations (2) and (3), that the expression for U can be set into either of two forms:

$$U = -\underline{\omega} \cdot \oint (\underline{B}\,\underline{r})\, d\underline{s} = -\underline{\omega} \cdot \oint [\underline{n}\,\underline{B}]\, dS. \qquad (8)$$

With a homogeneous field, the unknown angular velocity stands in front of integrals that are vectors depending on the loop geometry only. The second form is especially convenient if the loop area is plane ($\underline{n} = $ const.); this, however, is not required.

A similar simplification takes place in the expression (5) of the acting moment. The same vector identity can be used to write it:

$$\underline{M}_i = -I \left\{ \underline{B} \cdot \oint \underline{r} \cdot d\underline{s} - \oint (\underline{B}\,\underline{r})\, d\underline{s} \right\}.$$

The first integral again is zero, and the second can be transformed into a surface integral, so that

$$\underline{M}_i = I \oint (\underline{B}\,\underline{r})\, d\underline{s} = I \int [\underline{n}\,\underline{B}]\, dS. \qquad (9)$$

It is now seen that, in a homogeneous field, the integral vectors in the expression for U have the direction $\underline{m}$ of the moment $\underline{M}_i$. When A denotes the absolute value of these integrals, we may write

$$U = -(\underline{\omega}\,\underline{m})\,A \quad \text{and}$$

$$\underline{M}_i = I\,A\,\underline{m}.$$

If in Ohm's law (7) the self-inductance is neglected,

$$\underline{M}_i = -\frac{1}{R}\,A^2\,(\underline{\omega}\,\underline{m})\,\underline{m}. \qquad (10)$$

Scalar multiplication by $\underline{\omega}$ shows that $\underline{\omega} \cdot \underline{M}_i$ is always negative, so that the vectors $\underline{\omega}$ and $\underline{M}_i$ form an obtuse angle, making the projection of $\underline{M}_i$ on $\underline{\omega}$ antiparallel to $\underline{\omega}$. Hence, the torque seeks to reduce the velocity through which it is created, in accordance with Lenz's rule. (The component of $\underline{M}_i$ normal to $\underline{\omega}$ affects the direction of $\underline{\omega}$ only). The moment is proportional to the square of the field strength and inversely proportional to the wire resistance. A better conductor experiences a stronger damping, other things being equal.

Let T_a, T_b, T_c be the loop's (or any other body's) principal moments of inertia corresponding to the (ξ, η, ζ)-axes of the body-fixed system, in which Euler's equations are set up:

$$\begin{cases} M_\xi = T_a\,\dot{\omega}_\xi - (T_b - T_c)\,\omega_\eta\,\omega_\zeta \\ M_\eta = T_b\,\dot{\omega}_\eta - (T_c - T_a)\,\omega_\zeta\,\omega_\xi \\ M_\zeta = T_c\,\dot{\omega}_\zeta - (T_a - T_b)\,\omega_\xi\,\omega_\zeta. \end{cases} \qquad (11)$$

The components M_ξ, M_η, M_ζ are those of the torque (10) plus those of other torques that might be present. The moment of the gravitational force is small for a freely moving loop (unless extraordinarily extended, so that the gravity field may have to be considered inhomogeneous). Dotting, as usual, denotes derivation with respect to time.

Closed solutions of the system (11) are obtainable with special settings, one of which will be used here for a first orientation.

Let the loop be a plane curve (without double points). If the common normal $\underline{n}$ then makes the angle ϑ with the field vector, it follows from the second expression (8) that

$$U = \mp\,BS \sin \vartheta\,(\underline{m}\,\underline{\omega}),$$

where B is the magnitude of the induction $\underline{B}$, and S is the area enclosed by the loop. Likewise,

$$\underline{M}_i = \pm\,I\,BS \sin \vartheta\,\underline{m}.$$

By the torque expression (9) the vector $\underline{m}$ is orthogonal both to $\underline{n}$ and $\underline{B}$. It is therefore feasible to orient the loop-normal such that $\underline{m}$ is identical with $\underline{i}$. This done, let us assume that the initial rotation

-is also in the i-direction. Finally, additional moments are not admitted.

The torque then cannot change the direction of $\underline{\omega}$, so that forever $\omega_\eta = \omega_\zeta = 0$ and $M_{i,\zeta} = M_{i,\eta} = 0$. Euler's system reduces to

$$M_{i,\xi} \equiv -\frac{B^2 S^2}{R} \sin^2 \vartheta \; \omega_\xi = T_a \dot{\omega}_\xi \; .$$

The motion remains a rotation* about the ξ-axis; it therefore is described by the variation of the angle $(\omega_\xi = \dot{\vartheta})$. Putting

$$\frac{B^2 S^2}{R T_a} = a^2 \; ,$$

we see that ϑ obeys the differential equation

$$\ddot{\vartheta} + a^2 \dot{\vartheta} \sin^2 \vartheta = 0 \qquad (12)$$

which has the first integral

$$\dot{\vartheta} = -\frac{a^2}{2}(\vartheta - \sin\vartheta \cos\vartheta) + \text{const.} \qquad (13)$$

The constant is zero with suitable initial conditions $\vartheta = \vartheta_o$, $\dot{\vartheta} = \dot{\vartheta}_o$. Equation (13) then shows that, with $\vartheta_o > 0$, the change of ϑ always goes to smaller values. If we restrict ourselves to the last phases of the process, the equation simplifies into

$$\dot{\vartheta} = -\frac{a^2}{3}\vartheta^3 + \frac{a^2}{15}\vartheta^5 \pm \ldots \qquad (14)$$

With the fifth-power term neglected, further integration gives

$$a^2 t = \frac{3}{2}\left(\frac{1}{\vartheta^2} - \frac{1}{\vartheta_o^2}\right) \; . \qquad (15)$$

For $t \to \infty$: $\vartheta \to 0$, $\dot{\vartheta} \to 0$, $\ddot{\vartheta} \to 0$; the motion has come to a complete standstill. In principle, the same result appears with any other initial value of $\dot{\vartheta}$, except that the final value of ϑ is no longer zero.

Equation (12) differs from the standard equation for an aperiodic process by the presence of the factor $\sin^2 \vartheta$. With such a process, too, the velocity tends to zero for $t \to \infty$.

If the same problem is handled including the effect of self-inductance, the first integral becomes

───────────────
* More general motions are studied in a later section.

$$\dot{\vartheta} = \frac{-a^2}{3}\vartheta^3 + \frac{a^2}{15}\left(1 - 4\frac{L}{R}a^2\right)\vartheta^5 \pm \ldots \; .$$

When compared to expression (14) this result shows that self-inductance tends to keep $|\dot{\vartheta}|$ larger, i.e., enhances the braking process, but that its contribution is rather unimportant, at least in the final stages of the motion. From general principles, self-inductance should seek to stem the dwindling of the current, thus making for larger torques and more effective braking. This tendency is seen here to outweigh the ensuing counteracting tendency through feedback, although not to any great extent.

IV. MOTION OF A CLOSED CONDUCTING SHELL IN A HOMOGENEOUS MAGNETIC FIELD

Expression (6) requires the shell to be rigid. (Otherwise, an additional term would appear at right.) For application of the force and torque formulas (4) and (5), it is necessary to define current paths or tubes in the shell that are comparable to thin wires of uniform cross section. Mutual inductance which, like self-inductance, is proportional to $\frac{dI}{dt}$, will be neglected.

When the force expression (4) is derived from the energy balance set up with a virtual displacement of the wire, the contribution of the magnetic field created by the current itself vanishes in explicit terms, while that of the undisturbed outside field stays on (which is described by the distribution of the vector $\underline{B}$). This happy circumstance enables us to calculate the forces and torques acting simultaneously on any number of loops without regard to their own fields, i.e., as if they existed singly (mutual inductance being neglected).

As a consequence, the translation of the shell is not affected; there is only a torque pulling on it, whatever the current paths may be.

We will adopt the principle that every current tube seeks to arrange itself such that the induced tension waxes as large as possible. This could be called a principle of maximum effect.* Path crossings will not be permitted. For example, with spherical shells, meridians do not appear as suitable paths, aside from the fact that a shell slice could not be given a uniform cross section (it would be zero at the poles).

───────────────
* Jeans (Math. Theory of Electricity and Magnetism) substitutes the current strength for the tension. The latter is preferred here since it is the more fundamental quantity.

The triple scalar product appearing in the second expression (8) assumes its largest value if the three vectors are mutually perpendicular. The vectors $\underline{\omega}$ and $\underline{B}$ will make any angle during the rotatory motion, but the unit vector $\underline{n}$ can be made normal to both. Thus, it will be defined as

$$\underline{n} = \frac{[\underline{B}\,\underline{\omega}]}{c} \, , \tag{16}$$

where the symbol c stands for the absolute value of the cross product in the numerator. Since $\underline{B}$ and $\underline{\omega}$ are constants for the integration, the surfaces enclosed by the paths are defined as plane and their shape is known; they are closed shell sections parallel to the plane determined by the (constant) field vector and the instantaneous angular velocity vector.

Expression (8) may now be put into the simpler form:

$$U = -\underline{\omega} \cdot [\underline{n}\,\underline{B}] \, S \tag{17}$$

where S is the section area.

If the space-fixed k'-direction is chosen parallel to $\underline{B}$ (as we are free to do in a homogeneous field), introduction of the vector $\underline{n}$ into the expression (17) yields

$$U = -c \, S.$$

Likewise, the second form of the torque (9) goes into

$$\underline{M}_i = I \, \frac{B^2}{c} \, S \, (i' \omega_x + j' \omega_y) \, ,$$

when ω_x, ω_y, ω_z denote the components of the vector $\underline{\omega}$ in the space-fixed system. With $I\,R = U$ one obtains

$$\underline{M}_i = - \frac{1}{R} \, B^2 \, S^2 \, (i' \omega_x + j' \omega_y) \, .$$

At any given instant the section normal $\underline{n}$ is the same for all tubes which are therefore all parallel, so that each can be given a constant differential width, db. If the thickness, h, of the shell is also constant, the differential cross section, h db, will be constant as required. A tube of length λ will have the resistance,

$$R = \frac{\lambda}{\sigma \, h \, db} \, ,$$

so that the expression for $\underline{M}_i$, now more properly written as a differential, assumes the final form

$$d\underline{M}_i = - \frac{\sigma h}{\lambda} \, B^2 \, S^2 \, (i' \omega_x + j' \omega_y) \, db \, . \tag{18}$$

The total torque, as any of its elements (18), will lie in the plane that is normal to the field and contains the mass center G. The integration over the shell surface must be performed at the instantaneous value of $\underline{\omega}$ after introducing a common parameter expressing λ, S, and db. The lengths and areas of the current paths will often be different at different instants, so that the integration may have to be repeated at every step of the solution process. Euler's equations require one to find the components of $\underline{M}_i$ in the (ξ, η, ζ) -system and, of course, to determine the principal moments of inertia.

Some of these calculations may prove to be difficult to do even with rather simple shell forms. For instance, the circular cylinder or the two-axial ellipsoid almost always call for the use of elliptic integrals when computing $\underline{M}_i$. With spherical shells, however, the task is quite easy, as will be seen in the next section.

It should be kept in mind that expression (18) is valid with $\underline{B}$ = const. only. In an unhomogeneous field, one would have to return to the original expression (6) for the induced tension and determine those nonintersecting curves on the surface that, given their lengths, maximize the integral, in which $\underline{r}$ and $\underline{B}$ are functions of two independent variables. (The third space variable is fixed by the surface equation.) This promises to be a problem of major dimensions, perhaps unsolvable altogether.

V. MOTION OF A SPHERICAL SHELL

The current paths here are circles parallel to the z - ($\underline{B}$-) -axis. They can be visualized as cut out by a cone with half opening angle θ whose tip is at the center G and whose axis, at any instant, is normal to $\underline{B}$. The angle θ serves as a suitable parameter; with r as the radius of the shell,

$$\lambda = 2\pi r \sin \theta$$

$$S = \pi r^2 \sin^2 \theta$$

$$db = r \, d\theta \, .$$

The time does not enter these relations. If one integrates over the half-sphere ($0 \leq \theta \leq \frac{\pi}{2}$) and then doubles the result, one arrives at

$$\underline{M}_i = - \frac{2}{3} \, \pi \, r^4 \, \sigma \, h \, B^2 \, (i' \omega_x + j' \omega_y) \, .$$

The shell has the same moment of inertia,

$$T = \frac{8}{3} \pi r^4 \rho h,$$

with respect to any axis through G (ρ = mass density in the shell). Euler's equations (11) lose the subtractive terms at the right. On multiplying successively by i, j, k and adding up, they go into the vector equation

$$\underline{M}_i = T \dot{\underline{\omega}},$$

which can be resolved again in the space-fixed system, thus eliminating the need for transformation relations. Indeed, the body-fixed system is not very well defined, since it can have any position relative to the shell.

With the abbreviation

$$C^2 = - \frac{|\underline{M}_i|}{T} = \frac{1}{4} \frac{\sigma}{\rho} B^2 ,$$

we obtain the equations

$$\dot{\omega}_x = - C^2 \omega_x, \quad \dot{\omega}_y = -C^2 \omega_y, \quad \dot{\omega}_z = 0$$

which are easily solved to give

$$\omega_x = (\omega_x)_o \, e^{-C^2 t}, \quad \omega_y = (\omega_y)_o \, e^{-C^2 t}, \quad \omega_z = (\omega_z)_o ,$$

where the factors with index o denote the components of $\underline{\omega}$ at t=0. One notices that ω_x and ω_y are finally damped out and that the rotation about the z-axis (field direction) retains its original value. Complete rest ensues with $(\omega_z)_o = 0$. Given the magnetic field strength, good conducting material with small mass density is more effectively retarded than poorly conducting material with large mass density.

A similar pattern is followed by any shell if it initially rotates about a principal axis either in field direction, when the rotation remains undisturbed, or normal to field direction, when the character of a mere rotation (no gyrating) is still preserved, but the motion is damped according to the equation

$$\dot{\omega} = -C^2 \omega .$$

The quantity C contains the lengths λ and enclosed areas, S, of the current paths which, as was mentioned, in general vary with time. With a circular cylinder, the only simple nontrivial case is provided when the original rotation is about its longitudinal axis placed normal to the field. The quantity C is

then a constant which depends on the cylinder's length and diameter. If the two are equal,

$$C^2 = \frac{2}{\pi} \frac{\sigma}{\rho} B^2 \, (4-\pi) .$$

Otherwise, the expression contains length and diameter explicitly and involves either a logarithmic term or an inverse cosine depending on whether the diameter-length ratio is larger or smaller than unity.

VI. MOTION OF A CIRCULAR CONDUCTING DISC IN A HOMOGENEOUS MAGNETIC FIELD

Again the rotatory portion needs to be considered only. Since of necessity the currents are all in the disc plane, condition (16) on their normals cannot be imposed here, and the use of the torque differential (18) is precluded. However, expression (17) is still valid. The tension described by it can be maximized by choosing the area, S, as large as possible, i.e., by taking it as circular for any given tube length. These circles must not intersect; they are therefore concentric to the midpoint (and mass center) of the disc. The tubes can be given a constant differential width, db, in the disc's radial direction, so that their cross sections, h db, are constant (h = constant thickness of disc, r = its radius).

The product [n B] is best evaluated in terms of the Eulerian angles which are depicted on Figure 1.

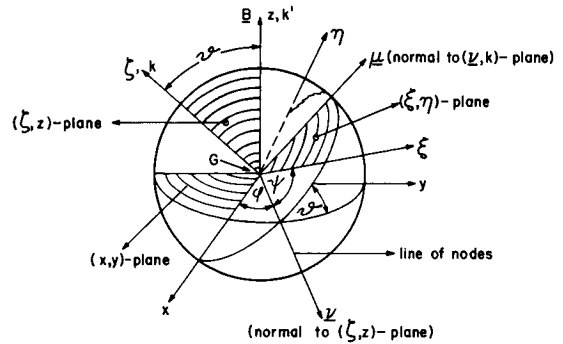FIGURE 1. THE SPACE-FIXED AND BODY-FIXED SYSTEMS. EULARIAN ANGLES ϑ, φ, ψ

The unit vector $\underline{\nu}$ is in the line of modes. A further unit vector, $\underline{\mu}$, forms, with $\underline{\nu}$ and k, a rectangular system in which the angular velocity appears as

$$\underline{\omega} = \underline{\nu}\,\dot{\vartheta} + \underline{\mu}\,\dot{\varphi}\sin\vartheta + k(\dot{\psi} + \dot{\varphi}\cos\vartheta). \qquad (19)$$

The vector $\underline{B}$ again will fix the direction k' of the z-axis. In the ν-system this direction appears as

$$k' = \underline{\mu}\sin\vartheta + k\cos\vartheta .$$

The normal, $\underline{n}$, is parallel to the disc's polar axis which we shall introduce as the principal axis, k. Thus,

$$[\underline{n}\,\underline{B}] = B[k,\underline{\mu}\sin\vartheta + k\cos\vartheta] = -\underline{\nu}\,B\sin\vartheta .$$

Furthermore,

$$U = -\underline{\omega} \cdot [\underline{n}\,\underline{B}]\,S = BS\,\dot{\vartheta}\sin\vartheta$$

$$dM_i = I\,[\underline{n}\,\underline{B}]\,S = -\underline{\nu}\,I\,BS\sin\vartheta .$$

It is seen that the torque acts along the line of nodes and therefore is again in the (x, y)-plane.

For a tube with center distance $b(0 \le b \le r)$,

$$S = \pi b^2 \quad \text{and} \quad R = \frac{2\pi b}{\sigma\,h\,db}$$

By Ohm's law (in the form $U = IR$)

$$dM_i = -\tfrac{1}{2}\,\pi\,b^3\,\sigma\,h\,B^2\,\dot{\vartheta}\sin^2\vartheta\,\underline{\nu}\,db .$$

On integrating over b,

$$\begin{cases} M_i = -A_i\,\dot{\vartheta}\sin^2\vartheta\,(i\cos\psi - j\sin\psi), \text{ where} \\[2mm] A_i = \dfrac{\pi}{8}\,r^4\,\sigma\,h\,B^2 . \end{cases} \qquad (20)$$

The vector term is the representation of $\underline{\nu}$ in the system of the principal axes, so that the components of $\underline{M}_i$ in Euler's equations are directly known here.

The polar and equatorial moments of inertia are $(m = $ mass of disc$)$

$$\begin{cases} T_c = \dfrac{mr^2}{2} \\[3mm] T_a = T_b = \dfrac{mr^2}{4}\left(1 + \dfrac{1}{3}\,\dfrac{h^2}{r^2}\right) . \end{cases} \qquad (21)$$

The integration of the system (11) is deferred to the next section after a further torque has been added to $\underline{M}_i$.

When the field is not homogeneous, finding suitable current curves is still a quite formidable task, although the surface is now plane. Methods for solving the isoperimetric problem could be put to use. The determination of a fitting current system would call for some ingenuity nonetheless. Since the distribution of the vector $\underline{B}$ over the disc will vary with attitude, these intricate calculations would have to be repeated many times. Moreover, a sequence of attitudes cannot be known before torques, i.e., momentary current paths, are known, so that even this simpler situation appears as rather hopelessly involved.

VII. MOTION OF A DISC WHEN SUBJECT TO LIGHT PRESSURE AND CARRYING A SURFACE CHARGE

To cope with a more practical situation let us suppose the disc is moving in outer space, but still within the magnetic cavity. Its face toward the sun is then exposed to light pressure; it is also likely to receive a surface charge. For establishing the essential features of the ensuing motion, we shall again idealize physical reality. The motion will be studied during a time interval in which $\underline{B}$ remains reasonably constant. This condition can be best satisfied on a circular equatorial orbit.

If the surface (area S) is a perfect reflector, the force exerted by radiation on it is given by

$$\underline{F}_r = -2p_0\,S\,(\underline{\lambda}\,k)^2\,k , \qquad (22)$$

where p_0 is the pressure on a surface placed normal to light direction (unit vector $\underline{\lambda}$). For sunlight in the earth's vicinity,

$$p_0 = 0.458 \times 10^{-4}\;\frac{\text{dyne}}{\text{cm}^2} \quad .$$

This figure is an average; it is slightly larger at perihel and slightly smaller at aphel.

If the surface is perfectly absorbing,

$$\underline{F}_r = -p_0\,S\,(\underline{\lambda}\,k)\,\underline{\lambda} . \qquad (23)$$

Note that the scalar product $(\underline{\lambda}\,k)$ is negative, since the disc normal k and the light direction enclose an obtuse angle.

Nothing definite can be known regarding the surface charge. For the sake of easy argument, it will be assumed that its density, δ, is constant over the disc during the time interval considered. The sign of δ can be positive or negative according to the kind of electricity accumulated.

The movements of the disc result in drift (convection) currents. If a point on it travels the distance,

$$d\underline{s} = \underline{v}\,dt,$$

it will experience the force

$$d\underline{F}_e = -I\,[\underline{B}\underline{v}]\,dt = I\,[\underline{v}\,\underline{B}]\,dt.$$

We have used here the differential form of the force law (4). The subscript e identifies a force (or torque) caused by the presence of a charge. Since I dt is the charge, $\delta\,d\underline{s}$, sitting on the elemental surface dS during its infinitesimal travel, the total force acting on the disc becomes

$$\underline{F}_e = \delta \int \left\{ [\underline{u}\,\underline{B}] + [\underline{\omega}\,\underline{r}] \times \underline{B} \right\}\,dS. \qquad (24)$$

The second integral vanishes as can be demonstrated by calculation, and directly inferred from the integrand: To each elemental surface located at the distance $\underline{r}$ from the center there corresponds another at the distance $-\underline{r}$; the contribution to the force by these elements cancel each other, $\underline{B}$ and $\underline{\omega}$ being constants on the surface at the instant of the integration.

The translational velocity is also the same for all dS. The equations of motion then become (r = radius of disc; m = its mass)

$$\pi\,r^2\,\delta\,[\underline{u}\,\underline{B}] + \underline{F}_g + \underline{F}_r = m\,\frac{d}{dt}\,\underline{u}, \qquad (25)$$

where $\underline{F}_g$ is the force caused by gravity, and the light force $\underline{F}_r$ is given, in two ideal cases, by expressions (22) or (23). The presence of the vector k there prevents the direct integration of equations (25). The instantaneous position of the disc's polar axis (k) in the (x,y,z)-system must be determined by solving the rotatory equations (which will be set up shortly).

If one disregards the light and gravitational forces, the solution is readily obtainable and can be interpreted as follows. Let the mass center G, at t = 0, occupy the point C which will serve as a fixed reference point with regard to earth. Assign to G the initial velocity u_o making the angle θ_o with the $\underline{B}$ - (z-) direction and determining with it the (z,x)-plane. Consider the special field line, $\underline{B}_m$, through the point

$$x_m = 0, \quad y_m = -\frac{m\,u_o\,\sin\theta}{\delta\,\pi\,r^2\,B}\,.$$

Around this line the center G begins to circle with the speed $u_o\,\sin\theta_o$, while, at the same time, it moves parallel to the field line $\underline{B}_m$ with the speed $u_o\,\cos\theta_o$. These speeds do not change. (Equation (25) indicates that the force is always perpendicular to $\underline{u}$). In short, the center G travels with constant speed on a spiral around the field line $\underline{B}_m$. Since both δ and B are apt to be very small, the y-component of the velocity,

$$\dot{y} = -u_o\,\sin\theta_o\,\sin\left(\frac{\delta\,\pi\,r^2\,B}{m}\,t\right)$$

remains nearly zero, so that the mass center G will not to any great degree leave the initial (z,x)-plane, if the field effect alone is considered. If the gravitational motion is added, however, the point G will wander out of this plane, provided it makes a nonzero angle with the direction of the gravitational pull. The presence of the force $\underline{F}_r$ will further complicate the picture, whereas the currents within the disc have no bearing on the translation (as long as the magnetic field is homogeneous).

The rotatory motion develops independently of the center's translational travel. With a disc of quasi-infinitesimal thickness and uniform surface texture, the light force produces no moment. A possible gravity gradient will be neglected, so that the torques associated with the induction and drift currents need be considered only. The total acting torque then is

$$\underline{M} = \underline{M}_e + \underline{M}_i\,.$$

$\underline{M}_i$ is already known by expression (20).

By the force integral (24), the electric charge contributes the torque

$$\underline{M}_e = \delta \int \underline{r} \times \left\{ [\underline{u}\,\underline{B}] + [\underline{\omega}\,\underline{r}] \times \underline{B} \right\}\,dS.$$

Here, the first integral expression is zero through cancellation of oppositely equal contributions. The second can be put into the form

$$\begin{cases} \underline{M}_e = -A_e\,\sin\vartheta\,[\,\omega_\zeta\,(i\cos\psi - j\sin\psi) - k\,\dot\vartheta\,],\ \text{where} \\ A_e = \frac{\pi\,r^4}{4}\,B\,\delta\,. \end{cases} \qquad (26)$$

Euler's equations (11) take the form

$$\begin{cases} -A_e\,\omega_\zeta\,\sin\vartheta\,\cos\psi - A_i\,\dot\vartheta\,\sin^2\vartheta\,\cos\psi \\ \qquad = T_a\,\dot\omega_\xi - \omega_\eta\,\omega_\zeta\,(T_a - T_c) \\ A_e\,\omega_\zeta\,\sin\vartheta\,\sin\psi + A_i\,\dot\vartheta\,\sin^2\vartheta\,\sin\psi \\ \qquad = T_a\,\dot\omega_\eta - \omega_\zeta\,\omega_\xi\,(T_c - T_a) \\ A_e\,\dot\vartheta\,\sin\vartheta = T_c\,\dot\omega_\zeta\,, \end{cases} \qquad (27)$$

where T_a and T_c are the moments (21). On multiplying in sequence by ω_ξ, ω_η, ω_ζ and adding the equations, the rate of change of kinetic energy is obtained:

$$-A_i\,\dot\vartheta^2\,\sin^2\vartheta = \tfrac{1}{2}\,\frac{d}{dt}\,[T_a\,(\omega_\xi{}^2 + \omega_\eta{}^2) + T_c\,\omega_\zeta{}^2]$$
$$= \tfrac{1}{2}\,\frac{d}{dt}\,[T_a(\dot\vartheta^2 + \dot\varphi^2\,\sin^2\vartheta) + T_c(\dot\psi + \dot\varphi\,\cos\vartheta)^2]. \qquad (28)$$

The left side here has simplified considerably since the relation exists

$$\dot\vartheta = \omega_\xi\,\cos\psi - \omega_\eta\,\sin\psi$$

It is seen that the rotatory energy decreases during the motion. However, the action on the drift currents alone (put $A_i = 0$) does not change the energy, i.e., the magnitude of the angular velocity, as it does not affect that of the translational velocity.

The third of Euler's equations yields the integral

$$T_c\,\omega_\zeta + A_e\,\cos\vartheta = C_1 = \text{const.} \qquad (29)$$

Note that in terms of the Eulerian angles

$$\begin{cases} \omega_\zeta = \dot\psi + \dot\varphi\,\cos\vartheta \\ \omega_\xi = \dot\vartheta\,\cos\psi + \dot\varphi\,\sin\psi\,\sin\vartheta \\ \omega_\eta = -\dot\vartheta\,\sin\psi + \dot\varphi\,\cos\psi\,\sin\vartheta \;. \end{cases} \qquad (30)$$

After suitable handling the first two equations give a further integral:

$$\tfrac{1}{2}A_e\,\sin^2\vartheta + C_1\,\cos\vartheta + T_a\,\dot\varphi\,\sin^2\vartheta$$
$$= C_2 = \text{const.} \qquad (31)$$

The relations (29), (30), (31) can be used to convert the rate of energy expression (28) into a

differential equation for the angle between the field direction and the disc normal:

$$-A_i\,\dot\vartheta\,\sin^2\vartheta$$
$$= T_a\,\ddot\vartheta + \frac{(C_2 - C_1\cos\vartheta)(C_1 - C_2\cos\vartheta)}{T_a\,\sin^3\vartheta}$$
$$+ A_e\,\sin\vartheta\left[\frac{A_e\cos\vartheta - 2C_1}{4\,T_a} + \frac{C_1 - A_e\cos\vartheta}{T_c}\right] \quad (32)$$

After solving this equation for $\vartheta(t)$, the functions $\varphi(t)$ and $\psi(t)$ can be gained from equations (31) and (29) by quadratures. The gryoscopic motion is then completely known, since the three angles determine the varying attitudes of the disc relative to the "space-fixed" system with origin at G (Fig. 1).

Let us first contemplate a situation where there is no surface charge ($A_e = 0$). A mathematically simple situation emerges with the initial conditions

$$\dot\varphi_o = \dot\psi_o = 0 \qquad (33)$$

so that both C_1, and C_2 are zero. As an immediate consequence

$$\dot\varphi \equiv 0, \quad \dot\psi \equiv 0.$$

The line of modes is space-fixed in this motion ($\varphi = \varphi_o = \text{const.}$). Since by expression (19) the angular velocity

$$\underline\omega = \underline\nu\,\dot\vartheta$$

is permanently in a direction opposite to that of the acting moment,

$$\underline M_i = -A_i\,\dot\vartheta\,\sin^2\vartheta\,\underline\nu\,,$$

the motion is simply a rotation about the $\underline\nu$-axis which is damped after the law (32)

$$\ddot\vartheta + \frac{A_i}{T_a}\,\dot\vartheta\,\sin^2\vartheta = 0\,.$$

This equation has the form of equation (12) and therefore first and second integrals of the forms (13) and (15). In this situation the disc behaves like the planar (not necessarily circular) wire, merely exhibiting a different damping rate. It is also seen that the restrictions introduced for the easy solution of equation (12) amount to imposing the initial conditions (33) and the condition $\psi_o = 0$ (the vector $\underline\nu$ replaces the former unit vector $\underline m$ which had been identified with i).

If C_1, alone is zero, equation (32) has the special solution

$$\vartheta = \frac{\pi}{2}$$

when $A_e = 0$ (no charges). Then, by the integrals (31) and (29),

$$\varphi = \varphi_o + \frac{C_2}{T_a} t$$

$$\psi = \psi_o .$$

The moment (20) is permanently zero, and the motion appears as a rotation about a diameter parallel to field direction, the polar axis turning about it at the constant angular velocity, $\omega = \dot{\varphi} = \frac{C_2}{T_a}$. This is one instance of a more general situation: an initial motion of the polar axis on a circular cone around field direction continues undisturbed by the presence of the magnetic field. It can be shown that the same is true if initially the disc rotated about the space-fixed polar axis.

As a general result any gyroscopic motion of an uncharged disc traveling in a homogeneous field will, in the long run, either disappear, or retain part of its energy, or all of it, depending on the initial state of the motion and on the initial angle, ϑ_o , between polar axis and field direction. (Since the choice of the ξ- and x-axes is free with the disc, one can always begin with $\psi_o = 0$ and $\varphi_o = 0$, letting both axes initially coincide with the line of modes.) One of these modes of behavior is to be expected of any uncharged conductor moving in a magnetic field. An increase of energy will never occur. The loss encountered goes into Joule's heat.

By contrast the rotatory motion of a nonconducting but charged disc ($A_i = 0$, $A_e \neq 0$) will retain its energy in all circumstances.

If it initially swings about a principal axis in field direction such a disc will persist in this motion without being disturbed by an interaction of the drift currents with the field.

As a nontrivial case the motion with $C_2 = C_1 = 0$ will be considered again. Rather succinct formulations emerge here if the disc's thickness, h, is negligible when compared to its radius, r, so that the relations (21) may be written as

$$\begin{cases} T_a = T_b = \dfrac{m r^2}{4} = T \\[2ex] T_c = 2T. \end{cases} \qquad (34)$$

It then follows from the integrals (31) and (29) that

$$\begin{cases} \varphi = -\dfrac{1}{2} \dfrac{A_e}{T} t \equiv -q\,t \\[2ex] \psi = 0. \end{cases} \qquad (35)$$

Equation (32) for ϑ assumes the form

$$\ddot{\vartheta} - q^2 \sin \vartheta \cos \vartheta = 0, \text{ where}$$
$$q = \frac{1}{2} \frac{A_e}{T} .$$

As a first integral

$$\dot{\vartheta} = \overset{-}{+} q \sin \vartheta , \qquad (36)$$

when the initial values are chosen such that $\dot{\vartheta}_o = \overset{-}{+} q \sin \vartheta_o$, allowing the representation

$$qt = \pm \log \frac{1 + \cos \vartheta}{\sin \vartheta} \cdot \frac{\sin \vartheta_o}{1 + \cos \vartheta_o} . \qquad (37)$$

The solutions (35) and (37) describe the motion. The ξ-axis always coincides with the line of modes ($\psi \equiv 0$). There is no turning about the polar axis. The line of modes performs a precession with the constant speed $\dot{\varphi} = -q$ carrying the polar axis with it which, if the upper sign is chosen in expression (36), incessantly decreases the initially acute (or obtuse) angle ϑ it makes with the field direction until finally, at $t = \infty$, that angle has become zero. The polar axis thus turns about the z-axis on a sort of spiral cone. At $t = \infty$, its speed has died down and cannot be revived, since $\dot{\vartheta}$ is also zero at $\vartheta = 0$. The total kinetic energy, at this time, is contained in the precessional motion and therefore has the constant value

$$\frac{1}{2} T_c \dot{\varphi}^2 = \frac{1}{4} \frac{A_e^2}{T} .$$

With the lower sign in expressions (36) and (37), a somewhat different course is followed. The angle ϑ is now increasing rather than decreasing. The time becomes infinite with $\vartheta = \pi$. Thus, the polar axis constantly takes on larger angles to field direction, again moving on a conical spiral, and comes to rest in a position opposite to that attained before.

If the motion of a charged as well as conducting disc is to be studied, an analytic first integral of

equation (32) does not seem to be obtainable even with $C_1 = C_2 = 0$ when the equation assumes the form

$$\ddot{\vartheta} + a^2 \dot{\vartheta} \sin^2 \vartheta - q^2 \sin \vartheta \cos \vartheta = 0,$$

where $a^2 = \dfrac{A_i}{T}$. For small angles, ϑ, one may write the first integral as

$$\dot{\vartheta} = b + \frac{q^2}{2b} \vartheta^2 - \frac{a^2}{3} \vartheta^3 \pm \ldots \quad . \qquad (38)$$

With $b < 0$ and $\vartheta_o > 0$ the angle ϑ will decrease to $\vartheta = 0$ at which value, however, the motion will not stop, $\dot{\vartheta}$ still being negative. If $|b|$ is of order q, and $q(\sim B\delta)$ is small enough, the angle ϑ will reach a minimum compatible with the approximation (38). A calculation shows that its value,

$$\vartheta^* = \frac{3}{b} \frac{q^2}{a^2} ,$$

is attained at $t = \infty$. Since the solutions (35) always apply with $C_2 = C_1 = 0$, the motion is seen to be not essentially different from the preceding one. The polar axis turns about the z-axis decreasing its initial small angle $\vartheta_o > 0$ to arrive at $\vartheta^* < 0$ after an infinite time has elapsed . The final (smallest) value of the kinetic energy here is

$$\frac{1}{8} \frac{A_e^2}{T} (1 + \cos^2 \vartheta^*) \approx \frac{1}{4} \frac{A_e^2}{T} (1 - \frac{\vartheta^{*2}}{4}),$$

which may be compared to the value at $\vartheta = 0$

$$\frac{1}{4} \frac{A_e^2}{T} (1 + \frac{1}{2} \frac{b^2}{q^2}) .$$

More intricate motions develop if C_2 and C_1 are not both zero. The investigation of the equations (29), (31), (32) must then use numerical methods as a rule.

VI. INSTRUMENTATION

AN ACOUSTIC WIND MEASURING TECHNIQUE

By

Wesley W. Bushman* and Orvel E. Smith**

ABSTRACT

An atmospheric wind measurement technique
has been developed and used to measure wind profiles
over Cape Kennedy from ground to 85 km. The
technique is an extension of the rocket grenade ex-
periment using as its sound source, rather than a
grenade, the acoustic noise of a rocket's exhaust.
To determine the wind profile from this continuous
sound source, a set of equations has been derived
and applied to measurements made during the flights
of several Saturn vehicles. The profiles agree well
with concurrent measurements at lower altitudes
(below 50 km.) and are consistent with atmospheric
circulation observations at higher altitudes. A
preliminary error analysis indicates that the tech-
nique can be used to make measurements of suf-
ficient precision to be useful in engineering and
meteorological studies.

I. INTRODUCTION

The problem of measuring winds in the upper
stratosphere and above has received considerable
attention since sounding rockets have rendered these
altitude regions accessible to direct measurements.
Interest in the winds comes primarily from two
sources. First, because atmospheric motions are
related to thermodynamic quantities such as tem-
perature, pressure and density and since they play
a role in energy exchange processes, knowledge of
these motions is essential to scientific understanding
of the atmosphere. Second, atmospheric wind re-
search has gained technological importance because
of requirements of aerospace vehicle research and
development programs.

The importance of atmospheric wind research
is evident from the large amount of research being
done on wind measuring devices. Among the ex-
periments currently being used are free lift balloons,
such as the double and triple theodolite techniques,
Jimsphere [1] and rawinsonde; meterological rocket-
deployed sensors; Robin balloon chaff and parachute;
the rocket grenade [2, 3] and sodium vapor [4] ex-
periments. Each of these experiments has recognized
altitude range limitations, i. e., to measure the wind
profile from ground to 85 km, two or three separate
systems are used.

The rocket exhaust noise technique presented
here offers the capability of economically deriving
wind profiles from ground to 85 km altitude. The
technique is similar to the grenade experiment to the
extent that both are based on the atmospheric tem-
perature and mass motion dependence of the velocity
of sound. In the grenade experiment, average tem-
peratures and winds between adjacent grenade det-
onations are determined by measuring the time re-
quired for sound to travel from a source of known
position to a ground-based microphone array, and its
angle of arrival at the array.

When rocket exhaust noise is used as a sound
source, the times and locations of the many noise
events that characterize the exhaust are not known.
If, however, the temperature is measured independ-
ently, then the arrival angles of the noise events can
be used to determine winds. A ground-based array
of microphones intercepts the acoustic wave front of
the noise, and the time of arrival at individual micro-
phones is used to calculate arrival angles. The noise
event is traced back by an iterative process until it
correctly intersects the vehicle trajectory. Each
noise event so traced leads to a wind data point,
giving rise to a wind profile in a stratified atmosphere
with the average wind in each layer between selected
noise events.

The assumptions made for the approach described
here are as follows:

1. The vertical component of wind is negligible
compared to the local speed of sound.

---

2. The source of sound is considered to be a point located at the nozzle of the engine or a known distance behind along the flight path. The sound wave is approximated by a plane wave at large distances from the source.

3. The atmosphere remains in a steady state for the duration of the measurement, i.e., it does not change with respect to time in the wind velocities and temperature.

II. THE EXPERIMENT

A. THE MEASUREMENT

A cross-shaped array of nine microphones was set up on the southeast point of Cape Kennedy to monitor launchings of space vehicles. A minimum of three microphones is necessary to determine the arrival angle of the sound; the additional microphones provide redundancy and increased accuracy.

The size of the microphone array shown in Figure 1 is about 1200 m along each axis. This size
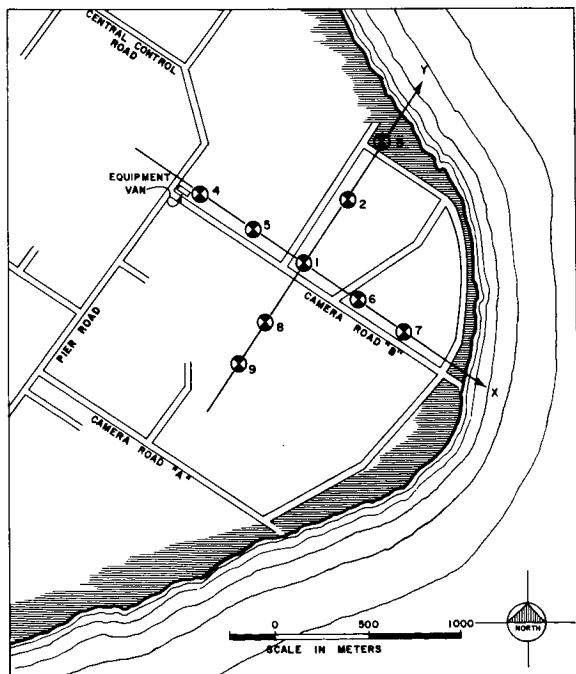
FIGURE 1. THE MICROPHONE ARRAY AND COORDINATE SYSTEM

was chosen to increase the accuracy of the experiment with respect to two sources of error, (1) errors which decrease with increasing array size introduced from finite resolution in reading arrival times and (2) errors which increase with array size introduced by the plane wave assumption.

The microphones are hot-wire, single-chamber Helmholtz resonators tuned to about 4 Hz. This low frequency is particularly well suited to extremely far-field acoustic measurements since the atmosphere tends to be a low-pass filter over long distances. The microphones were designed at Texas Western College for use in the rocket grenade experiment.

The microphones are located in heavily vegetated locations to minimize local wind noise. Each microphone is contained in a concrete box, recessed so its top is level with the ground surface. These boxes also serve as permanent survey markers defining the geodetic position of each microphone to within 15.24 cm (6 in.).

The electronic and recording equipment is housed in a van located near microphone 4. Although a location near microphone 1 would require about 4 km (2.5 mi) less cable, it was considered desirable to keep the van removed from the array to reduce the possibility of reflective interference.

For the Saturn series of launches, the exhaust noise was audible to the microphones from launch until the vehicle was about 100 km slant distance. Because of the wide range of sound levels, a manually operated variable attenuator was used to maintain the proper signal level into a magnetic tape recorder. Range time is simultaneously recorded with the microphone outputs.

B. THEORY

The theory and data reduction can conveniently be treated in three steps, (1) cross correlation to determine arrival times, (2) ray tracing through layers of known temperature and wind, and (3) solution for winds in the unknown layer.

1. Cross correlation to determine arrival times. In the absence of local interference, the acoustic wave front of a noise event appears essentially identical to microphones at separated locations. If identical microphones are used, the output wave form of one microphone matches that of another shifted in time. The first step in the data analysis is the cross correlation of the microphone output waveforms to determine this time difference.

Figure 2 is a typical record made about 55 seconds after launch of Saturn SA-9. The time differences can be read directly from this type of record.
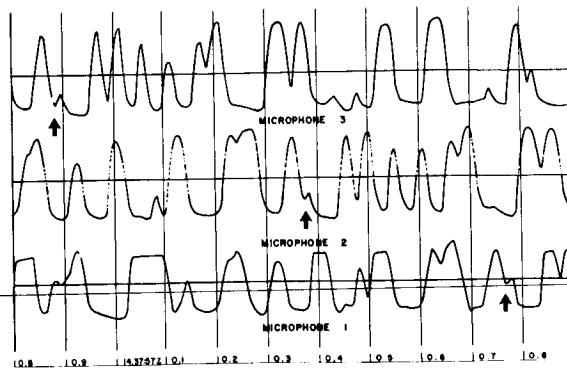

FIGURE 2. TYPICAL OSCILLOGRAM OF
MICROPHONE OUTPUTS

The manual cross correlation from records such as Figure 2 is both tedious and subject to human error. To avoid these problems and to permit rapid reduction of the data, the cross correlation is done automatically on a digital computer. The data from all microphones are digitized, and a cross-correlation function is computed for each microphone paired with microphone 1. This function is defined as

$$R(t') = N \int_{\substack{\text{SLICE} \\ \text{TIME}}} \psi^1(t) \, \psi^2(t + t') \, dt,$$

where R is the magnitude of the cross-correlation
function

t' is the time difference

N is a normalization factor

$\psi^1(t)$ & $\psi^2(t)$ are two time-dependent micro-
phone outputs

and

SLICE TIME is a pre-set integration time
interval.

A typical plot of $R(t')$ is shown in Figure 3. The magnitude of R at the principal maximum gives an indication of the degree of match of the waveforms, unity meaning that they are identical. The time of

occurrence of the peak is the time difference between microphones.
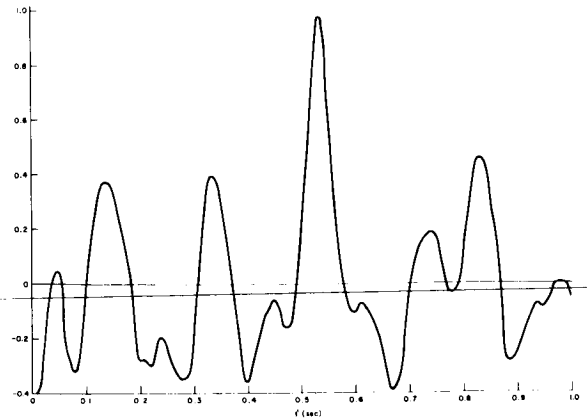
FIGURE 3. TYPICAL VARIATION OF CROSS
CORRELATION WITH TIME DIFFERENCE

2. Ray tracing through layers of known temperature and wind. The time difference determined by the cross correlation is a function of the sound arrival angle, speed of sound at the array and microphone placement. The arrival angles (or equivalently the characteristic velocities, K_x and K_y, defined as the velocities of intersection of the wave front with the x and y axis) are computed from the time difference with appropriate corrections for microphones not lying precisely on the x or y axis. Since there are five microphones along each axis, four independent measurements of K_x and K_y can be made. This redundancy is used to reduce random errors and to correct for deviations of the wave front from a plane.

Milne [5] has shown that the wave normal of the ray reaching the microphones remains parallel to the same vertical plane throughout its propagation. For a plane wave then, the characteristic velocities of a specific sound ray are constant. Since the temperature and wind are treated as constant in any layer, the segment of the sound ray in that layer is a straight line. The wave front is refracted at each layer interface in a way analogous to the refraction of light waves. This refraction is caused by a change in the speed of sound between layers. Further refraction occurs if wind direction and magnitude are not identical across layer boundaries. These considerations lead to an expression similar to Snell's law:

$$W + V \sec \theta = \text{constant}, \tag{1}$$

110

where

θ is the elevation angle of the wave front normal

V is the local speed of sound

W is the horizontal wind component in the vertical plane containing the wave front normal. The component of wind perpendicular to W simply displaces the ray along the plane of the wave front.

The constant in equation (1) is determined from the characteristic velocities. It is numerically equal to the characteristic velocity that would be measured along a horizontal axis parallel to W. If the measurements are made along any other two orthogonal axes x and y,

$$\frac{1}{(\text{constant})^2} = \frac{1}{K_x^2} + \frac{1}{K_y^2} \ . \qquad (2)$$

These equations can be used to ray trace through layers in which the temperature, speed of sound and winds are known. Otterman [3] has simplified the ray tracing calculation by expressing equations (1) and (2) in terms of quantities easily defined in Cartesian coordinates.

Figure 4 shows the ray tracing of a typical noise event. Since the winds have been computed from the previous noise events, the ray tracing through layers defined by these events proceeds according to equations (1) and (2). The coordinates and time of penetration of the ray at the top of the last layer are found by integrating the effect of the previous layers. Above this point, conventional ray tracing procedures must be abandoned since the wind is unknown. However, two independent requirements are available.

1. The sound ray must intersect the trajectory.

2. The correct intersection point must satisfy the criterion that the time of arrival of the noise event measured from launch equals the time of flight to the intersection plus the time required for the sound to travel from the intersection to the array.

These two conditions uniquely determine the coordinates of the source along the trajectory and the average wind in the interval.

3. <u>Solution for winds in the unknown layer.</u> Figure 5 shows the arrival of the jth noise event at the top of the $(j - 1)^{st}$ layer. Since the temperature
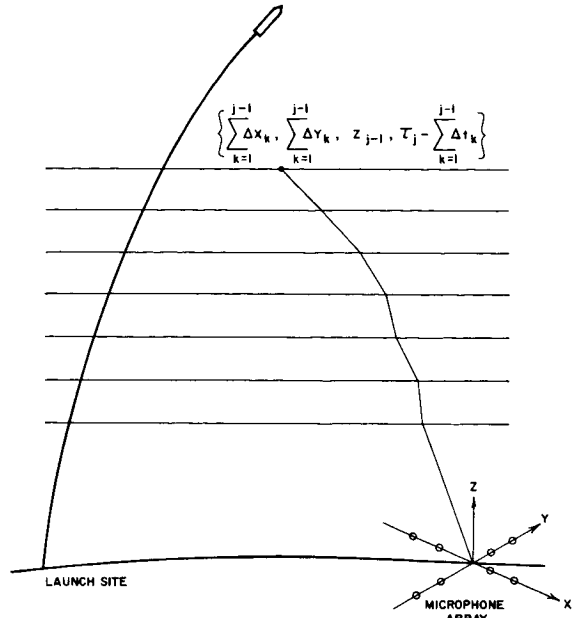

FIGURE 4. GEOMETRY OF THE WIND EXPERIMENT (THE SOUND IS HEARD AT THE ARRAY AT TIME τ_j.)
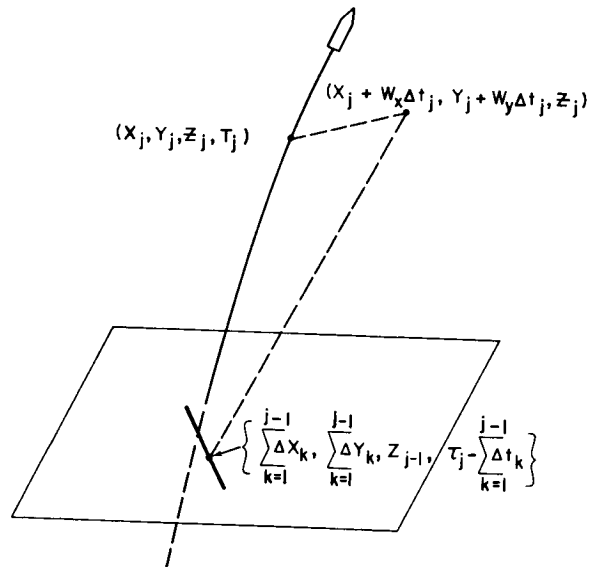

FIGURE 5. THE ARRIVAL OF A NOISE EVENT AT THE TOP OF THE LEAST KNOWN LAYER

and wind are assumed to be constant in this region, the apparent source is the center of a sphere moving with the wind. The direction cosines of the ray can be written by inspection and are

$$\alpha = \frac{x_j + W_y \Delta t_j - \sum_{k=1}^{j-1} \Delta x_k}{V_{avgj} \Delta t_j}$$

$$\beta = \frac{y_j + W_y t_j - \sum_{k=1}^{j-1} \Delta y_k}{V_{avgj} \Delta t_j}$$

$$\gamma = \frac{z_j - z_{j-1}}{V_{avgj} \Delta t_j} \quad ,$$

where

$$\Delta t_j = T_j - \sum_{k=1}^{j-1} \Delta t_k \quad .$$

The characteristic velocities are

$$K_x = -\frac{V_{avgj}}{\alpha} + W_x + W_y \frac{\beta}{\alpha}$$

and

$$K_y = -\frac{V_{avgj}}{\beta} + W_y + W_x \frac{\alpha}{\beta} \quad .$$

By simplifying the writing by substituting

$$V = V_{avgj} \, , \qquad x_0 = \sum_{k=1}^{j-1} \Delta x_k \, , \text{ etc.}$$

and remembering the trajectory, x_j, y_j and z_j can be related to T_j.

The above equations can be rearranged to give

$$F(K_x, K_y, W_x, W_y, T_j, t_0, x_0, y_0, V) = \tag{3}$$

$$(K_x - W_x)(x_j - W_x \Delta t_j - x_0) + V^2 \Delta t_j - W_y(y_j + W_y \Delta t_j - y_0) = 0$$

$$G(K_x, K_y, W_x, W_y, T_j, t_0, x_0, y_0, V) = \tag{4}$$

$$(K_y - W_y)(y_j - W_y \Delta t_j - y_0) + V^2 \Delta t_j - W_x(x_j + W_x \Delta t_j - x_0) = 0$$

$$H(K_x, K_y, W_x, W_y, T_j, t_0, x_0, y_0, V) = \tag{5}$$

$$(x_j + W_x \Delta t_j - x_0)^2 + (y_j + W_y \Delta t_j - y_0)^2 + (z_j - z_0)^2 - V^2 \Delta t_j^2 = 0.$$

The above relations F, G, H = 0 are three equations in the three unknowns W_x, W_y and T_j. The functional dependence indicated in F, G and H, although not shown explicitly in the equations, is to be inferred from the previous relations. These equations show only the principle of solution and not the method of computation. A flow chart displaying the computerized solution after time differences are determined is shown in Figures 6 and 7.
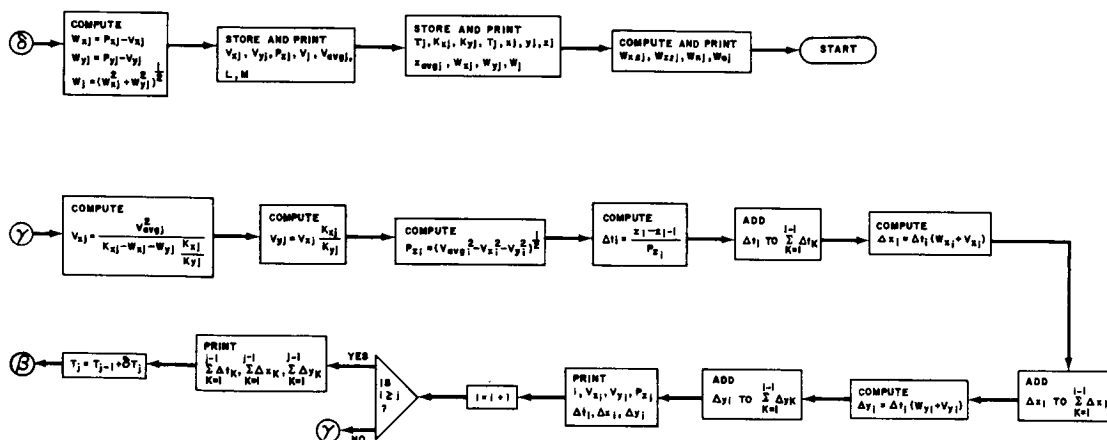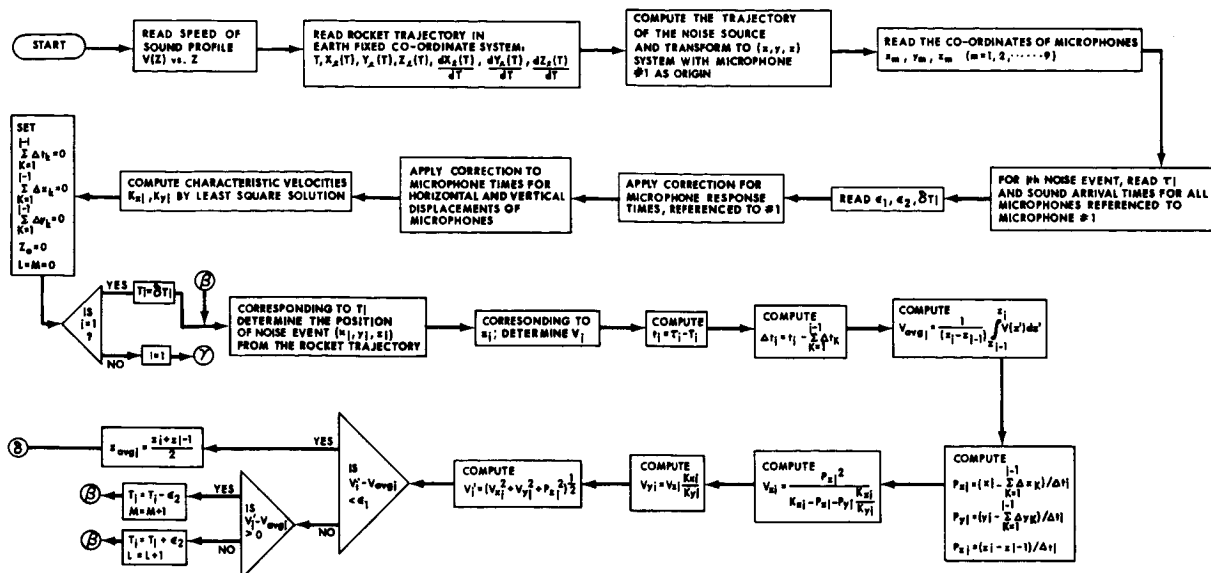
III. RESULTS

Wind profiles have been determined using the exhaust noise technique for the launchings of Saturns SA-8, SA-9, SA-10, Ranger 8 and Apollo Saturn AS-201. These wind profiles are presented in Figures 8 through 12. Also shown, in each case, are winds determined independently by other systems on the same days. The agreement between the data is consistent with the results of the error analysis of the rocket exhaust noise technique and errors inherent to the other systems used for comparison.

In the cases of Saturns SA-8, SA-9 and SA-10, winds were measured up to first-stage burnout, which occurred at approximately 85 km. The sound level at the ground from the second stage was not sufficiently intense to be useful for wind data.

In the case of Ranger 8, the trajectory was such that the vehicle was 100 km distant when it was only 45 km high. Thus, the sound faded into the background noise level before very high altitudes were attained.

The AS-201 first-stage burnout occurred at about 60 km, and the second stage did not generate sufficient sound to allow meaningful interpretation of data.
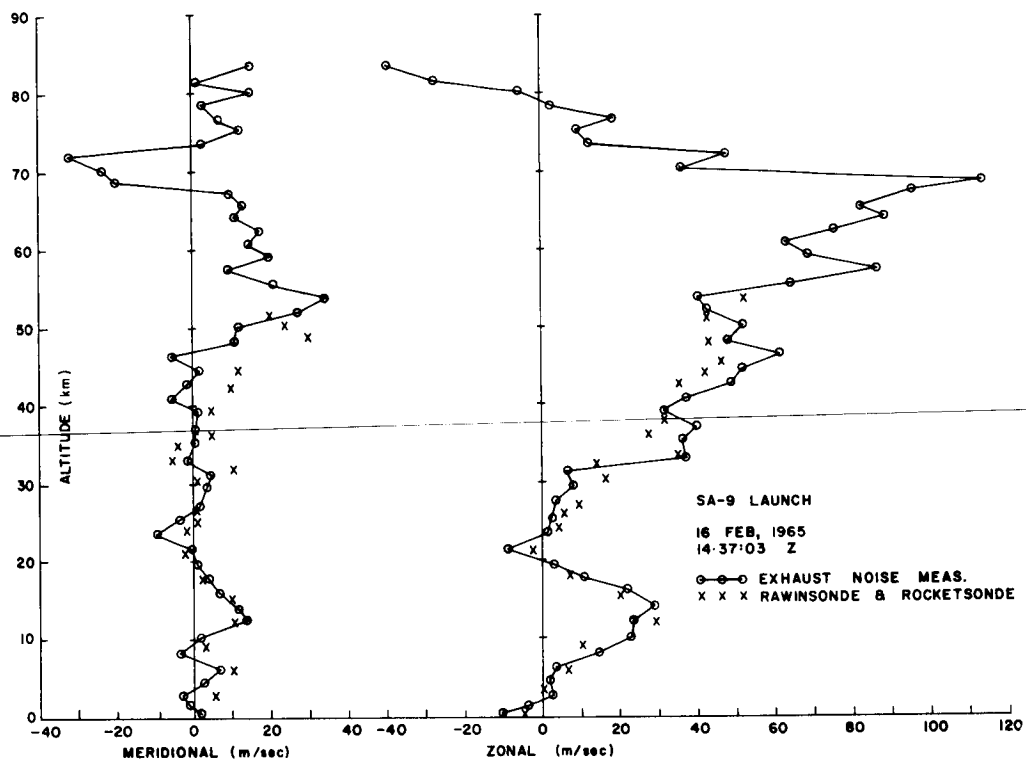
112

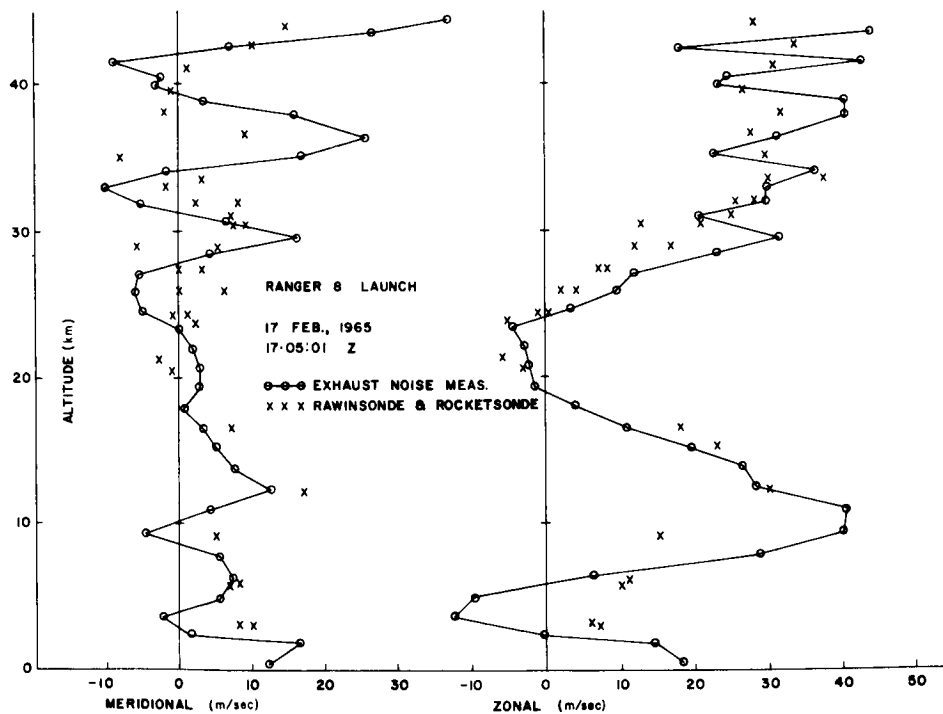FIGURE 6.   FLOW DIAGRAM FOR WIND COMPUTATION

FIGURE 7.   FLOW DIAGRAM FOR WIND COMPUTATION

IV.   ERROR ANALYSIS

Four error sources have been considered:

1.   Error in the measurement of sound arrival times (This results in errors in the derived values of characteristic velocities).

2.   Errors in the speed of sound profile (These can be introduced from inaccurate temperature data or by the finite amplitude effect).

3.   Uncertainty in the position of the noise source with respect to the vehicle.

4.   Errors introduced from the plane wave assumption.

investigation of these possibilities has shown that the error in measurement of arrival times is the most significant contributor to wind error by almost an order of magnitude [6]; therefore, analysis of the other sources will be omitted from this section.

Equations (3), (4) and (5) can be used to determine the magnitude of the expected errors.   The Jacobian of this system of equations is

FIGURE 8.   SA-9 WIND PROFILE

FIGURE 9.   RANGER 8 WIND PROFILE
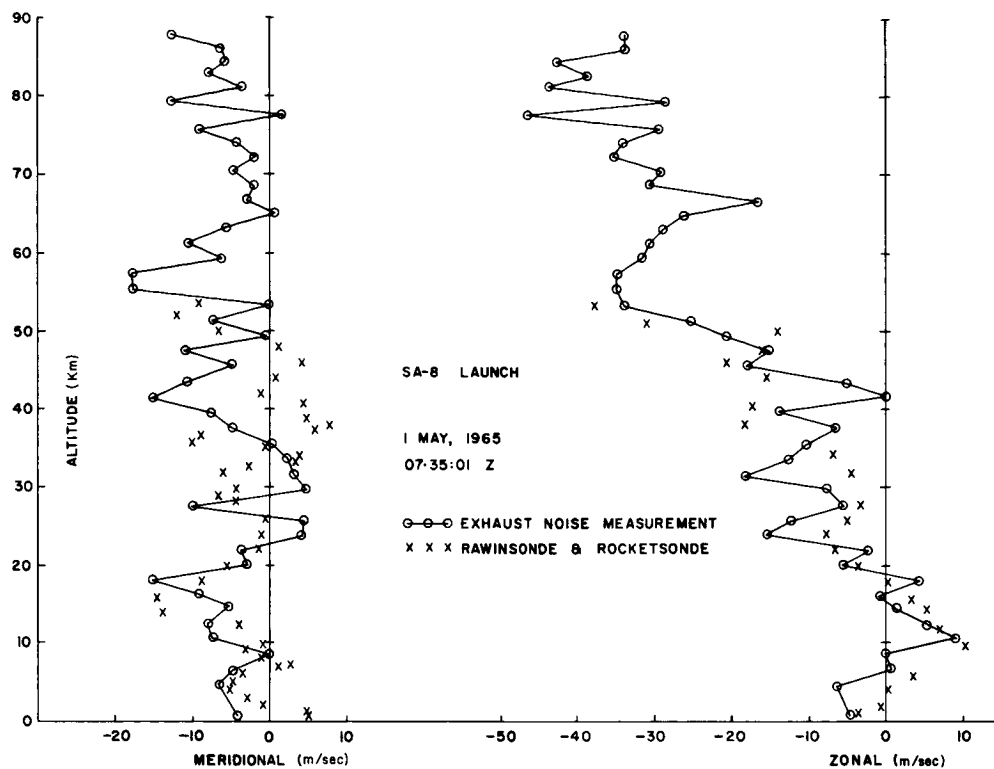
FIGURE 10.   SA-8 WIND PROFILE
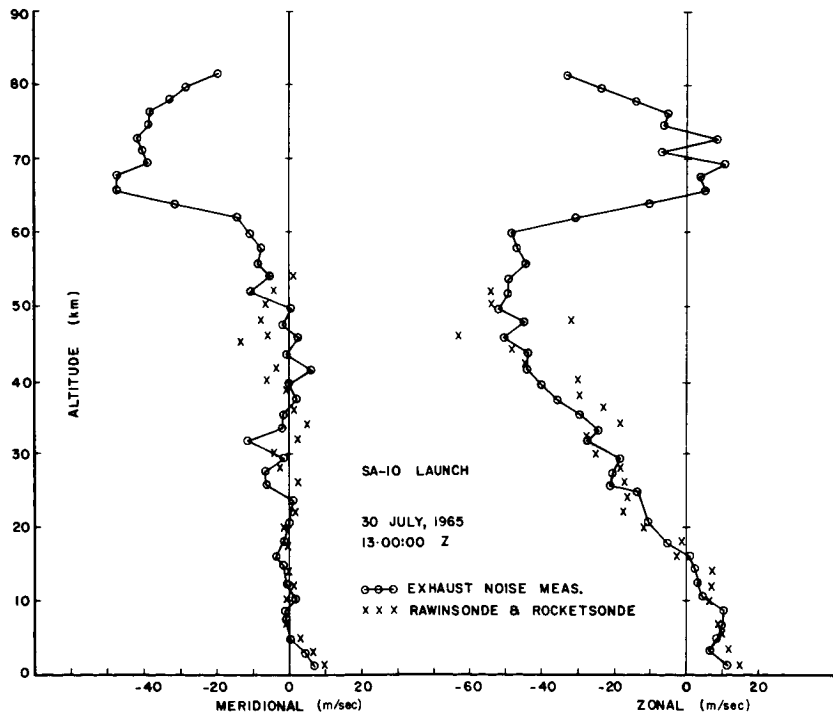
FIGURE 11.   SA-10 WIND PROFILE
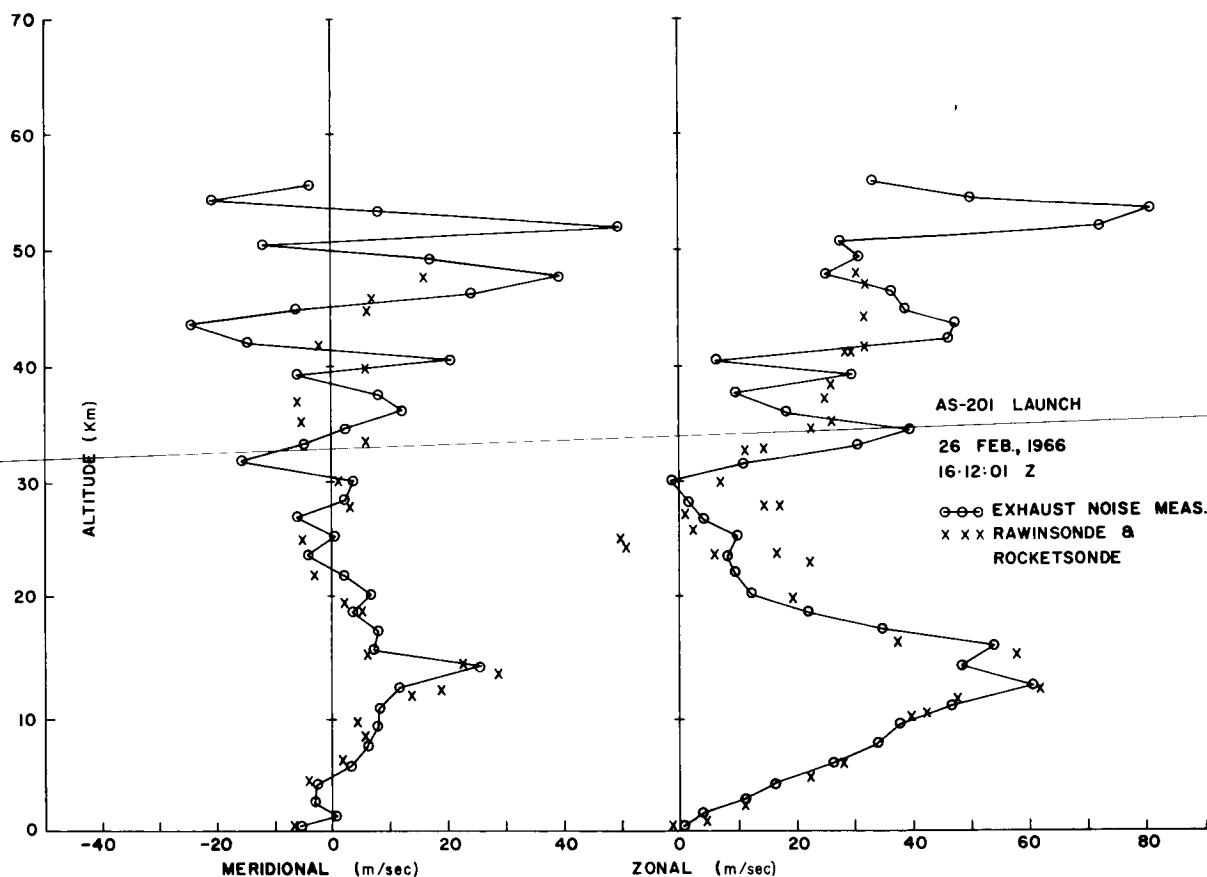
FIGURE 12. AS-201 WIND PROFILE

$$J = \frac{\partial(F, G, H)}{\partial(W_x, W_y, T)} = \begin{vmatrix} F_{W_x} & F_{W_y} & F_T \\ G_{W_x} & G_{W_y} & G_T \\ H_{W_x} & H_{W_y} & H_T \end{vmatrix} , \quad (6)$$

where $\dfrac{\partial F}{\partial W_x}$ is denoted by F_{W_x}, etc.

Then

$$\frac{\partial W_x}{\partial K_x} = - \frac{\begin{vmatrix} F_{K_x} & F_{W_y} & F_T \\ G_{K_x} & G_{W_y} & G_T \\ H_{K_x} & H_{W_y} & H_T \end{vmatrix}}{J} , \text{ etc.} \quad (7)$$

The wind errors caused by an error in measurement of characteristic velocity (arrival time) is then

$$\Delta W_x = \left(\frac{\partial W_x}{\partial K_x}\right) \Delta K_x + \left(\frac{\partial W_x}{\partial K_y}\right) \Delta K_y$$

$$+ \left(\frac{\partial W_x}{\partial x_0}\right) \Delta x_0 + \left(\frac{\partial W_x}{\partial y_0}\right) \Delta y_0 + \left(\frac{\partial W_x}{\partial t_0}\right) \Delta t_0 ,$$

with a similar equation for ΔW_y. Typical results of computation of ΔW_x and ΔW_y are shown in Figures 13 and 14.

Repeated reading of arrival times exhibits a scatter that indicates an uncertainty in the arrival times on the order of 2 or 3 milliseconds. The system parameters were chosen on the basis of uncertainties of about half this value. This large error is attributed to slight differences in microphone characteristics, differences in local background conditions and to possible acoustic anomalies of the atmosphere.
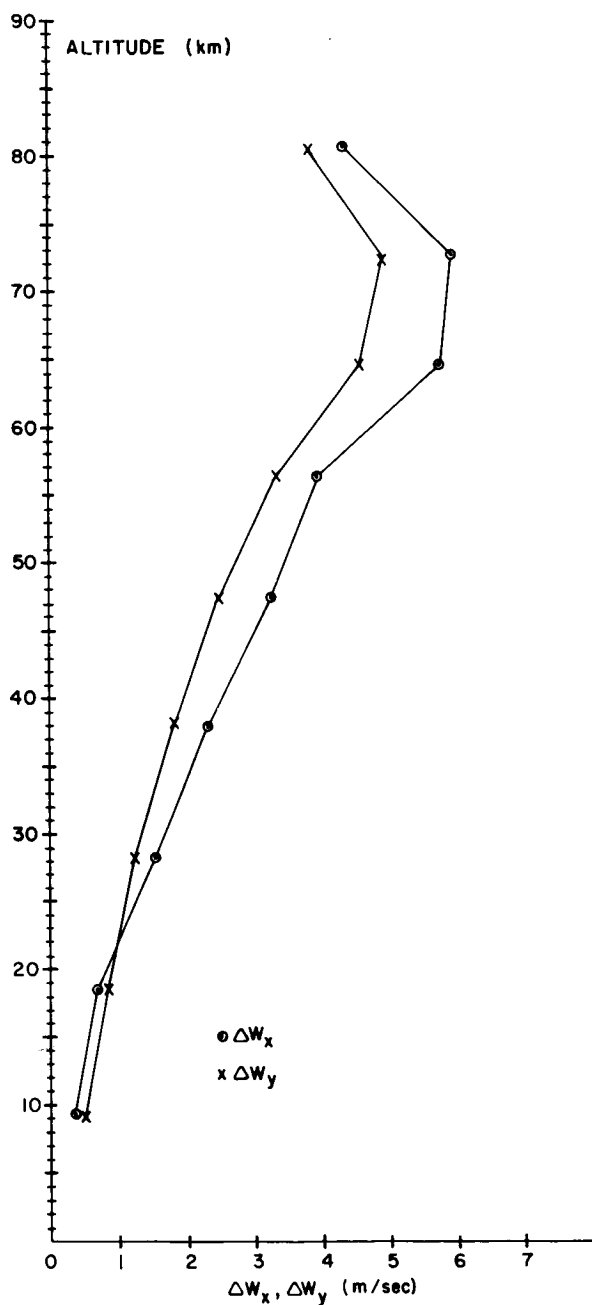
FIGURE 13.   EXPECTED MAXIMUM WIND ERROR
DUE TO 0. 5 MILLISECOND ERROR IN ALL
MICROPHONE TIMES

To the extent that these effects are random, they are reduced by use of the computer program for cross correlation since in this program the time difference between two channels is determined by an integration
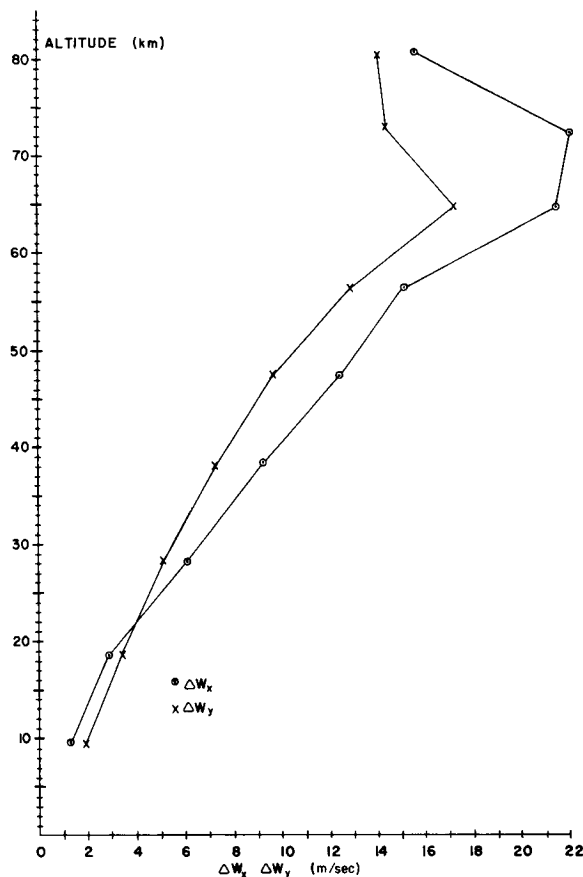

FIGURE 14.   EXPECTED MAXIMUM WIND
ERROR DUE TO 2 MILLISECONDS ERROR
IN ALL MICROPHONE TIMES

over a present segment of the data rather than from a single waveform characteristic.

The use of higher frequencies of the noise spectrum offers the possibility of increased precision in determining arrival times. Experimentation with wide-band microphones is planned to evaluate this possibility.

V.   CONCLUSION

The agreement between the wind profiles determined by the rocket exhaust noise technique and other simultaneous measurements is evidence of the validity of the acoustic technique described herein.

On the basis of the error analysis, the maximum errors are estimated to be about ± 20 m/sec at 85 km and decreasing to about ± 7 m/sec at 30 km.   These errors are attributed principally to inaccuracies in

117

determining arrival time and should be reducible by the use of improved measurement and data reduction techniques.

At locations where large booster rockets are launched regularly, a rather modest ground station can gather wind data from the ground to, in some cases, 85 km. These data measured concurrently with the space vehicle flight have important engineering value, and the upper atmospheric wind profiles measured on a regular basis would be an important supplement to the data available to meterologists.

REFERENCES

1. Scoggins, James R.: Aerodynamics of Spherical Balloon Wind Sensor. J. Geo. Res., vol. 69, no. 4, Feb. 1964, pp. 591-598.

REFERENCES (Cont'd)

2. Stroud, W. G.; Nordberg, W.; and Walsh, J. R.: Temperatures and Winds between 30 and 80 km. J. Geo. Res., vol. 61, no. 61, 1956, pp. 45-56.

3. Otterman, J.: A Simplified Method for Computing Upper Atmosphere Temperature and Winds in the Rocket-Grenade Experiment. Univ. of Mich. TR 2387-40-T, Army Contract No. DA-36-039-SC-64657, June 1958.

4. Manring, E.; Bedinger, J.; and Knaflich, H.: Space Research II. ed. H. C. van de Hulst, et al., North-Holland Publ. Co., Amsterdam, 1961, p. 1107.

5. Milne, E. A.: Sound Waves in the Atmosphere. Phil. Mag. 42, 1921, pp. 96-114.

6. Bushman, W. W.; Kakli, G. M.; Carignan, G. R.: An Acoustic Wind Measuring Technique. Univ. of Mich. TR 05911-2-T, Contract NAS8-11054, July 1965.

GROUND WIND MEASUREMENTS AND ANEMOMETER RESPONSE

By

James R. Scoggins and Dennis W. Camp

ABSTRACT

The theoretical response of inertia-type anemometers is presented. The determination of response parameters using theory and wind tunnel data is explained and examples given. A comparison of simultaneous anemometer measurements in a real wind environment is made from which inferences are drawn regarding the validity of response parameters determined in a wind tunnel. Finally, the ground (surface to 150 m) wind measurement program being conducted at the Eastern Test Range is discussed, and some practical problems in measuring ground winds are outlined.

I. INTRODUCTION

The measurement of wind speeds in a turbulent environment can be quite difficult depending upon the accuracy and resolution required. Reasonably accurate measurements of wind speeds averaged over time periods in excess of approximately one minute are easy to make. Such measurements are made routinely by government weather services and other organizations throughout the world. These measurements are considered adequate for general meteorological uses where gust structure is not considered important. Averaging in time filters out the gust structure regardless of how faithfully it may be reproduced by the instrument itself.

The accuracy and frequency resolution of wind measurements is determined by the response characteristics of the anemometer system. When measuring winds averaged over a few tens of seconds or longer, most conventional type anemometers probably provide adequate measurements (see section IV); however, if measurements of the gust structure are desired, conventional anemometers are, in general, not adequate (see sections II through IV).

The correct interpretation of measurements obtained by any anemometer is, in general, quite difficult but absolutely necessary if one is to draw correct conclusions. Think of how many "scientists" have drawn conclusions from data they themselves didn't understand!

It is the intent of this paper to review response theory as usually applied to inertia-type anemometers, to present results obtained in wind tunnels and in the free atmosphere, to describe the measurement program for ground winds at KSC, and to discuss some practical problems in measuring ground winds in general. The ultimate intent of this paper is to improve the overall understanding of measured ground winds and their interpretation, and to improve the understanding of the characteristics of anemometers commonly used to measure winds.

II. ANEMOMETER RESPONSE THEORY

The response of an anemometer is usually determined by assuming a linear relationship between input and output. This implies the relationship $0(t) = cI(t)$ where $0(t)$ is the output, $I(t)$ is the input, both a function of time, and c is constant for all time. In the general case, this relationship assumes the form of an ordinary linear differential equation of the form [1]

$$\sum_{k=0}^{n} A_k \frac{d^k}{dt^k} 0(t) = I(t) \qquad (1)$$

where the coefficients A_k are constant, and $I(t)$ is the input or forcing function. Equation (1) is a linear differential equation; however, $I(t)$ may contain nonlinear terms.

There are very few physical processes which are truly linear, and therefore may be accurately represented by equation (1). Why, then, is linearity so often assumed? In most cases, the primary reason is that the equations can be solved in closed form, and well defined and interpretable results can be obtained. The justification for assuming a linear system is that the solution approximates the true solution over a limited range of the variable. The range over which the solution is approximately valid depends upon the degree of nonlinearity of the system. A system is nonlinear if the A_k's are a function of $0(t)$ or if the derivatives in equation (1) are raised to a power greater than one.

The observed response of inertia-type anemometers may be approximated mathematically by the first-order linear differential equation [2]

$$\frac{dU}{dz} + \frac{1}{T} U = I(t),\qquad (2)$$

where U represents wind speed, I(t) the forcing function, and T the response time. This equation is a special form of equation (1) with $1/T$ replacing the ratio A_1/A_0. The solution of equation (2), where I(t) represents a step input function, is

$$U = \Delta U \left(1 - e^{-t/T}\right),\qquad (3)$$

where ΔU is the magnitude of the step input. From equation (3), we see that the response time is the time required for the variable to reach 63 percent of the final value of the step function. For example, if an anemometer experiences a sudden increase in wind speed of 5 m/sec, 63 percent of this sudden increase of wind will be indicated by the anemometer in a time equal to T. Obviously, the smaller T, the quicker the response of the anemometer. Now, if we define a response distance by the equation

$$L = U_0 T,\qquad (4)$$

where U_0 is the steady-state wind speed and L is the response distance, and letting X be the distance of wind flow past the anemometer, given by

$$X = U_0 t,\qquad (5)$$

then by substitution of equations (4) and (5) into equation (3) gives

$$U = \Delta U \left(1 - e^{-\frac{X}{L}}\right) .\qquad (6)$$

The parameters T and L may be used to define the response characteristics of an anemometer to a step input. The distance constant, L, is usually employed rather than T; the smaller the distance constant, the more rapid the response of the anemometer. From equations (3) or (6), we see that the wind speed as indicated by the anemometer approaches the true wind speed exponentially in time. During the time period equal to the response time, the anemometer will indicate 63 percent of the final value; during the next response time, it will indicate 63 percent of the remaining difference, etc. A graphical solution of equations (3) and (6) is shown in Figure 1.

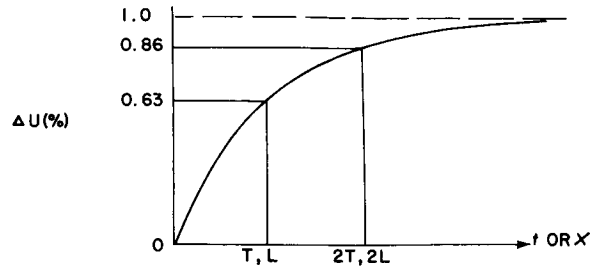A more realistic assumption regarding the forcing function, yet still grossly inadequate, is to assume

FIGURE 1. FIRST-ORDER RESPONSE TO STEP INPUT

$$I(t) = C \sin \omega t,\qquad (7)$$

where C is the amplitude of the sinusoidal input. The solution of equation (2) for this case is given by

$$U = C \left[\frac{1}{(1 + \omega^2 T^2)^{1/2}}\right] \sin (\omega T + \varphi)\qquad (8)$$

in terms of time, and by

$$U = C \left[\frac{1}{\left(1 + \frac{\omega^2 L^2}{U_0^2}\right)^{1/2}}\right] \sin\left(\frac{\omega X}{U_0} + \varphi\right)\qquad (9)$$

in terms of distance. In equations (8) and (9), φ represents the phase angle, ω is circular frequency and is given by $2\pi f$, where f is frequency in hertz, and the terms in brackets represent the amplitude ratio of the output to input. These equations show that the output differs from the input in both phase and amplitude. A plot of the amplitude ratio in either equation (8) or (9) as a function of frequency is called the response function or transfer function of the anemometer. It tells what percentage of the amplitude as a function of frequency is measured by the system for a given steady-state wind speed. A schematic representation of the transfer function and the phase angle is shown in Figure 2. It must be kept in mind that the solutions of the equations shown in
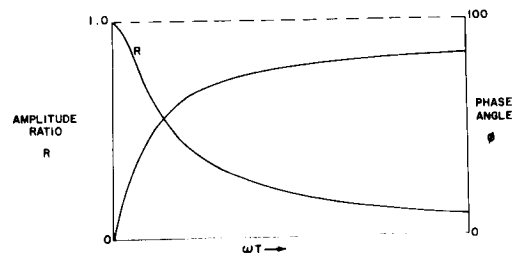

FIGURE 2. FIRST-ORDER RESPONSE TO SINUSOIDAL INPUT

120

Figures 1 and 2 are highly idealized by the assumption of linearity.

The mathematical treatment given above does not consider electronic filtering problems associated with most anemometers. Even if, say, a cup-type anemometer is determined to have a certain response capability defined by equation (2), its effective response may be much less because of signal conditioning and inadequate response of the data recording mechanism. Also, aerodynamics associated with the flow of air around the cups or the housing may produce additional uncertainties. Thus, the response of the system must be considered in the interpretation of data and not just the response of the sensor alone. Camp [3] gives a discussion regarding the effects of filtering on measured wind data.

In the mathematical treatment of wind sensors given above, only wind speed sensors were considered. For wind direction sensors (vanes), a second-order equation is required to represent the system mathematically. For purposes of this paper, it is sufficient to say that the solution to the second-order differential equation is in the form of exponentials. For those interested in the response of vanes, additional information may be found in reports by Camp [3], Adams [4], and Mazzarella [5].

A number of anemometers, which will not be discussed in detail in this paper, are available, but are not in general use. These include sonics, hot wires, drag spheres, vector vanes, etc. An attempt was made to perform comparison tests (see section IV) using these anemometers, but because of calibration, threshold speeds, drifts in calibration, head vibration of sonics, and other similar problems, it has not been possible to date to get satisfactory results. In general, these so-called faster response anemometers require constant personal attention during the period of operation, and even then, the accuracy and quality of the data are not adequately known.

III. WIND TUNNEL RESULTS OF ANEMOMETER RESPONSE

Camp [3] investigated the response of two anemometer systems in the White Sands Missile Range wind tunnel. Both of these anemometers were cup-types.*

_____

* In order that an endorsement of a particular anemometer system not be implied, the systems discussed in this paper will be denoted by A, B, C, D, and E rather than by their commercial names.

The procedure for determining the distance constant in a wind tunnel for an anemometer is to prevent the cups from rotating in the presence of a steady-state flow, then release the cups suddenly and note the acceleration. The position of the cups at the moment of release, especially for three-cup anemometers, influences the value of the response parameters determined. The initial cup orientation used by Camp in his work is shown in Figure 3.
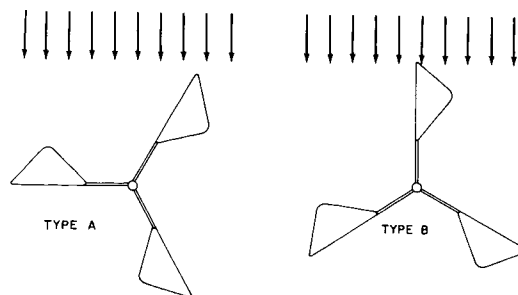

FIGURE 3. CUP ORIENTATION WITH REFERENCE TO WIND FLOW FOR ANEMOMETERS A AND B PRIOR TO RELEASE OF CUPS DURING WIND TUNNEL TESTS

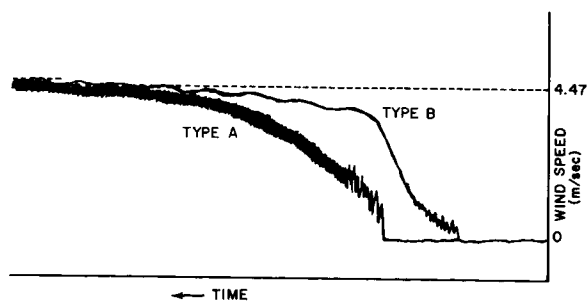Figures 4 and 5 show typical wind speed traces at wind speeds of 4.47 and 8.94 m/sec, respectively,

FIGURE 4. WIND SPEED TRACE FOR ANEMOMETERS A AND B FOR A TUNNEL WIND SPEED OF 4.47 M /SEC

obtained in the wind tunnel. The time constant is obtained by noting the time required for the anemometer to indicate 63 percent of the wind tunnel speed if one starts counting at the initial moment of release. The time constant may also be obtained by starting at any arbitrary point and determining the length of time required for the anemometer to indicate 63 percent of
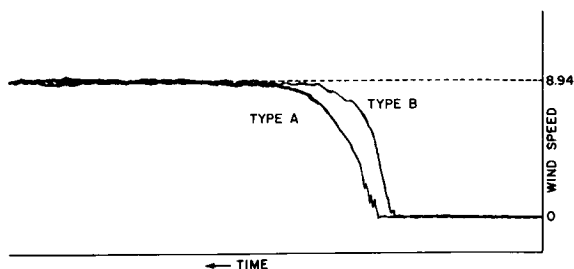
FIGURE 5. WIND SPEED TRACE FOR
ANEMOMETERS A AND B FOR A TUNNEL WIND
SPEED OF 8.94 M/ SEC

than does type A. However, for a different initial
cup orientation for the type B instrument, the re-
sponse distance may be somewhat larger.

Frequency response curves for the B type wind
sensor are shown in Figure 6 for the three wind speeds
employed in the wind tunnel tests. Similar curves
could be drawn for type A. As shown in the figure,
frequencies up to about 3 Hz can be measured with
reasonable amplitude resolution during high wind
speed conditions. Even during low wind speed con-
ditions (4.47 m/sec), 1 Hz can be measured reason-
ably well. These are highly idealized results which
must not be taken to represent the true response

the remaining difference between the indicated velo-
city and the tunnel velocity. Thus, we can obtain
several estimates of the time constant for an ane-
mometer for a given wind tunnel run.

Table I shows results taken from Camp's re-
port for anemometer types A and B for three wind
tunnel speeds, 4.47, 8.94, and 13.41 m/sec. As in-
dicated in the table, a number of wind tunnel runs
were made to establish the distance constant for
each speed category. The results obtained are be-
lieved to be highly accurate for the stated conditions
of the tests and the filters used to condition the out-
put signal. In all cases, the type B had a smaller
distance constant than the type A anemometer. This
means type B instrument has a faster response than
the type A, and therefore, if nonlinearities are in-
significant, this may be interpreted as meaning that
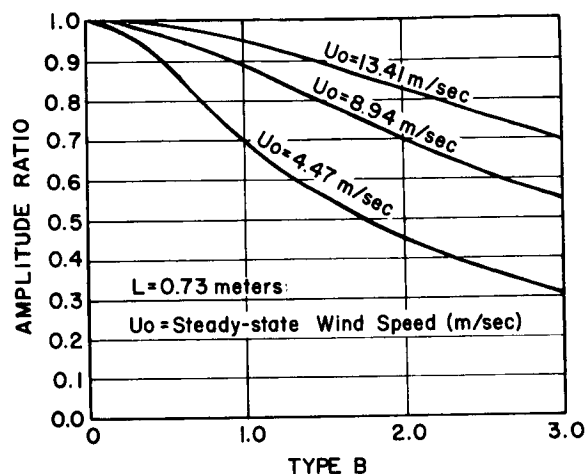the type B has a better frequency response resolution

FIGURE 6. FREQUENCY RESPONSE CURVES
FOR THE TYPE B WIND SENSOR

TABLE I. MEAN DISTANCE CONSTANT VALUES FOR ANEMOMETER TYPES A AND B OBTAINED
FROM WIND TUNNEL TESTS

| Instruments | Tunnel Wind Speed | | | | | |
| | 4.47 (m/sec) | | 8.94 (m/sec) | | 13.41 (m/sec) | |
	Distance Constant (m)	Number of Observations	Distance Constant (m)	Number of Observations	Distance Constant (m)	Number of Observations
A	1.22	42	1.12	35	1.09	38
B	0.72	31	0.72	31	0.77	38

characteristics of the anemometer (see section IV).

One of the most difficult problems to solve when acquiring high-resolution output from the cup anemometers discussed in this report is that of signal conditioning. The output from these anemometers is in the form of pulses. Anemometer type A gives forty pulses per revolution, while type B instrument gives 100 pulses per revolution. It turns out that the filtering problem is easier to handle and produces better results for the higher pulse rate. Figure 4 shows that the type A trace contains rather large amplitudes associated with each pulse and that these are superimposed on the average change of wind speed as a function of time. The trace from type B also contains superimposed small amplitude oscillations; however, the amplitude is much smaller and of a higher frequency than for the type A instrument. The output signal of type A had to be filtered more to reduce the amplitudes of the high-frequency ripple to within acceptable limits, whereas the output from the type B instrument could be filtered less and still achieve acceptable results. In principle, the type A anemometer should have a shorter distance constant than the type B anemometer, if we consider only the sensor response, but when we consider the system response, the type B anemometer, in this case at least, has the best response.

The turbulence level in wind tunnels is usually very low compared to the atmosphere. The extent of vibration in drag on the anemometer cups caused by turbulent flow is not known; however, it is known from space vehicle wind tunnel tests that the turbulence level does influence the vortex shedding and thereby changes the response of the vehicle to winds. It is reasonable to expect that a similar phenomenon occurs in relation to cup-type anemometers. Thus, the validity of distance constants determined in wind tunnel tests may not be directly applicable to measurements made in the free atmosphere. This subject is considered further in section IV.

IV. COMPARISON OF ANEMOMETERS IN THE REAL ENVIRONMENT

The theoretical response of anemometers was developed in section II and applied in section III. Wind tunnel results were used to establish the response characteristics of two anemometer systems. As pointed out in section II, the theoretical results may not be applicable in the real atmosphere because of nonlinearities. Applicability of theoretical and wind tunnel results was investigated by exposing several anemometers simultaneously to the real environment, then analyzing the results on a comparative basis. This section presents the results of those studies.

Four commonly used anemometers, type A, C, B and D were mounted on a crossarm perpendicular to the wind direction [6]. Time-correlated measurements from all anemometers were recorded on magnetic tape simultaneously. When facing into the wind, the anemometers were oriented on the crossarm in the following order reading from left to right: type A, C, D and B. These sensors were located approximately 3 ft (0.9144 m) apart. To eliminate a possible bias due to the separation of the instruments, only statistics of the measured wind speeds were analyzed.

Table II, taken from Camp's report, summarizes the statistical results from five anemometer comparison tests. Presented in the table are mean wind speeds for each anemometer, the variances about the mean, and the percent of the total variance for periods equal to or greater than 5 sec. The means and variances were computed for a 5-min time period. Considering tests 1, 2, and 3, the mean wind speeds differed by as much as 25 percent while the variances differed by more than 50 percent. Variances associated with the type D measurements are smaller than those associated with measurements of the other anemometers. This was expected since type D has a slower response than the other anemometers. However, one would not expect, based on the theoretical and wind tunnel results presented in sections I and II, anemometers A and B to provide significantly different results. Three cups

TABLE II. STATISTICS FOR FIVE ANEMOMETER COMPARISON TESTS

Anemometers	Mean Wind Speed (m/sec)	Variance About Mean (m²/sec²)	Percent Variance For P ≥ 5 sec
	Test 1		
A	6.73	1.66	0.89
B	7.77	1.14	0.91
C	7.97	2.26	0.93
D	6.16	0.99	0.99
	Test 2		
A	3.51	0.89	0.90
B	3.31	1.53	0.92
C	2.94	1.03	0.92
D	3.52	0.86	0.98
	Test 3		
A	3.88	1.48	0.85
B	3.06	2.12	0.87
C	3.32	1.77	0.86
D	3.74	1.38	0.93
	Test 4		
D	4.23	0.79	0.98
E	4.67	1.03	0.98
	Test 5		
D	4.28	0.39	0.98
E	4.47	0.54	0.97

were used with type A for these tests since the six-cup assembly was not available. This may have had some influence on the values obtained for this anemometer. Results from tests 4 and 5 presented in Table II compare anemometer types D and E. As shown in the table, there is no significant difference between these two anemometers.

Spectrum techniques were employed to examine the distribution of the total variance over frequency in an effort to account for the large differences in variances, and also to compare the results with theoretical and wind tunnel results presented above. Spectra associated with the five tests presented in Table II are shown in Figure 7. Aliasing was not considered, and trends, if any were present, were not removed. These spectra must be considered tentative until more comprehensive results are available.

In test 1, the spectra are quite different over all frequencies, but in all other tests, rather good agreement is shown for all frequencies. However, there is a divergence in the curves for periods greater than 5 to 10 sec with no noticeable consistency in tests 1 through 3. The normalized spectra were integrated to obtain the percent of variance accounted for by periods 5 sec and longer. These results are presented in Table II. Tests 4 and 5 are quite consistent and not very different over all frequencies. With the exception of type D, which filters out the higher frequencies rather effectively, differences in the measured variances are distributed over all frequencies rather than being confined to a particular region of the spectrum. This implies that gusts with periods of several seconds or longer may not be measured accurately. The spectrum curves were drawn by eye to best represent the calculated spectral estimates.
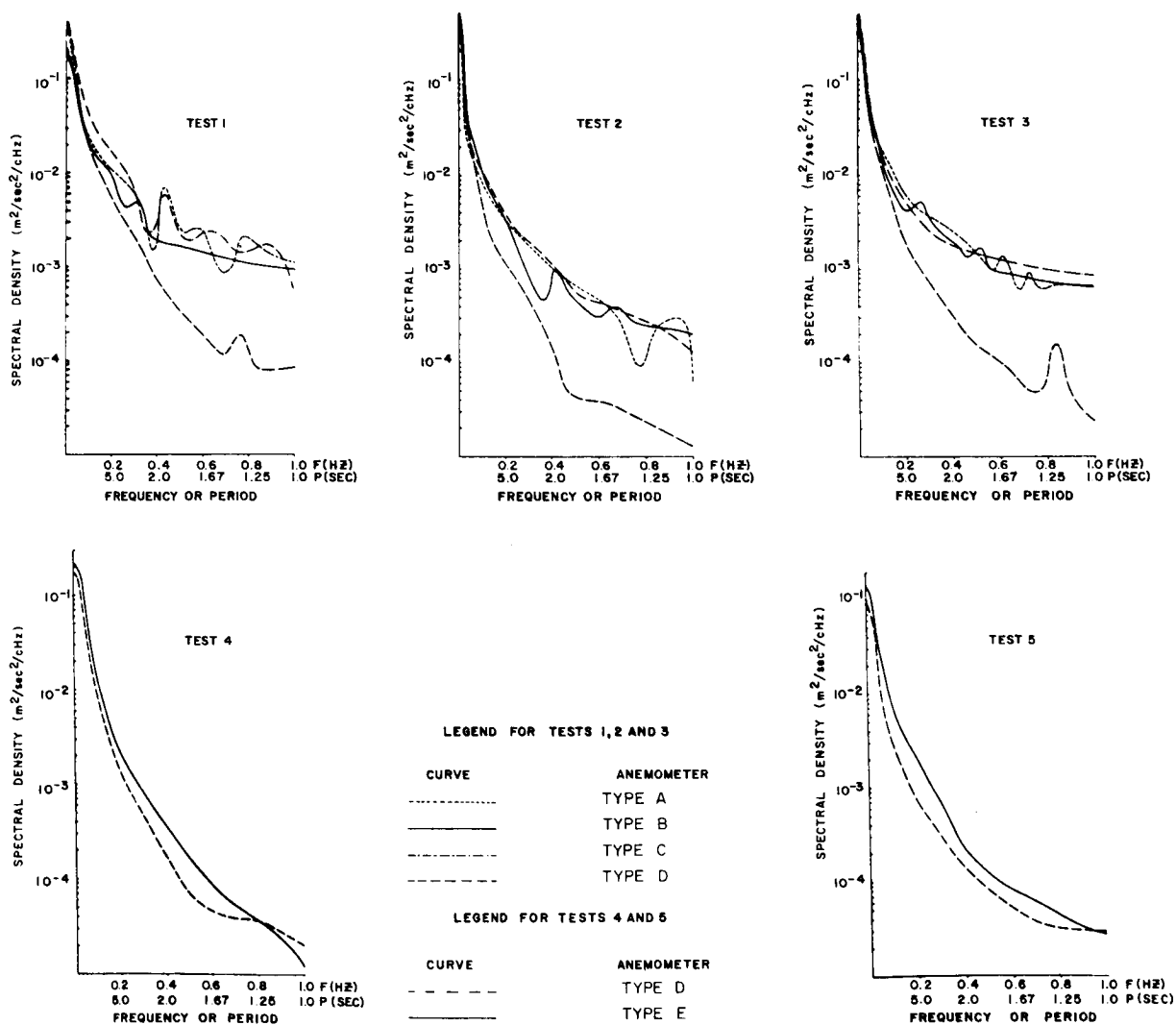

FIGURE 7. SPECTRA OF WIND SPEEDS FOR ANEMOMETER COMPARISON TESTS

124

.In drawing spectral curves through the computed spectral estimates a considerable amount of smoothing was done. An important conclusion which can be reached from these spectra is that the theoretical and wind tunnel results presented in sections II and III are not verified for the real environment. According to Figure 6, types A and B instruments should be capable of measuring gusts with periods on the order of one second or less with a reasonable amplitude resolution. Thus, the logical conclusion seems to be that nonlinearities occur which are not accounted for by the theory.

Results from tests 4 and 5 show that types D and E have very similar characteristics, measuring the same winds and variances, and have the same statistical distribution of the variances over frequency. From the results presented here, it does not appear that the higher frequencies (periods less than about 5 sec) can be measured with confidence using any of the anemometers tested.

V. THE MEASUREMENT OF LOW ALTITUDE (SURFACE TO 150 m) WIND AT THE KENNEDY SPACE CENTER (KSC)

There is a need for improved low-altitude wind measurements at KSC for use in such programs as the response of space vehicles to ground winds, atmospheric diffusion, launch operations, vehicle design studies, etc. Most wind measurements collected to date have been made at a single location near the ground or on structures with poor exposure. None of these measurements have provided adequate details of the gust structure. A 500-ft (150-m) meteorological tower has been built by NASA at Kennedy Space Center for the purpose of measuring low-altitude winds for use in various programs. Figure 8 shows a schematic of the tower facility and the location of wind, temperature, and humidity sensors. The tower facility is located on Merritt Island about 3 mi (4.8 km) from launch complex 39 and about the same distance from the coastline.

The main tower is triangular in shape, 8 feet (2.44 m) on a side, and contains instrumentation as shown in Figure 8. A small tower is located 18 m to the northeast of the major tower for collecting data near the ground where the exposure on the big tower is poor. Anemometers are dual-mounted on the northeast and southwest side of the big tower on 12-ft (3.66-m) booms, but only on the northeast side of the small tower. Humidity measurements are made at two locations, 3 and 120 m. The absolute value of temperatures is measured at the 3-m level
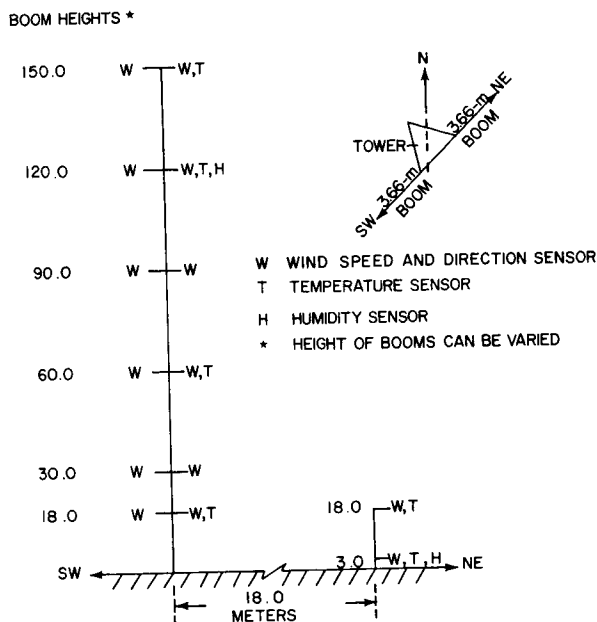

FIGURE 8. SCHEMATIC OF NASA'S 150-m METEOROLOGICAL TOWER AT CAPE KENNEDY FLORIDA

with temperature differences being measured between 3 and 18 m on both the large and small towers, 3 and 60, 3 and 120, and 3 and 150 m. Neither the temperature nor humidity elements are dual-mounted.

Paper strip chart recorders are used to record all wind, temperature, and humidity data inside a building located near the base of the tower. In addition, a 14-channel magnetic tape can be used to record wind data with high resolution and accuracy. Wind data are recorded from either the northeast or southwest side of the tower at all levels, but not from both sides simultaneously. An automatic switching device is included in the facility for selecting the best exposed bank of instruments. The tape recorder may be used automatically to record wind data once each hour or at other predetermined time periods, or it may be operated in a manual mode for collecting data upon command. The magnetic tape is used only to collect data for gust and turbulence studies.

The humidity is measured by the Foxboro dew cell, temperature by Climet aspirated thermocouples, and wind by Climet anemometers. The meteorological tower facility is fully operational.

125

VI. SOME PRACTICAL PROBLEMS IN MEASURING SURFACE WINDS

Accurate high-resolution wind measurements are difficult to make and, as pointed out above, the commonly used anemometers are not adequate for this purpose. When such measurements are attempted, there are several problem areas which must be considered. Some of these are discussed in this section, but there will no doubt be many others associated with specific installations.

One of the first problems which must be considered in the measurement of low-altitude winds is that of establishing the need for and applications of the wind measurements. If one needs only 5-min averaged winds, the instrumentation required may be different, and in some cases much simpler, than the instrumentation required for measuring high frequency fluctuations. Also, data recording requirements may be a function of the intended application of the measurements. The next problem is the selection and testing of instrumentation. It is important to select a reliable instrument with the desired operational characteristics. The importance of experimentally evaluating the instrumentation is quite clear from the results presented above.

Regardless of how good the sensor responds to the wind, the degree of signal conditioning (filtering) required to eliminate undesirable output signals is of primary importance. The output signal from most anemometers is in the form of pulses and must be smoothed or filtered to get an output which can be properly interpreted. As pointed out in section III, the effectiveness of the electronic filters is a function of the pulse rate. For a low pulse rate, a high degree of filtering may be required to eliminate undesirable output signals (see Fig. 4). A high degree of filtering may eliminate signals representing wind variations, especially the higher frequencies. Also related to the signal conditioning (filtering) problem is that of adequate data recording facilities. The accuracy and resolution of the data recording equipment should be slightly better than any other component of the system. Paper strip chart records commonly used have some maximum frequency response beyond which they are incapable of recording fluctuations in the output signal. In most cases, these recorders act as a filter for high-frequency signal variations and, therefore, may in effect reduce the capability of the anemometer system even though the sensor may have a far greater frequency response. This leads into perhaps the most important problem of all--the total system response characteristics. The old adage that "A chain is no stronger than its weakest link " might be paraphrased to "The response of an anemometer system is no better than the response of any one of its components. "

The last problem area discussed here is that of instrument exposure. While this had nothing to do with the capability of the instrumentation itself, it does influence the validity of the measurements. Because of structure interference, a dual system of anemometers was mounted on NASA's 150-m meteorological tower at KSC (see section V). With two sets of instrumentation, it is possible to eliminate some of the structure interference by recording wind data from the best exposed bank of anemometers; however, the problem is still not completely eliminated. Another important consideration in the exposure of anemometers is the interference due to the surrounding area. If instruments are mounted in the vicinity of man-made structures or in the wake of natural obstacles, the measured wind conditions would not be representative of the free atmosphere. The exposure problem is quite important when considering the response of space vehicles to winds. In this case, a free atmosphere exposure may not be the most desirable since there are usually structures located in the vicinity of the vehicle.

VII. COMMENTS AND CONCLUSIONS

The response characteristics of anemometers determined from wind tunnel results and based on first-order response theory are not consistent with results obtained from comparison tests of anemometers made in the real environment. A logical conclusion is that the linear response theory is not adequate or the aerodynamics associated with flow around the cups introduce unsteady torques which produce error in the measured wind speeds. One possible solution to the aerodynamics problem, as suggested recently to several instrument manufacturers, would be to perform flow visualization tests using smoke or some other tracer in a wind tunnel. Such tests might serve to pinpoint aerodynamics problems or cup interference.

There are many problems to consider when designing a wind measuring facility. Briefly stated, some of these are (1) establishing a need for and application of wind measurements, (2) selection and testing of instruments (sensors), (3) signal conditioning (filtering), (4) adequacy of data recording equipment, (5) system response characteristics, and (6) instrument exposure (structure interference and surrounding area).

All of the problem areas presented above were carefully considered in the planning and construction of NASA's 150-m meteorological tower at KSC. The primary purpose of this facility is to provide data for turbulence research, and therefore the measurement of gust structure is of primary importance. Dual anemometer systems were installed at each height on the 150-m tower. Strip chart recorders and anemometers are being replaced on the basis of the problem areas noted above. Provisions have been made to install high-response anemometers on the tower; this will be done as soon as a high-response system is proven to be reliable and accurate. Tower motions may prove to be a problem when high-response anemometers are installed. This problem remains to be investigated. With the exception of the high-response anemometers, the 150-m meteorological tower facility at KSC is fully operational, and is believed to be one of the best facilities of its type in the United States.

REFERENCES

1. Ferris, Clifford D.: Linear Network Theory. Charles E. Merrill Books, Inc., 1962.

REFERENCES (Concluded)

2. MacCready, Paul B., Jr.: Response Characteristics and Application Techniques of Some Meteorological Sensors. MRI 63 Pa-86, Meteorology Research, Inc., 1963.

3. Camp, Dennis W.: Analysis of Wind Tunnel Data for Several Beckman and Whitley Series 50 and Climet Model C1-14 Anemometers, NASA TM X-53271, 1965.

4. Adams, Gerald H.: Wind Equipment Evaluation. NBS Rept. 3316, 1954.

5. Mazzarella, Daniel A.: Wind Tunnel Tests on Seven Aerovanes. Rev. Sci. Instr., vol. 25, no. 1, 1954.

6. Camp, Dennis W.: Preliminary Results of Anemometer Comparison Tests, NASA TM X-53451, 1966.

VII. ORBIT FLIGHT MECHANICS

SOLAR PRESSURE PERTURBATIONS ON THE ORBIT OF A FLAT REFLECTOR

By

Scott Perrine

SUMMARY

Presented are the effects of solar pressure on a flat reflecting satellite. An equation for solar pressure is developed, and its effect on a two-dimensional orbital mechanics model is determined. Specific examples of 24-, 12-, and 6-hr period orbits are investigated. These orbits are, in general, shown to be perturbed into ellipses with constantly changing eccentricities, but with reasonably constant semi-major axes. Specific cases were found, however, where the eccentricity of the ellipses remained constant and the major axes remained oriented along the earth-sun line.

I. INTRODUCTION

It is evident for many cases that the basic Keplerian equations arising from an inverse square gravitation force law are not adequate for the precise calculation of positions and orbits of satellites and space probes. Perturbations to this simple law arise from numerous sources. Gravitational fields of other bodies, oblateness of the earth, atmospheric drag, and the barycenter of the earth-moon system are the principal causes of perturbing forces. A perturbation which is particularly important for satellites with large area-to-mass ratios results from solar pressure. Experimental evidence of this perturbation has been obtained from satellites such as Echo [1]. A considerable number of theoretical publications have addressed themselves to the effect of solar pressure on spherical satellites; this report considers the perturbations caused by solar radiation incident on a large planar satellite.

II. SOLAR RADIATION PRESSURE

Light pressure is derived from the interaction of matter and radiation. The derivation of this pressure can be made from electromagnetic theory [2] or from the standpoint of photons striking a surface. In the derivation here, the latter viewpoint will be considered for specularly reflected radiation. Figure 1 shows a photon being specularly reflected from a surface.
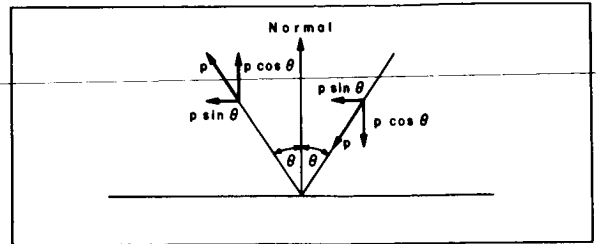

FIGURE 1. PHOTON REFLECTION

The detailed analysis of the interaction of the photon with the surface is unimportant if the momentum, p, of the photon is known before and after reflection. From the figure, it is evident that the component of the momentum parallel to the surface, $p \sin \theta$, is unchanged, while the change in the component normal to the surface is $2p \cos \theta$. The momentum of a photon with frequency, ν, is $h\nu/c$, where h is Planck's constant and c is the velocity of light. The number of photons with frequencies between ν and $\nu + d\nu$ incident on the area, dA, in time, dt, is evident from Figure 2.
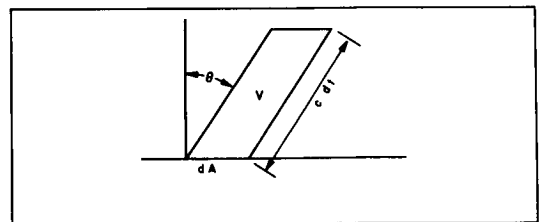

FIGURE 2. NUMBER OF PHOTONS STRIKING dA IN THE TIME dt

All the photons in the volume V in the figure will be incident on dA in time, dt.

$$V = c \, dt \, \cos \theta \, dA$$

If dn_ν is the number of photons per unit volume with frequencies between ν and $\nu + d\nu$, then the number

of these photons incident on dA in time, dt, is c $\cos\theta\, dn_\nu\, dA\, dt$. The force, dF_ν, on dA due to the photons with these frequencies is the change in momentum per photon, times the number of photons incident per time, dt.

$$dF_\nu = (2h\nu \cos\theta/c)(c \cos\theta\, dn_\nu\, dA)$$

$$= 2 h\nu \cos^2\theta\, dn_\nu\, dA$$

The direction of dF_ν is normal to dA since the component of momentum parallel to dA is unchanged. The force on dA caused by the entire spectrum, integrating over all frequencies, is given by

$$dF = \int_\nu 2h\nu \cos^2\theta\, dn_\nu\, dA,$$

and therefore the pressure is

$$P = 2 \cos^2\theta \int_\nu h\nu\, dn_\nu .$$

Now define the solar constant, S, as the total solar energy falling on a unit area, normal to the radiation, per unit time. As before, the number of photons with frequencies between ν and $\nu + d\nu$ incident on dA in time, dt, is $c\, dn_\nu\, dA\, dt$ (since θ is zero for a normal area). Since the energy of each of these photons is $h\nu$, the energy of the total is

$$dE_\nu = h\nu\, c\, dn_\nu\, dt\, dA.$$

The energy due to the entire spectrum is, then, integrating over all frequencies,

$$dE = \int_\nu h\nu\, c\, dn_\nu\, dt\, dA.$$

Since

$$S = \frac{dE}{dt\, dA} = \int_\nu h\nu c\, dn_\nu ,$$

$$P = \frac{2S}{c} \cos^2\theta$$

gives the pressure on an element of surface with a normal oriented at an angle θ from a vector directed to the sun. The solar constant, S, is a measurable quantity and at the distance of the earth's orbital radius from the sun is 1400 W/m^2 [3]. The pressure is quite small; to obtain a force of 1 lb, a circular disk approximately 0.5 mi in diameter is required.

However, as will be shown, the cumulative effect of this force on the motion of the satellite is considerable for low-density satellites in high-altitude orbits.

III. DISCUSSION AND RESULTS

A. POSIGRADE ORBITS

A majority of the important perturbation effects due to solar pressure can be discovered by the investigation of a two-dimensional model which considers all positions, velocities, and accelerations to be in one plane. Reasonable accuracy can be derived from this simulation for low-inclination satellite orbits. The shape of the satellite and its orientation history determine the perturbations that will be encountered. This report considers only a flat satellite which is specularly reflective on both sides. The satellite is reoriented continuously such that the sun's rays will be reflected toward the center of the earth; i.e., the normal to the satellite reflective surface bisects the angle between a vector to the sun and a vector to the earth's center. The solar pressure force is in the opposite direction from this normal and has a magnitude, from the first equation, $F = \frac{2SA}{c} \cos^2\theta$, where A is the area of one side of the satellite. The qualitative effect of the perturbing force is illustrated in Figure 3.
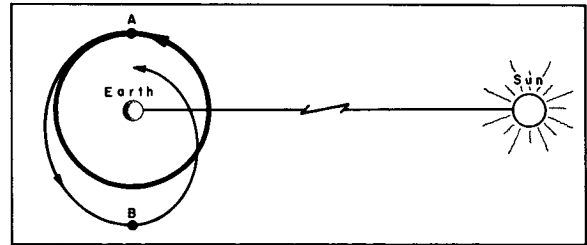

FIGURE 3. INITIAL PERTURBATION

Initially the satellite is in a circular orbit (heavy circle). While the satellite is on the upper half of the orbit, the perturbing force adds kinetic energy. This tends to create a perigee at point A and an apogee at point B. The contrary is true on the lower half as the solar pressure reduces the kinetic energy, thereby lowering perigee. As shown in Figure 4, this process continues with alternately increasing apogee and decreasing perigee, but with the semimajor axis remaining almost constant and aligned 90° from the earth-sun line.

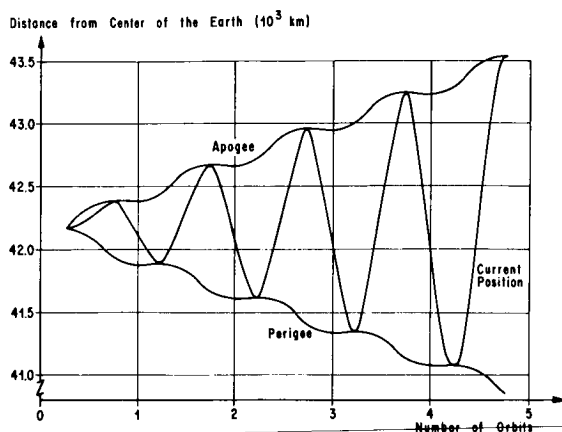Distance from Center of the Earth (10^3 km)

FIGURE 4. PERIGEE - APOGEE PROFILE

To facilitate the explanation of the long-term effects of these forces, it is expedient here to state several general principles, the first of which involves the motion of the major axis of the ellipse. If the major axis of the ellipse is not aligned perpendicular to the earth-sun line (nominal orientation), the same forces which were acting in Figure 3 will tend to restore the major axis to the nominal position.* The rate of the major axis rotation depends upon the eccentricity of the ellipse and its instantaneous orientation. For any given eccentricity, the rotation rate is a maximum when the major axis is oriented along the earth-sun line and zero when in the nominal position or 180° from the nominal position. For a specified orientation, the rotation rate decreases as the orbital eccentricity increases. Another principle involves the rate of change of the eccentricity of the ellipse. This rate is dependent upon the orientation of the perigee point relative to the earth-sun line. When the perigee point is on the earth-sun line between the earth and sun, the rate is zero. Measuring counterclockwise from this position, the rate reaches its positive maximum at the 90° point. At 180°, the rate is again zero. From 180° to 360°, the forces which acted in Figure 3 to increase eccentricity now tend to decrease the eccentricity of the elliptical orbit. The rate reaches a negative maximum when perigee is at the 270° point.

Keeping these effects in mind, consider the following example. A flat satellite with an area-to-mass ratio of 42 m²/kg is placed into a circular synchronous orbit (radius = 42 164 km). (Figure 5 presents a schematic of the perturbation history of such a case.) Initially, perigee begins to form 90° from the earth-sun line. As the earth revolves about the sun, the perpendicular to the earth-sun line moves away from the major axis of the ellipse;

however, the tendency of the major axis to return to the nominal position gradually rotates it counterclockwise. After approximately six months, the earth-sun line has rotated 180°, while the major axis
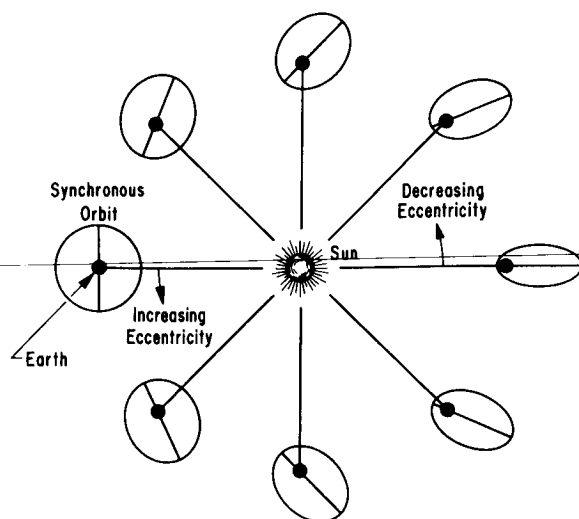

FIGURE 5. PERTURBATION HISTORY

has shifted only 90°, and the eccentricity has increased to the extreme value depicted. Beyond this time, the perigee point moves to the side of the orbit where the solar pressure decreases the kinetic energy; however, the opposite effect occurs at apogee. These two effects combine to decrease the eccentricity of the ellipse. After approximately one year, the orbit returns quite close to the original circular orbit. During this time, the semimajor axis, and thus the period (synchronous), remains almost constant. It is instructive to consider the locus of perigee and apogee relative to the earth-sun line in Figure 6. The perigee locus begins 90° from the earth-sun line and moves toward 0°. In this figure, the apparent motion is away from the nominal position since the earth-sun line is actually moving in a counterclockwise direction at a greater rate than the major axis. The rotation rate of the perigee point is approximately constant, apparently independent of the eccentricity. This can be explained from the first principle stated before. In the region where the eccentricity is at a maximum, the major axis is closest to the earth-sun line where its tendency to return to the nominal position is greatest. Thus, these two effects offset each other.

If this satellite had been injected into one of the ellipses which is a member of the locus in the figure, it is obvious that this ellipse would continue along the same locus shown. But now consider an orbit which

* This is the tendency caused by the solar pressure perturbation and neglects other effects such as the revolution of the earth about the sun.
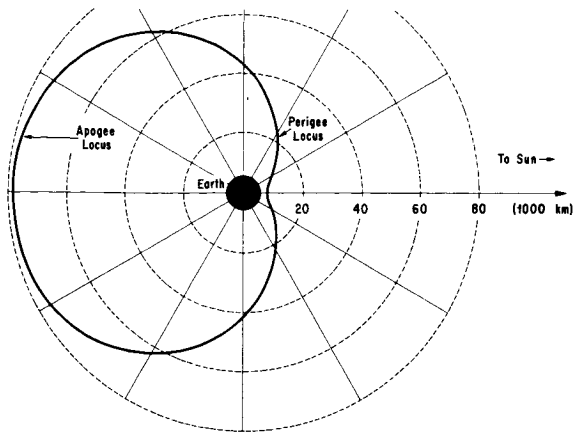
132

FIGURE 6. PERIGEE - APOGEE LOCUS RELATIVE
TO E-S LINE

is not a member of the locus. For example, inject
the satellite into an ellipse with perigee at A and
apogee at B, as in Figure 7, but keep the same
semimajor axis and orbital period as before. Now
the two effects mentioned before no longer offset
each other. The eccentricity of this conic is less;
therefore, the major axis moves counterclockwise
at a faster rate, and when the eccentricity becomes
small enough, this rate exceeds that of the earth-sun
line. The locus of perigee and apogee will make the
closed figures shown. On the other hand, if the
satellite had been injected into a more eccentric el-
lipse, for example, with perigee at C and apogee at
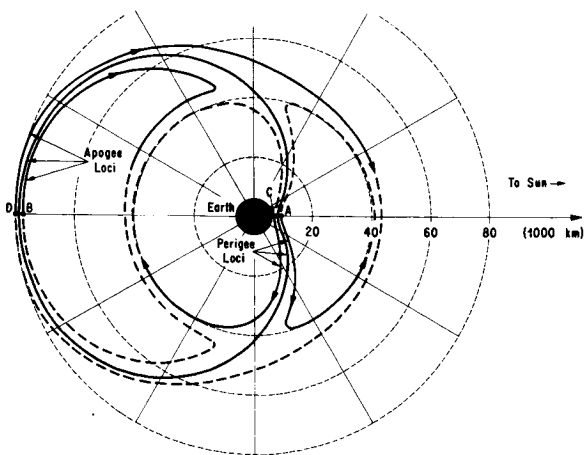
FIGURE 7. OTHER PERIGEE - APOGEE LOCI

D, the rotation of the major axis would be slower
than for the original case and the perigee point would
pass eventually on the opposite side of the earth from
the sun. In fact, while perigee is on this side, the
major axis actually rotates clockwise to return to
the nominal position. Thus, there are two families
of perigee loci and two corresponding families of
apogee loci separated by the perigee-apogee locus
of the original case. These families are shown in
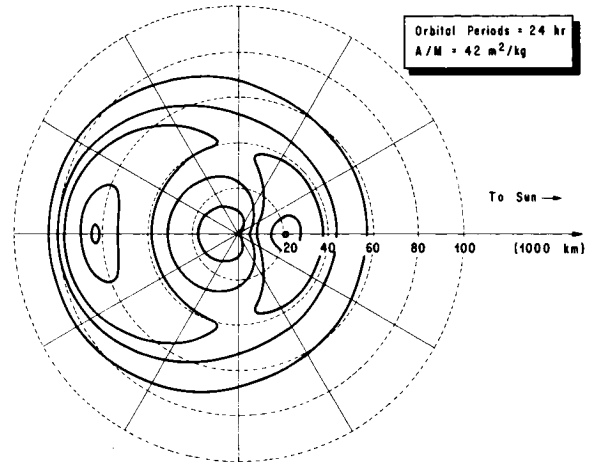Figure 8. Some of these cases are academic in that

FIGURE 8. PERIGEE - APOGEE LOCI
RELATIVE TO E-S LINE

their perigees lie beneath the earth's surface. There
is one case in each of these families in which the
eccentricity remains constant [4]. One of these
stable cases is a degenerate orbit with a perigee at
the center of the force field and an apogee at about
84 000 km. The stable orbit belonging to the other
family is of great interest. Its eccentricity not only
remains constant, but also it maintains a constant
orientation relative to the earth-sun line. The perigee
remains at a radius of 21 000 km directly between the
earth and sun, and apogee remains at 63 000 km on
the opposite side of the earth. This case is shown
schematically in Figure 9.

The above cases were all for a satellite with an
area-to-mass ratio of 42 m^2/kg. Figures 10 and 11
provide similar families of orbits with synchronous
periods for satellites with area-to-mass ratios of 21
and 10.5 m^2/kg, respectively. Note that the stable
orbits are evident in these cases also, and that the
eccentricity of the stable orbit decreases with de-
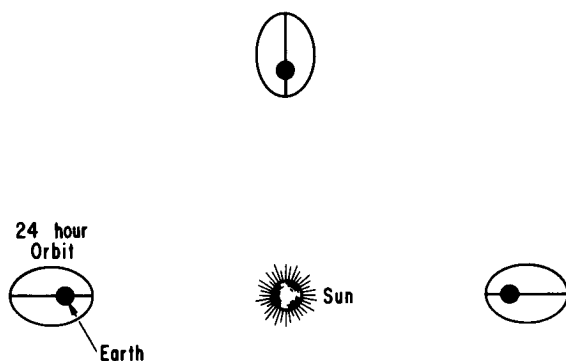creasing area-to-mass ratio.

24 hour
Orbit

Earth

Sun

Orbital Periods = 24 hr
A/M = 10.5 m²/kg

To Sun →

20   60   80   100   (1000 km)

FIGURE 11.   PERIGEE - APOGEE LOCI

FIGURE 9.   PERTURBATION HISTORY (STABLE)

Orbital Periods = 24 hr
A/M = 21 m²/kg

To Sun →

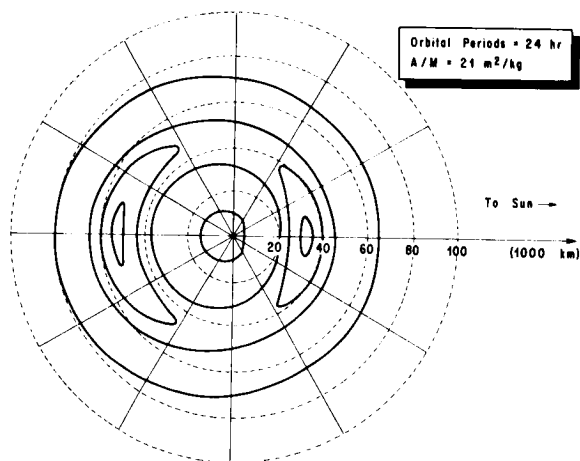20   40   60   80   100   (1000 km)

FIGURE 10.   PERIGEE - APOGEE LOCI

Orbits of other periods also were considered.
Figures 12, 13, and 14 show the families of orbit with
12-hr periods for various area-to-mass ratio, and
Figures 15, 16, and 17 show families of 6-hr orbits.

Figure 18 presents the eccentricities of the
stable orbits for intermediate values of the area-to-
mass ratio.

Orbital Periods = 12 hr
A/M = 42 m²/kg

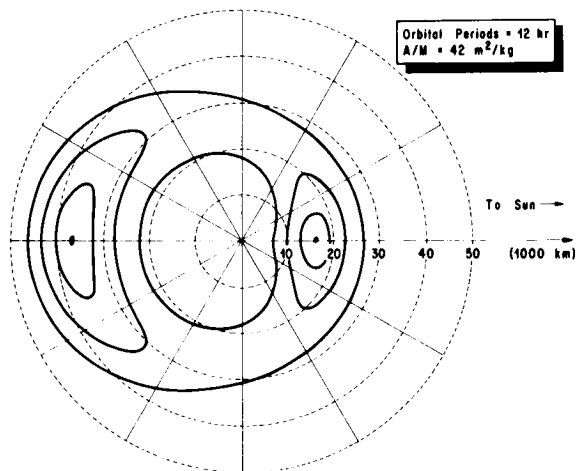To Sun →

10   20   30   40   50   (1000 km)

FIGURE 12.   PERIGEE - APOGEE LOCI

B.   RETROGRADE ORBITS

Thus far, only posigrade orbits have been
considered. The same principles apply to retrograde
orbits. For these orbits, the changes in kinetic
energy and apses location occur 180° away from their
posigrade counterparts. As before, elliptical orbits
whose major axes lie away from a new nominal
orientation (180° from the former) will tend to re-
turn to it.

Consider a satellite with an area-to-mass ratio
of 42 m²/kg injected into a 24-hr circular retrograde

134
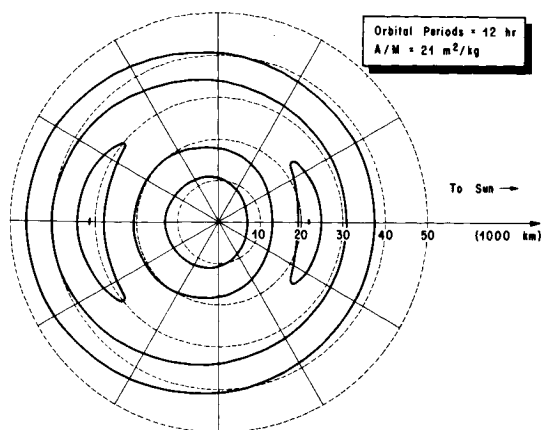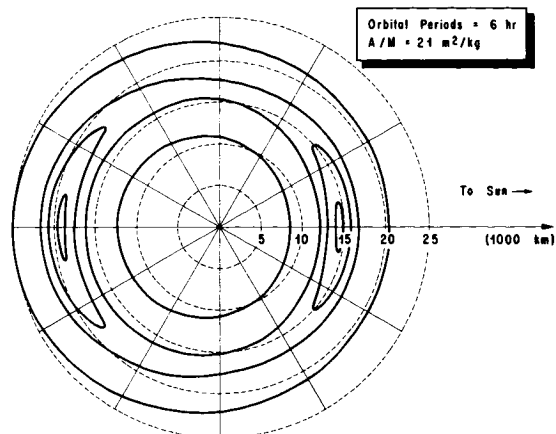
FIGURE 13.   PERIGEE - APOGEE LOCI
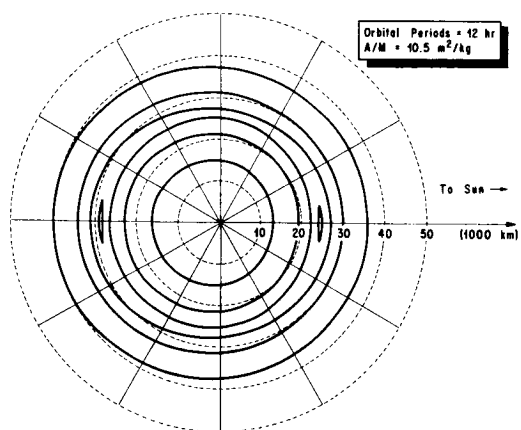

FIGURE 16.   PERIGEE - APOGEE LOCI

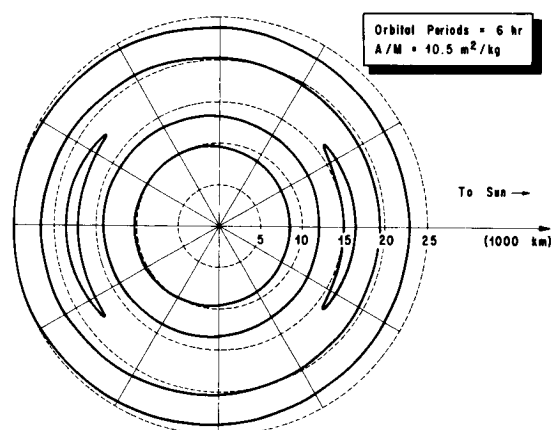FIGURE 14.   PERIGEE - APOGEE LOCI
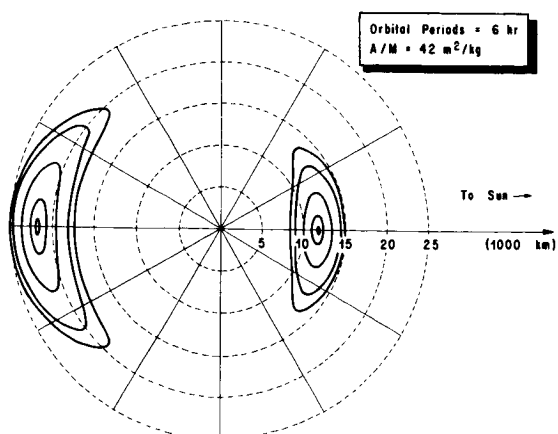

FIGURE 17.   PERIGEE - APOGEE LOCI

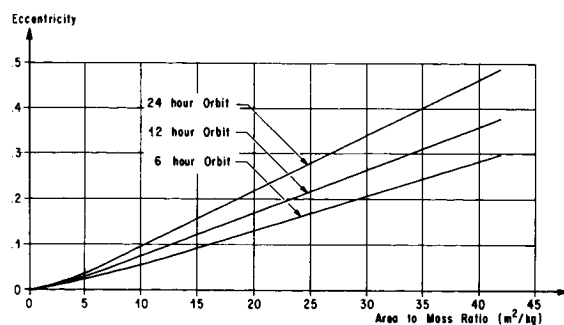FIGURE 15.   PERIGEE - APOGEE LOCI

FIGURE 18.   ECCENTRICITY OF STABLE
ORBITS

orbit. A perturbation history is obtained such as
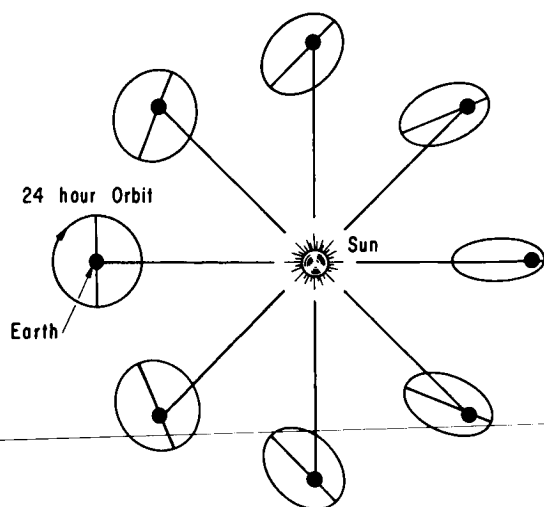shown in Figure 19. Note that the perigee locus falls

FIGURE 19. RETROGRADE PERTURBATION
HISTORY

FIGURE 20. RETROGRADE PERIGEE – APOGEE
LOCI

on the side of the earth opposite the sun. This case
divides two families of elliptical retrograde orbits
shown in Figure 20. As in the posigrade cases, there
is a practical stable case but with an apogee on the
sun side now. The eccentricity of this stable orbit
is considerably less than that for the posigrade orbit:
(0.27 as compared to 0.49.) This is due to the smaller
time average of the solar pressure in the retrograde
case.

IV. CURRENT ACTIVITIES

A more sophisticated simulation of the problem
is now being made. This simulation includes all
out-of-plane forces and seasonal effects. Perturbations
caused by the sun, moon, and oblateness of the earth
are being considered. The effects of other orientation
histories for the satellite are also being determined.
The results of these studies will appear in a later
publication.

REFERENCES

1. Shapiro, I. I. and Jones, H. M.: Perturbations
    of the Orbits of the Echo Balloon. Science 132,
    3438, 1960.

2. Heybey, W. H.: On Radiation Pressure and its
    Effects on Satellite Motion. NASA TM X-53462,
    1966.

3. OMSF document M-DE 8020.008B, Natural En-
    vironment and Physical Standards for the Apollo
    Program. Apr. 1965.

4. Shapiro, I. I.: Sunlight Pressure Perturbations
    on Satellite Orbits. Adv. Astron. Sci., 1963.

VIII. SELENOGRAPHY

LUNAR SURFACE: AN INTERPRETATION BASED ON PHOTOGRAPHIC DATA FROM THE RUSSIAN LUNA IX AND UNITED STATES SURVEYOR I

By

Otha H. Vaughan

I. INTRODUCTION

Even before the successful lunar landings on the moon, man was able, using earth-based techniques, to develop fairly reliable hypothetical models of the lunar surface. The successful hard landing of the Russian Luna IX and the successful soft landing of the United States Surveyor I have provided photographic data directly from the lunar surface which can help us to better determine the characteristics of the lunar soil. Presented in this paper are some of the latest data about the lunar surface, which show the striking similarity of different areas of the lunar terrain (based on photographic data obtained by two separate lunar craft landing in different areas), and some of the pitfalls in interpretations of a surface based on photographs alone. In addition, an interpretation of the probable material of the upper layer of the lunar surface is presented.

II. DISCUSSION OF LUNA IX PHOTOGRAPHIC DATA AND LUNAR SURFACE IMPLICATIONS

The following information was released by Tass on the Russian Luna IX. The spacecraft (Fig. 1) landed in Oceanus Procellarum (Ocean of Storms) at 18:45 hours Universal Time on February 3, 1966; the landing was 7° 8' N latitude and 64° 22' W longitude about 70 km (43.5 mi) northeast of the rim of Crater Cavalerius, which is about 64 km (39.7 mi) in diameter. The Russian lunar lander produced a series of photographs taken during the following times:

(1) 01:05 - 03:30 U. T., February 4, 1966

(2) 15:30 - 17:10 U. T., February 4, 1966

(3) 16:00 - 17:40 U. T., February 5, 1966

(4) 20:00 - 21:00 U. T., February 6, 1966

According to Tass, the Russian spacecraft weighed approximately 3480 lb (1578 kg) at separation from launch vehicle; the actual lander weighed about 220 lb (100 kg). The camera system was
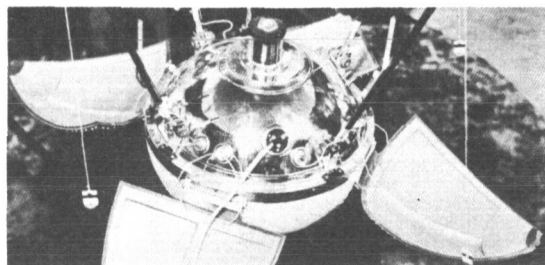

FIGURE 1. LUNA IX SPACECRAFT

designed to provide photographs in circular panorama by using a system of direct and mirror views to produce a series of stereo images. How the terrain appeared to the camera system, which was reported to be viewing the terrain from a height of 60 cm above the surface, is illustrated in Figures 2 and 3. The photograph in Figure 2 was taken early on February 4 with the sun angle about 7 degrees.
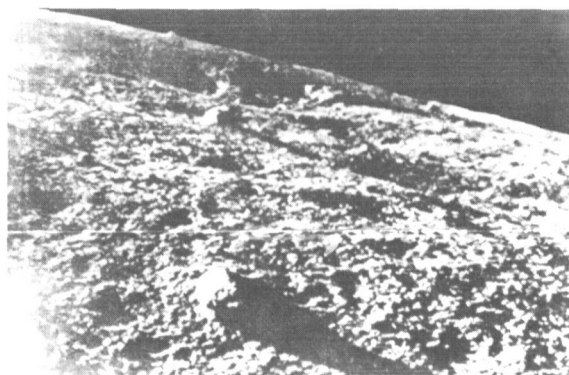

FIGURE 2. LUNAR SURFACE DURING FIRST PANORAMA ON FEBRUARY 4, 1966

The photograph in Figure 3, showing the same rock and terrain after Luna IX had appeared to shift its position, was taken at a sun angle of approximately 15 degrees. The apparent shift is noted by the displacement of the rock in relation to the spacecraft petal, the triangular shaped object, at the bottom of the photograph.
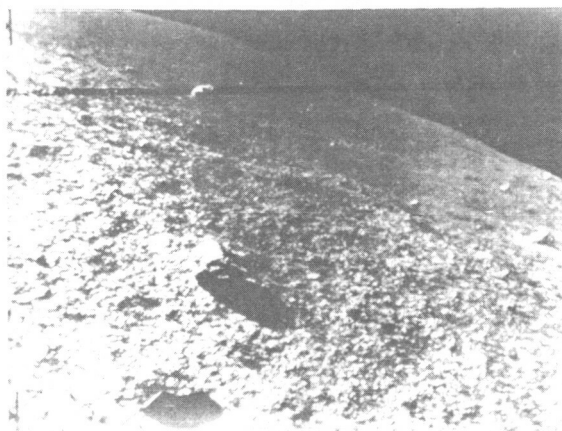
FIGURE 3. LUNAR SURFACE DURING SECOND
PANORAMA ON FEBRUARY 4, 1966

Figure 4 illustrates a pair of photographs which
can be used for stereo viewing of the lunar terrain.
These photographs were obtained from the Branch of
Astrogeology*, United States Geological Survey,
Flagstaff, Arizona.

Figure 5 is an artist's reconstruction of a sec-
tion of terrain as viewed through stereo viewing
equipment.

This stereo model offers the following sugges-
tions about the lunar surface:
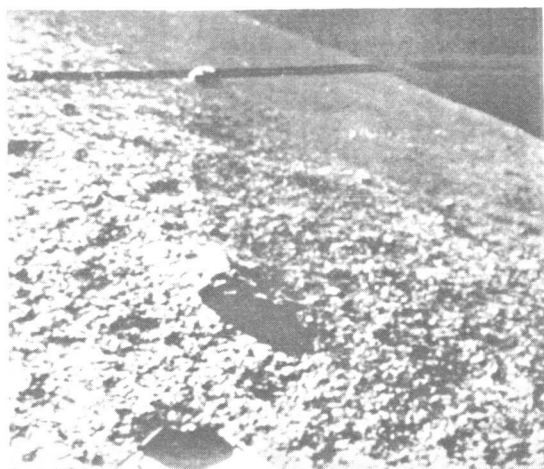
FIGURE 5. ARTIST'S CONCEPT OF LUNAR
TERRAIN

1.   The terrain appears to be undulating with
blocks of material of medium and small sizes
(roughly 3 m down to 10 cm).

2.   The blocky material appears to be resting
on a surface composed of a material similar in

texture to terrestrial scoriaceous lava of the AA type,
or composed of a rubble of fine-grained materials
overlying one another.

3.   Many craters or depression-like features

FIGURE 4.   PHOTOGRAPHS OF LUNAR TERRAIN SUITABLE FOR STEREOPSIS

*Morris, E. C.; Personal Communication.

dot the landscape. A very large crater, about 17 m in diameter, can be seen near the horizon, and craters as small as 10 cm can be discerned closer to the camera.

4. Although some of the craters seem to have small rims, others appear to be rimless. The difficulty in making an absolute determination as to whether or not the small craters have rims may be caused by the unique backscatter or photometric function of the lunar surface and the resolution of the basic photo.
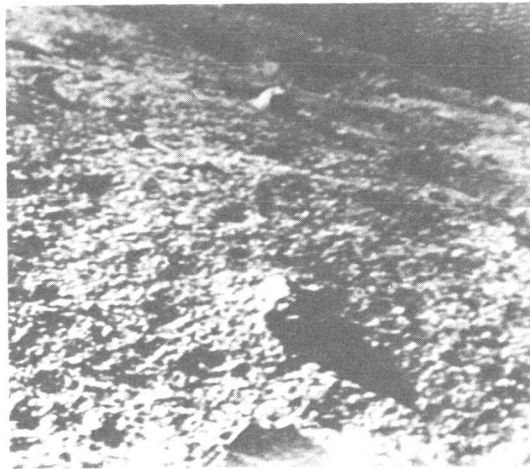
In Figure 6, we see rock-like bodies lying about 6 ft (1.8 m) from the camera. This rock, which is about 15 cm in diameter, appears to be vesicular as indicated by the many pits on its surface. This rock could possibly be a volcanic bomb, especially if the terrain around it consists of a lava flow. It could just as well be the result of secondary ejecta from the impact of a meteoroid, however. Thus, photographs alone are not adequate to establish the origin of this and many other features.
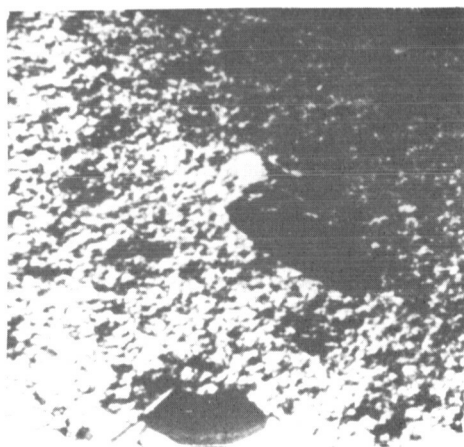

FIGURE 6. SMALL LUNAR ROCK

In summary, the terrain here could be a highly scoriaceous lava, or it could be of a material thoroughly reduced to fragments by continual micrometeoroid bombardment. Since the spacecraft did not penetrate the surface to any great depth, the upper layer appears sufficient to support the weight of the spacecraft. An astronaut would probably have little difficulty walking on this surface.

Although the Luna IX provided photographs of the lunar surface at close range, it still did not provide enough information to establish the actual surface characteristics. Whether the material is a volcanic

ash or lava or whether it is a fragmental material produced by repeated micrometeoroid bombardment remains unanswered. Interpretation of the photographic data is made more difficult because we do not know the specific limitations of the camera and its subsystems.

Let us now look at some of the information from the United States Surveyor I spacecraft and compare its usefulness to data from Luna IX in establishing the origin of the lunar terrain.

III. INTERPRETATIONS OF SURVEYOR I PHOTOGRAPHIC DATA

The United States Surveyor I spacecraft (Fig. 7) landed in Oceanus Procellarum (Ocean of Storms) at 23:17 hours Universal Time on June 1, 1966, at almost the pre-selected impact point. The spacecraft landed within the walls of an old ruined crater approximately 14 km (8.7 mi) north-northeast of the crater Flamsteed D at latitude 2.41° S and longitude 43.34° W.
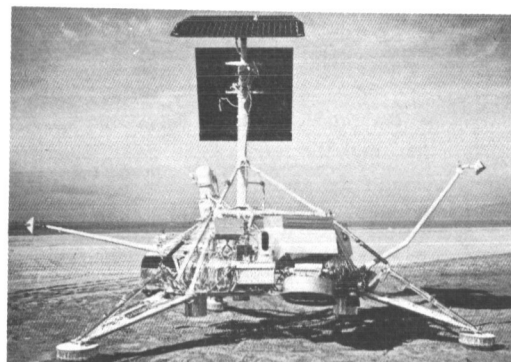
FIGURE 7. SURVEYOR SPACECRAFT

Surveyor I spacecraft is by far the most complex spacecraft yet to land on the moon. The spacecraft weighed 2193 lb (995 kg) at separation from the launch vehicle, and the actual lander weighed 634 lb (288 kg). The Surveyor I spacecraft mission has verified the advanced closed-loop soft landing techniques, which will be used to land men on the moon in the Apollo Program. It has also given us quantitative data on surface bearing strength, radar reflectivity from the lunar surface and temperature ranges. We have also learned from Surveyor I that there are no significant amounts of loose dust on the moon at the Surveyor site.

The Surveyor I spacecraft touched down at a velocity of only 11.6 ft/sec (3.54 m/sec) after free

falling from a distance of approximately 12 ft (3. 66 m) above the surface. During its next five days of operation, it photographed and sent to earth over 4000 pictures of exceptional data content. Shown in Figure 8 is the lunar surface in panorama.

FIGURE 8. SURVEYOR I LUNAR PANORAMA
AT LOW SUN ANGLE

This mosaic, prepared by the Surveyor experimenters, is a composite of photographs taken at low sun angle by the narrow angle camera (6-degree field of view). At first glance, the surface material looks strikingly similar to pumice which has been pockmarked by micrometeoroid bo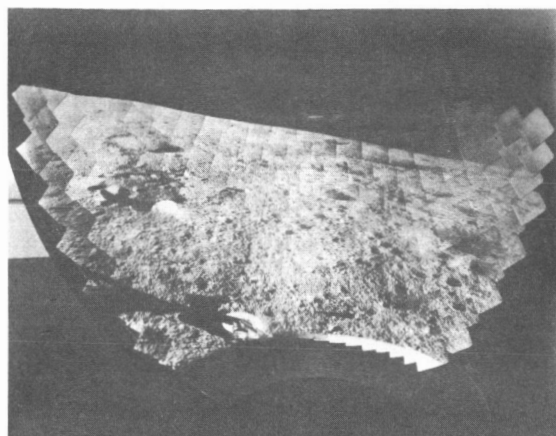mbardment. Substantiating the Luna IX photos, definite rims appear around some of the small craters; others appear rimless. The fact that there is a rim implies that the soil is probably a fine-grained material having a very small amount of cohesion. These assumptions are based on the data of Gault [1], Moore [2] and others who have performed cratering experiments in both cohesive and noncohesive terrestrial materials. Figure 9 is another photo-mosaic of the area under different illumination (higher sun angle).

Notice the difference in the appearance of this terrain. Many of the craters seen in Figure 8 cannot be seen so easily. The surface now has the appearance of a sandy or ash type of material in one area and a pumice-like appearance in other areas. The problem of identification of details is due to the unique photometric function of the lunar surface; this makes photographic interpretations difficult.

To aid in the photographic interpretations of data sent back by spacecraft whose mission is to photograph a body such as the moon, a series of computer programs was developed and made operational by R. Nathan and some of his associates [3-6]
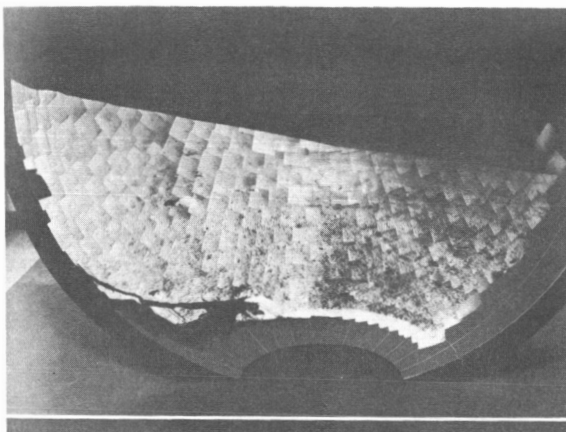

FIGURE 9. SURVEYOR I LUNAR PANORAMA
AT HIGHER SUN ANGLE

at the Jet Propulsion Laboratory. These computer techniques allow one to rework and edit the originally transmitted data so that details of interest to the photo-interpreter can be enhanced. The results of some of this work are illustrated in the Figures 10 and 11.

Figure 10 is constructed using the originally transmitted data. Although the photograph shows some detail, the fine-scale texture of the lunar soil cannot be resolved. The photograph on the right has been constructed using the original data enhanced by the photographic computer technique. The smallest particles which can now be resolved in this photograph are about 0. 5 mm in diameter; therefore, we are now able to establish that the surface, at this particular site, is composed of a fine-grained material. We can also determine that the surface at this site is slightly cohesive, as indicated by the clots observable in these pictures.

Surveyor I photography also demonstrated that there are various types of obstacles, in addition to the craters, in the maria. These obstacles and their distribution must be considered in determining the roughness of the terrain in terms of trafficability.

Figure 12 illustrates a crater lying several hundred yards southeast of the spacecraft. After further study of this crater and its obstacle distribution, designers will have a better model of the lunar surface in terms of obstacles and their distribution. The results of these studies can then be used in determining more realistic energy requirements in future exploration mission planning and trafficability studies. The crater is about 80 m in diameter and the largest rocks or blocky debris lying around the crater appear to be 1 m or larger
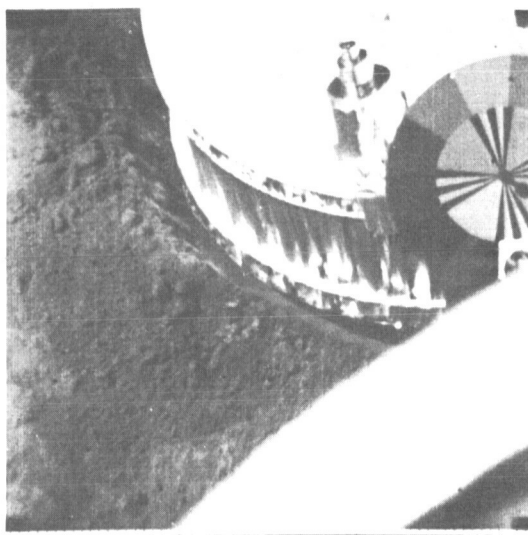
FIGURE 10. SURVEYOR DATA (ORIGINAL
TRANSMISSION)

in height and at least 2 m in length. The smallest
fragments are at least 2 cm in size.

A closer look at some of the rocks photographed
near the spacecraft are shown in Figure 13.
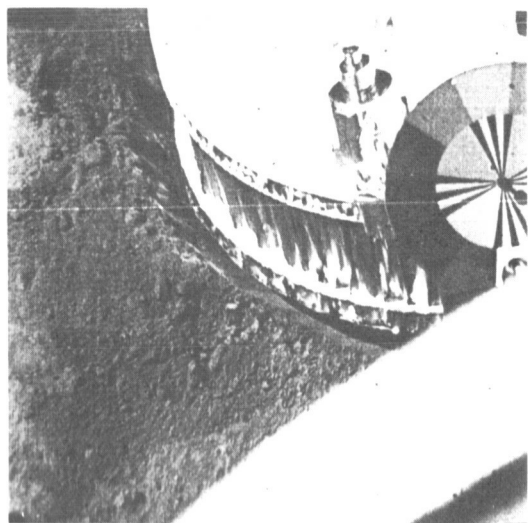
FIGURE 11. SURVEYOR DATA (ENHANCED
TRANSMISSION)
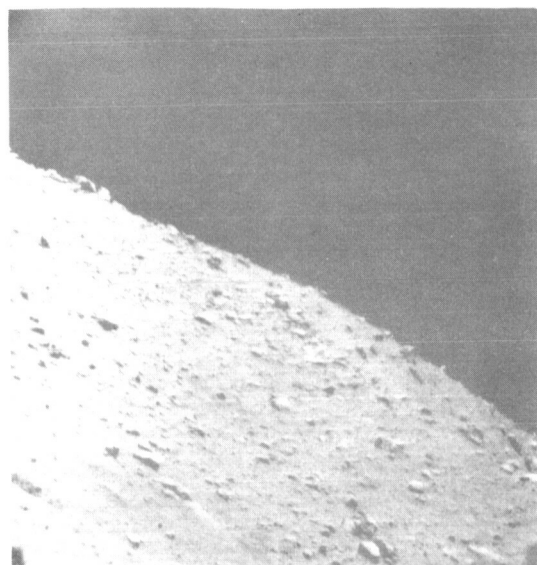
FIGURE 12. LUNAR CRATER AND BLOCKY
DEBRIS

The rock on the left, which is about 20 cm high
and 45 cm long and located about 5 m southeast of
the spacecraft, is similar in appearance to rocks
produced either by volcanic action or by the impact
of a meteoroid producing high temperatures and
pressures. The presence of small cavities in the
rock support this possible origin. The rock on the
right, about 15 cm high and 45 cm long and located
about 5 m southwest of the spacecraft, appears to
be older than the first rock because of the rounded
and mottled appearance. Also, the fact that it
appears to be partially buried in the soil indicates
passage of time. Notice also the well developed
cleavage planes in the rock. These appear to be
similar to the cleavage produced during the plastic
flow of terrestrial type materials when subjected to
high shock pressures.

Figure 14 is a rock photographed by Luna IX;
Figure 15 is a composite photograph of a rock photo-
graphed by Surveyor I. These rocks appear to be
similar in their formation, i.e., vesicular. Also,
each rock has definite cleavage planes, and both
appear to be resting on a frothy or a fine-grained
surface. By using the information obtained by the
Surveyor I photographic mission, one can postulate
that the two surfaces are composed of the same
fine-grained materials, and not the highly vesicular
surface which appears to be indicated by the Luna
IX photographic data.
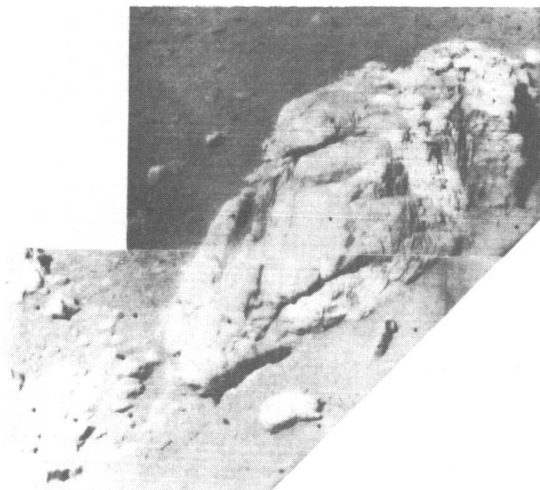
FIGURE 13.   LUNAR ROCKS

IV. CONCLUSIONS

Based on the data from Surveyor I and Luna IX data, a realistic model which represents the areas in which these two spacecraft landed is as follows:

1.   The basic mare surface at each site is covered by a layer of fine-grained material.

2.   Based on the distribution and size of craters and blocky materials seen lying near the Surveyor I site, the depth of the fragmental layer is estimated to be at least 1 to 15 m. This fragmental layer will be composed of both very small-grained material and large block size material, i. e. , a conglomerate of materials resulting from either meteoroid or volcanic ejecta.

Without the excellent detailed information obtained from the Surveyor I photographic data, it would not have been possible to establish that the lunar surface at the Surveyor I site was indeed composed of fine-grained materials. These data do not appear to have been established by the Luna IX photography.

In the interpretation of photographic data pertaining to the texture of material on an extraterrestrial surface, one must understand the photographic data limitations (different illumination levels, different film characteristics, different photometric functions, camera and data transmission subsystems characteristics, etc.) before one can make a valid interpretation of the materials.

REFERENCES

1.   Gault, D. E. ; Quaide, W. L. ; and Oberbeck, V. R. : Interpretating Ranger Photographs from Impact Cratering Studies. Proc Conference on the Nature of the Lunar Surface, GSFC, (NASA-IAU) Meeting, Greenbelt, Md. , Apr. 1965.
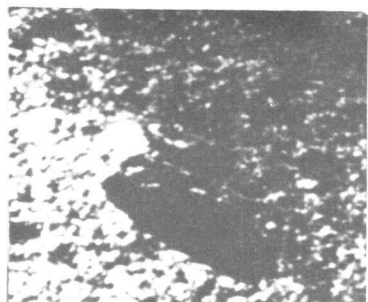
FIGURE 14.   LUNA IX ROCK

FIGURE 15.   SURVEYOR I ROCK

REFERENCES (Concluded)

2. Moore, H. J.: Jet Propulsion Laboratory Technical Report 32-800, 1966.

3. Smith, G. M. and Willingham, D. E.: Ranger Photometric Calibration. Jet Propulsion Laboratory Technical Report 32-665, Aug. 1965.

4. Rindfleisch, T.: A Photometric Method for Deriving Lunar Topographic Information. Jet Propulsion Technical Report 32-786, Sept. 15, 1965.

5. Nathan, R.: Digital Video Data Handling. Jet Propulsion Laboratory Technical Report 32-877, Jan. 5, 1966.

6. Billingsley, F. C.: Digital Video Processing at JPL. Paper No. 15, Seminar Proc. of Electronic Imaging Techniques for Engineering, Laboratory, Astronomical, and other scientific measurements, Society of Photo-optical Instrumentation Engineers, Apr. 26-27, 1965.

IX. STRUCTURAL DYNAMICS

CONSIDERATIONS AND PHILOSOPHY OF GROUND WINDS CRITERIA FORMULATION

By

William W. Vaughan

SUMMARY

The various practical design and operational considerations involved in establishing ground winds criteria for aerospace vehicle developments are presented. The concept of exposure period probabilities in terms of risk to vehicles exposed to wind loading during operations is considered. Applications of extreme value statistics to wind design criteria and the use of spectral methods to represent the time-dependence structure of ground winds are discussed. Future needs for inputs in vehicle designs are outlined in the discussion.

I. INTRODUCTION

The principal purpose of all ground wind criteria is to provide a description of the ambient wind environment, such that, when employed with other inputs to space vehicle and supporting structural design problems, a design which will be acceptable for operational use is produced. The first thing that must be recognized is that the wind criteria, although important, are but one of the many inputs and considerations that must be taken into account in establishing the design strength of a structure. It is, therefore, important that the users of these criteria work as a team with the developers of ambient ground wind models. Such a relationship helps to insure a physically realistic model and a practical and usable structural design.

This paper presents some considerations involved in establishing ground wind criteria, mainly from the atmospheric input viewpoint. From this presentation perhaps there will develop a basis for discussion of the subject which will promote an overall understanding of the current thinking and produce a consensus of direction for future activity.

Everyone concerned with this subject is well aware of the fact that ground winds ($\lesssim$ 150 m) are phenomena that vary in space and time. The following generalizations may be made: The longer term statistical analysis for most locations will show an increase in wind speed with height for a given risk level; the afternoon winds usually contain higher velocities than those in the early morning hours, and the distribution of obstacles (trees, buildings, etc.) contribute significantly to flow conditions at a specific place. However, even these relatively simple thoughts are overlooked in design or operational considerations.

In general, as many potential natural environment problems as practical should be designed out. This broad remark needs to be qualified since, from a risk viewpoint, for every measured ambient extreme there exists a finite probability that it will be exceeded. So there is no such thing as being 100 percent sure. Therefore, the ability or necessity to "design out" a potential natural environment problem depends on the trade-off between many things like cost, operational constraints, confidence in design approach, acceptable risks, etc. There is no single "right" answer to this problem. However, in some cases it appears to be controlled by one principal design input, money. This is illustrated by a case in which available money for a structure was equated to tons of steel which, in turn, was related to wind speed. Instead of deciding what risk would be acceptable and then selecting the wind speed, etc., the final design risk level was apparently arrived at by using the money available for the project.

Another aspect of this subject is the predictability of ground winds relative to design considerations. This question always arises whenever someone either has made a mistake in his design and it is too late to change, or he finally realizes that a 0.1 percent design risk does not mean he will not lose his vehicle tomorrow afternoon. This latter point is illustrated by a case where a design engineer stated that he wanted a 0.1 percent risk wind criteria with a 150 percent assurance that it would not be exceeded in an operational situation.

With the exception of a few rather well defined situations, it is impossible for present day weather forecasters (specialized or otherwise) to predict accurately peak ground winds. By accurately it is meant that one would, with a high degree of confidence, leave a space vehicle known to be incapable of withstanding any wind above 25 knots standing during an afternoon thunderstorm based on a weather forecaster's

prediction of a 22-knot peak wind. For certain well developed atmospheric situations, i.e., hurricanes, cold fronts, squall lines, and northeasters, the occurrence of these events can sometimes be predicted a few hours or a day in advance to permit protective action. But even here, no accurate prediction of the peak wind is possible in the sense mentioned earlier. The message intended is this: When one makes a design which is dependent on a wind prediction, consider carefully the element of increased risk.

II. DESIGN AND OPERATIONAL CONSIDERATIONS

Figure 1 provides a brief list of some considerations that should go into establishing ground wind criteria. It is rather obvious that the ground

1. OPERATIONAL CONDITIONS (LOCATION, UTILITY, ETC.) OF STRUCTURE

2. ACCEPTABLE RISK LEVEL - DESIRED LIFETIME

3. RELATIVE UNCERTAINTIES IN OTHER DESIGN INPUTS AND ANALYTICAL PROCEDURES

4. ABILITY OF DESIGN PROCEDURE TO ACCEPT WIND CRITERIA MODELS

5. DESIGN DATA REFERENCE PERIOD

6. AVAILABLE BASIC WIND STATISTICS

7. PHYSICAL REPRESENTATIVENESS OF MODEL(S)

8. WIND CRITERIA - INTEGRAL OR SEPARATE PART OF DESIGN PICTURE

9. RESEARCH VERSUS PROJECT REQUIREMENTS

10. COMPOUNDING OF SAFETY FACTORS

11. STRUCTURAL CHARACTERISTICS OF VEHICLE

12. CONSEQUENCE OF A FAILURE

FIGURE 1. SOME PRACTICAL CONSIDERATIONS INVOLVED IN ESTABLISHING CRITERIA

wind criteria immediately become an integral part of any design problem. They cannot be developed independently of the application. Before more is said, however, it should be understood that atmospheric physicists have been concerned with the behavior of ground winds for many decades. Volumes have been written on the subject, but there still is no universal model or criteria of ground wind behavior.

Most of the considerations itemized in Figure 1 are self-explanatory. Item No. 9 should be stressed. Here, one should make a rather clear distinction between the needs of projects for consistent design inputs, often of a somewhat simple nature, and research studies endeavoring to relate complex vehicle

responses to similarly complex forcing functions, as represented by wind inputs, for future application. The transition from the latter to the former should be made with due and deliberate consideration for the overall project impacts and consequences.

Wind loads criteria which have been established for buildings and other civil structures are used in the design of ordinary structures. The space program, however, has unusual structures in terms of size, shape, and utility; the Vertical Assembly Building and the Saturn V space vehicle are prime examples. The established engineering building codes are not directly applicable for the design of these structures. Once the considerations in Figure 1 can be accommodated or reasonable estimates inferred, wind criteria for initial analysis can be established. Design wind criteria cannot be established satisfactorily until the total engineering problem has been analyzed.

III. CURRENT DATA

Sufficient statistical records on ground winds exist, at best, only for some given height. These are the regular observations made by the US Weather Bureau and other organizations with similar interests. Unfortunately, these measurements were not made for space vehicle design use and, therefore, no special care has been exercised in producing the records beyond the normal weather forecasting and operation needs. Since it takes many irreplaceable years to acquire a usable record, we are forced to interpolate, extrapolate, theorize, and otherwise guess at sufficient additional information to establish even the simplest criteria relative to risk.

One of the older methods used to establish structural wind criteria consisted of taking the largest wind speed (measured or assumed) for a location, and then in some cases doubling the value. Until rather recently, few, if any, vehicle designs considered anything other than a single wind speed for all heights regardless of location. Insofar as gust considerations are concerned, this appears to be a complicated input for design, even in the simplest form of description. Apparently most actual vehicle designs employ a peak wind as a steady force and then include a design allowance for dynamics, vortex shedding, etc. Use of various relatively sophisticated input models, such as power spectral relationships, still suffers from concern over spectral description representativeness, response characteristics of vehicle, and acceptable analytical models.

Two reports and the references thereto provide a relatively good background on what ground wind data are available relative to current-day use as criteria: NASA TM X-53328, Terrestrial Environment (Climatic) Criteria Guidelines for Use in Space Vehicle Development, 1966 Revision, [1] and the Air Force Handbook of Geophysics and Space Environment, 1965 Revision [2].

IV. EXTREME VALUE WIND ANALYSIS FOR CRITERIA*

Statistical methods are acquiring an increasing role of importance in the physical sciences. The statistical analysis of wind is very difficult, because of the extreme variability of this atmospheric element in time and space.

The theory of extreme values proposed by E. J. Gumbel [3] is one of the most efficient methods presently available for the analysis of extreme winds and the resulting definition of design criteria for structures affected by strong winds.

The strongest wind a structure may encounter in its lifetime is very difficult to determine. Wind, more than any other atmospheric element, varies so widely in time and space that none of the many estimates of "design wind" have been found to be completely satisfactory. Classical statistical methods, which usually concern average values, are not adequate when the variable of interest is the largest (or smallest) in a set of observations. For many years engineers have used extreme values of wind speed in various forms to determine design wind pressures and loads. Often the design wind was defined simply as the highest speed ever recorded at a particular station. It was soon discovered that the value of this extreme depended on the length of record, which varies from station to station. The variation of the single extreme is so large that it provides only an indication of what the design wind should be. It is at this point that the theory of extreme values developed by E. J. Gumbel may be introduced.

For a wind whose design return period**, T_d, is greater than 10 (so that the Poisson approximation

is valid), the number of trials (desired lifetime), N, within which recurrence is likely, can be expressed, for various probabilities, in terms of percentages of the design return period, T_d, as

$$N = \frac{T_d}{R} , \qquad (1)$$

where R is any positive number; i.e., R is the percentage of the desired lifetime, N, which will give the design return period, T_d.

Now let

P = probability of the event not occurring in any of N trials.

and

P_1 = probability of the event occurring at least once in N trials.

We now introduce the concept of calculated risk, U, which is equal to P_1 above. Now,

$$P = (1 - \frac{1}{T_d})^N \qquad (2)$$

and

$$U = P_1 = 1 - (1 - \frac{1}{T_d})^N . \qquad (3)$$

Substituting T_d/R for N from equation (1) into equation (3), we have

$$U = P_1 = 1 - (1 - \frac{1}{T_d})^{T_d/R} \xrightarrow[T_d \to \infty]{} 1 - e^{-1/R} . \qquad (4)$$

Thus, T_d may be obtained as a function of calculated risk. By plotting the range of U, $0 \leq U \leq 1$, versus various values of R, equation (4) gives us Figure 2 as a convenient method to obtain the value of R for any level of calculated risk, U.

Example:

Suppose we are given that a certain structure requires a desired lifetime of thirty days with a

---

* This section was contributed by Mr. L. Falls, MSFC, R-AERO-YT.

** Average interval between recurrences of an event in a particular series of trials.
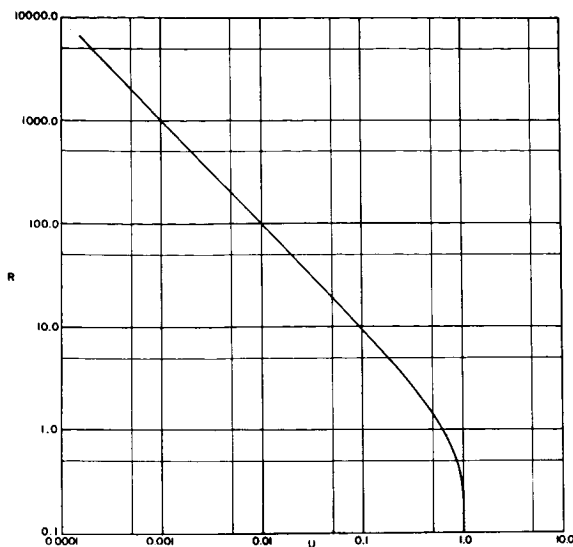
FIGURE 2.   R EXPRESSED AS A FUNCTION OF
CALCULATED RISK, U

calculated risk of being destroyed by extreme winds of five percent.   We are required to find the average time interval between recurrence of a critical wind and the corresponding critical wind value.

The data sample used for this example is the serially complete peak wind speeds at the surface (10 meter reference height), Cape Kennedy, Florida, for all months, February 1950 to December 1964. Figure 3 is the extreme value plot of these data with a sample size of N = 179 months.   Thus, given N = 30 days = desired lifetime

$$U = 0.05 = \text{calculated risk.}$$

Find:

$$T_d = \text{design return period}$$

$$W^* = \text{critical wind.}$$

From Figure 2, for U = 0.05, we have R = 19.5. Now from equation (1),

$$T_d = RN = 19.5 \times 30 = 585 \text{ days} = 19.5 \text{ months.}$$
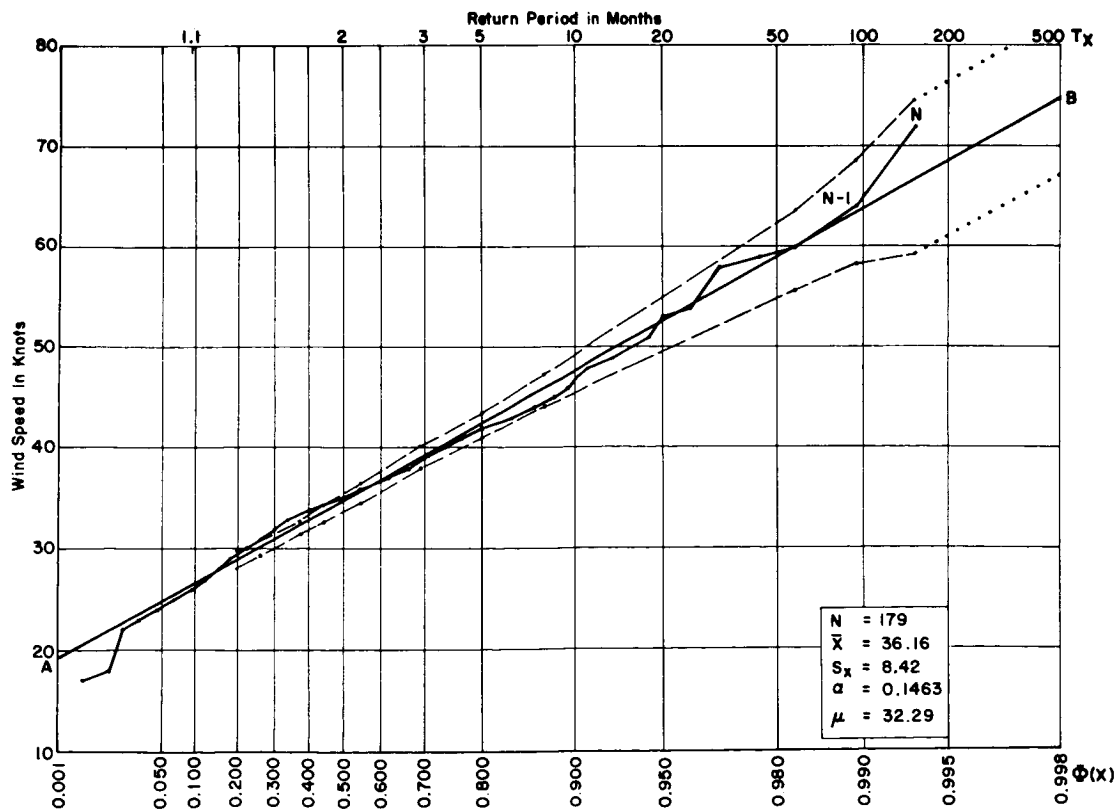
FIGURE 3.   MONTHLY PEAK WIND SPEEDS – CAPE KENNEDY, FLORIDA, 10 METER REFERENCE HEIGHT
(EXCLUDING HURRICANE WINDS)

Entering the extreme-value graph, Figure 3, at a return period equal to 19.5 months, we read (on the least squares line AB) a corresponding critical wind speed of W* = 52.5 knots.

Following are several values of T_d (in months) and W* (in knots) corresponding to the indicated values of N for a calculated risk U = 0.05.

N	30 Days	60 Days	90 Days
T_d	19.5	39.0	58.5
W*	52.5	57.2	60.2

A combination of probability theory and Gumbel's recent theory of extreme values provides a theoretical method for analyzing and interpreting a random variable such as wind speed.

The basic theory of extreme values involves the development of a theoretical function for the probability that a given extreme value will not be exceeded by any of a large set of extremes. Observed extremes are fitted to this function by a least squares procedure, and the assumption is made that the sample of observed extremes is large so that limiting values can be used.

Several "calculated risks" were computed using the extreme value criteria. These calculated risks were compared to "exposure period probabilities" [4] which represent the empirical relative frequency of occurrence of the event, W* . The results were as follows for the indicated values of N = desired lifetime and W* = critical wind.

N	W* = 40.2 knots			W* = 59.2 knots		
	30 days	60 days	90 days	30 days	60 days	90 days
Calculated Risk	0.240	0.400	0.550	0.020	0.039	0.060
Exposure Period Probability	0.245	0.400	0.520	0.020	0.043	0.068

As shown by the above table, the agreement between the theory of extreme values and the empirical "exposure period probabilities" is very close for the selected sample. Thus, we may conclude, from a limited number of trials, that the "goodness of fit" between theory and observations is very good.

The derivation of the extreme value distribution is a theoretical procedure as opposed to empirical methods used by many engineers who believe that everything should be "normal" and whatever turns out not to be so can be made "normal" by a transformation. This is not true or practical in this situation.

No theory can explain all observations for which it is the proposed statistical model. The conditions for the use of the theory are not always fully satisfied by the observations. Therefore, certain areas of nonagreement must occur between theory and observation. This cannot be considered as a failure of the theory.

V. GROUND WIND PROFILE AND SPECTRAL REPRESENTATIONS*

During the design and fabrication stages of launch vehicles, the design engineer must be cognizant of the final weight of the launch configuration so that unnecessary weight penalties are avoided. Because the ground handling equipment will remain behind on the ground at launch, the present design philosophy, in the industry, is to design the auxiliary ground equipment to attenuate and alleviate some loads caused by the ground winds. However, it is conceivable that ground handling equipment may have to be so sophisticated that to provide this capability will be impractical. Thus, it is imperative that the ground wind environment be defined in usable engineering terms as accurately and precisely as possible so that the engineer need not overdesign the ground handling equipment and the space vehicle structure. This is especially true if the space vehicle is required to withstand ground wind loads if the ground handling equipment cannot be designed to completely alleviate or attenuate the entire design ground wind loadings. Thus, the purpose of this section is to discuss the philosophy employed in the development of design criteria in the context of the ground winds problem.

The types of ground wind design criteria may be conveniently divided into two categories, mainly, the quasi-steady and unsteady properties. The quasi-steady characteristics produce steady drag forces which cause bending and an oscillatory lateral loading perpendicular to the wind direction which is a consequence of von Karman vortex shedding. Thus, it is important that the ground wind design criteria reflect the coupling between these wind characteristics. The unsteady characteristics will cause the launch

---

* This section was contributed by Mr. George H. Fichtl, MSFC, R-AERO-YE.

vehicle configuration to experience oscillatory bending in both the drag and lateral directions [5]. However, one must bear in mind that the effects produced by these wind characteristics are coupled. For example, it appears that the mechanism for the vortex shedding produced by the steady-state wind is controlled by the unsteady characteristics (turbulence) which produce oscillatory deflections in both the drag and lateral directions. In the past, ground wind design criteria have been presented in the forms of discrete profiles and spectra. In the remainder of this section, these types of criteria will be discussed in the context of defining the unsteady wind with a view toward determining the future needs for spectral type and related design inputs.

A. WIND PROFILES REPRESENTATION

One of the primary goals of atmospheric research concerning the atmospheric boundary layer is to establish an analytical representation of the wind profile. Researchers have found that the analytical form of the wind profile depends upon the stability configuration of the boundary layer as manifested by the Richardson number, the pressure gradient and Coriolis forces, and the vertical heat fluxes and Reynolds stresses that reside within and on the boundary of the atmospheric boundary layer. Accordingly, the literature abounds with profile equations that account for some or all of these effects. For example, in the surface boundary layer, the log profile is valid in neutral air [6], the log-linear profile due to Monin and Obukhov is valid for near neutral conditions [7], and the diabatic wind profiles due to Panofsky [8] and Deacon [9] are valid in unstable as well as in stable air. On the other hand, in the spiral layer where the Reynolds stresses are of the same order of magnitude as the pressure gradient and Coriolis forces, the theory first due to Ekman [6] and recently expanded by Blackadar [10] is applicable.

At the present time, however, it appears that the empirically derived power law is the primary wind profile that is being employed for defining ground wind profile envelopes for design criteria application. It is given by

$$u = u_1 \left(\frac{z}{z_1}\right)^p , \qquad (5)$$

where u is the wind speed at height z, u_1 is the wind speed at the reference height z_1, and p is a non-dimensional quantity which depends upon the surface roughness, the wind speed, Richardson number, and perhaps other parameters. The exponent p is usually

represented as a function of wind velocity at the reference level. Figure 4 shows p as a function of u_1 for the reference height z_1 based upon data obtained at Cape Kennedy, Florida, White Sands Missile Range, New Mexico, and Brookhaven National Laboratory, New York [11]. The apparent reasons for the popularity of the power law as compared with the more theoretically acceptable profile equations mentioned above are twofold. First, the power law fits envelopes of wind data observations over a wide variety of meteorological conditions. Secondly, the power law may be applied to wind data with relative ease, which one does not enjoy with the other profile formulas.
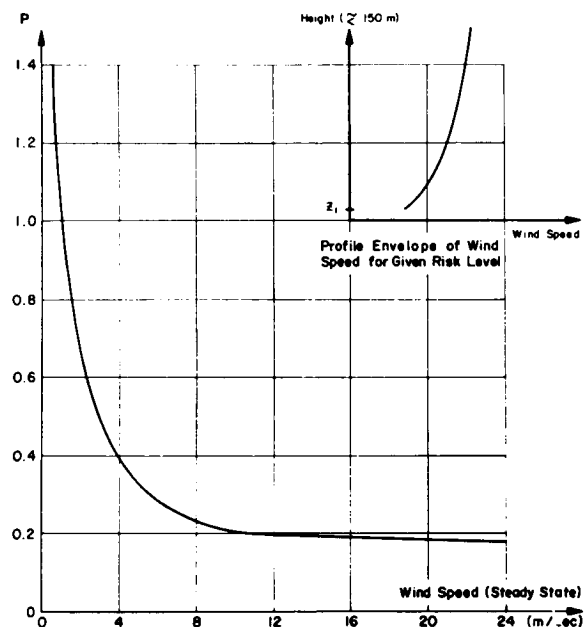
FIGURE 4. VARIATION OF P WITH WIND SPEED (STEADY STATE) AT REFERENCE LEVEL Z_1

At most launch sites there are insufficient wind data in the vertical to perform statistical studies for constructing wind profile envelopes. Accordingly, a stable statistical sample must be constructed by supplementing the existing single height climatological sample with wind profile data from other observation sites. If the power law profile is employed, wind measurements at any height may be transformed to any other height so that the wind data may be combined consistently for design use. Upon establishing this sample, one may then determine the statistical distribution of u_1 at the reference level, and consequently construct the associated wind profile

envelopes of the quasi-steady-state winds with the aid of equation (5). An obvious uncertainty in this procedure is that the resulting wind envelopes may not necessarily correspond to the true wind envelopes that would have resulted from using the actual wind data if they had existed.

In addition to providing wind profile envelopes of the quasi-steady wind field, it is equally important to define a design gust configuration for each envelope. At the present time, the philosophy for developing this type of criterion is to treat the gust as acting over the complete length of the vehicle. This supposedly provides the most detrimental gust loadings and reduces the problem of developing design criteria to providing gust factors and associated gust acceleration times. The gust factor G is defined as follows:

$$G = \frac{u_{max}}{\bar{u}} \quad ,$$

where $\bar{u}$ is the mean wind and u_{max} is the wind speed associated with the peak gust. It is known that the gust factor is a function of the steady-state (mean) wind speed, the length of time used to obtain the mean wind, the prevailing stability conditions, terrain features, and height. The design gust factor adopted by Marshall Space Flight Center is 1.4, and the associated time for the wind to accelerate from the quasi-steady state to the peak wind condition is 2 sec. These criteria appear to be in agreement with the results of Mitsuta [12].

B. SPECTRAL TYPE REPRESENTATION

1. Atmospheric Turbulence. As discussed previously, gust loading data are currently defined in terms of a steady-state wind profile, a gust factor, and the time it takes for the gust to obtain its maximum amplitude. However, to account for the interaction of the atmosphere with the launch vehicle in a more comprehensive manner, power spectral methods may be employed. In this case, design gust load inputs must be defined in terms of spectra. Spectral methods are not new in the aerospace industry, for one needs only to glance at the literature concerning aircraft gust response to see that spectral methods have enjoyed wide popularity. Particularly noteworthy is the work of Press [13], Lappe [14] and Pritchard et al. [15] with regard to defining spectral gust inputs for aircraft design. Bohne (Sissenwine and Kasten, [16]) has shown that the spectral methods which are now frequently employed in the determination of aircraft flight gust loads are useful in the analysis of the nonlinear ground wind drag problem.

Wind spectra are obtained from both tower and low flying aircraft measurements. The aircraft observations yield spectra for various horizontal directions along the flight path of the plane, while tower measurements give Eulerian spectra that are represented as space spectra by using the Taylor hypothesis. In recent years, this hypothesis has been the cause of much discussion; however, Lumley and Panofsky [17] have concluded from a survey of the available information that it appears that the Taylor hypothesis is generally applicable except for the low wave number components associated with vertical velocity fluctuations.

At the present time, only a limited amount of low level turbulence spectra exists. Thus, researchers have been able only to fix the general shape of the longitudinal spectrum, while the shape of the lateral spectrum appears to be even more elusive than that of the former. However, in the limit of small wavelengths or high frequencies, the spectrum of the lateral and longitudinal components varies approximately to the -5/3 power of frequency. The present method employed for determining the analytical forms of spectra from turbulence data is essentially trial-and-error fitting of assumed analytical forms to data, with intuition and theory to serve as a guide. In general, the analytical forms of the spectra are chosen so that for large frequencies they possess the -5/3 behavior which is characteristic of the inertial subrange first predicted by Kolmogorov [8]. However, it appears that the major effort toward defining spectra for vehicle response studies has been expended in the area of defining a longitudinal design spectrum. This apparently is caused by the fact that, only until very recently, there has been little need for lateral spectra in vehicle response problems. In the case of longitudinal spectra, the normalizing parameters that occur in the analytical representation are based upon similarity considerations.

Henry [18], who has examined wind spectra associated with a range of stability conditions, has found an altitude dependence as indicated by the similarity theory. However, it appears that the present state of the art of the methods employed in spectral response studies of vertically erect launch vehicles does not have the degree of sophistication necessary for using design spectra which depend upon altitude. Thus, the analytical representation of the longitudinal spectrum due to Panofsky [17] and based upon the strong wind spectra compiled by Davenport [19] may develop to be an appropriate type spectral input for response calculations. His analytical representation is independent of z and is given by

$$\omega\phi(\omega) = 4u*^2 \frac{900\,\Omega}{1 + (900\Omega)^{5/3}} , \qquad (6)$$

where $\Omega = \omega/u_{10}$, u_{10} being the wind speed at 10 m and $u*$ is a constant for the particular location during high wind. The MKS system of units is being employed and ω has the units of cycles $\sec^{-1}$. Figure 5 shows $\phi\omega(\omega)/u*^2$ as a function of Ω. Two wind profile parameters, namely, $u*$ and u_{10}, occur in this representation of the longitudinal spectra. These parameters serve to couple the spectrum of turbulence and the wind profile, thus permitting the atmospheric scientist to define the steady-state wind profile and the associated spectra consistently. Even though this seems to be a logical development, it should be verified for a specific location.

2. Isotropic Turbulence. It is common practice in launch vehicle response studies to use the longitudinal spectra of isotropic turbulence due to Dryden [20] and von Karman (Pitchard et al., [15]) as a representation of atmospheric turbulence. In the case of the Dryden spectrum it is given by

$$\phi(\omega) = 2\sigma^2 \frac{L}{\Pi} \frac{1}{1 + L^2\Omega^2} , \qquad (7)$$

where σ^2 is the variance of the longitudinal component of the turbulent fluctuations, L is the scale of turbulence, and Ω is now equal to ω/u_o, u_o being a quasi-steady characteristic wind speed. Figure 6 shows a plot of this spectrum in dimensionless variables. Usually the variance σ^2 is determined by integrating the above expression over all frequencies and comparing the resulting relationship with the corresponding integral of experimentally determined spectra. The major difficulty with using the isotropic turbulence model is the specification of the scale of turbulence, which in reality varies, as noted previously, with height in the atmospheric boundary layer and thus takes on a variety of values ranging from approximately 10 to 350 m. For example, Webb [21], who has analyzed correlation functions of atmospheric turbulence, suggests that the scale of longitudinal turbulence is proportioned to the square root of the height, while Panofsky and Singer
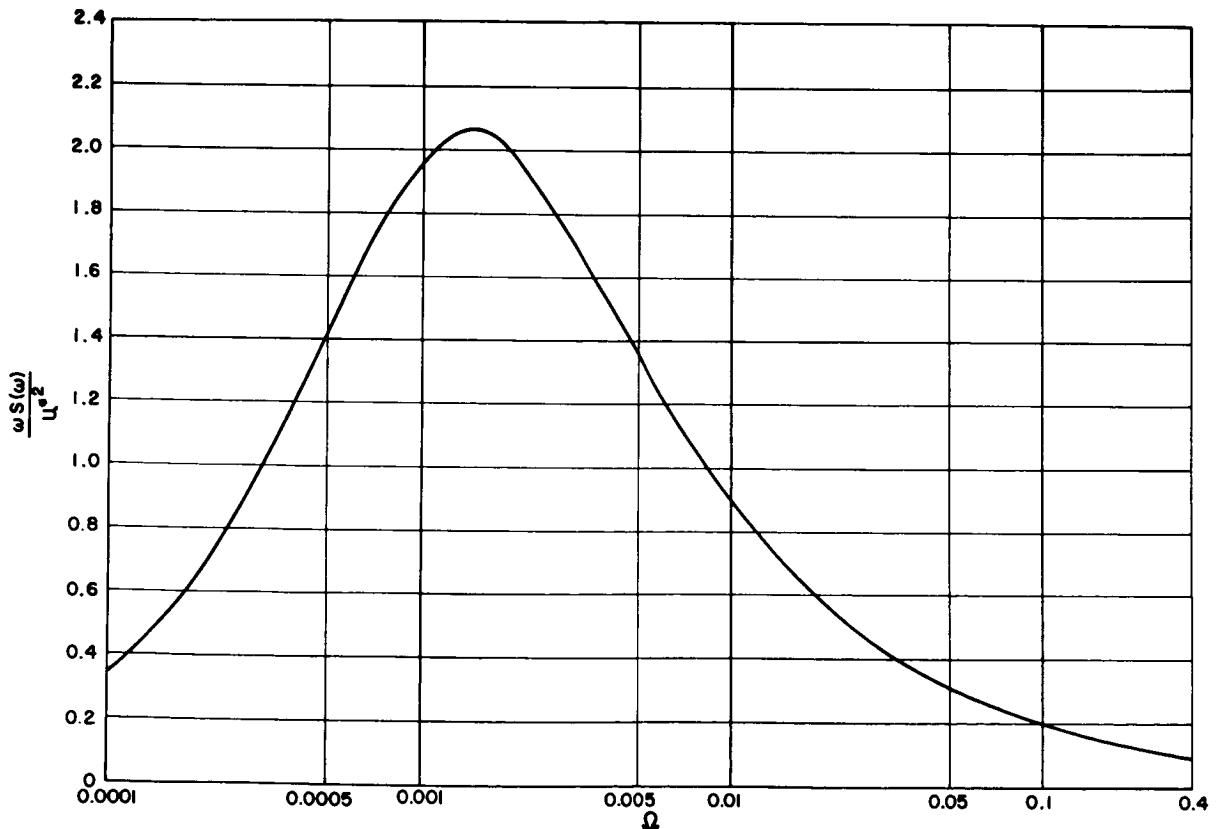

FIGURE 5. $\dfrac{\omega S(\omega)}{u*^2}$ VERSUS Ω ACCORDING TO THE EQUATION $\dfrac{\omega S(\omega)}{u*^2} = 4 \dfrac{900\,\Omega}{1 + (900\Omega)^{5/3}}$
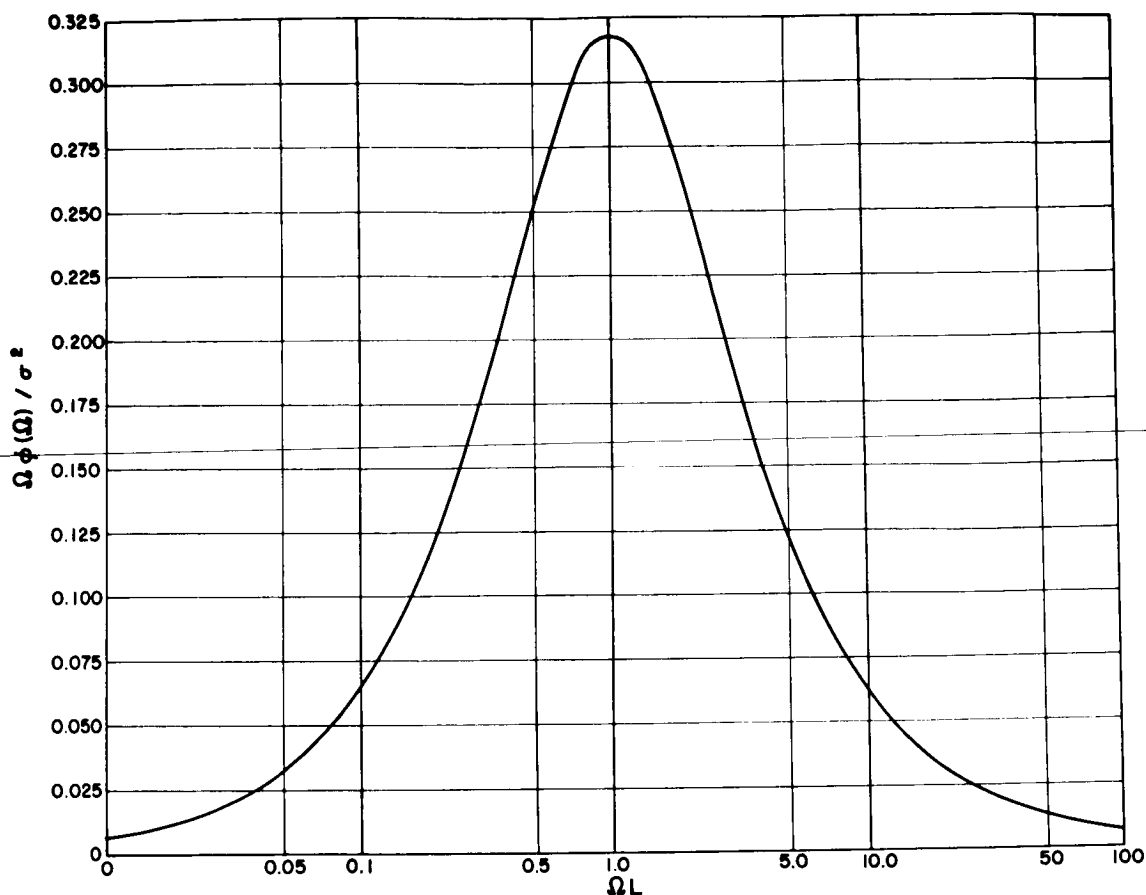
FIGURE 6.   PLOT OF $\dfrac{\Omega\phi(\Omega)}{\sigma^2}$ VERSUS ΩL ACCORDING TO THE EQUATION $\dfrac{\Omega\phi(\Omega)}{\sigma^2} = \dfrac{2}{\pi}\left(\dfrac{\Omega L}{1+(L\Omega)^2}\right)$

[22] have recently suggested a two-thirds power dependence upon height.

Frequently in response calculations, the turbulent portion of the velocity field is assumed to vary randomly in time but uniformly over the complete length of the vehicle. It is possible that such a procedure could yield extremely conservative estimates of the vehicle's response. However, this simplification reduces the problem of specifying a spectral ground wind input to only defining a longitudinal power spectrum as discussed previously. Recently, there has been some interest in expanding response calculations to include the correlation between horizontal wind gusts in the vertical. The procedure is to assume that atmospheric turbulence is locally homogeneous and isotropic so that the cross spectra between like components of the wind depend only upon the distance between the correlated velocity components. In view of the assumption of

isotropy, the cross correlations between unlike velocity components vanish and the quad-power of the spectrum associated with the correlation between the like components of velocity is zero for all frequencies. Particularly noteworthy is the extension of Hanbolt's work [23] by Reed [24]. Reed developed analytical expressions for the cross correlation functions for the horizontal, lateral and longitudinal components of turbulence by assuming that the patterns of turbulence are frozen into the fluid and convected at the rate of the mean wind speed for the case of isotropic turbulence as observed in a wind tunnel.

The popularity that the isotropic turbulence model has experienced in the aerospace industry may be attributed to its relatively simple mathematical form, as well as to the philosophy contained in the phrase "since so little is known about atmospheric turbulence, why not use the isotropic turbulence

154

model which has proven itself in the aircraft industry." Although this philosophy may have been acceptable in the past, it may not be justified in the future when response calculations become more sophisticated, especially in view of the knowledge that has already been accumulated concerning atmospheric turbulence.

VI. FUTURE OUTLOOK

In coming years, we may reasonably expect that design loading calculations with regard to ground wind inputs will become more sophisticated as experience is gained. It is thus imperative that the atmospheric scientist anticipate the future requirements for ground wind design inputs on the part of the design engineer. Currently, this calls for no less than a complete description of (1) the time dependent structure of the wind field, (2) the quasistatic wind field, and (3) the interactions and interrelationships of these two portions of the wind field. Clearly, the atmospheric scientist will have to work in close coordination with the design engineer so that the appropriate decisions can be made regarding the processing of wind data.

In addition to considering loads upon vertically erect vehicles, consideration must also be given to the possibility of other modes of launch. For example, horizontally launched vehicle configurations are being considered. This type of configuration is envisioned as being launched with the aid of a launching sled. Before the launch vehicle initiates flight, it may experience severe loadings caused by horizontal gusts while attached to the sled. Upon initiation of flight, the vehicle will experience a combination of wind loads due to vertical and horizontal gusts, as well as loads due to the mean wind profile while penetrating the atmospheric boundary layer. Accordingly, information will be needed about the horizontal as well as the vertical distribution of turbulence. Fortunately, a body of information exists concerning aircraft wind gust loading.

Another future problem area concerns vehicle booster recovery. As vehicle boosters increase in size, the cost of one-shot booster operations could become prohibitive, and it is conceivable that booster recovery operations will become common practice. Accordingly, the engineer will have to consider the problem of structural fatigue. This means that, in addition to spectral type ground wind inputs, there could be future need for exceedance probability models of atmospheric turbulence for space vehicle applications.

In developing any type of wind input for vehicle response and loading calculations, the ideal situation would be to have available a large body of existing data which will yield statistically stable results. However, in the case of wind spectra, one does not have available a statistical sample of spectra that a statistician would call stable. Thus, the atmospheric scientist must turn to other sources of data and develop design spectra in an indirect manner. At the present time, the only ground wind data that exist in large quantities are the surface wind records obtained for given heights at US Weather Bureau and military weather stations. Through our present knowledge of the wind profile, these data may be extrapolated into design wind profile envelopes. Thus, the question that remains is how do we specify spectral type inputs based upon wind profile statistics? It is apparent that the atmospheric scientist must establish the intimate relationships that exist between the wind profile and atmospheric turbulence by performing extensive field experiments. Hopefully, upon establishing these relationships, design spectra could then be prescribed, based upon a statistically stable sample of hourly wind observations. At the present time, this procedure is being followed on a very limited scale.

In addition to specifying spectral type inputs, it appears that there will also be requirements for wind inputs that depend explicitly upon the time. Recently, it has been suggested that the undulatory characteristics of the wind profile, both in magnitude and more so in direction, could significantly affect the von Karman vortex shedding mechanism. Thus, it is likely that information about the unsteadiness of the so-called "steady-state" wind profile will be needed in the very near future. It will be equally important to give some consideration to the development of a comprehensive discrete gust model. Such a model is envisioned to give statistical information about the shapes of discrete gusts both in the vertical and in time, in addition to information about gust exceedance probabilities.

A continued need will exist for better and more representative expressions of risk relative to ground wind exposure problems. In particular, the need to establish theoretical statistical models which may be employed without risk of change in the design values established therefrom, when another year or two of measurements become available, is apparent. Since the ground wind loads problem is, from a natural environment viewpoint, only one of many interrelated input problems, it is likely that in the future we will see more emphasis on the "total" design problem of a space vehicle incorporating the multitude of interrelationships to formulate a design relative to an overall system risk.

REFERENCES

1. Daniels, Glenn E. ; Scoggins, James R. ; and
   Smith, Orvel E. : Terrestrial Environment
   (Climatic) Criteria Guidelines for Use in
   Space Vehicle Development, 1966 Revision.
   NASA TM X-53328, May 1966.

2. Valley, Shea L. : Handbook of Geophysics and
   Space Environments. Air Force Cambridge
   Research Laboratories, Bedford, Mass, 1965.

3. Gumbel, E. J. : Statistics of Extremes.
   Columbia University Press, New York, 1958.

4. Lifsey, David J. : An Empirical Analysis of
   Daily Peak Surface Wind at Cape Kennedy,
   Florida for Project Apollo. NASA TM X-
   53116, Aug. 1964.

5. Cardinale, S. V. ; England, F. G. ; and Kahudo,
   M. M. : Loads Requirements for Aerospace
   Vehicle Structures. Air Force Systems
   Command Technical Report #FDL-TDR-64-5,
   Wright-Patterson AFB, Ohio, Nov. 1964.

6. Sutton, O. G. : Micrometeorology. McGraw-
   Hill Book Company, Inc. , New York, 1953.

7. Panofsky, H. A. ; Blackadar, A. K. ; and
   McVehil, G. E. : The Diabatic Wind Profile.
   Quart. J. Roy. Meteorol. Soc. , 86, 1960,
   p. 390.

8. Panofsky, H. A. : Determination of Stress
   from Wind and Temperature Measurements.
   Quart. J. Roy. Meteorol. Soc. , 89, 1963,
   p. 85.

9. Deacon, E. L. : Vertical Diffusion in the
   Lowest Layers of the Atmosphere. Quart. J.
   Roy. Meteorol. Soc. , 75, 1949, p. 89.

10. Blackadar, A. K. : A Single Layer Theory
    of the Vertical Distribution of Wind in a
    Baroclinic Neutral Atmospheric Boundary
    Layer. Flux of Heat and Momentum in the
    Planetary Boundary Layer of the Atmosphere,
    Final Report, Contract No. AF9604-6641,
    The Mineral Industries Experiment Station,
    Penn. State University, 1965.

REFERENCES (Cont'd)

11. Scoggins, J. R. ; Vaughan, W. W. ; and Smith,
    O. E. : Low Level Wind Profiles Applicable in
    the Study of Vertically Rising Vehicle Per-
    formance between 3 Meters and 120 Meters,
    Cape Canaveral (Atlantic Missile Range),
    Florida. NASA MTP-AERO-60-23, MSFC,
    Dec. 29, 1960.

12. Mitsuta, Y. : Gust Factor and Analysis Time of
    Gust. J. Meteorol. Soc. , Japan, 40, 1962,
    p. 242.

13. Press, Harry: Atmospheric Turbulence En-
    vironment with Spherical Reference to Continuous
    Turbulence. Advisory Group for Aeronautical
    Research and Development, Report 115. North
    Atlantic Treaty Organization, Polais De Chaillat,
    Paris 16, Apr. -May 1957.

14. Lappe, Oscar V. : A Low Altitude Turbulence
    Model for Estimating Gust Loads on Aircraft.
    AIAA 2nd Aerospace Sciences Meeting, New
    York, N. Y. , Jan. 25-27, 1965.

15. Pritchard, F. E. ; et al. : Spectral and Ex-
    ceedance Probability Models of Atmospheric
    Turbulence for Use in Aircraft Design and
    Operation. AF Flight Dynamics Laboratory,
    Research and Technology Division, Air Force
    Systems Command, Wright-Patterson Air Force
    Base, Ohio, Nov. 1965.

16. Sissenwine, N. and Kasten, H. G. : Proceedings
    of the National Symposium on Winds for Aero-
    space Vehicle Design. Air Force Survey in
    Geophysics, no. 140, AFCRL-62-273(I), March
    1962.

17. Lumley, J. L. and Panofsky, H. A. : The
    Structure of Atmospheric Turbulence. Inter-
    science Publishers, New York.

18. Henry, Robert M. : A Study of Effects of Wind
    Speed, Lapse Rate and Altitude on the Spectrum
    of Atmospheric Turbulence at Low Altitudes.
    Inst. Aero. Sci. , Report No. 59-43.

19. Davenport, A. G. : The Spectrum of Horizontal
    Gustiness Near the Ground in High Winds.
    Quart. J. Roy. Meteorol. Soc. , 87, 1961,
    p. 194.

REFERENCES (Concluded)

20. Dryden, Hugh L.: A Review of the Statistical Theory of Turbulence. Quart. Appl. Math., 1, 1943, p. 7.

21. Webb, E. K.: Autocorrelations and Spectra of Atmospheric Turbulence. CSIRO Div. Met. Phys., Tech. Paper No. 5, Melbourne, 1955.

22. Panofsky, H. A. and Singer, I. A.: Vertical Structure of Turbulence. Quart. J. Roy. Meteorol. Soc., 9, 1965, p. 339.

23. Hanbolt, John C.: On the Response of Structures Having Multiple Random Inputs. Jahr. 1957 der WGL, Frieds. Vieweg and Sohn (Braunshwlig), 1957, pp. 296-305.

24. Reed, Wilmer H., III: Models for Obtaining Effects of Ground Winds on Space Vehicles Erected on the Launch Pad. NASA - Langley Research Center, presented at Conference on Role of Simulation in Space Technology, Blacksburg, Virginia, Aug. 17-21, 1964.

BIBLIOGRAPHY

1. Anon.: Prelaunch Ground Wind Loads. NASA Space Vehicle Design Criteria Monograph, NASA-OART, Washington, D. C., 1966.

BIBLIOGRAPHY (Concluded)

2. Camp, Dennis W. and Kaufman, John W.: The Use of Filtering and Smoothing Functions in the Analysis of Atmospheric Data. NASA MTP-AERO-62-54, MSFC, June 27, 1962.

3. Court, A.: Some New Statistical Techniques in Geophysics. Advances in Geophysics, I, ed. by H. E. Landsberg, New York, Academic Press, 1952, pp. 45-85.

4. Court, A.: Wind Extremes as Design Factors. J. Franklin Inst., vol. 256, 1953, pp. 39-56.

5. Gleeson, T. A.: Risk and Extreme Value Statistics Applied to Design Criteria. Department of Meteorology, Florida State University, Dec. 1964.

6. Lieblein, J.: A New Method of Analyzing Extreme Value Data. National Advisory Committee for Aeronautics, TN 3053, Washington, 1954.

7. Scoggins, J. R.; Smith, O. E.; and Vaughan, W. W.: Role of Applied Meteorology in the Development of Large Space Vehicles. NASA-MSFC, Presented at Fourth AMS Conference on Applied Meteorology, Hampton, Virginia, Sept. 10-14, 1962.

8. Smith, J. W. and Smith, O. E.: Surface Wind Statistics for Patrick AFB (Cape Canaveral), Florida. NASA - Marshall Space Flight Center, MTP-AERO-61-78, Huntsville, Alabama, Oct. 1961.

ON DYNAMIC RESPONSE OF A RECTANGULAR PLATE TO A
SERIES OF MOVING LOADS

By

Frank C. Liu

SUMMARY

This paper deals with an elastic rectangular plate with all edges clamped and subjected to a series of evenly spaced moving loads. Two types of loads are treated; one, a uniformly distributed pressure over a fractional length of the plate and the other, an impulsive load. The loads are assumed to be uniform across the plate. The solution of the partial differential equation of vibration of plate is assumed in the form of a double series with the generalized coordinates solved by using the Laplace transform method. Viscous damping is included.

Based on a two-term approximation, the steady-state dynamic response of the plate is obtained in analytical form from which the upper bounds of the maximum deflection and maximum bending stress are formulated. Numerical examples are given to illustrate the effect of thickness of plate, aspect ratio and velocity of loads on the dynamic response. Three types of resonance conditions are derived.

DEFINITION OF SYMBOLS

Symbol	Definition
a	length of plate
b	width of plate
$\bar{c}$	velocity of moving loads
D	$= Eh^3/12(1 - \nu^2)$, bending stiffness of plate
E	modulus of elasticity
h	thickness of plate
$\bar{L}$	length of distributed loads
$\bar{P}_0$	intensity of load

Symbol	Definition
r	$= a/b$, plate aspect ratio
s	Laplace transform variable of t
t	time variable
$\bar{x}, \bar{y}$	coordinates of plate
ζ	damping factor
λ_n	eigenvalues of a clamped-clamped beam ($\lambda_1 = 4.7300 = 1.5056\pi$, $\lambda_2 = 7.8532 = 2.4997\pi$)
μ_n	$= c\lambda_n/\omega_n$
ρ	mass density of plate
$\bar{\tau}$	time interval between two consecutive loads
$\bar{\omega}_n$	$= \omega_n/T$, natural frequency of plate

I. INTRODUCTION

We are concerned with the determination of the dynamic response of an elastic, rectangular plate subjected to a series of evenly spaced moving loads. Two types of loads are treated, a uniformly distributed pressure over a fractional length of the plate and the impulsive load. The latter is a limiting case of the former when the length of the distributed pressure becomes infinitesimal and the product of the length and the intensity takes a finite value, $\bar{P}_0$. We can find some practical applications of this mathematical model to acoustic problems or stress analysis of a shell structure in an aerodynamic flow. We may consider that the plate is an idealized panel of an airplane wing or a skin panel of a large shell structure while the moving loads resemble shock waves or pressure disturbance originated from a noise source.

If the loads travel at very high speed relative to the plate, say at sonic velocity, it takes less than one hundredth of a second for the load to go across a plate. When this is in the same order of magnitude of the period of vibration, resonance may take place under certain relationships between velocity of the loads and natural frequency of the plate. Furthermore, conditions of resonance may be related to both velocity and frequency of the moving loads. We are also interested in determining the dynamic response of the plate at resonance conditions if the viscous damping factor is known. To a structural designer, all this information may be helpful for the determination of the optimum aspect ratio and thickness of a panel.

We shall limit ourselves to the assumptions that the loads travel in one direction only and that the space between two consecutive loads is greater than the length of plate. For other cases the principle of superposition of the present case may apply. The coordinates and dimensions of the plate and loads are shown in Figure 1. We shall begin our analysis from the vibration of a rectangular plate with clamped edges.
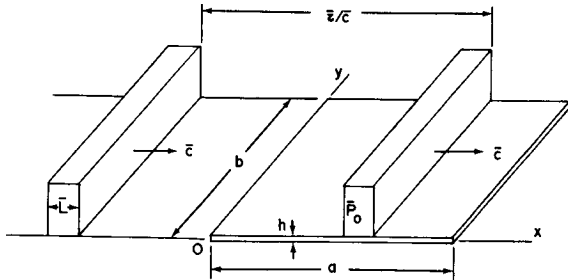

FIGURE 1. DIMENSIONS OF PLATE AND MOVING LOADS

II. ANALYSIS

A. EQUATION OF MOTION

The response of an elastic plate $w(x, y, t)$ to a dynamic load $p(x, y, t)$ is governed by the vibration of plate. For the convenience of manipulation, this equation is written in the nondimensional form:

$$\frac{1}{\lambda_1^4} (w_{xxxx} + 2r^2 w_{xxyy} + r^4 w_{yyyy}) + w_{tt} = p(x, y, t),$$

(1)

in which the subscripts x, y and t denote the partial derivatives of w. The load function of the two types of loads to be treated are

$$p(x, y, t) = P_0 \sum_{k=0}^{\infty} \delta(t - x/c - k\tau)$$

for impulsive loads

$$p(x, y, t) = P_0 \sum_{k=0}^{\infty} [u(t - x/c - k\tau) - u(t - \frac{x-L}{c} - k\tau)]$$

for distributed loads where $\delta(t)$ is the Dirac function and $u(t)$ is the unit step function. In the above equations the nondimensional quantities, denoted by unbarred symbols, and their counterparts, denoted by barred symbols, are related as follows:

$$w = \bar{w}/a, \quad x = \bar{x}/a, \quad y = r\bar{y}/a, \quad r = a/b,$$

$$P_0 = \bar{P}_0 T^2/a\rho h, \quad L = \bar{L}/a, \quad t = \bar{t}/T, \quad c = \bar{c}T/a,$$

$$\tau = \bar{\tau}/T, \quad T = \sqrt{a^4 \rho h/D\lambda_1^4}$$

$\lambda_1 = 4.7300$ (the first eigenvalue of a clamped-clamped beam).

B. METHOD OF SOLUTION

Laplace transform with respect to variable t is applied to equation (1); then, the solution of the transform function is assumed in the form [1]

$$W(x, y, s) = \sum_{n=1}^{\infty} \sum_{m=1}^{\infty} A_{nm}(s) \phi_n(x) \phi_m(y),$$

(2)

where ϕ is the eigen-function of a clamped-clamped beam [2]. The assumed solution satisfies the boundary conditions along all edges. The differential equation can be satisfied approximately, if we expand the middle term on the left-hand side and the load function of equation (1) also in infinite series in terms of $\phi_n(x)\phi_m(y)$. Let us now add to the equation of motion a viscous damping term of which the damping coefficient is assumed to be $e_{nm}\phi_n(x)\phi_m(y)$. This leads to a set of infinite number of simultaneous algebraic equations in the generalized coordinates $A_{nm}(s)$,

159

$$(\delta_n^4 + r^4\delta_m^4 + e_{nm}s + s^2)A_{nm}$$

$$+ \sum_{i,j=1}^{\infty} 2r^2\delta_i^2\delta_j^2 k_{ni}k_{mj}A_{ij} = P_0 a_n(s)b_m \qquad (3)$$

$$\delta_n = \lambda_n/\lambda_1, \quad n, m = 1, 2, \ldots,$$

in which k_{ni}, k_{mj}[3], $a_n(s)$ and b_m are the coefficients of eigen-function expansions.

Evidently, the expression of $A_{nm}(s)$ will be cumbersome if a large number of equations are used to obtain the solution of equation (3), and the task of finding their inverse Laplace transform will become prohibitive. To serve the purpose of the present study, a simple approximation which takes $m = 1$ and $n = 1$ and 2 is treated. The solution of $A_{11}(s)$ and $A_{21}(s)$ can be obtained readily from the reduced system of equations. Based on this approximation we obtain the first two natural frequencies of the plate

$$\bar{\omega}_n = \omega_n/T = 2.267\omega_n \frac{\pi^2}{a^2} \sqrt{\frac{D}{\rho h}}$$

$$n = 1, 2 \qquad (4)$$

$$\omega_n = \sqrt{\delta_n^4 + r^4 + 2\delta_n^2 r^2 k_{11}k_{nn}} \ .$$

Note that $k_{12} = k_{21} = 0$. The nondimensional frequencies ω_n versus the plate aspect ratio are plotted in Figure 2. To further simplify our solution of A_{11} and A_{21}, we assume the damping factors for the first and second modes are equal, i.e.,

$$\zeta = \tfrac{1}{2}e_{11}\omega_1 = \tfrac{1}{2}e_{22}\omega_2$$

and

$$\omega_{nd} = \omega_n\sqrt{1 - \zeta^2} \ ,$$

where ω_{nd} are the damped natural frequencies of the plate.

C. THE STEADY-STATE DYNAMIC RESPONSE FOR IMPULSIVE LOADS

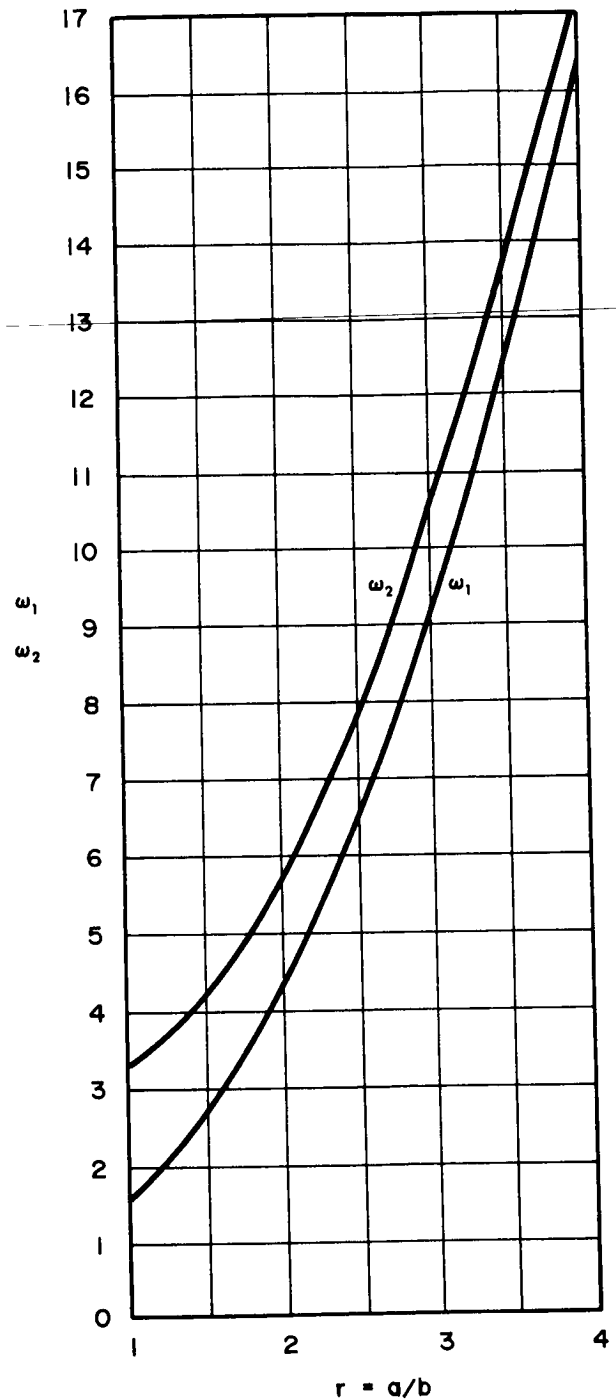The steady-state solution of the dynamic response for the case of impulsive loads, as derived in Liu [4], is

FIGURE 2. NONDIMENSIONAL FREQUENCIES

$$\overset{\cdot}{w}(x,y,t) = P_0 b_1 \sum_{n=1}^{2} (c/\omega_n^2)[\hat{f}_n(\hat{t}) + \hat{g}_n(\hat{t})] \phi_n(x) \phi_1(y)$$

$$-\tau < \hat{t} < 0 \qquad\qquad (5)$$

and

$$K\tau < t < (K+1)\tau.$$
$$K = 1, 2, \ldots$$

where

$$\hat{f}(\hat{t}) = \left(\frac{1}{1 + \mu^2 - 2\zeta\mu}\right) \frac{e^{-c\lambda\hat{t}}}{e^{c\lambda\tau} - 1}$$

$$\qquad\qquad (6)$$

$$+ \frac{e^{-\zeta\omega\tau}}{\cosh\zeta\omega\tau - \cos\omega_d\tau} \ F\cos(\omega_d\hat{t} - \psi)$$

$$\hat{g}(\hat{t}) = \begin{cases} \sqrt{2B}\sin(c\lambda\hat{t} + \eta) & -\tau < \hat{t} < -\tau + 1/c \\ \frac{1}{2}\sqrt{2B[1 - (-1)^n \sin\lambda_n]} \ \csc\frac{1}{2}c\lambda_n\tau \ \sin(c\lambda_n\hat{t} + \eta) \end{cases}$$

$$-\tau + 1/c < \hat{t} < 0 \qquad\qquad (7)$$

$$B = [(1 - \mu^2)^2 + 4\zeta^2\mu^2]^{-1}$$

and

$$\mu_n = c\lambda_n/\omega_n.$$

The expressions of F, ψ and η which are complicated functions of c, τ, ζ, ω and μ are not presented here; and the subscripts n have been removed from the symbols in equations (6) and (7) for brevity.

The solution of the dynamic response for the case of distributed loads is omitted here.

D. THE CONDITIONS OF RESONANCE

Three resonance conditions, i.e., conditions that make the coefficient of any term in equations (6) and (7) become unbounded when $\zeta = 0$, can be seen easily.

1. $\mu_n^2 = 1$ or $c = \omega_n/\lambda_n$ makes F and B unbounded.

2. $\frac{1}{2}\omega_n\tau = k\pi$ or $\tau = 2k\pi/\omega_n$ (k = 1, 2, ...) gives $\cosh\zeta\omega\tau - \cos\omega_d\tau = 0$.

3. $\frac{1}{2}c\lambda_n\tau = k\pi$ or $c\tau = 2k\pi/\lambda_n$ leads to $\csc\frac{1}{2}\lambda_n\tau = \infty$.

Condition 3 has little significance because of the higher order of smallness of $1 - (-1)^n \sin\lambda_n$ as a result of $\lambda_n \cong \frac{1}{2}(2n+1)\pi$. The critical nondimensional values of the velocity and period of traveling loads plotted against aspect ratio are shown in Figures 3 and 4, respectively. These above conditions are applicable also for the case of distributed loads.
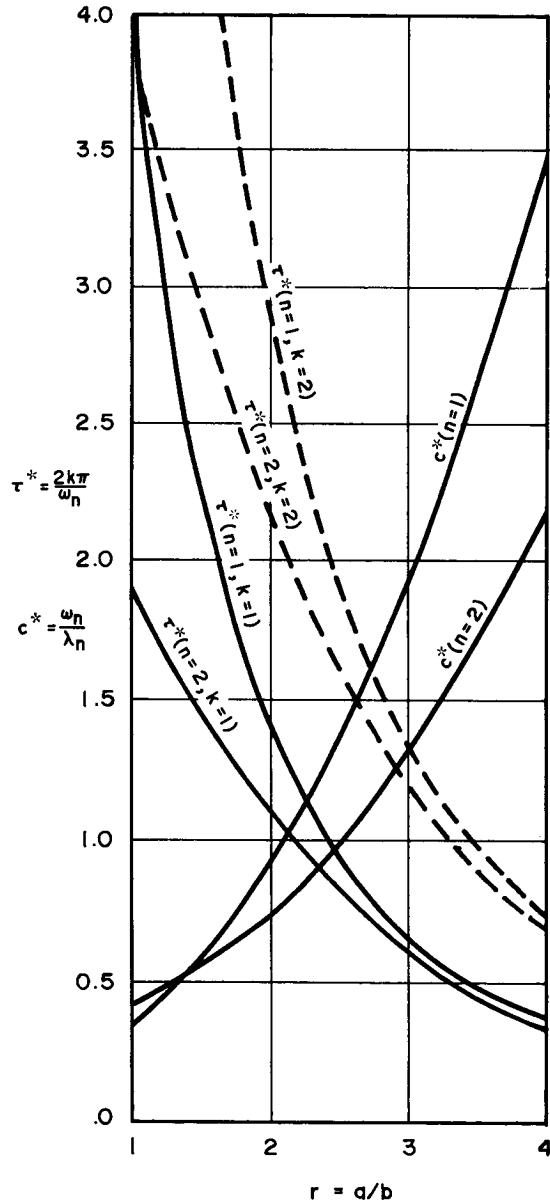
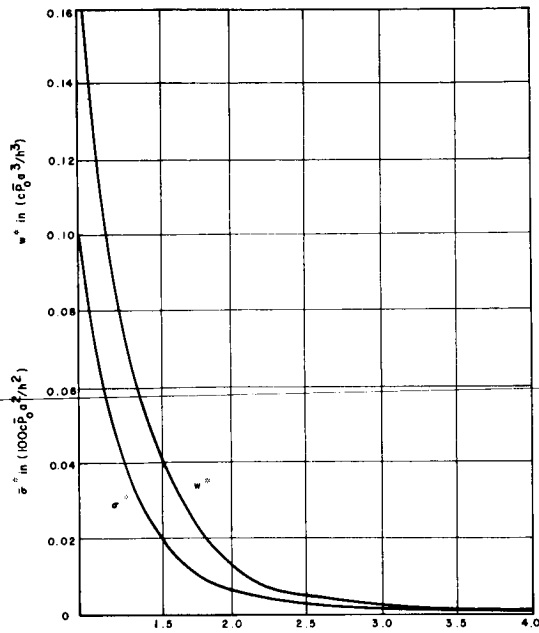

FIGURE 3.   c* AND τ* VERSUS r

FIGURE 4. w* AND σ* VERSUS r FOR
$\mu << 1$

E. THE UPPER BOUNDS OF MAXIMUM DE-FLECTION AND MAXIMUM BENDING STRESS

The maximum deflection and maximum bending stress can be computed from equation (5) provided the greatest absolute value of $\left(\hat{f}_n(t) + \hat{g}_n(t)\right)\dfrac{c}{\omega_n^2}$

denoted by A_n is determined. Determination of A_n is tedious; however, the upper bound of this quantity can be written out readily. Thus, the upper bounds of the maximum deflection and maximum bending stress are

$$w^* = 0.02812 \frac{\overline{P}_0 a^3}{Eh^3} (A_1 \Phi) \qquad (8)$$

and

$$\sigma^* = 0.4718 \frac{\overline{P}_0 a^2}{h^2} (A_1 S), \qquad (9)$$

respectively.

The relationships between Φ versus A_2/A_1 and S versus A_2/A_1 for various aspect ratios are presented graphically in Liu [4].

It has been shown [4] that if $c >> \omega_n/\lambda_n$, w^* and σ^* are independent of c, and that if $c << \omega_n/\lambda_n$,

w* and σ* are directly proportional to c. Plots of w* and σ* versus aspect ratio for the second case are shown in Figure 4, while these plots for the first case are given next, in the example.

F. EXAMPLE

Let us consider a steel plate with the following data:

a = 0.6096 m(24 in.)

$E = 20.67$ N/m²(30x10⁶ psi)

$\zeta = 0.1$

$\rho = 7855$ kg/m³ (15.24 slug/ft³)

and the velocity of the moving impulses is in the neighborhood of the speed of sound in a standard atmosphere with 265 impulses passing the plate in a second. Now we shall examine how the stiffness of the plate affects the dynamic response by taking h = 0.0254 mm(0.01 in.) and h = 0.0803 mm (0.03162 in.), respectively.

Case I. h = 0.0254 mm(0.01 in.)

From the given data, we calculated

T = 0.04186

τ = 1/265T = 0.09

c_s = $\overline{c}_s$ T/a = 23.41

where c_s is the nondimensional velocity of sound. Notice that

$c_s \cong 0.01(a/h)$

for both steel and aluminum plates. The dynamic responses w* and σ* are computed for the three velocities, c = 15, 20 and 25. The results show that there is no noticeable difference for the three velocities since $c >> \omega_n/\lambda_n$. The w* and σ* are plotted versus aspect ratio in Figures 5 and 6.

Case II. h = 0.0803 mm(0.03162)

When we increase the thickness of the plate by $\sqrt{10}$ times that of Case I, the values of T, c and μ_n are reduced to 1/10 of the values calculated in Case I, and $\tau = 0.9$. The dynamic responses w* and σ*

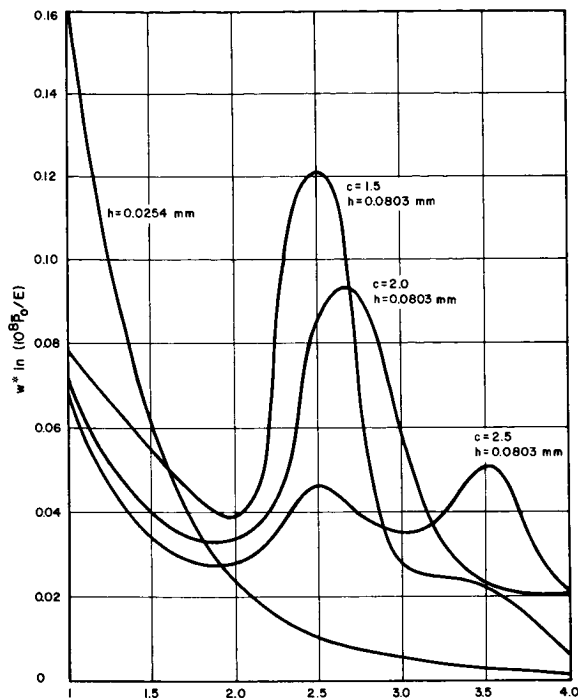calculated for c = 1.5, 2.0 and 2.5 (c_s = 2.341 for this case) are shown in Figures 5 and 6, respectively.

predominant factor; whereas, for small damping, (b) is more significant, and item (c) can always be disregarded.

FIGURE 5. w* VERSUS r

FIGURE 6. σ* VERSUS r

CONCLUSIONS

For a given frequency of the moving loads, the effect of plate thickness, plate aspect ratio and velocity of the loads on the dynamic response of a plate is illustrated in Figures 5 to 6. These are some of the interesting results that have been observed.

1. If $c \gg \omega_n/\lambda_n$, i.e., with high velocity loads moving on a thin plate, the dynamic response of the plate is almost independent of the velocity.

2. If $c \ll \omega_n/\lambda_n$, the dynamic response is directly proportional to the velocity.

3. The conditions of resonance at which the greatest dynamic response occurs are (a) $c = \omega_1/\lambda_1$ and ω_2/λ_2, (b) $\tau = 2k\pi/\omega_n$, and (c) $\frac{1}{2}c\lambda_n\tau = k\pi$. If the plate has large structural damping, (a) is the

4. The peaks of the curves shown in Figures 5 and 6 correspond to the critical values of c* or τ* or both as given in Figure 3.

5. For small aspect ratio, r, the value of A_2/A_1 is small. This is an indication that the two-term approximation used in solving equation (3) is satisfactory. It is obvious that more terms are required to cope with the higher modes of vibration, if r is large.

6. The dynamic responses w* and σ* presented here are the upper bounds; in reality, these values could be considerably higher than the actual values.

REFERENCES

1. Nowacki, W.: Dynamics of Elastic Systems. English Translation, John Wiley & Sons, Inc., New York, 1963, pp. 240-243.

REFERENCES (cont'd)

2. Young, D. and Felgar, R. P.: Tables of
    Characteristic Functions Representing Normal
    Modes of Vibration of a Beam. University of
    Texas Publication, July 1, 1949.

3. Felgar, R P.: Formulas for Integrals Con-
    taining Characteristic Functions of a Vibrating

REFERENCES (Concluded)

Beam. The University of Texas, Bureau of
Engineering Research, 1950.

4. Liu, F. C.: On Dynamic Response of a Rec-
    tangular Plate to a Series of Moving Loads. NASA
    TM X-53506

X. PUBLICATIONS AND PRESENTATIONS

TECHNICAL MEMORANDUM X-53380

January 21, 1966

AS-201 LAUNCH VEHICLE DYNAMICS
ANALYSES (U)

By Elbert Sullivan, Dan McNiel,
and Herschel Harmon

George C. Marshall Space Flight Center
Huntsville, Alabama

ABSTRACT

This report contains the results of control and collision studies performed on the AS-201 vehicle from lift-off to S-IVB/Apollo separation. Post-separation S-IVB maneuvers are also included.

The following prelaunch surface wind restrictions are imposed on the vehicle: freestanding, unfueled, 13.9 m/sec; freestanding, fueled, 21.1 m/sec; launch release, 12.6 m/sec. (Unfueled and fueled refer to the conditions that no propellants are in the vehicle and all propellants are loaded, respectively.) The probability of exceeding these peak winds in January is 0.026, 0.0005, and 0.062, respectively, and for February these probabilities are 0.063, 0.0016, and 0.105.

In flight, wind speed limits have been established based on the structural capabilities of the AS-201 vehicle for the 5- to 18-km altitude region. The most restrictive time point is 71 sec, which is nominally when the maximum $\alpha \cdot q$ product occurs. Wind restrictions based on this time point are 60 m/sec tail-wind, 40 m/sec crosswind, 25 m/sec headwind. Based on these wind limits, the probability for launch in January is 90 percent and for February, 86 percent. Also, wind limits as a function of altitude are established and the launch probabilities are reduced to 86 percent for January and 82 percent for February.

Separation studies of S-I/S-IVB show that a nomalfunctioning AS-201 vehicle will have sufficient clearance and control through this phase of flight.

An analysis of S-IVB powered flight reveals no control problems. Predicted APS (Auxiliary Propulsion System) fuel requirements to S-IVB/Apollo separation are nominally 18.6 kg, and three-sigma conditions increase this to 28.2 kg. This 28.2 kg is 51 percent of the available 55.3 kg of hypergolic fuel.

TECHNICAL MEMORANDUM X-53385

February 1, 1966

EARTH ORBITAL LIFETIME PREDICTION
MODEL AND PROGRAM (U)

By Ann R. McNair and Edward P. Boykin

George C. Marshall Space Flight Center
Huntsville, Alabama

ABSTRACT

An earth orbital satellite lifetime deck has been developed and programmed in Fortran IV language for the IBM 7094. The deck represents the development of a sophisticated and accurate lifetime prediction technique, which includes the effect of aerodynamic drag and the nonspherical gravitational potential of the earth. The computer program can be used to predict lifetime based on only a gross description of the initial orbit and drag parameters, or based on a very exact definition of the initial orbit and detailed description of the drag parameters and their variations, depending on the amount of information available. The primary factor contributing to uncertainty in lifetime predictions using this model is the atmospheric density. A very flexible model based on data from Discoverer, Gemini, and Saturn flights has been established. The primary uncertainty remaining in this model is prediction for future years of solar activity behavior and its influence on density as a function of altitude. As additional flight data and solar activity observations become available, they may readily be incorporated into the model, thus providing a rapidly changing density model which insures the best representation possible. Efforts to refine the models as presently defined and to perform pertinent studies in the lifetime area are continuing. This report represents only the present status of model definitions and defines the computer program now in use.

TECHNICAL MEMORANDUM X-53386

February 1, 1966

A MONTE CARLO PROGRAM FOR TRANSMISSION
PROBABILITY CALCULATIONS INCLUDING MASS
MOTIONS (U)

By James O. Ballance

George C. Marshall Space Flight Center
Huntsville, Alabama

ABSTRACT

A Monte Carlo computer program which can be used to calculate the transmission probabilities for two cylindrical tubes in series is described, as well as the technique of adding directed mass motion to the random thermal motion of the molecules. The results for a simple straight cylindrical duct are compared to other solutions, and angle-of-attack effects are examined. Complex systems for which no adequate solutions have previously been found are easily analyzed by this method. The Fortran instructions are listed along with a typical program solution.

TECHNICAL MEMORANDUM X-53387

February 2, 1966

THE EFFECT OF BENDING DYNAMICS AND CONTROL GAIN ON THE BENDING MOMENT (U)

By Alberta C. King

George C. Marshall Space Flight Center
Huntsville, Alabama

ABSTRACT

A response study was made using the Saturn 504 vehicle with the MSFC synthetic wind profile as the forcing function. The effect on the bending moment of the bending dynamics and various control gains was noted. It was found that the bending dynamics contribute greatly to the bending moment near the nose end of the vehicle. Also, as the accelerometer gain increases the overall bending moment decreases.

TECHNICAL MEMORANDUM X-53391

February 7, 1966

NEWTONIAN AERODYNAMICS FOR GENERAL BODY SHAPES WITH SEVERAL APPLICATIONS (U)

By W. H. Heybey

George C. Marshall Space Flight Center
Huntsville, Alabama

ABSTRACT

The Aero-Astrodynamics Research No. 2 (NASA TM X-53295) contains a succinct account of Newton-

ian aerodynamics for general analytical surfaces. Much of the detail passed over there when dealing with applications, together with a more thorough exposition of the general approach, is given in the present report which, it is hoped, will be useful to those who wish to actually work with the Newtonian method. It ought to serve well in the high-Mach-number, low-density phase of reentry flight. The lemniscatic body chosen in the Research Review paper as an example for calculating blunt-nose forces is replaced here by a circular cone with spherical base cap, since this configuration seems to command more immediate interest.

TECHNICAL MEMORANDUM X-53398

February 23, 1966

SATURN I BLOCK II GUIDANCE SUMMARY REPORT (C)

By R. A. Chapman

George C. Marshall Space Flight Center
Huntsville, Alabama

ABSTRACT

One of the missions assigned to the Saturn I Block II vehicles was flight testing the ST-124 inertial guidance system. This is an analytic report of the ST-124 platforms and associated hardware flown on the six Saturn I Block II vehicles, SA-5 through SA-10. This report presents for each vehicle the velocity component errors versus time for the total powered flight, combinations of platform system errors that would produce the velocity error profiles, and the velocity component error corresponding to each platform system error.

TECHNICAL MEMORANDUM X-53399

February 23, 1966

THE LUNAR ATMOSPHERE (U)

By W. C. Lucas* and O. H. Vaughan, Jr.

George C. Marshall Space Flight Center
Huntsville, Alabama

*Northrop Space Laboratories, Huntsville, Alabama

ABSTRACT

A survey of the state of the art of lunar atmos-
pheric models is presented. Based on the results of
this survey, the authors conclude that the lunar at-
mosphere is extremely complex and that its com-
position and density probably vary locally and are
influenced by volcanic, meteoritic, and solar activity.
The major components of the atmosphere will prob-
ably be H_2, H_2O, Ar, He, Kr, and Xe. An engineer-
ing lunar atmospheric model (ELAM) is described.

TECHNICAL MEMORANDUM X-53401

February 24, 1966

RANGE SAFETY AERODYNAMIC
CHARACTERISTICS OF THE APOLLO-SATURN
IB VEHICLES (U)

By Billy W. Nunley

George C. Marshall Space Flight Center
Huntsville, Alabama

ABSTRACT

Aerodynamic characteristics of the Apollo-
Saturn IB vehicles are defined for range safety and
emergency detection system studies. Normal force
coefficient, axial force coefficient, and center of
pressure are presented for the first- and second-
stage flight configurations and first- and second-
stage aborted configurations. These data are defined
for power-on and power-off conditions at various
Mach numbers (0 - 8.0) as a function of angle of
attack (0° - 180°). Aerodynamic characteristics are
also included for the S-IB stage plus interstage and
S-IB stage alone for the power-off condition. Drag
coefficient is defined for various stages, components,
etc., as a function of Mach number at various angles
of attack. Local normal force coefficient distributions
are defined at various Mach numbers (0.5 - 2.86)
and angles of attack ($20° \leq \alpha \leq 50°$) for emergency
detection system studies.

TECHNICAL MEMORANDUM X-53408

March 9, 1966

AS-205 LAUNCH VEHICLE REFERENCE
TRAJECTORY (C)

By J. W. Cremin, W. M. Gillis and T. W. Telfer

George C. Marshall Space Flight Center
Huntsville, Alabama

ABSTRACT

Presented is the official launch vehicle reference
trajectory for the second manned Apollo orbital
flight of the Saturn IB, AS-205. The various launch
vehicle (S-IB and S-IVB stage), spacecraft, and
system constraints that have produced this trajectory
shaping are reported. The nominal launch vehicle
mission is the injection of the command and service
module into an earth orbital ellipse of 85 nautical
miles perigee and 130 nautical miles apogee.

TECHNICAL MEMORANDUM X-53409

March 11, 1966

APOLLO LAUNCH WINDOW DISPLAYS FOR THE
YEARS 1967 THROUGH 1972 (U)

By Sam Walls and Scott Perrine

George C. Marshall Space Flight Center
Huntsville, Alabama

ABSTRACT

This document is intended as a quick reference
for mission planning purposes as to the availability
of launch windows using the Apollo Operational Nom-
inal Trajectory Ground Rules. The constraints used
in this document did not include the daylight launch
constraint; i. e., launches were considered at night
as well as day. This document covers a six-year
period beginning January 1967 and ending December
1972. The graphs show times of the day and days of
the month in which there are launch windows avail-
able for both direct ascent and parking orbit trajec-
tories.

TECHNICAL MEMORANDUM X-53410

March 14, 1966

STUDY OF POROUS WALL LOW DENSITY WIND
TUNNEL DIFFUSERS (U)

By K. W. Rogers, A. I. Lindsay
and M. R. Bottorff

ABSTRACT

A theoretical and experimental investigation was made of a porous wall diffuser used with a low density hypersonic nozzle. The Reynolds number range of the experiment varied from 1000 to 20,000 based on the nozzle diameter. At the low Reynolds numbers, nearly all of the flow passed through the pores of the diffuser. At the higher Reynolds numbers, 70 to 85 percent of the flow passed through the throat of the diffuser. The measured pressure recoveries varied from 1 to 10 times the test section normal shock pressure. When models were introduced into the test section stream, the mass flow and pressure recovery of the diffuser were markedly reduced. Although the model used to describe the flow through the porous wall appears incorrect, the theoretical and experimental pressure recoveries and mass flows were in good agreement.

TECHNICAL MEMORANDUM X-53414

March 22, 1966

GENERAL FORMULATION OF THE ITERATIVE GUIDANCE MODE (U)

By I. E. Smith

George C. Marshall Space Flight Center
Huntsville, Alabama

ABSTRACT

This report discusses the iterative guidance mode and its application to three-dimensional upper stage vacuum flight. It is an inertial or closed system mode in that the only inputs required after liftoff are available from the onboard navigation system. That is, the iterative scheme computes steering commands as a function of the state of the vehicle - velocity, position, longitudinal acceleration, and gravitational acceleration - and the desired cutoff conditions. The guidance commands are updated each guidance cycle, using the updated state of the vehicle. The iterative guidance scheme is a path adaptive guidance scheme in that it will retain its optimization properties under all expected types and magnitudes of vehicle perturbations without any loss in accuracy at cutoff.

The terminal conditions for the iterative scheme are defined by five quantities: radial distance from the center of the earth, velocity magnitude, path angle against the local horizontal, inclination of the orbit plane to the equator, and descending node of the orbit plane relative to the launch meridian. The velocity will be forced to lie in a plane defined by the inclination and descending node. The radius and path angle will also lie in the same plane.

TECHNICAL MEMORANDUM X-53415

March 22, 1966

A LOW DENSITY WIND TUNNEL RESIDUAL GAS MONITORING SYSTEM (U)

By W. W. Youngblood

George C. Marshall Space Flight Center
Huntsville, Alabama

ABSTRACT

A conceptual design was developed for a residual gas monitoring system planned for monitoring the composition of residual gases in the MSFC Aero-Astrodynamics Laboratory Low Density Chamber during low density wind tunnel experiments. The residual gas analyzer chamber is designed to operate at pressures in the range of 10^{-7} torr at the same time the Low Density Chamber operates over a pressure range of 10^{-3} to 10^{-7} torr. A unique design concept is introduced for adjusting the conductance for flow of the residual gases from the Low Density Chamber to the residual gas analyzer chamber. A movable circular conductance plate containing orifices of various sizes will permit external adjustment of the pressure within the residual gas analyzer chamber in discrete steps while a test is in progress. This concept is described in detail.

TECHNICAL MEMORANDUM X-53422

March 30, 1966

ESTIMATION OF PARAMETERS IN COMPOUND WEIBULL DISTRIBUTIONS (U)

By Lee W. Falls

George C. Marshall Space Flight Center
Huntsville, Alabama

ABSTRACT

The two-parameter Weibull distribution has been recognized as a useful model for survival populations associated with reliability studies and life testing experiments. In the analysis of atmospheric data, the distributions encountered are often a result of combining two or more component distributions. These compound distributions are consequently of interest to aerospace scientists. Presented is a method for estimation of the parameters of a compound Weibull distribution with two shape parameters, two scale parameters and a proportionality factor. The most general case of estimation will be considered in addition to a number of special cases that may be of practical value.

TECHNICAL MEMORANDUM X-53421

March 30, 1966

IMPLEMENTATION OF METHODS TO REDUCE THE SENSITIVITY OF THE ITERATIVE GUIDANCE MODE TO THRUST FLUCTUATIONS OF THE AS-501 VEHICLE (U)

By Volis L. Buckelew

George C. Marshall Space Flight Center
Huntsville, Alabama

ABSTRACT

Presented is a set of three-stage, three-dimensional iterative guidance mode equations with recommended modifications to reduce the sensitivity of the steering command to thrust fluctuations. Although the equations are specifically for AS-501 flight, they are applicable to all planned Saturn V flights except for the precalculation sections.

TECHNICAL MEMORANDUM X-53423

March 30, 1966

STATIC AERODYNAMIC CHARACTERISTICS OF OF THE ABORTED APOLLO-SATURN IB VEHICLE (U)

By Billy W. Nunley

George C. Marshall Space Flight Center
Huntsville, Alabama

ABSTRACT

Aerodynamic characteristics of the aborted Apollo-Saturn IB vehicles are defined for control and structural analyses. Static stability characteristics are presented at various angles of attack ($0°$ - $15°$) as a function of Mach number. Local normal force coefficient distributions are included at various angles of attack ($0°$ - $15°$) for the Mach numbers ranging from 0.5 to 2.86. Axial force coefficients for power-off and power-on conditions are defined at zero angle of attack throughout the Mach number range. Local axial force coefficient and local pressure coefficient distributions are presented at zero angle of attack at Mach numbers from 0.5 to 2.86. These data are based primarily on wind tunnel tests of scale models.

TECHNICAL MEMORANDUM X-53427

April 12, 1966

A CALCULATION METHOD FOR THE ABLATION OF GLASS-TIPPED BLUNT BODIES (U)

By John D. Warmbrod

George C. Marshall Space Flight Center
Huntsville, Alabama

ABSTRACT

This report presents in detail a calculation method to compute the trajectory and ablation characteristics at the stagnation point of a glass sphere entering into the atmosphere of the earth from an arbitrary point in space. The underlying equations employed by the method include the transient effects, internal radiation, melting and nonequilibrium vaporization of the glass-liquid layer. A computer program written in Fortran IV language and a detailed description of the preparation of input for this program are included. The program is particularly applicable to the study of tektites and their atmospheric entry. The method and program could easily be altered to calculate the ablation at the stagnation point of a spherical glass tip on a missile-shaped body.

TECHNICAL MEMORANDUM X-53434

April 12, 1966

ANALYSIS OF AN INTERPLANETARY
TRAJECTORY TARGETING TECHNIQUE WITH
APPLICATION TO A 1975 VENUS FLYBY MISSION
(U)

By Bobby Ellison

George C. Marshall Space Flight Center
Huntsville, Alabama

ABSTRACT

A trajectory technique is discussed that, when
systematically applied, enables the trajectory ana-
lyst to obtain a continuous, free-flight integrated
trajectory from planet A to a desired target planet
C via some intermediate target planet B. Basically,
the scheme defines targeting parameters at the inter-
mediate planet B in terms of the desired values at
planet C. This allows an actual search between
planets A and B, while, in reality, a targeting at
planet C is taking place. An application of this tar-
beting technique to a Venus flyby trajectory, i.e.,
A = Earth, B = Venus, C = Earth, is described in
this report.

TECHNICAL MEMORANDUM X-53452

April 26, 1966

PROBABILITIES OF ZERO WIND SHEAR
PHENOMENA BASED ON RAWINSONDE DATA
RECORDS (U)

By Lawrence E. Truppi

George C. Marshall Space Flight Center
Huntsville, Alabama

ABSTRACT

The term zero wind shear is defined for the con-
dition where winds aloft attain speeds of 36 m/sec
or higher and persist through a vertical distance
such that there is maintained a vector wind shear in
the interval ± 5 m/sec/km between successive 1-km
levels.

Data are obtained from two RAWIN observations
per day for six years from Cape Kennedy, Florida,
and four RAWIN observations per day for five years
from Santa Monica, California. Both data decks
were edited, checked and serially completed before
use. Results are presented as graphs of zero shear
thickness versus peak wind speed, and as empirical
probabilities of occurrence of zero wind shear con-
ditions at altitudes above and below the mean height
of the level of peak wind. Probabilities of total
depth of zero wind shear are also presented.

TECHNICAL MEMORANDUM X-53455

April 27, 1966

CONTROL FACTORS FOR SATURN
SA-203 VEHICLE (U)

By Billy W. Nunley

George C. Marshall Space Flight Center
Huntsville, Alabama

ABSTRACT

Control factors and three-sigma variations are
defined as a function of flight time for the Saturn
SA-203 vehicle control studies. Included are angular
velocities, angular accelerations, and linear accele-
rations due to engine and aerodynamic forces. The
three-sigma variations of the more important con-
trol factors include variation in mass flow, specific
impulse, lift-off weight, atmospheric density, pitch-
yaw moment of inertia, roll moment of inertia, nor-
mal force coefficient, axial force coefficient, and
center of pressure. Also, three-sigma winds were
incorporated. These data do not include engine-out
effects.

TECHNICAL MEMORANDUM X-53458

May 5, 1966

AS-501/S-IC STABILITY ANALYSIS CONSIDERING
FOUR DIFFERENT CONTROL SYSTEMS (U)

By Charles W. Billups

George C. Marshall Space Flight Center
Huntsville, Alabama

ABSTRACT

This report compares the control-feedback stability characteristics of the Saturn AS-501 booster stage configuration in the pitch plane for each of four preliminary control systems. The characteristics are presented by means of gain and/or phase root locus plots for three selected flight times: 0 sec (liftoff), 77.9 sec (max q), and 146.1 sec (cutoff).

The four systems which were investigated include two attitude systems (designated by ATT #1 and ATT # 2) and two accelerometer systems (designated by AZ #1 and AZ #2). Only the ATT #2 system was found to provide acceptable stability characteristics for all modes of oscillation. In general, the addition of an accelerometer to the system decreases in stability. However, response studies indicate that a slight (7 percent) load reduction can be achieved with accelerometer control. If an accelerometer system is implemented on Saturn V to take advantage of this load alleviation, it must be a system which holds the adverse effects upon stability at a minimum.

████████████

TECHNICAL MEMORANDUM X-53459

May 9, 1966

VARIATIONAL PROBLEMS AND THEIR SOLUTION
BY THE ADJOINT METHOD (U)

By Roger R. Burrows

George C. Marshall Space Flight Center
Huntsville, Alabama

ABSTRACT

A variational problem typical of those encountered in flight mechanics is posed. The adjoint technique is then developed in a manner to indicate its application to general two-point boundary value problems. It is then specifically applied to the variational problem. Finally, the practicality of the adjoint method is illustrated by solving three typical problems of exo-atmospheric flight and one problem involving an ascent through the atmosphere to low earth orbit.

████████████

TECHNICAL MEMORANDUM X-53460

May 10, 1966

CONTROL FACTORS FOR APOLLO-SATURN
204 VEHICLE (U)

By Billy W. Nunley

George C. Marshall Space Flight Center
Huntsville, Alabama

ABSTRACT

Nominal control factors and three-sigma variations are defined as a function of time for the Apollo-Saturn 204 vehicle. The nominal control factor data include angular velocities, linear velocities, angular accelerations, and linear accelerations due to aerodynamic and engine forces. Three-sigma variations, tabulated for the more important control factors, are presented for the standard eight-engine operation, i.e., no engine out. Included in the analysis are variations in specific impulse, lift-off weight, axial force, atmospheric density, mass flow, roll moment of inertia, pitch yaw moment of inertia, normal force, center of pressure, and center of gravity. Three-sigma winds were also incorporated.

████████████

TECHNICAL MEMORANDUM X-53461

May 12, 1966

PERCENTAGE LEVELS OF WIND SPEED
DIFFERENCES COMPUTED BY USING
RAWINSONDE WIND PROFILE DATA FROM CAPE
KENNEDY, FLORIDA (U)

By Dennis W. Camp and Michael Susko

George C. Marshall Space Flight Center
Huntsville, Alabama

ABSTRACT

Presented are percentage levels of wind speed differences calculated from AN/GMD-1 upper atmospheric wind profile data observed at Cape Kennedy, Florida. Eight years of rawinsonde wind profile data (5844 profiles) were used: January 1, 1956, through December 31, 1963. The results are based on each kilometer of data using wind velocity measurements obtained for the 1.0- through 25.0-km altitude interval. The results presented may be used (1) to aid in predicting statistical limits of upper level winds, and (2) to provide an understanding of the statistical results of wind speed change as a function of time. This type of information is important for space vehicle launch operations.

TECHNICAL MEMORANDUM X-53464

May 25, 1966

TRAJECTORY OPTIMIZATION BY EXPLICIT
NUMERICAL METHODS (U)

By Lyle R. Dickey

George C. Marshall Space Flight Center
Huntsville, Alabama

ABSTRACT

The problem of trajectory optimization is con-
sidered from the standpoint of numerical analysis.
A numerical solution is obtained for an assumed thrust
angle history, and an explicit numerical solution is
obtained for the linearized equations of motion for
neighboring solutions. With the explicit solution
available, it is not difficult to determine whether or
not the assumed solution is optimum. The first and
second variations together provide a straightforward
iteration method of approaching the optimum solution.
It is of particular interest that the procedure remains
unaltered even by the introduction of discontinuities
and intermediate constraints.

TECHNICAL MEMORANDUM X-53468

May 26, 1966

AN ORBITING DENSITY MEASURING INSTRUMENT
(U)

By D. A. Wallace, K W. Rogers, J. B. Wainwright
and R. L. Chuan

George C. Marshall Space Flight Center
Huntsville, Alabama

ABSTRACT

A design study has been conducted for a direct
air density measuring device that can be carried on-
board an orbiting spacecraft in the altitude range
from 140 to 280 km. The resulting design calls
for a free molecular cryopumped gas collector of
nearly unity capture coefficient, using an orifice
collector and a cooled piezoelectric crystal acting
as a microbalance. Refrigeration is by heat sinks
pre-conditioned before launch. Measurement is
through beat-frequency (between cryopumping crys-
tal and a variable oscillator) converted to dc voltage,
thence to telemetry.

TECHNICAL MEMORANDUM X-53469

June 3, 1966

STATIC AERODYNAMIC CHARACTERISTICS OF
THE ABORTED APOLLO-SATURN V VEHICLE (U)

By V. K. Henson and R. M. Glasgow

George C. Marshall Space Flight Center
Huntsville, Alabama

ABSTRACT

This report presents the static aerodynamic
characteristics of the aborted Apollo-Saturn V vehicle
for use in performance, control, and structural
analyses. The data, which include vehicle normal
and axial forces and their distributions, are based
primarily on wind tunnel tests of scale models. All
data are presented for various Mach numbers be-
tween 0 and 3.0 and vehicle angles of attack between
$0°$ and $14°$.

TECHNICAL MEMORANDUM X-53470

June 3, 1966

AS-202 LAUNCH VEHICLE OPERATIONAL FLIGHT
TRAJECTORY (U)

By Pamelia B. Pack

George C. Marshall Space Flight Center
Huntsville, Alabama

ABSTRACT

This report presents the launch vehicle oper-
ational flight trajectory for the Saturn IB vehicle
AS-202. Included is a discussion of the predicted
trajectory, the mission objectives, and constraints,
plus the associated dispersion study, and tracking
summary. A successful flight will place an Apollo
spacecraft into a lob-type trajectory and will aid in
determining the performance of the launch vehicle
and spacecraft subsystems in preparation of manned
orbital missions.

TECHNICAL MEMORANDUM X-53472

June 6, 1966

SATURN AS-201/APOLLO POSTFLIGHT
TRAJECTORY (U)

By J. B. Haussler and W. G. Smith

George C. Marshall Space Flight Center
Huntsville, Alabama

ABSTRACT

This report presents the postflight trajectory
for the Saturn AS-201/Apollo test flight. First of the
Saturn IB series, AS-201 was the first vehicle to
carry an Apollo spacecraft. Trajectory-dependent
parameters are given in earth-fixed, space-fixed
ephemeris and geographic coordinate systems. A
complete time history of the powered flight trajectory
is presented at 1.0-sec intervals from first motion
to S-IB/S-IVB separation, 5.0-sec intervals from
S-IB/S-IVB separation to S-IVB cutoff and 10.0-sec
intervals from S-IVB cutoff to S-IVB/CSM separation.

TECHNICAL MEMORANDUM X-53476

June 22, 1966

AN EVALUATION OF THE LOW G PROPELLANT
BEHAVIOR OF A SPACE VEHICLE DURING
WAITING ORBIT (U)

By Robert S. Ryan and Harry Buchanan

George C. Marshall Space Flight Center
Huntsville, Alabama

ABSTRACT

The performance of a space vehicle in waiting
orbit requires an adequate description of interaction
of vehicle dynamics and control. The vehicle dynamics
required a description of the behavior of liquids in a
low g environment. This paper discusses the behav-
ior of liquid in low g and its interaction with vehicle
dynamics and control.

TECHNICAL MEMORANDUM X-53479

June 24, 1966

FOCAL POINT COMPUTATION IN A THREE-
LAYERED ATMOSPHERE (U)

By James E. Mabry

George C. Marshall Space Flight Center
Huntsville, Alabama

ABSTRACT

This report outlines a computer program for
calculating, directly from the atmospheric data,
the location of ground level acoustic foci resulting
from meteorological conditions in a three-layered
atmosphere. Also, a procedure is given whereby
one obtains the average intensity level in the immed-
iate neighborhood of a focus. Finally, it is shown,
by means of examples, that a systematic use of the
computer program can lead to a deepened insight
into the relationship of the focus location and the
atmospheric parameters.

TECHNICAL MEMORANDUM X- 53478

June 23, 1966

PROGRESS REPORT NO. 8. PROCEEDINGS OF THE
TWENTY-FOURTH SEMINAR ON SPACE FLIGHT
AND GUIDANCE THEORY (U)

Sponsored by the Aero-Astrodynamics Laboratory

George C. Marshall Space Flight Center
Huntsville, Alabama

ABSTRACT

Progress reports of NASA-sponsored studies
in space flight and guidance theory are presented.
The studies are made by several universities and
industrial firms under contract to MSFC. This
progress report reflects work done on the contracts
during the period from April 1, 1965, to December
31, 1965. The contracts are technically monitored
by personnel of the Astrodynamics and Guidance
Theory Division, Aero-Astrodynamics Laboratory,
George C. Marshall Space Flight Center.

TECHNICAL MEMORANDUM X-53484

June 29, 1966

THE ATMOSPHERE OF MARS: A DERIVATION OF
ENGINEERING AND DESIGN PARAMETERS (U)

By W. T. Roberts and G. S. West

George C. Marshall Space Flight Center
Huntsville, Alabama

ABSTRACT

Three model atmospheres have been derived for
use in mission planning, aerospace lander design,
and Martian orbiter and flyby studies. Atmospheric
parameters for these three models have been calcu-
lated from the planetary surface to 10 000 km. These
three model atmospheres of differing atmospheric
composition, surface pressure, and surface temper-
ature are the upper density model (60 percent CO_2
and 40 percent N_2); the mean density model (100 per-
cent CO_2); and the lower density model (80 percent
CO_2 and 20 percent Ar). The general program of
Kern and Schilling, with a few revisions, was used;
this publication contains the details of the mathemat-
ical basis and program routines in considerable
depth. The models chosen should provide values
which will be of use as guidelines for the engineering
and design of orbiting and landing vehicles.

TECHNICAL MEMORANDUM X-53485

June 29, 1966

THE CLASSICAL "SPHERE-OF-INFLUENCE" (U)

By Roger R. Burrows

George C. Marshall Space Flight Center
Huntsville, Alabama

ABSTRACT

The classical definition of the "sphere-of-
influence" is given and the equation implicitly defin-
ing its radius is derived. This equation was solved
using a little known iteration technique attributed to
Wegstein. Two analytic approximations are derived
and the Fourier coefficients through 12th order for
the exact result are displayed for the moon and each
planet in the solar system. Several "spheres" about
the moon computed according to these results are
displayed graphically for the earth-moon system.

TECHNICAL MEMORANDUM X-53473

June 7, 1966

A WORST DISTURBANCE DESIGN CRITERION IN
THE THEORY OF ANALYTIC CONTROL SYSTEMS
SYNTHESIS (U)

By T. E. Carter

George C. Marshall Space Flight Center
Huntsville, Alabama

ABSTRACT

Design techniques of linear optimal control are
found to apply to a minimax problem. With a bounded
energy constraint on the class of admissible distur-
bances the minimax value of an integral quadratic
form of state variables and control can be obtained
by finding a positive definite steady-state solution
of a matrix Riccati equation. The optimal strategies
for control and disturbance are linear functions of
state which depend on the numerical bound of the class
of disturbances, the set of initial conditions, and rel-
ative weighting of the state variables in the cost func-
tional. Analytical design procedures such as the
root square locus of Chang which appear in optimal
linear control problems are also valid for this prob-
lem. An equivalent optimal multivariable control
problem has been found whose steady-state solution
is obtained by solving the same matrix Riccati equa-
tion as was obtained from the minimax problem.
Sufficient conditions for existence of solutions to the
minimax problem are thus obtained from the proper-
ties of the equivalent optimal multivariable control
problem. The results are illustrated by solving a
second-order example.

TECHNICAL NOTE D-3440

June 1966

QUASI-SLENDER BODY THEORY FOR SLOWLY
OSCILLATING BODIES OF REVOLUTION IN
SUPERSONIC FLOW (U)

By M. F. Platzer and G. H. Hoffman*

George C. Marshall Space Flight Center
Huntsville, Alabama

* Lockheed Missiles and Space Company. Huntsville
Alabama

ABSTRACT

An analysis is presented which accounts for body shape and Mach number dependence of the aerodynamic forces on slowly oscillating pointed bodies of revolution in supersonic flow. By using body-fixed coordinates, the first-order velocity potential is expanded in an elementary fashion for small radial distances from the body. This expansion is equivalent to the Adams-Sears expansion technique using Laplace or Fourier transforms. Analytical closed-form expressions for the stability derivatives are obtained. These results are valid to second-order in terms of Mach number and body thickness ratio.

Three specific body shapes are analyzed in detail: a cone, a convex parabolic ogive, and a concave parabolic ogive. Numerical results for the four stability derivatives C_{N_α}, C_{M_α}, $C_{N_{\dot{\alpha}}} + C_{N_q}$, and $C_{M_{\dot{\alpha}}} + C_{M_q}$ are presented to illustrate their dependence on Mach number and body thickness ratio. Comparisons with other theories are given, and the range of validity of the present results is discussed. Comments on application of quasi-slender-body theory to other body shapes are made.

TECHNICAL NOTE D-3450

June 1966

A REVIEW OF SOME EXISTING LITERATURE CONCERNING DISCONTINUOUS STATE VARIABLES IN THE CALCULUS OF VARIATIONS (U)

By Rowland E. Burns

George C. Marshall Space Flight Center
Huntsville, Alabama

ABSTRACT

The important problem of determining optimal trajectories for problems with discontinuous state variables has been treated by a few authors in rather esoteric papers. This paper summarizes the contents of two of these in a fairly detailed discussion. An attempt has been made to develop explicitly those relationships which are not contained in material dealing with the case of continuous state variables.

The essential feature of the discussion is a transformation from a set of state variables with points of discontinuity to a set of new variables which, though greater in number, are continuous. The necessary conditions of Euler, Weierstrass, and Clebsch, along with the transversality conditions, are discussed in the transformed problem; the results are rewritten in the original variables.

The bulk of material covered assumes that the magnitudes of the discontinuities are known a priori, but the case of unknown discontinuities is treated in the latter portion of the paper.

B. PRESENTATIONS

REMOTE SENSING WITH OPTICAL CROSS CORRELATION METHODS

By Fritz Krause

ABSTRACT

Our basic concept is to employ the cross correlation of two narrow light beams for remote sensing. The problem with most optical methods such as schlieren, shadowgraph systems or spectrometers is that the received signal is always integrated along the line of sight. However, we want information for a particular spot along the line of sight. To this purpose we adjust a second beam to intersect the first at the point of interest. The integration along the two beams is then eliminated by a cross-correlation of the detected fluctuations. This paper indicates how this new concept of combining standard spectroscopy with a statistical cross-correlation analysis might be used for dynamic and kinematic studies such as the formation and motion of water vapor or dust clouds, the dynamics and production of the ozone layers, and the generation and motion of radiation belts.

The concept has been demonstrated successfully by measuring the turbulent fluctuations in subsonic jets. The main problems in AAP applications are formulated in terms of questions, such that the background information which is needed to establish the feasibility of particular experiments becomes apparent.

ACOUSTIC AND HEAT TRANSFER ASPECTS OF LAUNCH VEHICLE TURBULENCE

By Fritz Krause

ABSTRACT

The base of a Saturn V launch vehicle is exposed to hot gases recirculated from the plume of the clustered rocket exhausts. The resulting high heat transfer rate and acoustic loading necessitate special precaution if mission failures are to be avoided. This paper treats the efforts which have been made by NASA to estimate the magnitude of these effects in order that the best compromise between cost and payload can be obtained.

CURRENT RESEARCH ON INFRARED RADIATION FROM ROCKET EXHAUSTS

By Robert M. Huffaker

ABSTRACT

Infrared radiation from rocket exhausts has been of particular interest to NASA in the area of radiative heating of Saturn-type vehicles. It was deemed necessary, for design purposes, to improve the existing calculation procedures for radiative transfer through inhomogeneous hot gases and carbon particles. The rocket engines of principal interest are the J-2 of which H_2O is the only radiating species and the F-1 for which H_2O, CO_2, CO and carbon particles are the radiating species. A computer program has been developed to calculate infrared radiant heat transfer through inhomogeneous gases. This program uses a band model approach to the absorption coefficients of the gases. The band model parameters necessary are the mean line strength, the mean line half-width, the mean line spacing, averaged over 25 cm^{-1} increments. Analytical and experimental programs are in process to complete the determination of these parameters at long path lengths and to include the effects of foreign gas broadening on these parameters.

In lieu of this experimental data, which should be completed by November 1966, an approximate set

of γ's, l/d's, S/d's have been determined, using data and analytical expressions coming principally from the literature. A modified Curtis-Godson Approximation is used in the radiative heat transfer calculations which effectively averages the band model parameters over the inhomogeneous path, i.e., substitutes a hypothetical homogeneous path for the inhomogeneous path. This approximation has been used successfully in predicting atmospheric radiative transmission. This modified Curtis-Godson Approximation has been experimentally shown to be applicable for strong temperature and concentration gradients for certain wavelengths in the H_2O and CO_2 infrared spectrums. The Curtis-Godson approach to the radiant heat transfer calculation is planned to be compared to an exact calculation in a worst-case analysis for a typical rocket exhaust plume at altitude over a selected wavelength increment.

A TECHNIQUE FOR ANALYZING CONTROL GAINS USING FREQUENCY RESPONSE METHODS

By

Robert S. Ryan
Aero-Astrodynamics Lab, MSFC
Huntsville, Alabama

Harry Harcrow
Martin Company
Denver, Colorado

ABSTRACT

Minimum control gains are determined by writing the control equation dependent upon gain ratios rather than specific gains. These gain ratios, alpha meter or accelerometer gains to attitude gains, are varied to achieve an optimum control system. Optimum gains are the gains that occur for a load minimum condition at some specified vehicle station.

The vehicle is described as a linear, dynamic system consisting of ten degrees of freedom. Rigid body motion consists of lateral translation and rotation in either the pitch or yaw plane. Effects of elastic deformation are incorporated. Propellant oscillations

are described by an equivalent spring-mass-damper system using only the first mode of each propellant tank. Vehicle responses are determined over all significant frequencies. Vehicle bending moment, assumed as the only effective structural load, is determined using a load separation technique. The effects of control system gains are determined by comparisons of exceedances, probabilities of such an occurrence, and the number of cycles of response expected. Root mean squares and variances are used in determining response levels.

These results are directly applicable to both control synthesis and structural response since they indicate frequency sensitivity to atmospheric turbulence. Nonstationary effects are synthetically introduced by completing studies at different flight bandwidth periods.

MISSILE RANGE REFERENCE ATMOSPHERES- THEIR ORIGIN AND USE

By Orvel E. Smith and William W. Vaughan

ABSTRACT

The national aerospace research and development programs have created a demand for specialized static atmospheric thermodynamic models which describe the mean state of the thermodynamic quantities over particular vehicle launch sites and reentry areas. To meet this requirement reference atmospheres are being derived for the several major missile ranges. The concept of Range Reference Atmospheres, their development, data tabulations, use, and comparison with the US Standard Atmosphere 1962 will be discussed.

ANALYSIS OF DETAILED WIND PROFILES FOR THE LAUNCH OF SATURN AS-201 ON FEBRUARY 26, 1966

By Kelly Hill

ABSTRACT

An analysis has been conducted on some significant changes in the detailed wind profile data measured at Cape Kennedy, Florida, for the launch of Saturn AS-201 on February 26, 1966. Relationships are shown between the jet stream and related small-scale motions or perturbations in the profile data. The critical vector wind shears which developed as a result of the profile changes are described. The results of this study indicate that in this particular case useful forecasts of the significant tendencies in the detailed wind velocity profiles over short periods were possible.

FIRST-ORDER SECULAR PERTURBATIONS OF AN ARTIFICIAL EARTH SATELLITE DUE TO SUN AND MOON

By C. C. Dearman, Jr.

ABSTRACT

In this report formulas are derived which permit calculation of the first-order secular perturbations of the orbital elements of an artificial earth satellite that are caused by the sun and moon. The problem of determining these perturbations has been presented in many articles but always, insofar as a careful search has revealed, under some restriction as to orbit inclination, eccentricity or number of orbital elements considered. The purpose of this report is to present a procedure for the calculation of first-order secular perturbations caused by the sun and moon without these restrictions.

EXPERIMENTAL INVESTIGATION OF WIND INDUCED OSCILLATION EFFECTS ON CYLINDERS IN TWO-DIMENSIONAL FLOW AT HIGH REYNOLDS NUMBERS

By

J. J. Ancotta
Martin Company

G. W. Jones
Langley Research Center

R. Walker
Marshall Space Flight Center

ABSTRACT

This paper presents the salient results of an experimental investigation of the steady drag and unsteady lift forces acting on a two-dimensional circular cylinder subjected to flow perpendicular to its axis. The study includes the effects of model motion, Strouhal Number and Mach Number over a range of Reynolds Number from 0.6×10^6 to 18.7×10^6. These tests were performed on a stationary and oscillating model for a model Strouhal Number range from 0.06 to 0.5.

It was found that with increasing Reynolds Number the unsteady lift force characteristic changes from wide-band random to narrow-band random to random plus periodic with these transitions occurring at approximately 3.5 million and 6 million Reynolds Number. The Strouhal Number of the unsteady aerodynamic force on the stationary model increased with increasing Reynolds Number to a constant value of 0.3 in the random plus periodic (Transcritical) Reynolds Number range.

In the transcritical regime, the unsteady lift forces were found to increase with amplitude of model oscillation, with the maximum amplification occurring when the model oscillating frequency was approximately equal to the aerodynamic Strouhal frequency. For model oscillation frequencies below the stationary model aerodynamic Strouhal frequency, the unsteady lift forces exhibited negative aerodynamic damping characteristics.

Mach Number was found to affect both the static drag and unsteady lift data for Mach Number greater than 0.2. For Reynolds Numbers above 3 million and Mach Number less than or equal to 0.2 the static drag coefficient was relatively constant at approximately 0.54.

NONLINEAR DYNAMICS OF AN ARTIFICIAL GRAVITY ORBITING SYSTEM

By H. E. Worley and G. F. McDonough

ABSTRACT

The nonlinear dynamics of an automatically controlled rotating orbiting system consisting of two masses connected by long cables, and a docking structure at the total c.g. are analyzed. During counterweight deployment, the control system stabilizes torsional oscillations, and wobbling of cabin and cable extensional vibrations.

During manned operations, movements of personnel and equipment impart forces to the structure and affect its dynamic characteristics: the control system maintains the c.g. at the docking structure to facilitate docking maneuvers and maintains a prescribed angular velocity of the system. Radial motion of the counterweight and structural damping are considered.

Analysis of this system yields nonlinear differential equations which reveal the coupling between control system and station motion. These equations are attacked by analog computer methods to avoid the extreme difficulties of obtaining closed solutions or meaningful numerical solutions and to facilitate parameter variation studies. Important parameters are control system scheme, sensor types and locations, time variation of vehicle mass and stiffness distribution, station orbit and attitude and schemes for rotation maintenance.

Results are presented in the form of graphs indicating the effect of control scheme on the system motion.

INHOMOGENEOUS RADIANT HEAT TRANSFER FROM SATURN-TYPE ROCKET EXHAUST PLUMES

By Robert M. Huffaker

ABSTRACT

A radiant heat transfer computer program has been developed by R-AERO-A to calculate radiation from inhomogeneous gases prevalent in Saturn-type exhaust plumes. The radiating species considered in this computer program are water vapor, carbon dioxide, carbon monoxide and carbon particles. The infrared spectral absorption characteristics of these species have been determined under NASA contract. Band model parameters have been used to represent the infrared spectral absorption coefficients over 25 cm^{-1} increments. A modified Curtis-Godson approximation is used in the inhomogeneous heat transfer calculation. This has been shown to give satisfactory results over the temperature and pressure range of interest in Saturn exhaust plumes. Results are shown for the Saturn-type engines for specific flow field assumptions. Some comparison with experimental spectroscopic data is also to be presented. The effect of wavelength increment, field of view, and distance increment along the line of sight on the heat transfer will be discussed. Computer techniques for minimum computer time in calculating radiation from a three-dimensional flow field will also be outlined.

THEORETICAL AND EXPERIMENTAL
INVESTIGATION OF HEATING FROM SATURN
SOLID PROPELLANT ROCKET EXHAUSTS

By William C. Rochelle

ABSTRACT

This paper presents both a theoretical and experimental analysis involving heating from Saturn solid propellant ullage and retrorocket exhausts. Experimental data and theoretical correlations are presented for seven MSFC-sponsored test programs performed at five different test facilities. The solid propellant motors tested were the S-II ullage motors, S-IB retromotors (same as S-II retromotors), S-IVB retromotors, S-IV ullage motors, and Centaur retromotors. Tests were performed at Arnold Engineering Development Center, Tullahoma, Tennessee (2 programs), Ordnance Aerophysics Laboratory, Daingerfield, Texas (2 programs), Cornell Aeronautical Laboratory, Buffalo, N. Y. (1 program), MSFC Test Laboratory (1 program), and Rocketdyne, McGregor, Texas (1 program).

All of the programs involved full scale motors and full duration firings except the Cornell program which involved 1/10 scale motors and components and short duration firings. All of the tests except the ones at the Rocketdyne facility involved altitude firings.

Excessive heating from these solid propellant motor exhausts can result in problems during separation of stages of the Saturn vehicles. Two major problem areas arise. The solid motor exhaust can either damage the nearby structure on the same stage on which the motors are mounted, or they can damage certain components on the stage from which they have separated. An example of the first case is the S-IB retro exhaust impinging on the S-IB/ S-IVB aft interstage, resulting in more insulation having to be added to the interstage. An example of the second case is the S-II ullage motor exhaust impinging on the S-IC ordnance disconnect and confined detonating fuse assembly, resulting in more insulation requirements and rerouting of the confined detonating fuse.

Experimental data from the tests were obtained by three general methods, (1) mounting instrumented probes directly in the flow to obtain stagnation-type measurements, (2) mounting instrumented flat plates or curved panels parallel or at a small angle to the flow to obtain flat plate-type measurements, and (3) viewing outside the plume with optical instrumentation. Instrumentation included the following: (1) total calorimeters (five tests), (2) radiation calorimeters (four tests), (3) pressure transducers (four tests), (4) radiometers (three tests), (5) spectrometers (three tests), and (6) ablation sensors (one test). In addition, physical erosion by solid particles was investigated in two tests and the effect of scaling was investigated in one test.

For the theoretical analysis, three different means of heating from the solid propellant exhausts were investigated, (1) gaseous convection, (2) solid particle radiation, and (3) solid particle impingement heating. For objects in which stagnation point heating theory was valid and where the particle mass flow was significant, the principal means of heating was solid particle impingement heating. For objects in which flat plate theory was valid, and where the particle mass flow was comparatively small, the principal means of heating was convection heating. Both one-phase plumes (real gas-equilibrium flow) and two-phase plumes (uncoupled method of characteristics program) were investigated theoretically. A theoretical Teflon ablation analysis was also performed to compare with experimental data.

It is believed that valuable data were obtained from these tests and that the theory checked fairly well with experiment in most of the tests. In some of the tests modifications to the theory were made because of the experimental data obtained.

━━━━━━━━━━

THE VERIFICATION OF A MATHEMATICAL MODEL WHICH REPRESENTS LARGE, LIQUID ROCKET-ENGINE EXHAUST PLUMES

By

R. C. Farmer,
Aero-Astrodynamics Lab, MSFC
Huntsville, Alabama

R. J. Prozan and L. R. McGimsey,
Lockheed Missiles and Space Company
Huntsville, Alabama

ABSTRACT

This paper presents a mathematical model which describes the exhaust plume of a single rocket engine and the experimental data which substantiate the model. The desired goal of this research was an accurate description of the thermal fields created by the F-1, H-1, J-2, and RL-10 engines. The model presented here is shown to be reasonably complete and accurate; its shortcomings and anticipated improvements are discussed.

This analysis consisted of the following phases: (1) an overall look at engine properties which cause the plume properties to be complex; (2) for the RP-1 fueled engines, a determination of an appropriate chemistry model; (3) a determination of which kinetic and thermochemical data was to be used; (4) the description of the fluid mechanics of the plume. The unique feature of this analysis is the inclusion of phase (1) and the consequences of this inclusion.

The first three phases are so basic to this analysis that few general statements can be made regarding them. Detailed investigation of these phases is presented in the paper. The only major observation is that, because the exhaust gases are fuel rich, afterburning must be included in a plume description.

The fluid mechanics of the flow was described by combining the output of the following computer programs:

1. A method of characteristics program with logic for crossing one shock for equilibrium of frozen flow was used to describe the inviscid nozzle and plume flow.

2. A frozen boundary-layer with mass injection program was used to describe nozzle wall effects.

3. A mixing program with equilibrium, frozen, or finite-rate chemistry with or without lateral pressure gradients was used to describe the free-shear layer.

4. Programs for describing multiple shocks and/or entirely viscous jets were used to describe the far field.

5. Streamline tracing programs were used to provide best possible estimates of local composition. Electrons were included as a component. Particular emphasis was given to the near plume so that reversed-gas properties could be estimated.

The bulk of experimental evidence used to substantiate this model was radiation measurements made with narrow view angle instruments. However, many of the finer points of the comparison were made with small scale rocket test results.

The mathematical model may be improved by refining component programs, but no comprehensive plume program is ever likely to replace the type presented here. The detailed comparisons presented in the paper indicate the accuracy of the model. This model is representative of the current progress of plume analysis and is more complete than any other published work.

━━━━━━━━━━

VELOCITY DEPENDENCE OF METEOR LUMINOUS EFFICIENCY AND CONSEQUENT STATISTICAL RESULTS

By

Charles C. Dalton

ABSTRACT

A systems analysis basis of decision between Öpik's and Verniani's velocity dependence of meteor luminous efficiency is given. A weighting function is used to transform Hawkins and Southworth's random sample of 285 sporadic photographic meteors into a random sample of meteoroids incident upon a randomly placed and randomly oriented surface at air-entry altitude. Each of the sample sets of mass values for the two luminous efficiency formulations is ranked with respect to material mass and partitioned at a mass value which gives subsets of comparable statistical weight. The extent to which the subsets of a set give different distributions of a parameter such as velocity tends to be more generally convincing than the numerical value of the linear correlation between that parameter and mass. The results favor Öpik's theory and give some basis, when a sufficiently large sample is used, for showing the directional dependence of the cumulative flux with respect to a function of mass and velocity.

AN ACOUSTIC WIND MEASURING TECHNIQUE

By

Wesley W. Bushman
University of Michigan
Ann Arbor, Michigan

Orvel E. Smith
Aero-Astrodynamics Lab, MSFC
Huntsville, Alabama

ABSTRACT

An atmospheric wind measurement technique has been developed and used to measure wind profiles over Cape Kennedy from ground to 85 kilometers The technique is an extension of the Rocket Grenade Experiment utilizing as its sound source, rather than a grenade, the acoustic noise of a rocket's exhaust. To determine the wind profile from this continuous sound source, a set of equations has been derived and applied to measurements made during the flights of several Saturn vehicles. The profiles agree well with concurrent measurements at lower altitudes (below 50 km) and are consistent with atmospheric circulation observations at higher altitudes. A preliminary error analysis indicates that the technique can be used to make measurements of sufficient precision to be useful in engineering and meteorological studies.

HEAT TRANSFER AND FLUID MECHANICS

By H. B. Wilson, Jr.

ABSTRACT

A short-duration technique has been developed which provides excellent simulation of thermodynamic properties and composition of the exhaust products of long-duration model and full-scale rocket engines using liquid or solid propellant. Flow durations through the scale model rocket nozzle (on the order of 10 milliseconds) are sufficient to achieve steady-state operation and alleviate many of the usual complex engineering problems associated with conventional continuous operating hot flow rocket models. The short-duration experimental technique has been employed in scaled Saturn booster studies in conventional wind tunnels at altitudes and velocities where external flow effects are important, as well as in the high altitude chamber where external flow effects can be neglected. The primary advantages of the short-duration approach are are: scale model testing may be done by an economical method that avoids the complex engineering and operational problems associated with the fueling, combustion, ignition and required cooling of conventional continuous-flow engines; high-altitude simulation is practical with a very modest vacuum pumping system; and reliable instrumentation techniques, particularly for heat transfer and pressure, which have been developed for hypersonic shock tunnel testing may be employed.

The short-duration technique has been used in conducting tests of a four-engine base configuration to determine the recovery temperature of the recirculating flow, the effects of Reynolds number on base film coefficient and recovery temperature, the effect of a temperature discontinuity on base film coefficient, and the influence of nozzle wall temperature on the recovery temperature of the recirculating flow.

The results show that the base film coefficient and recovery temperatures can be accurately obtained with the short-duration technique and that the recovery temperatures are approximately 40 percent of the chamber temperatures. The Reynolds number study showed that the variation in heat transfer coefficient and recovery temperature could be correlated with existing theory for laminar and turbulent flow through use of local heat shield parameters. The temperature discontinuity between the heat shield and heat transfer gages installed in the heat shield have significant effect on the heating rates. These trends are predicted by available theories. Many assumptions necessary in this prediction make it difficult to apply correction methods to all cases. Increases in recovery temperature are noted with increasing nozzle wall temperatures.

A short-duration wind tunnel capable of producing flow over a range of Mach numbers has been developed and is currently in operation with short-duration base heating tests. The short-duration wind tunnel and and some typical results are briefly described.